

## Copyright Undertaking

This thesis is protected by copyright, with all rights reserved.

**By reading and using the thesis, the reader understands and agrees to the following terms:**

1. The reader will abide by the rules and legal ordinances governing copyright regarding the use of the thesis.
2. The reader will use the thesis for the purpose of research or private study only and not for distribution or further reproduction or any other purpose.
3. The reader agrees to indemnify and hold the University harmless from and against any loss, damage, cost, liability or expenses arising from copyright infringement or unauthorized usage.

### IMPORTANT

If you have reasons to believe that any materials in this thesis are deemed not suitable to be distributed in this form, or a copyright owner having difficulty with the material being included in our database, please contact [lbsys@polyu.edu.hk](mailto:lbsys@polyu.edu.hk) providing details. The Library will look into your claim and consider taking remedial action upon receipt of the written requests.

**BASELINE-FREE ELECTROMECHANICAL  
IMPEDANCE TECHNIQUE FOR MATERIAL  
CHARACTERIZATION AND DELAMINATION  
DETECTION IN CONCRETE**

**SHA XIONG**

**PhD**

**The Hong Kong Polytechnic University**

**2025**

The Hong Kong Polytechnic University  
Department of Civil and Environmental Engineering

**Baseline-free electromechanical impedance technique  
for material characterization and delamination  
detection in concrete**

**SHA Xiong**

A thesis submitted in partial fulfilment of the requirements for the  
degree of Doctor of Philosophy

November 2024

## **CERTIFICATE OF ORIGINALITY**

I hereby declare that this thesis is my own work and that, to the best of my knowledge and belief, it reproduces no material previously published or written, nor material that has been accepted for the award of any other degree or diploma, except where due acknowledgement has been made in the text.

\_\_\_\_\_ (Signed)

\_\_\_\_\_ SHA Xiong (Name of student)



*To science and engineering  
for the art of understanding and shaping the world*

## ABSTRACT

Concrete is the most used construction material in modern society, and it is complex because of the anisotropy and inhomogeneity caused by its multiphase characteristics. As one of the smart materials, piezoelectric materials provide new opportunities to measure and understand concrete properties. When used together with piezoelectric materials, the electromechanical impedance (EMI) technique is a promising tool for localized monitoring/detection because of its high operational frequency range, high flexibility in sensor installation, and convenient implementation. In practice, the EMI technique can quickly and easily measure the electrical impedance of piezoelectric sensors, which are coupled with the mechanical impedance of the structures and the piezoelectric sensors.

Baseline-dependent EMI techniques, which attempt to correlate the variation of signals and changes of the structure via statistical indices obtained before and after damage, are popular in real practice. Although these techniques are easy to conduct and model-free, their results are greatly affected by sensor selection, bonding status, and temperature changes, thus limiting their applicability in actual structures. In contrast, baseline-free EMI techniques, which can utilize the mode shapes and corresponding resonant frequencies of target structures to evaluate structural features quantitatively, have rarely been reported, especially in the concrete field. In this thesis, baseline-free EMI techniques were systematically developed for concrete by using different types of sensors. Fixed and detachable piezoelectric sensors were employed to characterize concrete materials and detect delamination in the concrete cover, respectively.

Taking advantage of the easy installation of the surface-bonded sensor (SBP), a baseline-free EMI technique was proposed for the first time to quickly and accurately measure the modulus of elasticity of standard concrete cubes. The generality, repeatability, stability, and accuracy of the proposed method were validated regarding different piezoelectric sensors, bonding status, temperatures, and concrete mixes.

Then, the mode shapes of a concrete cube were carefully investigated, and special

modes that are insensitive to material anisotropy and inhomogeneity were selected. Subsequently, a novel SBP installation strategy for extracting the target modes and corresponding assessments was developed to accurately measure the elastic constants (including modulus of elasticity and Poisson's ratio) of concrete materials. The effectiveness and accuracy of the proposed method were validated on standard concrete cubes, and the method was compared with the traditional dynamic resonance method.

Given that an embeddable piezoelectric sensor (EBP) can be installed in advance, vibration modes of concrete cubes that are easy to identify and measure even at a high damping ratio were selected. The corresponding sensor installation and signal processing were developed to measure the concrete elastic properties at a very early age, which is a stage that traditional dynamic resonance methods can hardly cover. Effectiveness and accuracy of the proposed method were validated by comparing it with traditional dynamic resonance methods after demolding.

EBP was further utilized to widen the applicability of the baseline-free EMI technique in terms of element size. The length-insensitive vibration modes of a prism were selected, and the corresponding sensor installations and signal processing were developed to measure the modulus of elasticity. Effectiveness and accuracy of the proposed method were validated in comparison with that using global fundamental vibration modes.

Finally, the feasibility of the detachable sensor installation was investigated to increase applicability of the EMI technique to damage detection in a large area, and a baseline-free assessment was developed to detect the delamination of concrete cover. Effectiveness and robustness of the proposed method were validated by conducting laboratory tests and on-site trials.

Through systematic, comprehensive numerical and experimental studies, this thesis explores a series of innovative applications of the baseline-free EMI technique in concrete. The outcomes of this thesis offer an enhanced understanding of concrete materials/structures and pave a new avenue for applying EMI techniques.

## **PUBLICATIONS ARISING FROM THE THESIS**

### **Journal Papers**

Sha, X. and Zhu, S. (2024). “A baseline-free electromechanical impedance resonance method for measuring the modulus of elasticity of concrete cubes using surface-bonded PZT patches.” *Structural Control and Health Monitoring*, Article ID 6153935: 18 pages.

Sha, X. and Zhu, S. (2024). “Joint measurement of modulus of elasticity and Poisson’s ratio of concrete by actuating special vibration modes: a novel baseline-free technique.” *Journal of Sound and Vibration*, under review.

Sha, X. and Zhu, S. (2024). “A novel baseline-free electromechanical impedance technique for measuring the modulus of elasticity of very-early-age concrete cubes using embedded PZT sensors.” *Construction and Building Materials*, under review.

Sha, X. and Zhu, S. (2024). “Measure modulus of elasticity of concrete prisms by developing a baseline-free electromechanical impedance technique using length-insensitive resonant modes.” under preparation.

Sha, X. and Zhu, S. (2024). “Detecting the delamination of concrete cover by using detachable PZT sensors and electromechanical impedance resonance technique.” *Structural Health Monitoring*, under review.

### **Conference papers:**

Sha, X. and Zhu, S. (2023). “Direct strength prediction of concrete cubes using surface bonded PZT patch based electromechanical impedance resonance method.” SHMII-12: 12<sup>th</sup> International Conference on Structural Health Monitoring of Intelligent Infrastructure, Hangzhou, China, 19-22 October.

## ACKNOWLEDGEMENTS

What an amazing journey filled with memories of excitement and happiness.

First and foremost, I would like to express my utmost respect and gratitude to Prof. Songye Zhu for providing me with such a platform for free exploration and a project to let me dive in. I value and appreciate his constructive guidance, continuous support, insightful comments, and interesting sharing in academic and daily life over the last five years. I once had a dream in which he said, “Do something interesting and worth doing.” I took this statement as my goal, hoping my work meets this requirement.

I would also like to thank my academic colleagues for their support and constructive discussions during my thesis: Dr. Qinlin Cai, Dr. Zhipeng Chen, Dr. Yifei Xu, Dr. Qiuhan Meng, Dr. Zimo Zhu, Dr. Qianyi Chen, Dr. Lingfang Li, Mr. Yi-Ang Zhang, Mr. Kaiqing Liu, and Mr. Tommy Sui Yam Chan. Special thanks go to the groupmates and friends at PolyU for sharing joy in daily life, Dr. Yingyu Hua, Dr. Haorao Zuo, Dr. Shiguang Wang, Dr. Jiahao Huang, Dr. Shuling Hu, Mr. Jubin Lu, Ms. Jiayang Shen, Ms. Yiwen Li, Mr. Jian Zhang, Dr. Rongrong Hou, Dr. Xiaoyou Wang, Dr. Lu Zhang, Dr. Shuai Li, Dr. Jiachen Guo, and Mr. Jiancong Lao.

Special thanks go to my beloved fiancée, Ms. Aga Lu, for creating romantic love during the period of COVID-19. Additionally, I am grateful to my landlord, Ms. Ellen Man Ching Wat, for her warm care and daily concern over the past four years. Thanks also go to my friends outside of Hong Kong, Ms. Jianlan Ma, Mr. Yisheng Aku, Ms. Shiyi Jipa, Ms. Axing Ouluo, Ms. Guoguo Lewu, Ms. Yuanyi Liang, Ms. Luxi Pan, Mr. Hai Lan, Dr. Lanie Abi, Dr. Decai Mao, Mr. Amu Jili, Mr. Hati Mi, and Ms. Jinzhu Qubie. With the help of the Internet, we can share our lives and dreams.

Lastly, my deepest gratitude goes to my family members, Mr. Heize Shama, Ms. Guomo Aba, Ms. Ying Sha, Mr. Rigu Aer, and my relatives, for their unconditional love throughout my life.

# TABLE OF CONTENTS

<b>ABSTRACT.....</b>	<b>i</b>
<b>PUBLICATIONS ARISING FROM THE THESIS.....</b>	<b>iii</b>
<b>ACKNOWLEDGEMENTS .....</b>	<b>iv</b>
<b>TABLE OF CONTENTS .....</b>	<b>v</b>
<b>LIST OF FIGURES .....</b>	<b>x</b>
<b>LIST OF TABLES .....</b>	<b>xv</b>
<b>LIST OF ABBREVIATIONS .....</b>	<b>xix</b>
<b>LIST OF SYMBOLS .....</b>	<b>xxi</b>
<b>CHAPTER 1 INTRODUCTION.....</b>	<b>1</b>
1.1 Motivations.....	1
1.2 Objectives.....	3
1.3 Thesis Structure.....	3
<b>CHAPTER 2 LITERATURE REVIEW .....</b>	<b>7</b>
2.1 Standard Destructive Tests of Concrete Specimens.....	7
2.2 NDT Methods in Concrete Field.....	8
2.2.1 NDT Methods for Material Characterization .....	9
2.2.2 NDT Methods for Predicting Strength .....	20
2.2.3 NDT Methods for Detecting Concrete Delamination.....	24
2.3 EMI Technique in Concrete Field.....	30
2.3.1 Basic Concept and Principles of EMI Techniques .....	30
2.3.2 Sensor Types and Installations .....	36
2.3.3 Acquisition Devices and Setup.....	41
2.3.4 Signal Processing Methods.....	42
2.3.5 Applications in Concrete .....	53
2.4 Summary and Remarks .....	60
<b>CHAPTER 3 MEASURE MODULUS OF ELASTICITY OF CONCRETE CUBES USING SBP .....</b>	<b>66</b>
3.1 Introduction .....	66
3.2 Numerical Investigations on Suitable EMI Indicators .....	68

3.2.1 Numerical Simulation Setup.....	68
3.2.2 Repeatable Signature for Different Sizes of PZT Patches.....	71
3.2.3 Vibration Modes of Interested Peaks.....	73
3.2.4 Repeatability of Signal Characteristics with Different Thickness of Adhesive Layer.....	74
3.2.5 Repeatability of Signal Characteristics at Different Temperatures .....	76
3.2.6 Correlations between Signal Characteristics and Concrete Properties.....	78
3.3 Experimental Validations .....	81
3.3.1 Measurement of Modulus of Elasticity .....	81
3.3.2 Repeatability Tests for Different Types of Sensor Systems.....	86
3.3.3 Temperature Tests .....	89
3.4. Summary .....	91
<b>CHAPTER 4 MEASURE ELASTIC CONSTANTS OF CONCRETE CUBES USING SBPS .....</b>	<b>94</b>
4.1 Introduction .....	94
4.2 Principle and Assessment Procedure of the Improved Method .....	97
4.2.1 Vibration Modes Selection .....	97
4.2.2 Sensors Installation Strategies for Identifying Selected Modes .....	102
4.2.3 Evaluate Elastic Constants from Selected Modes .....	105
4.3 Accuracy and Stability Considering Multiple Influencing Factors.....	110
4.3.1 Modification Regarding Imperfect Edge Dimensions.....	110
4.3.2 Effect of Anisotropy .....	114
4.3.3 Effect of Concrete Skin .....	120
4.4 Experimental Validations .....	123
4.4.1 Measurement of Elastic Constants at 400 Days .....	124
4.4.2 Measurement of Elastic Constants in the First 28 Days .....	131
4.4.3 Measurement of Elastic Constants of Concrete Cores .....	138
4.5 Summary .....	141
<b>CHAPTER 5 MEASURING ELASTIC CONSTANTS OF VERY-ERALLY-AGE CONCRETE CUBES USING EBP .....</b>	<b>143</b>
5.1 Introduction .....	143

5.2 Vibration Modes Related to Shear Modulus .....	147
5.3 EBP Design and Installation Strategies.....	148
5.3.1 EBP Configuration .....	148
5.3.2 Installation Strategies .....	150
5.4 Numerical Investigations of the Proposed EMI-R Methods .....	151
5.4.1 Numerical Modeling of Concrete Cubes with EBPs .....	151
5.4.2 Signal Spectra and Captured Vibration Modes .....	152
5.4.3 Effect of Damping Ratio and Corresponding Signal Processing .....	154
5.4.4 Determination of Elastic Properties.....	158
5.5 Modification of the Proposed Methods .....	161
5.5.1 Effect of Edge Dimension Imperfection.....	161
5.5.2 Modification for inclusion of EBP .....	162
5.6 Experimental Validations .....	165
5.6.1 Experimental Preparation and Setup .....	166
5.6.2 Spectral Evolution in the First 48 Hours .....	172
5.6.3 Comparison with Different Testing Methods.....	175
5.6.4 Continuous Monitoring in First 10 Hours .....	179
5.6 Summary .....	182
<b>CHAPTER 6 MEASURING MODULUS OF ELASTICITY OF CONCRETE</b>	
<b>PRISMS USING LENGTH-INSENSITIVE RESONANT MODES.....</b>	<b>184</b>
6.1 Introduction .....	185
6.2 Concept and Identification of Length-insensitive Modes of a Prism.....	186
6.2.1 Concept of Length-insensitive Vibration Modes.....	186
6.2.2 Modal Density Variation with Different Symmetric Boundaries.....	188
6.2.3 Length-insensitive Modes with High Symmetries .....	190
6.3 Capture Length-insensitive Modes of a Prism in the EMI-R Technique.....	193
6.3.1 Different Installation Strategies and Actuation Mechanism.....	193
6.3.2 Modeling of Prisms with PZT Sensors.....	197
6.3.3 Length-insensitive Modes Captured by Proposed Installation Strategies ..	198
6.3.4 Effects of Lengths and Boundary Conditions on In-plane Modes .....	203
6.3.5 Correlations between Target Frequencies and Modulus of Elasticity .....	205



6.4 Experimental Validations .....	208
6.4.1 Experimental Design and Preparation .....	208
6.4.2 Spectra of Various Installation Strategies in Different Specimens .....	214
6.4.3 Evaluation Accuracy of Modulus of Elasticity.....	218
6.4.4 Advantages of Length-insensitive Modes at Early Curing Age .....	220
6.4.5 Effect of End Boundary Conditions .....	221
6.5 Summary .....	222
<b>CHAPTER 7 DETECT DELAMINATION OF CONCRETE COVER USING DETACHABLE SENSOR.....</b>	<b>224</b>
7.1 Introduction .....	224
7.2 Concept and Principle of Detachable PZT Sensors for Delamination Detection .....	226
7.2.1 Detachable PZT Sensors.....	226
7.2.2 Corrosion-induced Cracking and Spalling .....	229
7.2.3 Principle of Delamination Detection Using a Detachable PZT Sensor.....	230
7.3 Numerical Feasibility Study.....	232
7.3.1 Numerical Simulation Model .....	232
7.3.2 Signal Characteristics Regarding Different Damage Level .....	234
7.3.3 Effect of Bonding Layer .....	239
7.3.4 Effects of Slab Size and Boundary Conditions .....	241
7.3.5 Quantitative Analyses of the First Local Resonant Frequency .....	242
7.4 Laboratory Experimental Validations .....	246
7.4.1 Experimental Setup and Procedure.....	247
7.4.2 Damage Detection .....	250
7.4.3 Cutting Results for Verification .....	257
7.5 On-site Testing Validations.....	261
7.5.1 Site and Testing Information .....	262
7.5.2 Suspected Delamination Area and Corresponding Signals .....	263
7.5.3 Cover Opening for Verification.....	265
7.6 Summary .....	266
<b>CHAPTER 8 CONCLUSIONS AND FUTURE WORK .....</b>	<b>268</b>

8.1 Summary .....	268
8.2 Conclusions .....	270
8.3 Future Work .....	273
<b>REFERENCES.....</b>	<b>277</b>

## LIST OF FIGURES

Figure 1.1 Organization of the thesis .....	6
Figure 2.1 Testing setup for each resonant frequency in ASTM C215 [2019] using impact force and an accelerometer .....	11
Figure 2.2 Testing setup for ultrasonic pulse velocity in ASTM C597 [2022].....	14
Figure 2.3 Hypothetical relation between $\mu_{cd}$ and $\mu_{cs}$ and age for saturated concrete mixes [Anson and Newman, 1966].....	19
Figure 2.4 Schematic of the test setup and apparatus for impulse-response test [ASTM C1740, 2016].....	25
Figure 2.5 Schematic of the impact-echo method and principal for detecting a shallow delamination [Sansalone and Streett, 1997].....	27
Figure 2.6 Schematic of the GPR method and its signal of A-scan [Dinh and Gucunski, 2021] .....	29
Figure 2.7 Schematic diagram of test diagram of MIA and details of the impedance transducer [Cawley, 1985; Cawley and Nguyen, 1988] .....	32
Figure 2.8 Schematic diagram of a PZT actuator driven mechanical system represented by its structural impedance [Liang et al., 1994].....	33
Figure 2.9 Determination of structural natural frequency by electric admittance matching [Sun et al., 1994] .....	35
Figure 2.10 Interaction between PZT active sensor and a substructure [Giurgiutiu and Zagrai, 2002].....	36
Figure 2.11 Commonly used electrode patterns of the square piezoelectric patch.....	38
Figure 2.12 Comparison of the working frequency dimension ranges of the reviewed techniques .....	62
Figure 3.1 A quarter-model adopted for simulations .....	70
Figure 3.2 Effect of PZT size on different frequency ranges.....	72
Figure 3.3 Summary of vibration modes .....	74
Figure 3.4 Effect of thickness of the adhesive layer on different frequency ranges....	76

Figure 3.5 Temperature-induced changes in the PZT and adhesive materials.....	78
Figure 3.6 Effect of the properties of concrete material and regression results of the peaks .....	80
Figure 3.7 Test setup for measurement .....	82
Figure 3.8 The measured $\arctan(G/B)$ spectra for two batches of concrete.....	84
Figure 3.9 Test setup for measurement .....	85
Figure 3.10 Experimental validation of the repeatability of the signals .....	88
Figure 3.11 Test setup for temperature effects.....	89
Figure 3.12 Temperature effects on signals and evaluation results .....	91
Figure 4.1 Nine symmetric planes for a cube .....	98
Figure 4.2 First 73 vibration modes of a concrete cube from an isotropy model.....	100
Figure 4.3 First five equivalent isotropic vibration modes .....	101
Figure 4.4 Installation strategy EMI-I and its corresponding signal spectra .....	103
Figure 4.5 Strategy EMI-II and its corresponding signal spectra .....	105
Figure 4.6 Regression results for calculating $\mu_c$ .....	109
Figure 4.7 Dimension labels of the tested samples.....	115
Figure 4.8 Effect of anisotropy on the signal spectra of two proposed strategies .....	117
Figure 4.9 Anisotropy-induced evaluation errors with different methods.....	120
Figure 4.10 Schematics of the skin of the concrete for different samples .....	122
Figure 4.11 Effect of the skin of concrete on different methods.....	123
Figure 4.12 Experimental design for the measurement of the elastic constants by different methods .....	127
Figure 4.13 Comparison of different methods on evaluations.....	129
Figure 4.14 Specimens for various methods at different curing ages.....	131
Figure 4.15 Comparison of various methods at different curing age.....	134
Figure 4.16 Concrete core of the specimens C100-1 and C100-2 .....	139
Figure 5.1 Vibration modes only related to the shear modulus .....	148
Figure 5.2 Proposed sensor installation strategy and their actuation mechanism .....	150

Figure 5.3 Recorded EMI signals and the corresponding vibration modes .....	153
Figure 5.4 Simulated behaviors of the signal spectra with concrete hardening.....	156
Figure 5.5 Signal spectra after detrending processing .....	158
Figure 5.6 Normalized frequencies by mode E as a linear function of $\mu_c$ .....	160
Figure 5.7 Details of the sensor fabrication and installation .....	166
Figure 5.8 Test setup for the concrete monitoring .....	169
Figure 5.9 Test setup for standard dynamic and static tests.....	171
Figure 5.10 Experimental EMI signals in the first 24 hours as cubes with plastic molds .....	174
Figure 5.11 Experimental EMI signals at 24 and 48 hours as cubes demolded .....	174
Figure 5.12 Comparison of the evaluation results with and without modification regarding package effect (24-hour age of Batch I) .....	175
Figure 5.13 Comparisons of the evaluation results from the different testing methods .....	178
Figure 5.14 Evaluation results using the proposed EMI-R methods for the cubes with molds.....	179
Figure 5.15 Continuous monitoring using the proposed strategies in the first 10 hours .....	181
Figure 5.16 Evaluation results of continuous monitoring using the proposed EMI-based strategies in the first 10 hours .....	182
Figure 6.1 Symmetric planes of a prism .....	190
Figure 6.2 Mode shapes and corresponding frequencies of seven length-insensitive modes of prisms with high symmetries .....	192
Figure 6.3 Installation strategies of the PZT sensors in the prism adopted in this study .....	195
Figure 6.4 Schematic of the actuation type induced by different installation strategies on a concrete prism .....	196
Figure 6.5 EMI peaks and the corresponding resonant modes in different relative	

positions .....	200
Figure 6.6 Classic modes and selected modes from the different installation strategies .....	201
Figure 6.7 Behavior of mode $C_P$ and mode 1-L of concrete prisms with different lengths (EBP-E- $\perp$ ; $x=l/4$ ) .....	204
Figure 6.8 Behavior of mode $C_P$ at different boundary conditions (EBP-E- $\perp$ ; $x=l/4$ ) .....	205
Figure 6.9 PZT patches and embedded sensors used in this chapter .....	209
Figure 6.10 Design of layout of sensors in each specimen .....	210
Figure 6.11 Standard static tests for the modulus of elasticity .....	212
Figure 6.12 Installation of the embedded sensors and experimental setup for the EMI-R measurements .....	213
Figure 6.13 EMI Signal spectra of the SBP sensors from specimens P1, P2, and P3 at 28-day age .....	215
Figure 6.14 EMI Signal spectra of the EBP sensors at $x=l/4$ at 28-day age .....	216
Figure 6.15 EMI Signal spectra of the EBP sensors at $x=0$ at 28-day age .....	217
Figure 6.16 Comparisons of moduli of elasticity from different strategies (The results are normalized by $E_{cd}$ from mode 1-L) .....	219
Figure 6.17 The comparison of identification and accessibility of mode 1-L and length-insensitive modes at 1-day, 7-day, and 28-day age .....	221
Figure 7.1 Actuating mechanisms of the traditional fixed PZT sensor and the proposed detachable PZT sensor .....	228
Figure 7.2 The adopted PZT sensor and bonding tape .....	229
Figure 7.3 Crack types and development process of corrosion-induced spalling .....	230
Figure 7.4 Working principle of the detachable sensor for detecting the delamination of the concrete cover of a concrete slab .....	231
Figure 7.5 Geometric information of the numerical model .....	233
Figure 7.6 Different damage levels for simulating the spalling process .....	235

Figure 7.7 Signal spectra at different damage levels .....	238
Figure 7.8 Classic vibration mode shapes corresponding to the characteristic peaks in the spectra .....	239
Figure 7.9 Effect of the modulus of elasticity of the bonding layer .....	241
Figure 7.10 Effect of slab size and boundary conditions .....	242
Figure 7.11 Geometry of the specimen and details of the steel rebars .....	247
Figure 7.12 Experimental setup for the accelerated corrosion tests and delamination detection using the EMI technique .....	250
Figure 7.13 Signals comparison after 0 and 60 corrosion hours measured at different locations .....	251
Figure 7.14 Visual inspection of the concrete slab over time .....	252
Figure 7.15 Signal spectra of the checkpoints on Axes LO and RO at different statuses .....	254
Figure 7.16 Signal spectra of the checkpoints above the rebars at different statuses .....	255
Figure 7.17 Signal spectra of the checkpoints on Axis C at different statuses .....	256
Figure 7.18 Maps of the first resonant frequencies .....	257
Figure 7.19 Setup for slab cutting .....	257
Figure 7.20 Pictures of the cutting sections and schematics of the crack distributions .....	261
Figure 7.21 On-site testing procedures and details of the testing techniques .....	262
Figure 7.22 Suspected delamination area, checkpoints, and the corresponding EMI signals .....	264
Figure 7.23 Signal spectra from the impact-echo method .....	264
Figure 7.24 Signal spectra recorded at Point B at different times and with different sensors .....	265
Figure 7.25 Opening results for verification .....	266

## LIST OF TABLES

Table 1.1 Comparison among piezoceramic sensor-based NDT techniques .....	2
Table 2.1 Comparison of methods commonly used for measuring elastic constants ....	9
Table 2.2 Resonance methods for different materials in ASTM standards.....	12
Table 2.3 Resonance methods for measuring elastic constants of concrete .....	13
Table 2.4 UPV methods for concrete in standards.....	14
Table 2.5 UPV methods for measuring elastic constants of concrete materials .....	15
Table 2.6 Static and dynamic moduli correlations selected from the literature.....	17
Table 2.7 Useful compressive strength ranges for in-place NDT methods [ACI, 2003] .....	21
Table 2.8 Concrete strength estimated by resonance methods .....	23
Table 2.9 EBP for monitoring concrete by using EMI techniques .....	39
Table 2.10 Analytical models for extracting the mechanical impedance of the structure .....	48
Table 2.11 Baseline-free EMI techniques .....	52
Table 2.12 Summaries of applications of the EMI techniques for predicting the properties of concrete/cementitious materials .....	55
Table 2.13 Summary of the EMI techniques for hydrating concrete monitoring .....	57
Table 3.1 Material properties of PZT used in simulations.....	70
Table 3.2 Material properties of epoxy and concrete used in simulations.....	70
Table 3.3 Temperature dependence of material coefficients.....	77
Table 3.4 Summary of the simulation results of peaks a to d .....	81
Table 3.5 Mix proportions of the tested concrete materials.....	82
Table 3.6 Experimental results for $E_c$ measurement .....	85
Table 3.7 Results of repeatability of the indexes .....	89
Table 3.8 Temperature tests on the measurement results.....	91
Table 4.1 Symmetric type of for different types of modes .....	101
Table 4.2 Resonant frequency related to the changes in $\mu_c$ .....	108



Table 4.3 Effect of edge imperfections on the evaluation results of the proposed strategies .....	113
Table 4.4 Summary of assessment of the proposed methods regarding different anisotropy statuses .....	118
Table 4.5 Summary of the assessment by the prism regarding different anisotropy statuses .....	119
Table 4.6 Effect of the skin of concrete on the proposed methods .....	122
Table 4.7 Effect of the skin of concrete on the traditional testing methods.....	122
Table 4.8 Material proportions of the adopted concrete materials.....	125
Table 4.9 Experimental results of prisms from the traditional dynamic resonance and static tests .....	126
Table 4.10 Comparison of different testing methods .....	128
Table 4.11 Experimental results from the EMI-R methods .....	130
Table 4.12 Comparison of various methods at different curing age .....	133
Table 4.13 Experimental results from the traditional dynamic resonance method at different curing age .....	135
Table 4.14 Experimental results from the EMI-R methods at different curing age...	136
Table 4.14 Experimental results from the EMI-R methods at different curing age ( <i>Continued</i> ) .....	137
Table 4.15 Experimental results from the standard static method at different curing age .....	138
Table 4.16 Experimental results for the specimen C-100-1 and specimen C-100-2 before and after cutting .....	140
Table 4.17 Evaluation results of different methods for the intact and core cubes .....	140
Table 5.1 Summary of the NDT methods for measuring the elastic constants of concrete at early ages.....	146
Table 5.2 Symmetric type of the vibration modes only related to the shear modulus .....	148

Table 5.3 Material properties of epoxy and concrete for simulation .....	149
Table 5.4 Details of the different cases for simulating evolutions of concrete at early ages .....	155
Table 5.5 Frequencies of the target modes regarding the variation of Poisson's ratio .....	159
Table 5.6 Frequency of the target modes with cube imperfection .....	162
Table 5.7 Combinations in simulations for considering the package of the EBP .....	165
Table 5.8 Summary of the type and numbers of the specimens in this chapter .....	168
Table 5.9 Summary of test information of the standard dynamic tests .....	170
Table 5.10 Material properties of concrete from the first batch based on standard dynamic resonance tests .....	170
Table 5.11 Material properties of concrete from three batches based on the standard static tests .....	171
Table 5.12 Summary of test information of the standard static tests .....	172
Table 5.13 Dimensions and mass of the tested concrete cubes .....	176
Table 6.1 Numbers of vibration modes in various frequency ranges under different symmetric boundaries (Prism specimen: $150 \times 150 \times 550 \text{ mm}^3$ ) .....	190
Table 6.2 Details of different installation strategies .....	195
Table 6.3 Material properties of epoxy and concrete for simulation .....	198
Table 6.4 Regressed coefficients for the target length-insensitive modes .....	207
Table 6.5 Material proportions of the adopted concrete materials .....	210
Table 6.6 Summary of sensors and installation strategies for prisms P1–P7 .....	211
Table 6.7 Static properties of concrete of three batches .....	212
Table 6.8 Geometric information and density for each specimen .....	214
Table 6.9 Summary of the frequencies of target modes .....	217
Table 6.10 Summary of evaluations of selected modes using different installation strategies .....	219
Table 7.1 Material properties of adhesion and concrete .....	234

Table 7.2 The normalized first local defect resonance of a square defect .....	246
Table 7.3 Material proportions of the adopted concrete materials.....	248
Table 7.4 Corrosion time procedure at the wetting stage.....	249

## LIST OF ABBREVIATIONS

The main abbreviations used in this thesis are listed below:

1D	One dimensional
2D	Two dimensional
3D	Three dimensional
AC	Alternating current
CC	Cross-correlation
CCD	Cross-correlation deviation
CoV	Coefficient of Variation
EBP	Embeddable PZT sensor
EMI	Electromechanical impedance
FEM	Finite element method
FFT	Fast Fourier transform
GPR	Ground penetration radar
HSC	High-strength concrete
MAPD	Mean absolute percentage deviation
MIA	Mechanical impedance analysis
NC	Normal concrete
NDT	Nondestructive testing
PZT	Lead Zirconate Titanate
RC	Reinforced concrete
RMSD	Root mean square deviation
RUS	Resonance ultrasound spectroscopy
SBP	Surface-bonded PZT sensor
SDOF	Single-degree-of-freedom
SHM	Structural health monitoring
SSC	Seawater sea-sand concrete
UHPC	Ultra-high-performance concrete

UPV

Ultrasonic pulse velocity

## LIST OF SYMBOLS

$B$	Imaginary part of electric admittance
$E_c$	Modulus of elasticity of concrete
$E_{cd}$	Dynamic modulus of elasticity of concrete
$E_{ce}$	Modulus of elasticity obtained from the EMI technique
$E_{cs}$	Static or chord modulus of elasticity of concrete
$E_e$	Modulus of elasticity of epoxy
$E_g$	Modulus of elasticity of granite
$f_{1-B}$	Resonant frequency of the first bending mode
$f_{1-L}$	Resonant frequency of the first longitudinal mode
$f_{1-T}$	Resonant frequency of the first torsional mode
$f_{2-L}$	Resonant frequency of the second longitudinal mode
$f_c'$	Compressive strength of standard concrete cylinder
$f_{cp}$	Compressive strength of standard concrete prism
$f_{cu}$	Compressive strength of standard concrete cube
$f_{PZT}$	Resonant frequency of the first PZT peak
$f_p$	Flexural strength of standard concrete prism
$G$	Real part of electric admittance
$G_c$	Shear modulus of concrete
$G_{cd}$	Dynamic shear modulus of concrete
$G_{ce}$	Shear modulus obtained from the EMI technique
$G_{cs}$	Static shear modulus of concrete
$V_1$	Velocity of compressional stress waves
$V_s$	Velocity of shear stress waves
$Y$	Electric admittance
$Y_{11}^E$	Young's modulus of PZT material
$Z$	Electric impedance
$Z_{stru}$	Mechanical impedance of the structure system

$Z_{\text{PZT}}$	Mechanical impedance of PZT
$\mu_{\text{c}}$	Poisson's ratio of concrete
$\mu_{\text{cs}}$	Static or chord Poisson's ratio of concrete
$\mu_{\text{cd}}$	Dynamic Poisson's ratio of concrete
$\mu_{\text{ce}}$	Poisson's ratio obtained from the EMI technique
$\mu_{\text{e}}$	Poisson's ratio of epoxy
$\mu_{\text{g}}$	Poisson's ratio of granite
$\mu_{\text{PZT}}$	Poisson's ratio of PZT material
$\rho_{\text{c}}$	Density of concrete
$\rho_{\text{e}}$	Density of epoxy
$\rho_{\text{g}}$	Density of granite
$\rho_{\text{PZT}}$	Density of PZT material

# CHAPTER 1 INTRODUCTION

## 1.1 Motivations

The demands for employing structural health monitoring (SHM) and nondestructive testing (NDT) techniques in civil engineering have been increasing in recent years [McCann and Forde, 2001; Li et al., 2004; Song et al., 2008; Fan and Qiao, 2011; Kim et al., 2011]. Concrete, a multiphase material, is the most used construction material because of its ease of procurement, cost-effectiveness, and durability [Ji et al., 2023]. Accelerated construction of new structures and concrete degradation in old structures require effective SHM and NDT techniques to provide engineers with important in-situ information about concrete conditions [Rehman et al., 2016; Lim et al., 2021].

Piezoceramic, as one of smart materials, is widely utilized as actuators and/or receivers in SHM and NDT techniques because of its piezoelectricity. Curie brothers (Pierre and Jacques Curie) and Lippmann discovered direct and converse piezoelectric effects in 1880 and 1881, respectively [Trainer, 2003]. When the piezoceramic, a solid piezoelectric material, is applied with stress, it generates electric charge (i.e., direct piezoelectric effect); when the piezoceramic is applied with alternating voltage, it generates mechanical deformation (i.e., converse piezoelectric effect). Both effects are reversible. Lead zirconate titanate (PZT) is a common type of piezoceramic with high sensitivity. The PZT-based NDT techniques, such as wave propagation (WP), acoustic emission (AE), and electromechanical impedance (EMI) techniques, are widely applied in aerospace, mechanical, and civil structures [Yang and Qiao, 2005; Park et al., 2006; Li et al., 2016; Ji et al., 2023]. A comparison among these three piezoceramic sensor-based techniques is presented in Table 1.1. From the operability perspective, unlike the other two techniques, the EMI technique requires one impedance analyzer and one single sensor only for measurement, thus showing its ease of operation. The piezoceramic sensors used in EMI techniques act as actuators and receivers simultaneously. Moreover, the recorded data by EMI techniques are much less than



those by the other techniques because it can actively record the data in the frequency domain at the interested stage, thereby ensuring its ability to achieve automated testing.

Table 1.1 Comparison among piezoceramic sensor-based NDT techniques

Technique	Minimum number of sensors	Sensor role	Acquisition Device(s)	Signal type
WP	2	Actuator; Receiver	Wave generator, oscilloscope, amplifier	Time domain
AE	1	Receiver	Amplifier, datalogger	Time domain
EMI	1	Actuator cum receiver	Impedance analyzer	Frequency domain

EMI techniques provide accurate actuation and high-fidelity receiving in an extensive frequency range (from several kilohertz to several megahertz), showing its potential to detect local damage in large structures on sites [Song et al., 2013] and quantify the material properties of standard specimens in laboratories [Kong and Lu, 2020; Xie and Li, 2020].

However, the conventional assessment methods limited the further applications of EMI techniques; in most existing studies and applications of EMI techniques, damage or changes were identified by statistically comparing the signals from the inspection with “baseline” signals from the pristine condition of a structure [Kim et al., 2011; Zahedi and Huang, 2017]. Although baseline-dependent EMI techniques using statistical indices are model-free and easy to operate, the effective mechanical information of the target structures may be lost. In contrast, baseline-free EMI techniques are considered a more effective method to assess target structures by using their vibration modes [Giurgiutiu and Zagrai, 2002; Zagrai and Giurgiutiu, 2002; Yan et al., 2007; Kim et al., 2011; Kong and Lu, 2020; Xie and Li, 2020]. However, existing studies mainly focused on thin metal plates, beams, and cylindrical specimens in small

sizes, which cannot be directly extended to the concrete field, where structures or members are large and in diversified geometric shapes.

The following conclusions can be drawn from the literature review in [Chapter 2](#): (a) no effective baseline-free EMI technique is available for concrete structures or standard concrete specimens, and (b) how a baseline-free EMI technique may facilitate the understanding of concrete materials and structures is unclear. These two points are the initial motivation of this thesis, and systematic numerical and experimental studies were conducted to this end.

## **1.2 Objectives**

The major goal of this thesis is to propose, develop, and validate baseline-free EMI techniques that are suitable for concrete specimens, to improve the measurement accuracy of concrete properties, and to detect concrete cover damages that existing techniques could hardly cover, which is achieved on the basis of the in-depth investigation and understanding of the nature of various vibration modes. To accomplish this major goal, four specific objectives are listed as follows:

- (1) To develop a generalizable baseline-free framework for the EMI technique that can be applied to different materials and structures.
- (2) To utilize the proposed framework to tackle the challenges in measuring the elastic constants of concrete materials, such as Poisson's ratio and very-early-age properties of concrete.
- (3) To improve the applicability of the proposed EMI technique to large-size members, considering that fundamental resonances may be lower than the working frequencies of PZT sensors.
- (4) To enhance the flexibility of the EMI technique in detecting delamination in concrete covers, which exist in large areas of concrete structures and cannot be easily detected using the traditional NDT methods.

## **1.3 Thesis Structure**

The structure of the thesis to achieve the above-mentioned objectives is presented

in [Figure 1.1](#). Eight chapters are included in the thesis. The main content can be divided into two parts: material characterization and delamination detection. These two parts were achieved using fixed and detachable PZT sensors, respectively. Fixed sensors were employed for material characterization in laboratories, and detachable sensors with high installation flexibility were used for in-situ delamination detection. For the fixed sensors, surface-bonded PZT (SBP) sensors that are easy to install were utilized to measure the elastic constants after demolding. Embeddable PZT (EBP) sensors that could be embedded in concrete in advance were utilized for measuring the elastic constants shortly after casting and extracting length-insensitive modes. The detachable sensor was used for delamination detection to achieve large area detection using a single mobile sensor only. The specific objective for each chapter is presented below.

[Chapter 1](#) (i.e., this present chapter) introduces the research background and motivation first and then presents the research objectives and scope of work of this thesis.

[Chapter 2](#) reviews the current applications and limitations of NDT methods in concrete materials characterization and concrete cover delamination detection. Then, state-of-the-art reviews of EMI techniques are provided from the perspectives of the concepts, sensors, data acquisition devices, assessments, and applications in the concrete field.

[Chapter 3](#) develops a methodology for the baseline-free EMI technique by utilizing a standard concrete cube and an SBP. Considering that a quantitative and general evaluation method suitable for different materials and temperatures is desirable, the baseline-free EMI technique utilizes signal characteristics that are highly related to the target structures and insensitive to the properties of PZT sensors and bonding materials, showing superior applicability for measuring the modulus of elasticity stably, quickly, and accurately.

[Chapter 4](#) introduces a new method that utilizes a standard concrete cube installed with two SBPs to achieve accurate measurements of two elastic constants (namely,

modulus of elasticity and Poisson's ratio) by improving the baseline-free EMI technique in [Chapter 3](#). The evaluation results were examined in terms of material anisotropy and inhomogeneity, outperforming the traditional resonance methods with respect to stability and accuracy. The evolution of the elastic constants from 1-day to 28-day ages is presented.

[Chapter 5](#) reports a new method that employs a standard concrete cube installed with an EBP to achieve accurate measurements of two elastic constants (i.e., shear modulus and Poisson's ratio) at a very early age (i.e., within 12 hours after casting) that the traditional resonance methods cannot cover properly. The proposed method presents the evolution of the elastic constants in the first 24 hours.

[Chapter 6](#) presents a new framework for a baseline-free EMI technique using the EBPs, which takes advantage of length-insensitive modes and symmetry concepts to extend its applicability in terms of element sizes. The proposed method evaluated the modulus of elasticity of the concrete prism, and its accuracy was compared with that of the traditional methods.

[Chapter 7](#) presents a new baseline-free EMI technique that utilizes a detachable sensor to increase the flexibility of examining large areas of concrete structures. The proposed method was mainly designed to detect the delamination of concrete covers for indoor concrete structures. Comprehensive studies, including numerical feasibility, laboratory validation, and on-site verification, are presented to show the effectiveness of the proposed method.

[Chapter 8](#) summarizes the major works and presents the major conclusions of this thesis. It discusses the limitations and future works of the investigated baseline-free EMI techniques at the material and structural levels.

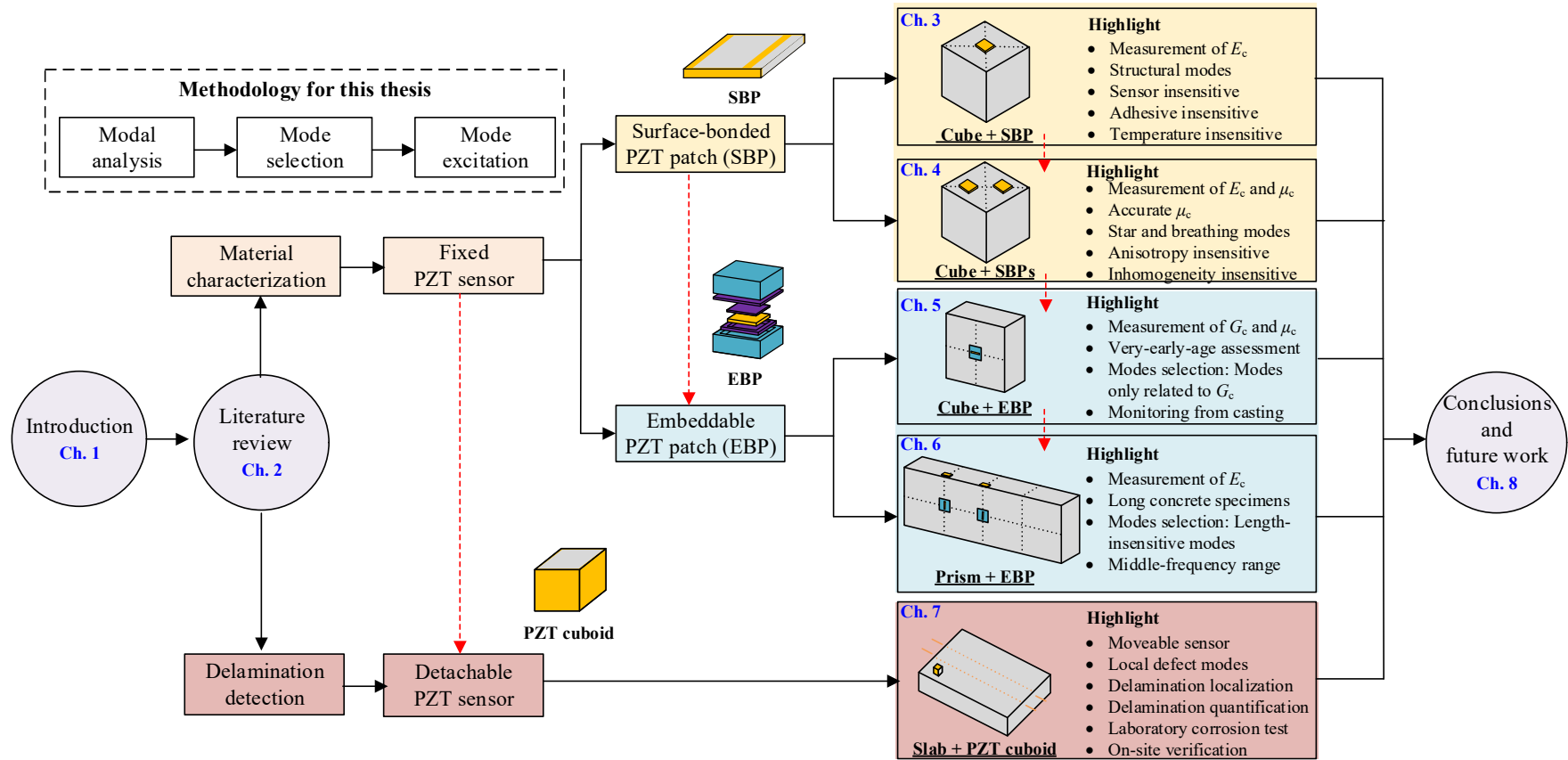


Figure 1.1 Organization of the thesis

## CHAPTER 2 LITERATURE REVIEW

This chapter reviews past research in the concrete field relevant to the work presented in this thesis. The review starts with the standard destructive tests for concrete, followed by the NDT methods commonly used for concrete, focusing on the material characterization and in-place active delamination detection. Subsequently, the available EMI techniques in the concrete field are reviewed. Finally, summaries and remarks are presented.

### 2.1 Standard Destructive Tests of Concrete Specimens

The measurement of elastic constants is vital in material characterization [Li and Gladden, 2010]. Static modulus of elasticity ( $E_{cs}$ ) and Poisson's ratio ( $\mu_{cs}$ ) are the two most used elastic constants for concrete under the assumption of isotropic materials. For example, the accurate measurement or prediction of  $E_{cs}$  was crucial to the long-term performance of reinforced and prestressed concrete structures [Vakhshouri, 2018]. Traditionally, these elastic constants are measured from destructive uniaxial compressive tests using concrete cylinders or prisms according to standards and design codes, such as ASTM C469/C469M [2022] and GB/T 50081 [2019].  $E_{cs}$  and  $\mu_{cs}$  are derived from two points in the stress-strain curve under longitudinal compressive stress [ASTM C469/C469M, 2022]. Therefore,  $E_{cs}$  and  $\mu_{cs}$  are also known as the chord modulus of elasticity and chord Poisson's ratio, which are considered to represent the initial tangential elastic constants of concrete [Carrazedo et al., 2017]. The first point for the calculation is selected at a very small stress or strain. For example, 0.5 MPa and 50  $\mu\epsilon$  are recommended in GB/T 50081 [2019] and ASTM C469/C496M [2022] for stress and strain, respectively. The second point for the calculation is typically a percentage of the compressive strength, such as 33% and 40% in GB/T 50081 [2019] and ASTM C469/C469M [2022], respectively. The stress can be derived from the force measured by load cells, and the strain can be measured by displacement sensors or strain gauges. Although the static destructive methods are simple to conduct, they have some limitations. Regarding the experimental process, destructive methods require many

specimens to be prepared to obtain the long-term performance of concrete materials. For example, three identical specimens are needed to measure the mechanical properties of concrete at the target curing age due to the low stability of the testing methods. Meanwhile, the in-place elastic properties of concrete structures cannot be measured directly [Popovics, 2008]. Moreover, the experiments are time-consuming and labor-intensive. The accuracy of the evaluation results is limited, and the stability is low [Carrazedo et al., 2017].

In practice, values of  $E_{cs}$  are usually estimated from compressive strength, especially in most construction projects [Vakhshouri, 2018]. For example, ACI 318-08 [2008] provides two empirical equations to estimate  $E_{cs}$ , as shown in Equations (2.1–2.2)

$$E_{cs} = 4730(f'_c)^{0.5} \text{ (in MPa)} \quad (2.1)$$

$$E_{cs} = 0.043(\rho_c)^{1.5}(f'_c)^{0.5} \text{ (in MPa)} \quad (2.2)$$

where  $f'_c$  is the compressive strength according to ASTM C39/C39M [2020]. It is worth highlighting that the different design codes provide different empirical models for estimating  $E_{cs}$ . Vakhshouri [2018] demonstrated that Equation (2.2) was relatively compatible with the random test results after comparing the estimated  $E_{cs}$  by using 54 models.

## 2.2 NDT Methods in Concrete Field

Many NDT methods have been developed for assessing civil engineering structures (including concrete structures). They are based on diverse principles and produce different sets and types of information that can reflect structural physical properties [McCann and Forde, 2001]. These properties, such as wave velocities and resonant frequencies, can be interpreted and correlated to other engineering properties. ACI 228.2 R-98 [2004] pointed out that NDT methods are utilized in concrete construction for quality control in new construction, quality assurance in repair works, and condition assessment in existing structures. McCann and Forde [2001] considered that NDT could provide a better understanding of material properties and complex

structures and help improve modeling in the future.

### 2.1.1 NDT Methods for Material Characterization

NDT methods are considered effective alternative tools to measure the elastic constants of solids. It can quickly estimate  $E_{cs}$  without destruction and provide more information on the tested specimens, such as uniformity. Table 2.1 presents the commonly used methods for measuring elastic constants. Pulse-echo method and resonance ultrasound spectroscopy (RUS) are the most used methods that utilize the sound velocity and free vibration frequencies, respectively. Both techniques employed ultrasonic transducers, such as piezoelectric transducers. However, RUS methods are only suitable for small sizes and materials with high-quality factors because high viscoelastic damping of materials (e.g., quality factor equals 20) results in the overlapping of resonant peaks, causing difficulties in assessment [Cai et al., 2017]. For these reasons, their applications to concrete have not been realized yet.

Table 2.1 Comparison of methods commonly used for measuring elastic constants

Main parameters measured/computed	Representative methods
Stress-strain	Quasi-static, indentation
Resonant frequency	Resonance, RUS
Velocity of wave	Pulse-echo, continuous wave

Note: RUS refers to Resonant ultrasound spectroscopy

#### 2.2.1.1 Stress-strain Method

Besides the static method, the quasi-static and indentation methods also utilized to measure the stress-strain curve to evaluate the elastic constants of target material [Li and Gladden, 2010]. The quasi-static method loads the specimen with a small, harmonic external force. The frequency of the external force is much lower than the fundamental resonant frequencies of the specimen. The quasi-static method is widely used in asphalt materials [ASTM D3497-79, 2003]. The indentation method continuously measures the penetration depth as a function of the imposed indentation load in the target specimen surface through measurement of the localized contact response [Constantinides et al., 2003]. Then, the elastic constants can be determined from the continuous record.



### 2.2.1.2 Resonance Method

Resonance is one of the popular NDT methods in the concrete field. It is easy and quick to conduct and nearly 10 times faster than static tests [Thomaz et al., 2021]. ASTM C215 [2019] provides the standard testing procedures for measuring the dynamic elastic constants of concrete, as shown in Figure 2.1. The impact excitation and an accelerometer are recommended. Kolluru et al. [2000] defined elastic constants of concrete measured at low-strain levels using NDT methods as dynamic elastic constants.

The fundamental transverse (or bending) and longitudinal (or compressional) modes are measured to calculate dynamic modulus of elasticity ( $E_{cd}$ ), and the fundamental torsional mode is used to derive dynamic shear modulus ( $G_{cd}$ ). Then, the dynamic Poisson's ratio ( $\mu_{cd}$ ) is obtained using the correlations under the isotropic assumptions. Equations (2.3–2.6) present the equations for calculating the dynamic elastic constants,

$$f_{1-L} = \frac{1}{2l_c} \sqrt{\frac{E_{cd}}{\rho_c}} \quad (2.3)$$

$$f_{1-B} = \frac{1}{\sqrt{0.9464T}} \frac{1}{l_c} \frac{h_c}{l_c} \sqrt{\frac{E_{cd}}{\rho_c}} \quad (2.4)$$

$$f_{1-T} = \frac{1}{\sqrt{R}} \frac{1}{2l_c} \sqrt{\frac{G_{cd}}{\rho_c}} \quad (2.5)$$

$$\mu_{cd} = \frac{E_{cd}}{2G_{cd}} - 1 \quad (2.6)$$

where  $f_{1-L}$ ,  $f_{1-B}$ , and  $f_{1-T}$  are the resonant frequencies of the first longitudinal, bending, and torsional modes, respectively;  $l_c$  and  $h_c$  are the length and height of the specimens, respectively;  $T$  is the shape factor that depends on the ratio of the radius of gyration, while  $R$  is the shape factor depends on the section dimensions only and equals to 1.183 for a square cross-section prism.

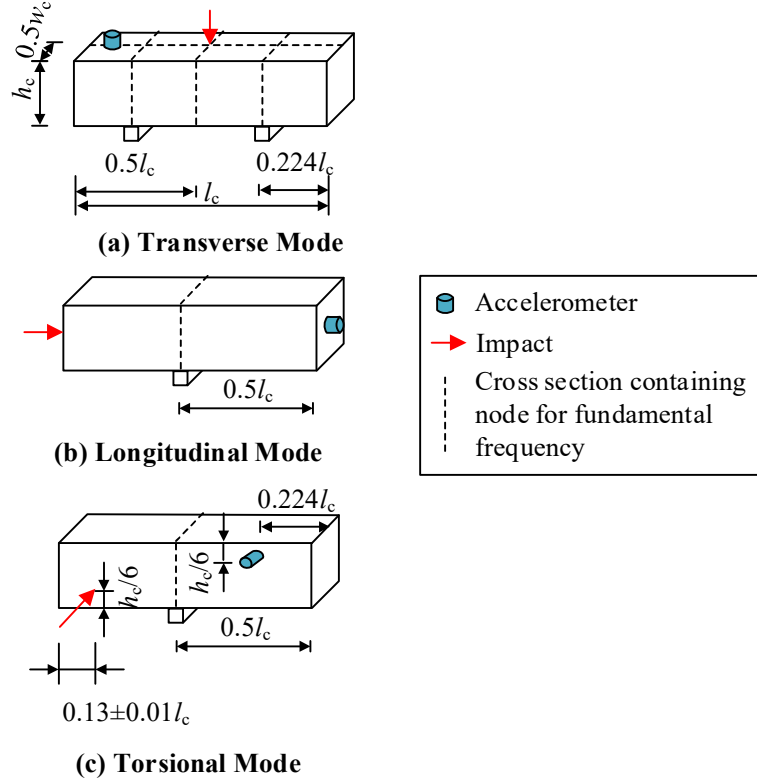


Figure 2.1 Testing setup for each resonant frequency in ASTM C215 [2019] using impact force and an accelerometer

Table 2.2 summarizes the resonant methods for different materials in ASTM standards, including concrete materials. The resonance methods can be classified as continuous excitation (i.e., sonic) and impulse excitation (i.e., impact) according to how the specimens are excited [Smith et al., 1990]. Impact excitation can provide accuracy close to the sonic excitation results but combines rapid testing and simplicity. Although prisms and cylinders are selected as the specimens for most standards, the prisms are preferred because of the great testing difficulties in capturing torsional resonant frequencies from a cylindrical specimen [ASTM C848, 2020; ASTM C1198, 2020]. Consequently, without the torsional mode,  $G_{cd}$  and  $\mu_{cd}$  cannot be calculated from the evaluation methods in the ASTM standards. Notably, in the test setup shown in Figure 2.1, the resonant frequencies of different mode types are obtained using separate corresponding testing setups. An accelerometer is employed to record the signals. Regarding the requirements on dimensions, in most standards, length-to-width (or

length-to-diameter) ratio of the specimen is from 2 to 5, because very small or large ratios lead to difficulties in actuating the fundamental vibration modes.

Table 2.2 Resonance methods for different materials in ASTM standards

Code	Material	Excitation type	Specimen shape	Dimension required
<a href="#">ASTM C215 [2019]</a>	Concrete	Impact	Prism; cylinder	$2 \leq \text{Length-to-width or length-to-diameter ratios} \leq 5$
<a href="#">ASTM C747 [2023]</a>	Carbon and graphite	Impact	Prism; cylinder	$5 \leq \text{Length-to-thickness or length-to-diameter ratios} \leq 20$
<a href="#">ASTM C848 [2020]</a>	Ceramic whiteware	Sonic	Prism; cylinder	Prism: $125 \times 15 \times 6 \text{ mm}^3$ Cylinder: $125 \text{ mm} \times 10\text{--}12 \text{ mm}$
<a href="#">ASTM C1198 [2020]</a>	Advanced ceramic	Sonic	Prism; cylinder	Prism: $75 \times 15 \times 5 \text{ mm}^3$ Cylinder: $125 \text{ mm} \times 6 \text{ mm}$
<a href="#">ASTM C1259 [2021]</a>	Advanced ceramic	Impact	Disc	Diameter-to-thickness ratio $\geq 4$
<a href="#">ASTM C1548 [2002]</a>	Refractory materials	Impact	Prism	$2 \leq \text{Length-to-width ratio} \leq 5$

Besides the methods recommended by the ASTM standards, several researchers attempted to measure the elastic constants using resonance methods but with different setups or signal processing methods. [Table 2.3](#) summarizes other resonance methods for measuring the elastic constants of concrete. [Kolluru et al. \[2000\]](#) utilized the first two longitudinal modes to calculate the  $E_{cd}$  and  $\mu_{cd}$  using standard cylinders (with a length-to-diameter ratio of 2) and an accelerometer. The  $\mu_{cd}$  is calculated using a frequency ratio of  $f_{2-L}/f_{1-L}$ , and then  $E_{cd}$  is obtained by substituting the  $\mu_{cd}$  into the regressed equations. [Wang et al. \[2015\]](#) utilized  $f_{1-B}$  and  $f_{1-T}$  of free slabs to calculate the  $E_{cd}$  and  $G_{cd}$ , respectively. Then,  $\mu_{cd}$  was measured using strain gauges in a steady-state test with a frequency equal to  $f_{1-B}$ . [Chen and Leon \[2019\]](#) adopted the same experimental setup recommended by [ASTM C215 \[2019\]](#) but improved the evaluation methods. The predefined  $\mu_{cd}$  was removed when using  $f_{1-B}$ ,  $f_{1-T}$  and the frequency ratio

$f_{1-T}/f_{1-B}$  were measured and employed to calculate the  $G_{cd}$  and  $\mu_{cd}$ , respectively, and then  $E_{cd}$  was derived using  $G_{cd}$  and  $\mu_{cd}$ .

Kong and Lu [2020] employed the EMI technique to measure the  $f_{1-L}$  and  $f_{2-L}$  using standard cylinders and embedded piezoelectric patches and then evaluated the  $E_{cd}$  and  $\mu_{cd}$  using the equations established by Kolluru et al. [2000]. This technique is called EMI-R technique to differentiate it from the traditional EMI technique. Liu et al. [2023] employed the EMI technique to measure the  $f_{1-L}$  and  $f_{1-T}$  using special cylinders (40 mm  $\times$  120 mm) and PZT rings.  $E_{cd}$  and  $G_{cd}$  were calculated using equations established in advance, which was the so-called quantitative EMI (Q-EMI) method. A more detailed review of the EMI techniques is presented in Section 2.3.4.

Table 2.3 Resonance methods for measuring elastic constants of concrete

Reference	Specimen type	Sensor type	Measured	No. <sup>b</sup>	Elastic constants
Kolluru et al. [2000]	Standard cylinder	Accelerometer	$f_{1-L}; f_{2-L}$	1	$E_{cd}, \mu_{cd}$
Wang et al. [2015]	Slab	Accelerometer	$f_{1-B}; f_{1-T}$	2	$E_{cd}, G_{cd}$
		Strain gauges	Dynamic strains <sup>a</sup>	1	$\mu_{cd}$
Chen and Leon [2019]	Prism	Accelerometer	$f_{1-B}; f_{1-T}$	2	$E_{cd}, G_{cd}, \mu_{cd}$
Kong and Lu [2020]	Standard cylinder	PZT patches	$f_{1-L}; f_{2-L}$	1	$E_{cd}, \mu_{cd}$
Liu et al. [2023]	Special cylinder	PZT rings	$f_{1-L}; f_{1-T}$	2	$E_{cd}, G_{cd}$

<sup>a</sup>Dynamic strains: values are tested using the quasi-static method.

<sup>b</sup>No.: number of independent tests for measuring the target physical quantity

#### 2.2.1.3 Ultrasonic Pulse Velocity (UPV) Method

The ultrasonic pulse velocity (UPV) method is another popular NDT method in the concrete field. Figure 2.2 presents the experimental setup for the UPV methods in ASTM C597 [2022]. Two ultrasonic transducers act as an actuator and a receiver, respectively. In the given length, the actuator generates pulses of longitudinal ultrasonic

stress waves. After transmitting through the concrete, pulses are recorded by the receiver. Then, the velocity of the compressional stress waves ( $V_l$ ) is calculated by dividing  $l_c$  by transit time  $t$ . Furthermore, the compressional stress wave velocity  $V_l$  can be expressed as follows,

$$V_l = \sqrt{\frac{E_{cd}(1 - \mu_{cd})}{\rho_c(1 + \mu_{cd})(1 - 2\mu_{cd})}} \quad (2.7)$$

where  $E_{cd}$  is measured from the resonance methods using the 1<sup>st</sup> longitudinal mode, which is considered independent of the  $\mu_{cd}$  in the related standards. Equation (2.7) indicates that the UPV methods cannot measure two elastic constants using only one set of devices. In practice, researchers often fixed  $\mu_{cd}$  and calculated  $E_{cd}$ , as the modulus of elasticity is a more important parameter [Popovics, 2008; Lu et al., 2013; Lee et al., 2017; Thomaz et al., 2021]. A Poisson's ratio of 0.2 is reasonable for common concrete in practice. Table 2.4 presents two commonly used standards for concrete materials that combine the resonance and UPV methods to estimate two elastic constants.

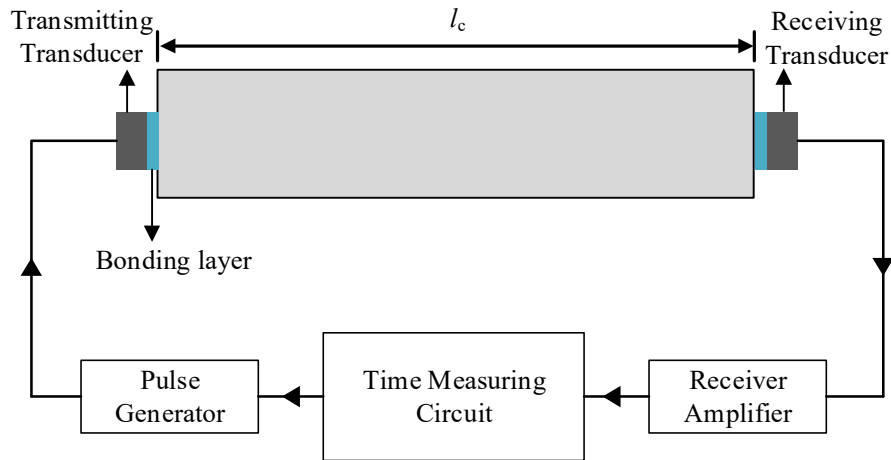


Figure 2.2 Testing setup for ultrasonic pulse velocity in ASTM C597 [2022]

Table 2.4 UPV methods for concrete in standards

Standards	Method	Measurements	Elastic constants
BS 1881	Resonance	First longitudinal mode	$E_{cd}$
[1986]	UPV	Compressional wave	$\mu_{cd}$
ASTM C597	Resonance	First longitudinal mode	$E_{cd}$
[2022]	UPV	Compressional wave	$\mu_{cd}$

Table 2.5 presents other UPV methods for measuring the elastic constant of concrete materials by using different setups from the above standards. In the listed references, shear wave velocity ( $V_s$ ) was utilized together with  $V_l$  to calculate  $E_{cd}$  only or both  $E_{cd}$  and  $\mu_{cd}$ , where the shear wave velocity can be expressed as

$$V_s = \sqrt{\frac{E_{cd}}{2(1 + \mu_{cd})\rho_c}} \quad (2.8)$$

KrauB and Hariri [2006] investigated the properties of concrete at early ages using  $V_l$  and  $V_s$ . Their results showed that  $\mu_{cd}$  could be measured from 5 hours and decreased from 0.45 to 0.26 in the first 100 hours. Yu et al. [2020] utilized the Rayleigh wave velocity to measure  $E_{cd}$  in concrete slabs using SBPs. Bezerra et al. [2023] presented the calculated  $\mu_{cd}$  using the  $V_l$  and  $V_s$ , ranging from 0.26 to 0.44, which is considerably larger than the classic value (i.e., 0.2).

Table 2.5 UPV methods for measuring elastic constants of concrete materials

Reference	Specimen type	Sensor type	Measured	Elastic constants
KrauB and Hariri [2006]	Designed specimen	Ultrasonic transducers	$V_s, V_l$	$E_{cd}, \mu_{cd}$
Lee et al. [2017]	Standard cylinder	Ultrasonic transducers	$V_s, V_l$	$E_{cd}$
Yu et al. [2020]	Slab	SBP	Rayleigh wave velocity	$E_{cd}$
Bezerra et al. [2023]	Standard cylinder	Ultrasonic transducers	$V_s, V_l$	$E_{cd}, \mu_{cd}$

#### 2.2.1.4 Comparison of Resonance and UPV Methods

Two types of  $E_{cd}$  obtained from the resonance and UPV methods individually are reviewed. From the perspective of the evaluation differences, although both are called dynamic modulus of elasticity,  $E_{cd}$  values from two dynamic tests are inconsistent with each other, wherein the UPV method often provides higher evaluations than the resonance methods [Popovics, 2008; Thomaz et al., 2021]. Within the resonance methods, Carrazedo et al. [2018] and Bassim and Issa [2020] showed that the values of  $E_{cd}$  from  $f_{1-B}$  are 2% and 1.3% higher than those from  $f_{1-L}$ , respectively. It can be

concluded that they are almost coincident [Swamy and Rigby, 1971; Carrazedo et al., 2018; Thomaz et al., 2021].

From the perspective of the stability of the results, within the resonance methods, values from  $f_{1-L}$  showed a lower dispersion than those from  $f_{1-B}$  [Carrazedo et al., 2018]. The comparison between the UPV and resonance methods indicated that values from  $V_l$  showed comparable dispersion with those from  $f_{1-B}$  [Lee et al., 2017].

#### 2.2.1.5 Correlations between Dynamic and Static Elastic Constants

After successfully measuring the dynamic elastic constants of concrete, their correlations with the static elastic constants can be discussed.

##### *Modulus of Elasticity*

Several attempts have been made to correlate static and dynamic moduli of elasticity for concrete (i.e., the relationship of  $E_{cs}$ - $E_{cd}$ ) through empirical relations, which are summarized in Table 2.6. Values of  $E_{cs}$  are measured according to ASTM C469/C469M [2022], and values of  $E_{cd}$  are measured according to ASTM C215 [2019] or ASTM C597 [2022]. Researchers employed different formulas to correlate these two moduli, including linear fitting without density, and power function fitting with and without density. It is worth highlighting that all these relationships were established at the 28-day curing age, which shows an apparent limitation.

Researchers have investigated the reasons for the difference between  $E_{cd}$  and  $E_{cs}$  in the past few years. From the perspective of definition,  $E_{cs}$  is the chord value from the stress-strain curve, and  $E_{cd}$  is assumed to be the initial tangent modulus [Bassim and Issa, 2020]. In other words,  $E_{cs}$  is measured at a relatively large strain level, while  $E_{cd}$  is measured at a very low strain level. In addition, static testing is usually conducted at relatively large elastic strains and low strain rates (e.g., 1 mm/min is recommended by ASTM C469/C469M [2022], equals to  $5.56 \times 10^{-5} \text{ s}^{-1}$  for the standard cylinder having 300-mm height), while dynamic testing involves small strain (on the order of  $10^{-6}$ ) and high strain rates [Smith et al., 1990]. The nonlinear behavior of concrete provides a basis for the conventionally accepted view of why  $E_{cd}$  is higher  $E_{cs}$  [Popovics, 2008].

Han and Kim [2003] presented that the initial chord modulus of elasticity measured at a low strain level (i.e., 10-50  $\mu\epsilon$ ) was close to the  $E_{cd}$  measured using  $f_{1-L}$ .

Table 2.6 Static and dynamic moduli correlations selected from the literature

Reference	$E_{cd}$ - $E_{cs}$ relationship	Unit of measure	ASTM standards	
			$E_{cs}$	$E_{cd}$
Popvics [1975]	$E_{cs}=0.23E_{cd}^{1.4}\rho_c^{-1}$	psi for $E$ lb/cu ft for $\rho_c$	C469/C 469M	C215: $f_{1-L}, f_{1-B}$
Lydon and Balendran [1986]	$E_{cs}=0.83E_{cd}$	-	C469/C 469M	C215: $f_{1-L}$
Mesbah et al. [2002]	$E_{cd}=9\times 10^{-11}(65E_{cs}+1600)^{3.2}$	MPa	C469	C597
Lee et al. [2017]	$E_{cs}=0.16E_{cd}^{1.36}$	GPa	C469	C597
Carrazedo et al. [2018]	$E_{cd}=0.813E_{cs}+12.304$	GPa	C469	C215: $f_{1-B}$
Bassim and Issa [2020]	$E_{cs}=0.84E_{cd}-0.74$	GPa	C469	C215: $f_{1-B}$

Note:  $f_{1-B}$  and  $f_{1-L}$  refer to the frequencies of the first bending and longitudinal modes, respectively.

Mehta and Monteiro [1993] presented that the difference between  $E_{cd}$  and  $E_{cs}$  decreases as concrete strength increases:  $E_{cd}$  is generally 20, 30, and 40% higher than  $E_{cs}$  for high-, medium-, and low-strength concrete, respectively. Lu et al. [2012] found that the type of aggregate has unignorable effects on the relationship of  $E_{cs}$ - $E_{cd}$ . For hard aggregates like limestone,  $E_{cs}$  is only 5-8% lower than  $E_{cd}$ , but for weak aggregates like schist, the difference rises sharply to 40-45%. Zhou et al. [2015] presented that the aggregate volume content and maximum size are dominant factors in the relationship



of  $E_{cs}-E_{cd}$ , where  $E_{cd}$  was obtained using  $f_{1-L}$ . Thomaz et al. [2021] presented that the aggregate volume content and density of aggregate type play important roles in the relationship of  $E_{cs}-E_{cd}$ .

#### *Poisson's Ratio*

Research about investigating  $\mu_{cs}$  and relationships of  $\mu_{cd}-\mu_{cs}$  is relatively rare. However,  $\mu_{cs}$  is important for assessing the shear modulus of concrete structures [Carrillo et al., 2019] and the long-term serviceability of the prestressed concrete structures [Aili et al., 2016]. For example, time-dependent Poisson's ratio, an important parameter for creep behavior, can be estimated by  $\mu_{cs}$ . Simmons [1955] investigated relationships between dynamic and static Poisson's ratios of concrete. The  $\mu_{cd}$  was measured by two methods: the first employed  $f_{1-L}$  and  $f_{1-T}$ , and the other used  $f_{1-L}$  and  $V_1$ . The results showed the  $\mu_{cs}$  was smaller than  $\mu_{cd}$ , and the values of  $\mu_{cd}$  obtained by the latter one were larger.

Figure 2.3 presents the hypothetical variation of  $\mu_{cd}$  and  $\mu_{cs}$  with curing ages for saturated concrete mixes, proposed by Anson and Newman [1966]. The value of  $\mu_{cs}$  and  $\mu_{cd}$  for cement paste at the beginning is 0.5 since the cement pastes are likely incompressible visco-plastic solids. With the cement paste maturing and increasing in strength,  $\mu_{cd}$  decreases gradually and steadily due to no inelastic deformations. In contrast, once the final setting has occurred, the paste will be weak, and  $\mu_{cs}$  will be reduced significantly, even to zero. With hydration developing and the strength of the paste structure increasing, an increase in the  $\mu_{cs}$  might occur. Then,  $\mu_{cs}$  and  $\mu_{cd}$  will converge at infinite time. Persson [1999] investigated the evolution of  $\mu_{cs}$  of high-performance concrete in the first 28 days. The specimens were tested at 1-day, 2-day, and 28-day ages. The results presented  $\mu_{cs}$  increased as the curing age increased.

Besides the curing age, Persson [1999] also presented that the aggregate type affected the Poisson's ratio. In his results, specimens with granite had 30% larger  $\mu_{cs}$  than those with quartzite for both young and mature high-performance concrete.

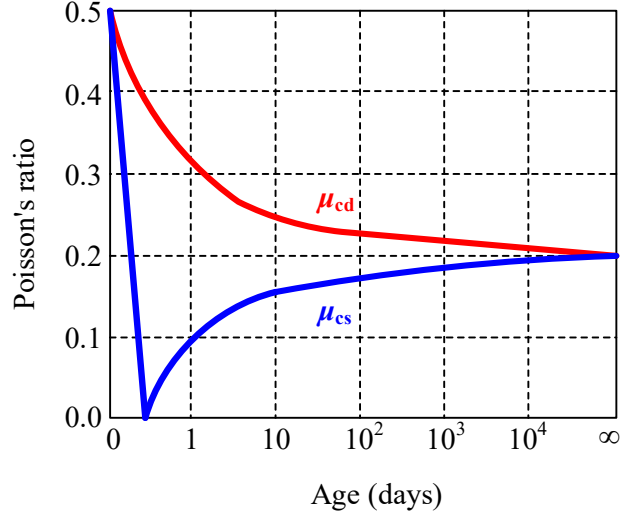


Figure 2.3 Hypothetical relation between  $\mu_{cd}$  and  $\mu_{cs}$  and age for saturated concrete mixes [Anson and Newman, 1966]

Swamy [1971] investigated the evolutions of  $\mu_{cd}$  of concrete using the resonance (i.e.,  $f_{1-L}$  and  $f_{1-T}$ ) and UPV (i.e.,  $f_{1-L}$  and  $V_l$ ) methods recommended by ASTM C215 [2019] and ASTM C597 [2022]. The results showed  $\mu_{cd}$  of concrete, evaluated by the resonance method (using  $f_{1-L}$  and  $f_{1-T}$ ), was initially high and decreased with age and continued hydration. The greatest decrease in  $\mu_{cd}$  occurred between 1 and 7 days. After the 7-day age, the decrease was slower, and at the end of the 60-day age, the values were still decreasing slowly. Similar results were presented using the UPV method (using  $f_{1-L}$  and  $V_l$ ). The values of  $\mu_{cd}$  were affected by water-cement ratio, aggregate type, aggregate content, and curing age. The comparison of  $\mu_{cd}$  evaluated by two different methods indicated that values from values of  $\mu_{cd}$  using  $f_{1-L}$  and  $f_{1-T}$  were lower than those using  $f_{1-L}$  and  $V_l$ , which were consistent with Simmons [1955]. The considerable scatter and discrepancies of the resonance methods were due to the poorly conditioned nature of Equation (2.6) and the anisotropy of concrete. Jin and Li [2002] evaluated  $\mu_{cd}$  of concrete using  $f_{1-L}$  and  $f_{2-L}$  from 0.5 to 28 days. Their results were evaluated using standard cylinders and equations developed by Kolluru et al. [2000] and showed that the values ranged from 0.18 to 0.21, a small variation with curing age. Thus, they regarded  $\mu_{cd}$  as a constant.

In summary, the NDT methods for measuring the elastic constants are reviewed in this subsection. The resonance methods and UPV methods are widely used, especially the resonance methods. The measurement of  $E_{cd}$  and its correlation with  $E_{cs}$  have been extensively studied; while the other parameter,  $\mu_{cd}$ , is not well investigated to the knowledge of the author. For example, no mathematical relationships between  $\mu_{cd}$  and  $\mu_{cs}$  were presented in the literature.

## **2.2.2 NDT Methods for Predicting Strength**

Compressive strength is an essential material parameter in design codes and is used to obtain the nominal strengths of structural members. When standard destructive testing procedures are conducted (e.g., standard cylinders tested according to [ASTM C39/C39M \[2020\]](#)), the results represent the possible strength of concrete on construction sites. The test is only used for concrete quality control to meet requirements. It cannot determine the in-place concrete strength since placing, compaction, and curing effects cannot be considered [\[ACI, 2003\]](#). In addition, standard-cured cylinders are usually prepared and tested for acceptance purposes at 28-day age, indicating their results cannot be used to determine strength at earlier ages directly.

### *2.2.2.1 In-place NDT Methods*

Accelerated construction schedules aiming at economic gain are desired during construction [\[Oluokun et al., 1990\]](#). Therefore, reliable tests to estimate the in-place strength are needed to ensure safety. The in-place strength is typically determined through destructive testing in the laboratory or on a construction site, or through NDT such as the maturity method [\[ASTM C1074, 2019\]](#). The destructive test is usually conducted in the laboratory. Therefore, concrete specimens must be transported from construction sites to laboratories with testing facilities for strength determination [\[Bassim and Issa, 2020\]](#). In contrast, NDT methods measure some physical properties that can be correlated to compressive strength [\[Popovics, 1998\]](#). [Table 2.7](#) presents the recommended NDT for predicting in-place strength by [ACI 228.1R \[2003\]](#).

The operation procedures of the rebound method are presented according to

ASTM C805/C805M [2018]. It is required to correlate strength and rebound numbers for a given concrete and apparatus when using this test method. Although the rebound test is easy to perform, its evaluation accuracy is affected by many factors other than concrete strength, leading to relatively unreliable compared to other methods [ACI, 2010]. The UPV method is introduced in Section 2.1.1.3. For a given concrete,  $V_1$  is related to  $E_{cd}$  directly and to concrete strength indirectly. Therefore, the correlation between  $E_{cd}$  and concrete strength should be built first in the laboratory. However, the reliability of this method has not been rated. Strength estimation is only possible with  $\pm 20\%$  accuracy, and even this can be achieved only under the best conditions [Komlos et al., 1996]. The maturity index of the in-situ concrete, which is correlated to the concrete strength in advance, is calculated using the recorded temperature history. The fundamental assumption of this method is that the strengths are only related to the maturity index [ASTM C1074, 2019], which is highly questionable. The correct datum temperature is required to improve the accuracy of the strength estimation at early ages [ACI, 2003]. It should be highlighted that this method can be applied to new construction only.

Table 2.7 Useful compressive strength ranges for in-place NDT methods [ACI, 2003]

Test method	Range of $f'_c$ (MPa)	ASTM standard	Sensor or device
Rebound number	10–40	C805/C805M	Rebound hammer
UPV	1–70	C597	Ultrasonic transducers
Maturity	No limit	C1074	Temperature sensors

In practice, two or more in-place test methods are combined to estimate concrete strength, which is the so-called combined method. Combinations of two NDT methods, such as pulse velocity and rebound hammer, have resulted in higher accuracy than when used separately [Kheder, 1999]. However, the improvements are usually marginal [ACI, 2003]. The other combinations use NDT methods to estimate first, and then destructive tests are conducted to verify the results. For instance, the maturity method was

combined with another in-place destructive test, such as the pullout test or the break-off test [Soutsos, et al., 2000]. This approach is especially beneficial when in-place tests involve embedded hardware.

#### 2.2.2.2 Specimen-based NDT Methods

Compared to the NDT methods mentioned in Table 2.7, concrete strength estimation using the resonance methods is a less common option [Bassim and Issa, 2020], possibly because special specimens are needed. Table 2.8 presents concrete strength estimated by the resonance methods. Normal concrete (NC) and high-strength concrete (HSC) were tested, with  $f_c'$  ranging from 0.4 to 147 MPa. The curing ages were within 28 days. The earliest time for the tests was 0.5 days since the resonance cannot be tested before demolding, which needs time to prepare in practice. For most research, cylindrical specimens of different sizes were tested by correlating  $f_{1-B}$  or  $f_{1-L}$  to  $f_c'$ . On the other hand, some research employed prisms. Venkiteela et al. [2013] employed  $f_{1-T}$  measured using prisms to correlate with the  $f_c'$  tested using cylinders. Zhou et al. [2020] established correlations of  $E_{cd}$  and prismatic compressive strength ( $f_{cp}$ ) using the same prism directly. Bassim and Issa [2020] first established the correlations between flexural strength ( $f_{rp}$ ) and  $E_{cd}$  using the prism having a size of  $150 \times 150 \times 530 \text{ mm}^3$ , which is a standard specimen in the traffic field. The reasons that different types of specimens are used are as follows: (a) Standards in different countries recommend different specimens for obtaining compressive strength; for instance, the Chinese standard (i.e., GB/T 50081 [2019]) recommends prisms and cubes, while ASTM standards (i.e., ASTM C469/C469M [2022]) recommend the cylinders; (b) Torsional mode is hard to record in cylinders while it is easy to obtain in prisms; (c) some special application fields use prisms as standard specimens.

Table 2.8 Concrete strength estimated by resonance methods

References	Concrete type	Range of strength (MPa)	Measured	Specimens type	Curing age (day)
<a href="#">Hansen [1986]</a>	NC	$f_c'$ : 3.45–75.84	$f_{1-B}$	Cylinder: 100 mm×200 mm	1–28
<a href="#">Lee et al. [1997]</a>	NC	$f_c'$ : 3–28	$f_{1-L}$	Cylinder: 100 mm×200 mm	3–28
<a href="#">Jin and Li [2001]</a>	NC	$f_c'$ : 2.7–43.8	$f_{1-L}, f_{2-L}$	Cylinder: 100 mm×200 mm	0.75–28
<a href="#">Han and Kim [2004]</a>	NC	$f_c'$ : 2–45	$f_{1-L}$	Cylinder: 100 mm×200 mm	1–28
<a href="#">Venkateela et al. [2013]</a>	NC	$f_c'$ : 0.4–40.6	$f_{1-T}$	Cylinder for $f_c'$ : 75 mm×150 mm 100 mm×200 mm Prism for $f_{1-T}$ : 50×75×230 mm <sup>3</sup> 100×150×300 mm <sup>3</sup>	0.5–3
<a href="#">Lee et al. (2015)</a>	NC	$f_c'$ : 8–30	$f_{1-B}, f_{1-L}$	Cylinder: 100 mm×200 mm 150 mm×300 mm	4–28
<a href="#">Carrazedo et al. [2018]</a>	NC, HSC	$f_c'$ : 13–147	$f_{1-B}, f_{1-L}$	Cylinder: 50 mm×100 mm 100 mm×200 mm	2–28
<a href="#">Zhou et al. [2020]</a>	NC	$f_{cp}$ : 0.7–26	$f_{1-L}$	Prism: 100×100×300 mm <sup>3</sup>	0.5–28
<a href="#">Bassim and Issa [2020]</a>	NC	$f_c'$ : 2.92–49.92 $f_{rp}$ : 0.98–5.62	$f_{1-B}, f_{1-L}$	Cylinder for $f_c'$ : 150 mm×300 mm Prism for $f_{rp}$ : 150×150×530 mm <sup>3</sup>	0.5–28

Note: NC and HSC refer to normal concrete and high-strength concrete, respectively,  $f_c'$ ,  $f_{cp}$ , and  $f_{rp}$  refer to cylindrical compressive strength, prismatic compressive strength, and flexural strength, respectively.

In summary, the NDT methods for estimating the compressive strength of concrete are reviewed in this section, including rebound number tests, UPV, maturity method,

and resonance methods. The rebound number method is the most used among these four methods, while the resonance method is considered the most accurate.

### 2.2.3 NDT Methods for Detecting Concrete Delamination

Delamination can occur in bridge decks, concrete pavements, and indoor and outdoor concrete slabs. Delamination refers to a plane of separation that orients roughly parallel to the surface [Jana, 2007]. Several reasons may lead to delamination in concrete, such as corrosion of reinforcing steel rebars and cyclic freeze-thaw process at critically saturated conditions.

Metal tapping and chain dragging are the most common and traditional techniques for detecting delamination. They involve operating on the concrete surface under investigation and listening to its acoustic response [Khan, 2003], which highly relies on experience of operators. With the development of the NDT methods, some of them are used to detect delamination in the concrete field, including the impulse-response method, impact-echo method, ground penetrating radar (GPR), and infrared thermography.

#### 2.2.3.1 Impulse-response Method

The impulse-response method is an NDT method consisting of a mechanical impact for actuation, a broadband velocity transducer for recording, and a signal processing module for calculating the mobility spectrum of a tested element [ASTM C1740], as shown in Figure 2.4. The mobility spectrum, which can present the status of the test point, is calculated as Equation (2.9) from 0 to 800 Hz.

$$M(f) = \frac{V(f) \times F^*(f)}{F(f) \times F^*(f)} \quad (2.9)$$

where  $M(f)$  is the mobility spectrum;  $V(f)$  and  $F(f)$  refer to velocity and impact force spectra, respectively; and  $F^*(f)$  represents the complex conjugate of the force spectrum. With the mobility spectrum, two indices are extracted, including the ratio of the peak mobility value and the average mobility. For a plate-like structure, mobility can reflect the relative flexibility of the tested elements, which is related to the thickness of the plate, the modulus of elasticity of concrete, support conditions, and the presence of

internal defects. A higher mobility reflects more flexibility of the element at that test point. For example, void and honeycombed concrete may have a higher peak and average mobility ratio, respectively.

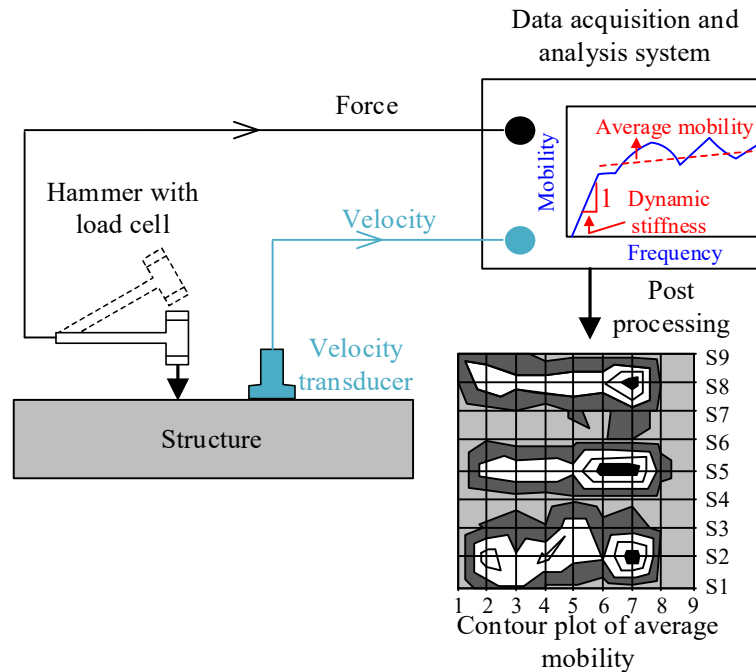


Figure 2.4 Schematic of the test setup and apparatus for impulse-response test

[ASTM C1740, 2016]

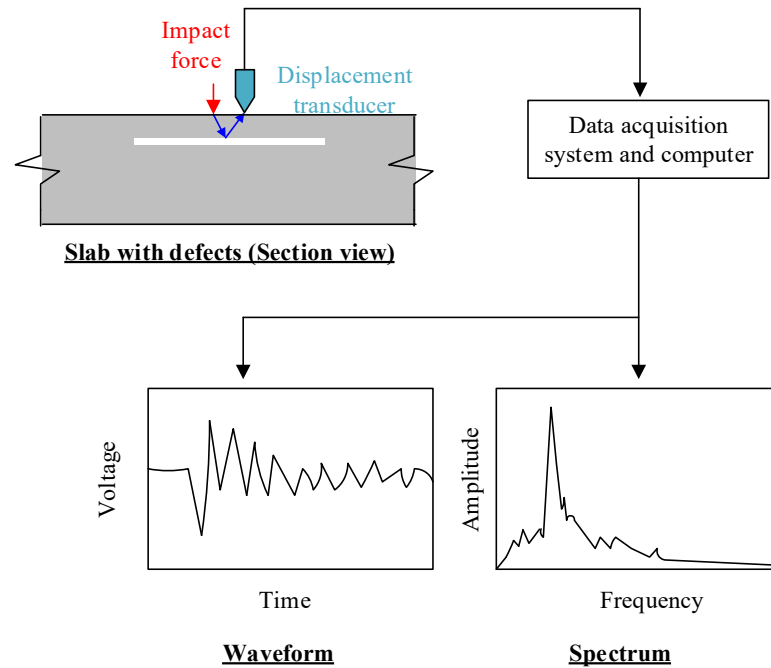
Nazarian and Reddy [1996] studied the parameters that would affect the sensitivity of the flexibility (defined as the ratio of displacement to force) spectrum, which was obtained by integrating the mobility (defined as the ratio of velocity to force) spectrum. They pointed out that the modulus of elasticity of concrete resulted in limited effects on the assessment. In contrast, the thickness of the slab and the modulus of elasticity of the subgrade were the main factors that affected the flexibility spectrum. Meanwhile, the delamination width should be at least four to five times the slab thickness. Applications using the impulse-response method in concrete structures have been reported since the 1980s. The first several attempts of the impulse-response method were to detect consolidation defects, voids, and poor support below pavement slabs. The method was then widely applied to evaluate other reinforced concrete structures such as floor slabs, pavements, bridge decks, and piers [Davis, 2003]. Clem et al. [2013]



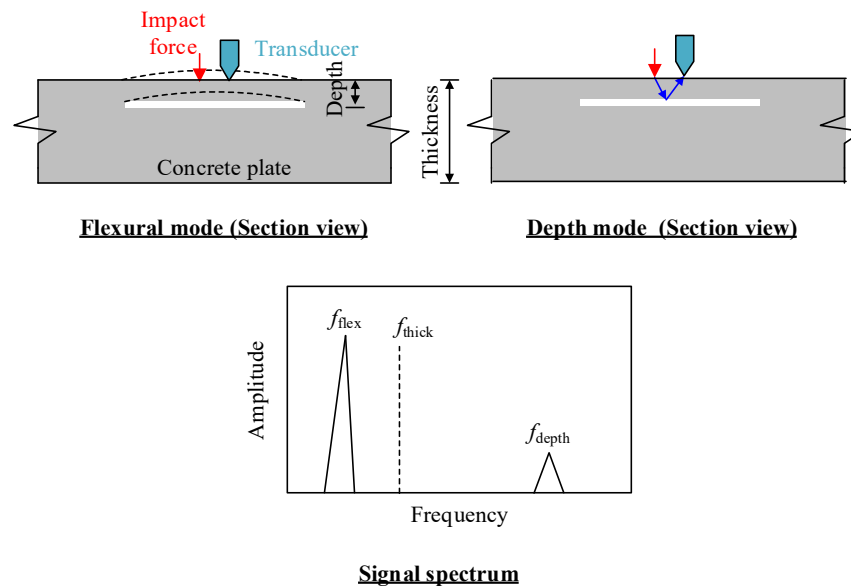
studied the difference between the accelerometer and velocity transducer and showed they were virtually identical. Meanwhile, they pointed out that the position of delamination relative to the girders appeared to have a larger effect on standard parameters than the size itself for small delamination. Besides the delamination detection, the impulse response method was also applied to characterize railway ballasts and detect localized damage in the steel truss systems [Tamrakar et al., 2018; Can et al., 2018].

#### 2.2.3.2 *Impact-echo Method*

The impact-echo method is an NDT technique based on transient stress (sound) waves [Sansalone, 1997]. Unlike the impulse response method using the average value or slope of the curve for assessment, the impact-echo method utilizes resonant frequencies to determine the integrity of a structure or the location of flaws. Impact-echo testing consists of three basic components: a mechanical impactor capable of producing high-frequency excitation, a high-fidelity receiver (i.e., displacement transducer), and a data acquisition-signal analysis system [Carino, 2001], as shown in Figure 2.5(a). It is worth noting that the same purpose can be successfully achieved using accelerometers [Olson, 1992; Sajid et al., 2022], while Sansalone and Streett [1997] believed a displacement transducer simplified signal interpretation since most of the theoretical studies of the impact-echo method have dealt with surface displacement. To accelerate the testing speed and avoid inconsistent coupling conditions when conventional contact sensors are used in large structures, such as bridge decks, displacement transducers might be replaced by contactless sensors, such as microphones [Zhu and Popovics, 2007; Kee et al., 2012; Choi et al., 2018; Sun et al., 2018; Kang et al., 2022].



(a) Schematic of the impact-echo method



(b) The principal components of the resonance produced by impact on the surface of concrete slab with a shallow delamination

Figure 2.5 Schematic of the impact-echo method and principal for detecting a shallow delamination [Sansalone and Streett, 1997]

The thickness stretch and flexural modes are the main resonant modes for delamination detection and characterization in the impact-echo method [Kee and

[Gucunski, 2016](#)]. Flexural vibration modes tend to dominate the spectral response of the shallow (near surface) delamination, which had a depth smaller than 100 mm, in the low-frequency range, while thickness stretch modes dominated the deep defect or delamination in the relatively higher frequency range, as shown in [Figure 2.5\(b\)](#). Besides detecting delamination in the plate-like concrete structure, the impact-echo tests were also applied to beam-like concrete members, such as T-beams and ungrouted tendon ducts, to detect voids or material degradation [[Hill et al., 2000](#); [Ohtsu and Alver, 2009](#); [Zein and Gassman, 2010](#)].

#### *2.2.3.3 GPR Technology*

GPR technology has been used to detect voids or delamination in various ways [[AL-Qadi and Lahouar, 2005](#)]. GPR is an active NDT method based on the transmission of short electromagnetic energy pulses into the medium and the analysis of scattering phenomenon due to changes in some physical properties, such as electric conductivity, dielectric permittivity, and magnetic permeability [[Capozzoli and Rizzo, 2017](#)]. Subsurface anomalies, such as cracks and delamination, may be identified via signal processing of the received waves. There are two types of GPR antennas, namely, ground-coupled and air-coupled types, as shown in [Figure 2.6](#). The ground-coupled GPR antenna, which is attached to the pavement surface during the survey, directly transmits electromagnetic energy to the pavement surface, allowing deeper penetration depth compared to the air-coupled antenna type [[Wang et al., 2023](#)]. Although the accuracy is relatively low, the ground-coupled antenna can rapidly detect damage in actual practice, reducing traffic interruption time [[Diamanti and Redman, 2012](#)].

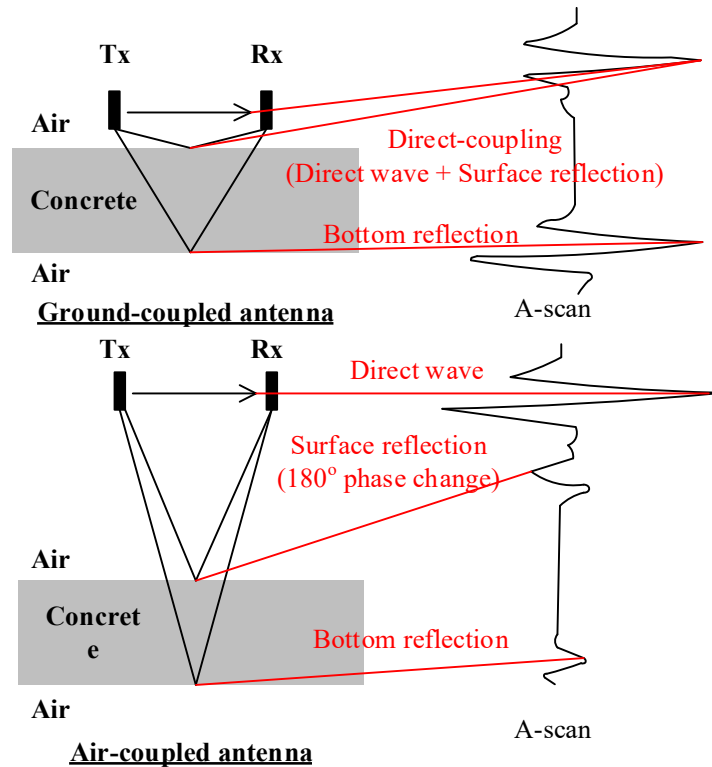


Figure 2.6 Schematic of the GPR method and its signal of A-scan [Dinh and Gucunski, 2021]

#### 2.2.3.4 Infrared Thermography Method

The infrared thermography method is a non-contact and non-intrusive method. This method can convert heat at any temperature into a thermal image using specialized cameras [Melo and Carlomagno, 2004]. Infrared thermography can be conducted actively and passively. Active infrared thermography heats the target regions using heating sources and collects data, while infrared passive thermography records data when natural heat exchange occurs [Omar et al., 2018]. It has been observed that buildings or structures with defects, such as debonded render and mosaic or delaminating concrete, emit differing amounts of infrared radiation. If there are any cracks or delamination within the concrete, the surface will heat up faster under solar irradiation in these areas, and hot spots will be observed in the thermal record [MaCann and Forde, 2001]. Compared with other NDT methods, infrared thermography can quickly detect subsurface delamination in a very short period, especially for high-rise

buildings, but identifying its size and depth is challenging [Huh et al., 2016]. The infrared thermography method has been applied to bridge structures in addition to high-rise buildings. It can quickly scan the 2D surface using an infrared camera without affecting the bridge operation. Meanwhile, the remote scanning capability allows the inspection of regions that are difficult to access by traditional inspection. Omar and Lehdi [2017] utilized unmanned aerial vehicles-carried infrared thermography to detect subsurface delamination in concrete bridge decks, which was friendly to traffic issues. Raja et al. [2021] successfully utilized infrared thermography to detect delamination at the bottom of concrete bridge decks, ensuring its broader applicability in actual practice. Their results showed that the temperature differences increased as the thickness of the bridge deck and delamination size increased.

To conclude, the existing methods for detecting delamination in concrete structures can be effective for the pavement, bridge decks, and exterior walls in high-rise buildings, which typically have delamination in large sizes and need quick and rough estimation. The delamination in the bottom side of the indoor concrete slabs in building structures is still not effectively addressed. This type of delamination is usually featured by small size, corresponding to high frequencies that make it difficult to detect.

## **2.3 EMI Technique in Concrete Field**

The EMI technique was proposed by Liang et al. [1994], It has been widely used in the concrete field because of its easy installation and operation. Their applications include but are not limited to the determination of setting time, evolution monitoring of hardening of concrete (e.g., strength), damage evaluations, and material properties characterization. This section reviews the EMI techniques, covering the basic concepts and principles, hardware used, signal processing methods, and application scenarios.

### **2.3.1 Basic Concept and Principles of EMI Techniques**

#### *2.3.1.1 Mechanical Impedance Analysis (MIA) Method*

The mechanical impedance analysis (MIA) method was invented by Lange in 1958 [Lange, 1994]. This method measures the responses to force actions perpendicular to

the test surface [Giurgiutiu, 2014]. A specialized transducer that can measure the applied force and the induced velocity at the same time is employed in the MIA method, as shown in Figure 2.7. A shaker applied force through a power amplifier. This method was quick to carry out, and dry contact was adequate, which is different from the high-frequency ultrasonic testing method [Cawley, 1984; Cawley and Nguyen, 1988]. Two piezoelectric sensors were installed as transducers: one was used to record the force signal, and the other was used to record the acceleration signal. The signals received were amplified by the charge amplifiers and then analyzed by a spectrum analyzer.

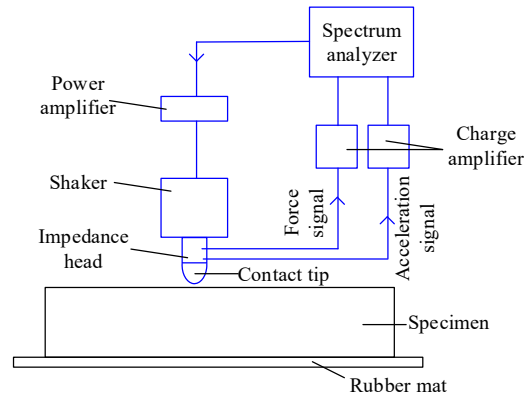
Cawley [1984] presented that the MIA method was suitable for detecting planar defects, which resulted in one or more layers being separated from the base layers, such as delamination in laminated structures, while it was not suitable for the detection of transverse cracks. Mathematically, the MIA method calculates the point impedance  $Z$  of a target structure, as shown in Equation (2.10)

$$Z = \frac{F}{v} \quad (2.10)$$

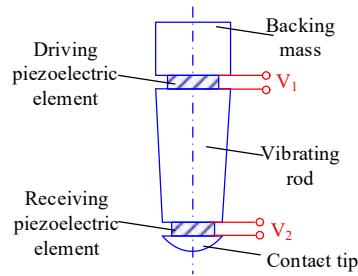
where  $F$  and  $v$  refer to the harmonic force and the resultant velocity at the same point, respectively. The measurements are conducted at a single frequency each time, while the investigated frequencies typically range from 1 and 10 kHz.

Cawley [1984] explained the physical basis of the MIA for detecting damage as follows: the defects (e.g., debonding or delamination) could be modeled as a spring, the spring with infinite stiffness if there was no defect. When there was a defect, the mechanical impedance of the modeled spring was highly related to the spring stiffness. Therefore, the MIA could be used to detect damage. In the MIA evaluations, reliable results were obtained when the excitation frequency was far away from structural resonances so that the results were insensitive to the structural damping. Cawley [1984] pointed out that MIA could effectively detect near-surface defects when the structure had a stiffness comparable to that of the impedance transducer. For example, regarding the defect size, the reliability of the test was greatly reduced when the honeycomb thickness was less than 10 mm [Cawley and Nguyen, 1988]; regarding the material type

of the base structure, when the depth was equal, MIA could detect the smaller size of the defect in aluminum materials than that in fiber reinforced polymer materials [Cawley, 1984]. Moreover, the sensitivity of the MIA method was limited by the stiffness of the dry point contact [Cawley, 1985]. To detect deeper defects, twin contact probes were used for this technique [Lange, 1994].



**Schematic diagram of test apparatus**



**Impedance transducer**

Figure 2.7 Schematic diagram of test diagram of MIA and details of the impedance transducer [Cawley, 1985; Cawley and Nguyen, 1988]

### 2.3.1.2 Principle and Physical Meaning of EMI Techniques

The EMI technique is essentially an extension of the MIA [Migot and Giurgiutiu, 2023]. The low-cost piezoelectric sensor has opened new windows to better understand material properties and complex structures. Piezoelectric sensors can act as both actuators and receivers through their intrinsic electromechanical coupling. Meanwhile, their working frequency range is much wider than that of conventional actuators, such as shakers and impact hammers [Giurgiutiu, 2014]. From the hardware perspective, the

EMI technique only needs a single piezoelectric sensor and a data acquisition system, making the EMI technique very attractive to operators [Zahedi and Huang, 2017]. From the working frequency perspective, the EMI technique can capture the high-frequency spectrum, which is very sensitive to minor damage.

Liang et al. [1994] first proposed the one-dimension analytical model to obtain the electric admittance (inverse of electric impedance) signatures, as shown in Figure 2.8. The target of the research was to investigate the power consumption of the PZT actuator and energy transfer within the system [Giurgiutiu and Zagrai, 2000]. A PZT actuator drove a single-degree-of-freedom (SDOF) system, modeled as a spring-mass-damper system.

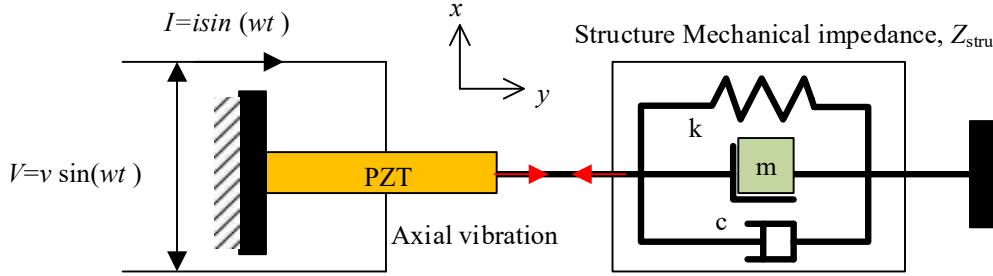


Figure 2.8 Schematic diagram of a PZT actuator driven mechanical system represented by its structural impedance [Liang et al., 1994]

Equation (2.11a) presents the equation of electric admittance of the bonded PZT transducer that involves the drive-point mechanical impedance of the host structure.

$$Y = \omega j \frac{w_{PZT} l_{PZT}}{h_{PZT}} \left[ \bar{\epsilon}_{33}^T - d_{31}^2 Y_{11}^E \frac{Z_{PZT}}{Z_{stru} + Z_{PZT}} \right], \quad (2.11a)$$

$$Y = \omega j C_{PZT} \left[ 1 - \kappa_{31}^2 \frac{Z_{PZT}}{Z_{stru} + Z_{PZT}} \right], \quad (2.11b)$$

where  $Y$  is the admittance,  $d_{31}$  refers to the piezoelectric strain coefficient,  $Y_{11}^E$  denotes the Young's modulus at constant electric field,  $\bar{\epsilon}_{33}^T$  represents the electric permittivity at the constant stress,  $Z_{stru}$  and  $Z_{PZT}$  are the mechanical impedance of the structural system and the quasi-static mechanical impedance of the piezoelectric sensor, respectively. Equation (2.11a) can be rewritten as Equation (2.11b), where  $C_{PZT}$  is the capacitance, and  $\kappa_{31}^2$  refers to the piezoelectric coupling factor. Equation (2.11b) clearly



shows that electric admittance, which is easy to measure, consists of the capacitance of the PZT transducer and mechanical interaction between the sensor and structure. When the  $Z_{\text{PZT}}$  and  $Z_{\text{stru}}$  match, the resonance of the electro-mechanical system occurs. In the analysis by [Liang et al. \[1994\]](#), the susceptance spectrum is almost the same as the admittance spectrum, indicating the strong reactive nature of the coupled electro-mechanical system. Meanwhile, the conductance spectrum included a distinct peak occurring at the resonance of the joint system. This peak in the real part of admittance means the actuator stores the maximum strain energy, which inevitably leads to more mechanical loss.

[Sun et al. \[1994\]](#) continued and extended the work using the half-power bandwidth to determine the natural frequencies accurately using an SDOF system. The EMI spectrum of the joint system is presented in [Figure 2.9](#). There are two admittances ( $Y$ ) for the PZT sensor: one is in free status (i.e.,  $Z_{\text{struc}}$  drops nearly to zero), and the other is in blocked status (i.e.,  $Z_{\text{struc}}$  becomes  $\infty$ ). Both susceptance spectra of the PZT sensor intersect with the susceptance spectrum of the joint system, and it is found the red intersection corresponds to natural frequency of the system, at which peaks in the conductance spectrum. Physically, there is no mechanical reactive power going into the joint system from PZT at the resonant frequency.

Although relatively easy to apply experimentally, the EMI technique is not easy to model. [Giurgiutiu and Zagrai \[2002\]](#), for the first time, developed an analytical model based on structural vibration theory and the theory of piezoelectricity using a 1D structure (steel beams) and surface-bonded PZT sensor for predicting the EMI response. [Figure 2.10](#) presents the interaction between the PZT sensor and a substructure. The model accounted for both axial and flexure vibrations of the steel beams. Elastically constrained piezoelectric active sensors permanently bonded to the structure were included. Experimental validations were conducted to show that the EMI spectrum measured by the PZT sensors can accurately illustrate the mechanical behavior of the target structure. Besides, [Giurgiutiu and Zagrai \[2002\]](#) also pointed out that the EMI

technique did not behave well below 5 kHz when being tuned to high-frequency explorations, and below 1 kHz was not recommended.

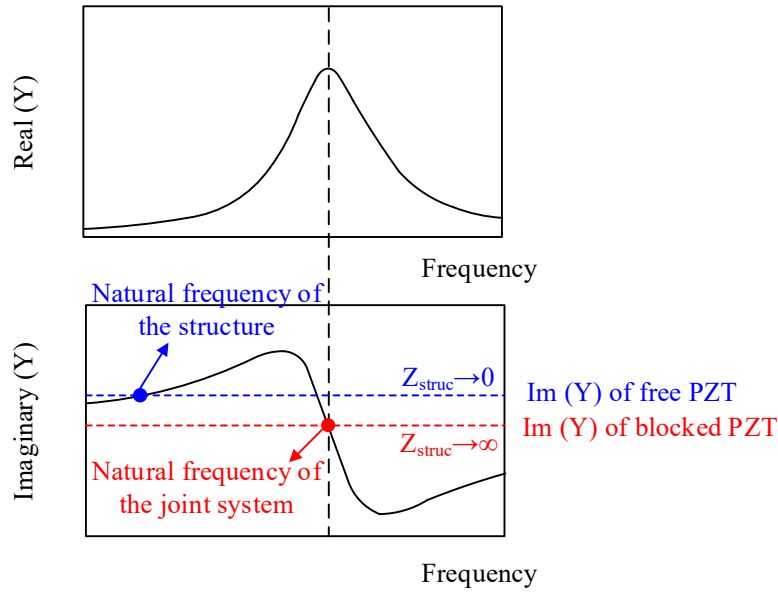


Figure 2.9 Determination of structural natural frequency by electric admittance matching [Sun et al., 1994]

Zahedi and Huang [2017] demonstrated that the EMI spectrum physically represents a pulse-echo signal in the frequency domain. Based on the generation mechanisms, the time-domain signal can be classified into three periods: the ‘main bang,’ ‘resonant phase,’ and ‘echo phase.’ The main bang occurs when the voltage is applied, which dominates this period. The resonant phase corresponds to when the sensor oscillates at its resonant frequencies. The frequency and duration of the resonant signals are determined by the features of the sensor resonances, which are highly related to the properties of the sensor and bonding layer (e.g., dimensions and material properties). The echo phase refers to the period that the sensor generates electric currents when the waves are reflected by structural discontinuities, such as cracks and free edges, back to the sensor.

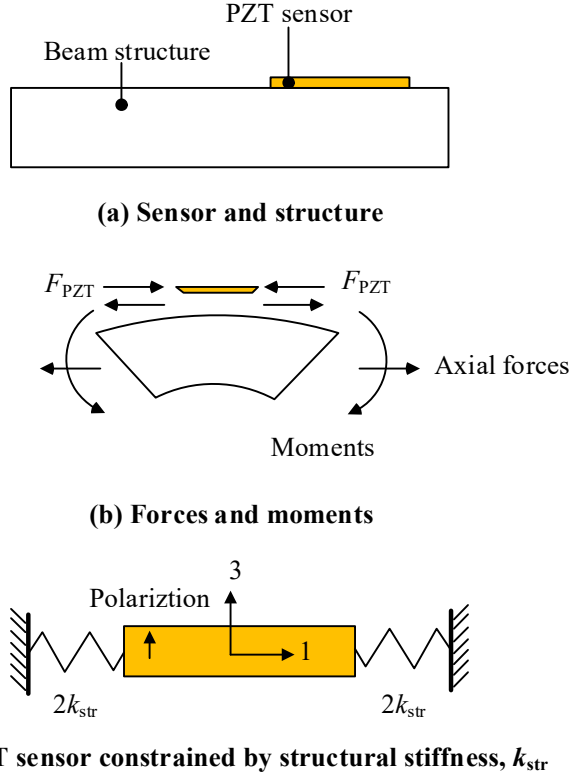


Figure 2.10 Interaction between PZT active sensor and a substructure [Giurgiutiu and Zagari, 2002]

### 2.3.2 Sensor Types and Installations

The EMI technique only needs one sensor for monitoring, implying that the status and properties of the sensor are very important for this technique. Sensors used in EMI techniques are in different interaction types, installation methods, and geometric shapes. Lee et al. [2019] categorized the sensors according to the interaction type, including direct interaction and indirect interaction. Direct interaction means that the piezoelectric sensors are directly installed on/in the target structures. Indirect interaction means that the piezoelectric sensors are installed on an agent (e.g., a metal element) first, and then the agent is installed on/in the target structures. The major advantages of direct interaction are that the practical implementation was straightforward, and the physical model was relatively easy to build. In contrast, indirect installations can be helpful for some special purposes, such as reusing the sensors in real practice. Surface-bonded piezoelectric (SBP) sensors and embeddable

piezoelectric (EBP) sensors are the two installation types that interact directly.

#### 2.3.2.1 Surface-bonded Piezoelectric Sensors

SBP is the most popular installation type in real practice due to its easy implementation. A thin and square sensor (i.e., thickness  $\ll$  width), which is the so-called piezoelectric patch or piezoelectric wafer, is preferred in civil engineering. [Figure 2.11](#) presents the commonly used piezoelectric patches with different electrode patterns. The yellow axes are the coordinate for describing the material properties of the piezoelectric materials. The 3-axis, which is along the thickness direction, represents the polarization direction of the piezoelectric patch. The 1-axis and 2-axis are mutually perpendicular and along the plane. The two electrodes are on the top and bottom surfaces of the piezoelectric patch. However, the designs are not totally the same. In the first electrode pattern, the insulation band is designed to isolate an electric input from a casing or housing. The electrode pattern that covers the whole surface is called the solid pattern. In the other two patterns, which are called wrap-around feedback patterns, both electrodes are available on one side of the patch, leading to convenience when the other side is bonded to a flat surface of the structure [\[Soh et al., 2000\]](#). According to Equation (2.11a), the patch with a larger width and thinner thickness leads to higher sensitivity for one specific piezoelectric material. The width or diameter of the PZT patch in the literature ranged from 5 to 30 mm, and the thickness ranged from 0.2 to 2.0 mm [\[Lim et al., 2021\]](#).

In most SBP applications, the frequency range lower than the first distinct resonant frequency is employed, indicating the in-plane vibration mode (i.e., in-plane extensional mode) of SBP, which is the so-called  $d_{31}$  mode. SBP is commonly installed through adhesive material (e.g., epoxy). This rigid bond ensures that the actuation forces can be transmitted. Protection layers over the unbonded surfaces of the sensor are required for long-term monitoring to provide waterproofing and protection since piezoelectric materials are brittle and fragile. When the SBP is excited by the alternating voltage, it introduces a pair of self-equilibrating axial forces and bending moments on

the target structures that are separated by a small distance [Giurgiutiu, 2014]. The advantages of using SBP are as follows: (a) the placement of the patch is easy to achieve; (b) the bonding status can be controlled, such as the thickness of the adhesive layer; (c) replacement of the sensor can be easily carried out. However, the SBP cannot be used before concrete is demolding since the operation can only be done after concrete setting.

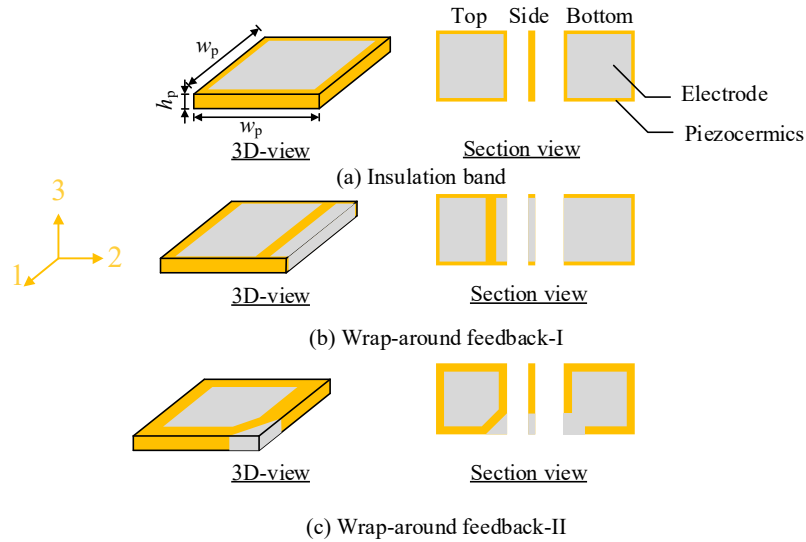


Figure 2.11 Commonly used electrode patterns of the square piezoelectric patch

### 2.3.2.2 Embedded Piezoelectric Sensors

Embedding a piezoelectric sensor into concrete structures or specimens is the other commonly used direct interaction installation. Embedded piezoceramic transducers in concrete fields were first investigated by Gu et al. [2006] and Song et al. [2007], who correlated the concrete strength and damage with the changes in wave signals, respectively. Table 2.9 summarizes the EBP sensors for monitoring concrete using EMI techniques. They were used to monitor concrete evolution at a very early age and the damage evolution under axial compressive loadings. Two shapes of PZT sensors were used, including the patch and spherical shell. The patches are in rectangular, square, and circular shapes. The motivation for choosing a spherical shell is to capture the information in all directions [Fan et al., 2021]. The PZT sensors must be protected using water-proofing materials to avoid electric short circuits. For example, Narayanan et al. [2017] and Zhang et al. [2020] fabricated an epoxy layer and liquid tape for the

embedded PZT patch, respectively. Coating layers were fabricated to protect the PZT sensors since the PZT materials are brittle and fragile. Moreover, the assembled package was helpful for installations. According to the different targets, different materials were used as the coating layers. For example, ultra-high-performance concrete (UHPC) was used since its high strength can provide enough protection [Fan et al., 2021]. Aluminum was selected for rapid fabrication since metal was easy to machine [Ai et al., 2021]. The cementitious material (i.e., cement past and mortar) and marble were selected to avoid changing the material properties of the concrete [Song et al., 2008], while the drawback of the cementitious coating layers was that they could only be used after the coating material properties became stable.

Table 2.9 EBP for monitoring concrete by using EMI techniques

Reference	Details of sensor		Details of coating	
	Shape	Size	Material	Size
Ai et al. [2016]	Rectangular patch	26×12×0.5 mm <sup>3</sup>	Cement paste	Diameter: 50 mm Height: 40 mm
Kong et al. [2017]	Spherical shell	Inner radius: 9.25 mm Outer radius: 10 mm	UHPC	Outer radius: 20 mm
Narayanan et al. [2017]	Square patch	20×10×1.0 mm <sup>3</sup>	Epoxy	20.4×20.4×1.4 mm <sup>3</sup>
Ai et al. [2020]	Square patch	10×10×0.5 mm <sup>3</sup>	Cement and aluminum	20×20×20 mm <sup>3</sup>
Fan et al. [2021]	Spherical shell	Inner radius: 9.25 mm Outer radius: 10 mm	UHPC	Outer radius: 20 mm
Zhang et al. [2020]	Circular patch	Diameter: 19.8 mm Thickness: 1.0 mm	Liquid electric tape	Diameter: 19.8 mm Height: 1.0 mm
Li et al. [2021]	Circular patch	Diameter: 10 mm Thickness: 1.0 mm	Mortar	Diameter: 20 mm Height: 10 mm
Li et al. [2023]	Circular patch	Diameter: 15.1 mm Thickness: 0.55 mm	Marble	Diameter: 24.3 mm Height: 21.5 mm

Note: UHPC refers to ultra-high-performance concrete

### 2.3.2.3 Indirect Installation of Piezoelectric Sensors

Indirect installations of piezoceramic sensors have also been developed in addition to directly installing the sensor on the target structures. The major motivations for indirect installations are (a) increasing the detectable range of each sensor, thus

significantly reducing the number of sensors, and (b) extending a well-established substructure to a larger structure for indirect reflection of its properties.

For metallic and composite structures, the indirect installations were developed for larger detecting regions with fewer sensors. [Na et al. \[2012\]](#) developed a reusable sensor by bonding a PZT patch to a commercial neodymium magnet to detect the damage of the adhesive layer of the composite plates, which were subjected to a corrosion solution. The developed sensor could be directly used for the metallic plate, while it was also used for composite structure by placing a support magnet on the opposite side. [Baral et al. \[2022\]](#) fabricated a reusable sensor by bonding a PZT sensor to a detachable nut-bolt-washer combination. The developed reusable sensor was employed to detect and localize the damage to the thin-walled steel structures. [Singh et al. \[2024\]](#) developed a reusable sensor for damage detection in a steel plate by bonding a PZT patch to Perspex glass sheets, which were assembled by screws, nuts, and magnets. The bond between the PZT sensor and the target steel structure was achieved using the magnets.

For cementitious materials, indirect installations were developed to reuse the sensor or extend the well-established method. [Yang et al. \[2010\]](#) fabricated a reusable piezoelectric transducer setup for monitoring the initial hydration of concrete. A PZT patch was attached to an enclosure first, and then the enclosure was tightened by two bolts. However, the setup could only be detached after compressive loading tests. [Lu et al. \[2018a, 2018b\]](#) developed a smart probe to monitor the development of cementitious materials (i.e., mortar) using a prefabricated aluminum beam with a surface-bonded PZT patch, which was partially embedded into the target structure. It is worth highlighting that the smart probe was permanently embedded into the target structure. The first resonant frequency of the smart probe, extracted from the conductance signatures, was correlated to the dynamic modulus and strength of the cementitious mortar. [Moharana and Bhalla \[2019\]](#) bonded a PZT patch to the free end of a thin metal foil, and the other end was embedded inside the concrete. The sensor was developed to

monitor the hydration of concrete.

### 2.3.3 Acquisition Devices and Setup

In the EMI technique, only an impedance analyzer that measures electric impedance in a wide frequency range is needed. Usually, the measurement of EMI impedance has been performed using a commercial impedance analyzer. Commercial impedance analyzers, equipped with integrated high-gain preamplifiers, can significantly amplify the amplitude of the output signals. Meanwhile, signals with a high signal-to-noise ratio and good repeatability can be measured [Song et al., 2013].

Currently, PZT sensors are quite cheap, approximately one dollar per sensor; while the commercial impedance analyzer is more than USD 20,000 [Peairs et al., 2004; Kaur et al., 2017]. Additionally, the commercial impedance analyzer is large and may be overweight for some applications [Tenreiro et al., 2022]. Peairs et al. [2004] suggested an alternative method involving a simple and cost-effective small current measuring circuit. This method consists of a voltage divider, an FFT analyzer, and an amplification circuit. Panigrahi et al. [2010] achieved the measurement of the electric impedance using a function generator to excite pure sine signals and an oscilloscope to measure voltage. Xu and Giurgiutiu [2005] developed a cost-effective setup with a function generator, a data-acquisition board, and a computer. They compared two types of signal sources, linear chirp and frequency-swept signal sources, and showed the frequency-swept signal source was slightly better. But Baptista and Filho [2009] utilized a chirp signal to excite a piezoelectric actuator. They recorded the signal using a data acquisition board connected to a computer for collecting the EMI signals, and precise results were obtained. Maruo et al. [2015] utilized a microcontroller to assemble a hardware and firmware system for measuring the multiple piezoelectric sensors using one single device. Their system did not require expensive FFT analyzers and high-speed data acquisition equipment. Their results agreed with those obtained by a commercial impedance analyzer. Kaur et al. [2016] extended the system developed by Peairs et al. [2004] without the amplification and showed satisfactory performance with similar



trends to the commercial device. Although the EMI techniques can effectively detect local damage, it has the disadvantage of requiring a network of sensors when applied to large structures [Tenreiro et al., 2022]. One alternative solution is to use wireless sensors and portable impedance measurement devices with multiple channels. Some researchers utilized the AD5933 impedance measurement evaluation board to establish networks for wireless sensors [Park et al., 2009; Park and Park, 2010; Li et al., 2024].

### 2.3.4 Signal Processing Methods

#### 2.3.4.1 Baseline-dependent EMI Technique: Model-free

As discussed, EMI techniques can present a signal spectrum in an extensive frequency range. Different types of damage changed the signal spectrum of the employed piezoelectric sensor. The baseline-dependent EMI technique is popular in applications. The signal processing method of the baseline-dependent EMI technique is as follows: a spectrum measured from a sensor bonded to a target structure in one status of interest, and then it is used to compare with a spectrum acquired in advance, which is considered as the baseline spectrum [Zahedi and Huang, 2017]. Any difference between these two spectra, evaluated by statistical indices, is considered relevant to damage [Annamdas and Soh, 2010; Lim et al., 2021]. The significant advantage of the qualitative signal processing method was that it was model-free (i.e., not based on any analytical model) and thus easily applied to complex structures [Giurgiutiu and Rogers, 1998]. The following paragraphs discuss several vital characteristics, including statistical metrics, frequency ranges, and physical quantities.

Sun et al. [1995] started to employ a simple statistical algorithm (i.e., relative deviation, RD), which is based on frequency-by-frequency comparison, to quantify the damage to the truss nodes. Then, the RD was also used by several researchers to quantify the damage [Giurgiutiu and Rogers, 1997; Ayres et al. 1998]. The RD can be calculated as shown in Equation (2.12).

$$RD_i = \frac{\sum_{j=1}^N (G_{ij}^1 - G_{ij}^0)^2}{\sum_{j=1}^N (G_{1j}^1 - G_{1j}^0)^2}, \quad (2.12)$$

where  $G_{ij}^1$  and  $G_{ij}^0$  are the conductance of the PZT sensor at frequency interval  $j$  after and before the  $i$ th damage, respectively;  $G_{1j}^1$  and  $G_{1j}^0$  are the conductance after and before the reference point is loosened, respectively;  $N$  is the numbers of frequency intervals.

Giurgiutiu et al. [1999] utilized root mean square deviation (RMSD) to quantify the damage of spot-welded structural joints, as shown in Equation (2.13),

$$RMSD = \sum_{i=1}^N \sqrt{\frac{(G_i - G_i^0)^2}{(G_i^0)^2}}, \quad (2.13)$$

where  $G_i$  and  $G_i^0$  are the conductance values at the damaged and initial (baseline) state of the structure, respectively. In an RMSD damage metric chart, the greater numerical value of the metric leads to a larger difference between the baseline readings and the subsequent reading, indicating the presence of damage in a structure [Park et al., 2023].

The most popular statistical indices include RMSD, cross-correlation (CC), cross-correlation deviation (CCD), cross-correlation coefficient (1-CC), and mean absolute percentage deviation (MAPD) [Lim et al., 2021]. In most cases, the results evaluated by these statistical quantifiers were consistent with those of RMSD, in which the metric values increase when there is an increase in the severity of damage [Park et al., 2023]. The first resonance peak of the PZT transducer is another widely used index to evaluate the changes (e.g., hardening of the concrete) of the target structure, which moves rightward as strength increases [Soh and Bhalla, 2005].

Frequency range is an important factor when using statistical indices. The evaluation sensitivity is highly related to the selected frequency range [Sun et al., 1995]. The frequency range was usually determined by trial and error, given that little analytical work was done about vibration modes of complex structures in such a high-frequency band. Sun et al. [1995] suggested that a frequency band with high mode density is preferred since more structural information about the condition of a structure can be contained. For instance, multiple frequency ranges containing 20-30 peaks were preferred since a higher density of modes indicates a greater dynamic interaction over

that frequency range [Park et al., 2003]. Baptista and Filho [2010] studied the relationship between the frequency range and sensitivity of the PZT transducer, considering the ratio of the mechanical impedance of the structure to the mechanical impedance of the transducer (i.e.,  $Z_{\text{strut}}/Z_{\text{PZT}}$ ). Their results showed that the sensitivity of the transducer decreased as the  $Z_{\text{strut}}/Z_{\text{PZT}}$  increased. Meanwhile, in the frequency range of 0 to 50 kHz, the sensitivity of the PZT transducer was optimal and almost constant in the function of  $Z_{\text{strut}}$ .

The sensing range (detectable range) of the PZT transducer was also affected by the frequency range [Annamdas and Soh, 2010; Lim et al., 2021]. Generally, a high frequency of excitation means that the sensing zone on the host structure is localized [Lim et al., 2021]. A frequency range higher than 200 kHz was favorable for localized sensing, while a frequency range lower than 70 kHz covered a larger sensing area [Park et al., 2003]. However, there is no guidance about the sensing ranges for applications. The material properties (e.g., damping ratios) and boundary conditions for the surrounding area may affect the sensing range.

Although easy and quick to implement, one of the disadvantages of the model-free EMI techniques is that they can only show the presence of damage but cannot show their location, type, size, or severity [Zahedi and Huang, 2017], and the values of the indices are not quantitatively correlated to the change in structural properties [Park et al., 2000].

Another challenge of the baseline-dependent EMI technique is that it highly relies on the sensory system (i.e., sensor and bonding layer). In most research, the electric admittance/impedance was directly evaluated using a statistical model, and empirical models were proposed to correlate the damage. However, the empirical models can hardly be extended to more general applications, considering the great variability in sensory systems. Geometric dimensions and piezoelectric properties determine the sensitivity of the piezoelectric sensor. For example, larger and thinner piezoelectric patches provide higher sensitivity, and larger absolute values of piezoelectric constant

$d_{31}$  are often preferred. Regarding the bonding layer, thinner thickness and stiffer material increase the sensitivity of the sensor.

Besides the sensory system, baseline selection is also important in some cases. For example, unlike damage detection, some research utilized the EMI technique to monitor the evolution process of the concrete. The concrete properties changed dramatically at early ages, indicating that the baseline measurement instant will govern the sensitivity of this method. However, the baseline selection is hard to regulate since concrete properties differ from mix to mix.

The temperature effect is another challenge for the baseline-dependent EMI technique. In real-world practice, impedance-based damage detection systems exhibit strong temperature dependence, which can introduce variations in the electric impedance within the same order of magnitude as the changes produced by moderate structural damage [Gianesini et al., 2020]. Park et al. [1999] presented that temperature effects observed for magnitude and real part of the electrical impedance/admittance could lead to vertical (i.e., electric impedance) and horizontal shifts (i.e., resonant frequency). Physically, temperature affects the material properties of the target system (i.e., sensor, adhesive layer, and target structures) [Tenreiro et al., 2022]. Regarding the piezoelectric sensor, the piezoelectric constants decreased as temperature increased. Meanwhile, different piezoelectric materials have different stability against temperature changes. For example, type PZT-5H has very different thermal behaviors from type PZT-5A [Piezo system, 2024]. At room temperature, the piezoelectric constants  $d_{31}$  of PZT-5H and PZT-5A are  $-320 \times 10^{-12}$  C/N and  $-190 \times 10^{-12}$  C/N, respectively. The higher absolute value of  $d_{31}$  indicates a higher sensitivity of the materials. However, the piezoelectric constant  $d_{31}$  of PZT-5A remains relatively stable from  $-50$  to  $150$  °C, while that of PZT-5H changed dramatically (i.e., the deviation is nearly 50%). Moreover, the dielectric and mechanical properties of piezoelectric materials also change with temperatures. Regarding the adhesive materials, the modulus of elasticity decreased considerably at high temperatures [Yang et al., 2008]. Therefore, compensation

methods are compulsory when using baseline-dependent and model-free EMI techniques.

In addition, the existence of wire resistance also changed the signals. When the wire length is long, it may negatively impact the measurements of the electric impedance [Tenreiro et al., 2022]. Annamdas and Yang [2012] pointed out all the characteristic peaks shifted leftward when the cable length increased.

#### 2.3.4.2 Baseline-dependent EMI Technique: Model-dependent

Although the model-free EMI techniques using statistical indices are quick and convenient, their real-world applications are still limited because of the aforementioned limitations. Although some compensation techniques have been developed to avoid false and unwanted alarms, the existing techniques need the collection of multiple baseline data in a wide range of environmental or operational conditions [Kim et al., 2011]. Meanwhile, compensation has been performed mainly for temperature. Besides, the temperature changes may introduce damage to the target system, which may be masked after compensation [Tenreiro et al., 2022].

Model-dependent EMI techniques extracted structural characteristics from the raw electric signals using an established analytical model of the sensory system. Thus, it is also called the equivalent structural parameters method. In this method, the structural impedance  $Z_{\text{stru}}$  was extracted from the electrical impedance recorded by the piezoelectric sensor using the analytical equations established in advance, such as Equation (2.11). The mechanical impedance of the structure often consists of mass, spring, and damper connected in series or in parallel, considered equivalent to the complex structure. The major advantage of this method is that the effect of the piezoelectric sensor can be removed since the material properties and geometric size are included in the analytical equations. Table 2.10 summarizes analytical models for extracting the mechanical impedance of the target structures. Bhalla and Soh [2003] first extracted mechanical impedance using the 1D analytical equations proposed by Liang et al. [1994] in an SBP-based application and showed the results had higher

sensitivity than conventional low-frequency vibration methods and the model-free EMI technique. After that, the adhesive layer of the SBP was considered in [Soh and Bhalla \[2004a\]](#), which was considered a proportion of  $Z_{\text{stru}}$ . [Soh and Bhalla \[2004a\]](#) found that the adhesive layer significantly affected the measured signals without carefully controlling them. Then, [Soh and Bhalla \[2004b\]](#) first proposed a 2D electro-mechanical coupling model to obtain the mechanical impedance of the host structure more accurately by using the concept of the effective impedance, as shown in Equation (2.14).

$$Y = 4\omega j \frac{l_{\text{PZT}}^2}{h_{\text{PZT}}} \left[ \bar{\epsilon}_{33}^T - \frac{2d_{31}^2 \bar{Y}^E}{(1 - \mu_{\text{PZT}})} + \frac{2d_{31}^2 \bar{Y}}{(1 - \mu_{\text{PZT}})} \left( \frac{Z_{\text{PZT,eff}}}{Z_{\text{stru,eff}} + Z_{\text{PZT,eff}}} \right) \bar{T} \right], \quad (2.14)$$

where  $Z_{\text{PZT,eff}}$  and  $Z_{\text{stru,eff}}$  denote the effective mechanical impedance of the piezoelectric sensor and the target structure, respectively, and  $\mu_{\text{PZT}}$  is the Poisson's ratio of the piezoelectric sensor. Conventionally, the existing model was based on the definition that the endpoint of PZT refers to the particular point to obtain the mechanical impedance of the host structure. However, in practice, the mechanical interaction extends all over the finite-sized PZT patch.

Based on the concept of effective mechanical impedance, the analytical models were extended to different installation types and sensor types. [Wang et al. \[2014\]](#) and [Zuo et al. \[2014\]](#) proposed a 3D analytical model for the embedded square and circular patch, respectively. [Ai et al. \[2016\]](#) derived a 2D analytical model for EBP, in which a rectangular PZT patch was employed and vibrated only along planes 31 and 33. [Wang et al. \[2016\]](#) developed a 3D analytical model for an embedded circle dual-PZT patch. [Ai et al. \[2017\]](#) considered the adhesive layer in the 2D analytical mode. [Zhu et al. \[2019\]](#) developed a 2D analytical model for circular SBP. On the other hand, [Annamdas and Soh \[2007\]](#) developed a 3D semi-analytical model for the SBP and EBP considering the extensional (i.e., along planes 31 and 32) and longitudinal vibration (i.e., along plane 33) of the transducer at the same time. The mechanical impedance of the target structure was obtained by linear combination, which is the so-called directional sum impedance. The experimental validations of the analytical models showed much higher sensitivity than the direct implementation of the model-free EMI technique. Meanwhile,

the results may be extended to different application scenarios [Bhalla and Soh, 2003].

Table 2.10 Analytical models for extracting the mechanical impedance of the structure

Reference	Sensor type	Model dimension	Vibration plane	Installation type	Contact layer
Liang et al. [1994]	Square patch	1D	31	SBP	No
Zhou et la. [1995]	Square patch	2D	31, 32	SBP	No
Soh and Bhalla [2004a]	Square patch	1D	31	SBP, EBP	Adhesive layer
Soh and Bhalla [2004b]	Square patch	2D	31, 32	SBP	No
Annamdas and Soh [2007]	Square patch	3D	31, 32, 33	SBP	No
Wang et al. [2014]	Square patch	3D	31, 32, 33	EBP	No
Zuo et al. [2014]	Circular patch	3D	31, 32, 33	EBP	No
Ai et al. [2016]	Rectangular patch	2D	31, 33	EBP	No
Wang et al. [2016]	Circular dual patch	3D	31, 32, 33	EBP	No
Ai et al. [2017]	Square patch	2D	31, 33	SBP	Adhesive layer
Zhu et al. [2019]	Circular patch	2D	31, 32	SBP	No

Although this equivalent structural parameter method can correlate the signal changes to the physical changes of structures, some limitations still exist. First, most of the models did not include the interface into their models. As discussed above, the bonding and coating layers are necessary for SBP and EBP, respectively, which may significantly affect the measured signals [Soh and Bhalla, 2004a]. For example, bonding defects may mask structural defects. Although some research considers the bonding layer in SBP, their model is too simple to implement in real practice. Moreover, the material properties of the piezoceramics are assumed to be constant and isotropy. In contrast, properties of piezoelectric sensors may vary (e.g., sensor degradation and temperature changes) and be anisotropic in real applications, indicating that the

corresponding modifications are necessary before practical implementation. Therefore, the extracted mechanical impedance is an oversimplified value instead of the actual mechanical impedance [Lim et al., 2019]. Finally, the responses of the target structure were not included in the analytical model, leading to the peaks not being quantitatively discussed.

#### *2.3.4.3 Baseline-free EMI Technique: Resonance-based Method*

Giurgiutiu [2014] pointed out that the peaks in the EMI spectrum coincided with those in the frequency response function obtained by traditional methods. The ability to detect structural resonance by one single sensor is the foundation of using the EMI technique for high-frequency structural identification and SHM. But multiple sensors were required to detect mode shapes [Giurgiutiu and Zagrai, 2002].

Considering their ability to detect structural resonance, the piezoceramic sensors were called modal sensors by Giurgiutiu [2014]. When the piezoceramic sensor was relatively smaller than the target structures, the mass and effect of the sensor could be ignored in a low-frequency range. Resonant frequencies of the structure are functions of the material properties, density, and geometric size under a confirmed boundary condition. Therefore, the resonant frequencies can measure material properties and detect damage directly, and no baseline (reference) data is required. The significant advantage of the resonance-based EMI technique is that the main parameters, structural resonant frequencies, are relatively insensitive to the sensory system (i.e., piezoelectric sensor and bonding or coating layer) in the low-frequency range.

Table 2.11 summarizes the resonance-based quantitative EMI techniques. Giurgiutiu and Zagrai [2002] derived the analytical model to include the responses of a steel beam (i.e., 1D structures) at free-free status using SBP. Axial forces and moments were applied from the piezoelectric sensors to the steel beam, leading to the actuation of the axial and bending modes. Zagrai and Giurgiutiu [2002] developed an analytical model to investigate circular plates (i.e., 2D structures) at free-free status using SBP. The longitudinal and bending modes were presented and discussed. Kuang et al. [2006]



also investigated the interaction between an Euler-Bernoulli beam and a pair of piezoelectric patches. The model could capture the resonant frequencies of the target beam and was used to detect a single open crack. [Yan et al. \[2007a, 2007b\]](#) developed analytical models of homogenous Euler-Bernoulli and Timoshenko beams with SBP. Pure bending modes were actuated by combining two piezoelectric sensors bonded to the beams to investigate high-frequency signatures. [Kim et al. \[2011\]](#) developed an analytical model to consider the  $S_0$  mode and  $A_0$  mode of a rectangular plate actuated by a pair of piezoelectric patches. Then, the resonant frequencies of these two modes were used to detect the damage. [Xie and Li \[2020\]](#) employed PZT rings and a cylinder specimen to measure the material properties of target materials (i.e.,  $\text{Fe}_{64}\text{Ni}_{36}$ ). Longitudinal and torsional modes were actuated for analyses. The method was extended to concrete to monitor the evolution of concrete at the hardening stage [\[Liu et al., 2023\]](#). [Kong and Lu \[2020\]](#) utilized the EBP and concrete cylinders to evaluate the material properties of concrete. The EBP was installed on the neutral axis, and the first two longitudinal modes were used for evaluation.

In summary, relatively rare attention has been paid to the resonance-based EMI technique, which is sometimes referred to as the EMI-R technique [\[Kong and Lu, 2020\]](#). In the EMI-R technique, the actuation mechanism of the piezoelectric sensors needs to be identified first. The vibration type of the piezoelectric sensor in the given frequency range and installation locations are directly related to the actuation mechanism. Then, the response of the target structure needs to be solved. Unlike traditional resonance tests, SBP and EBP transducers act as a pair of self-equilibrating forces [\[Giurgiutiu, 2014\]](#). The current research focuses on beam-like and plate-like structures in small sizes. In the beam-like structures, bending and longitudinal modes were employed. Global (i.e., bending and longitudinal) modes and local ( $S_0$  and  $A_0$ ) modes were employed for plate-like structures. In the concrete field, the geometries of host structures are more diverse, and the sizes are larger. For example, concrete cubes are widely used for measuring compressive strength. Concrete beams or slabs have a width or thickness larger than

100 mm, leading to difficulties for the existing evaluation methods. Meanwhile, the boundary conditions are more complex than free-free status in actual practice.

Table 2.11 Baseline-free EMI techniques

Reference	Sensor type	Host structure	Boundary conditions	Installation location and type	Structural mode types	Objectives
<a href="#">Giurgiutiu and Zagrai [2002]</a>	Square patch	Steel beams: 100 × 8 × 2.6 (5.2) mm <sup>3</sup> 100 × 19.6 × 2.6 (5.2) mm <sup>3</sup>	Free–free	Surface center: SBP	Longitudinal and bending modes	DD
<a href="#">Zagrai and Giurgiutiu [2002]</a>	Circular patch	Circular aluminum plate: Φ 100 mm × 0.8 mm	Free–free	Surface center: SBP	Longitudinal and bending modes	DD
<a href="#">Kuang et al. [2006]</a>	Square patch	Steel beam: 200 × 75 × 25 mm <sup>3</sup>	Free–free	Surface center: SBP	Bending mode	DD
<a href="#">Yan et al. [2007a, 2017b]</a>	Rectangular patch	Steel beam: 200 × 20 × 1.4 mm <sup>3</sup> 200 × 20 × 2.0 mm <sup>3</sup>	Free–free	Surface center: SBP	Bending mode	DD
<a href="#">Kim et al. [2011]</a>	Circular patch	Steel plate: 610 × 400 × 6 mm <sup>3</sup>	Free–free	Surface center: SBP	S <sub>0</sub> and A <sub>0</sub> modes	DD
<a href="#">Xie and Li [2020]</a>	Circular ring	Fe <sub>64</sub> Ni <sub>36</sub> Invar alloy: Φ 10 mm × 80 mm	Free–free	Top surface: SBP	Longitudinal and torsional modes	MPM
<a href="#">Kong and Lu [2020]</a>	Square patch	Concrete cylinder: Φ 76.2 mm × 152.4 mm	Free–free	Neutral axis: EBP	Longitudinal mode	MPM
<a href="#">Liu et al. [2023]</a>	Circular ring	Concrete cylinder: Φ 40 mm × 120 mm	Free–free	Top surface: SBP	Longitudinal and torsional modes	MPM

Note: DD refers to damage detection. MPM refers to material property measurement.

### 2.3.5 Applications in Concrete

Since [Liang et al. \[1994\]](#) developed the coupled EMI concept, the EMI techniques have been widely applied in aerospace, mechanical, and civil engineering, in which piezoelectric transducers are usually used as actuators and/or receivers [\[Annamdas and Soh, 2008\]](#). This section reviews focused on their applications in the concrete field. The major applications are focused on the following perspectives: (a) material properties characterization, including strength prediction and modulus of elasticity measurement; (b) hydrating concrete monitoring; (c) damage detection.

#### 2.3.5.1 Material Properties Characterization

SBP is widely used for strength prediction. In most research, the shift of the first resonant frequency of PZT ( $f_{PZT}$ ) was used to correlate with the concrete/cementitious strength or modulus of elasticity. Meanwhile, statistical models were popular to evaluate the strength gain of concrete/cementitious materials. [Table 2.12](#) summarizes the applications of the EMI technique for predicting the properties of concrete/cementitious materials. [Soh and Bhalla \[2005\]](#) adopted the first resonant frequency of the piezoelectric patch to predict the concrete strength tested by standard concrete cubes (150 mm in width). [Shin et al. \[2008\]](#) monitored the strength gain of early-age concrete. The shift of  $f_{PZT}$  and RMSD (data in day 3 set as the baseline) in the 100-400 kHz range was utilized to correlate the strength gain tested by the standard concrete cylinders ( $\Phi 100 \text{ mm} \times 200 \text{ mm}$ ). [Tawie and Lee \[2010\]](#) correlated the shift of  $f_{PZT}$  to the compressive strength of the standard concrete cube (150 mm in width). [Jothi Saravanan et al. \[2017\]](#) correlated RMSD (baseline: day 1) to the strength gain of concrete cubes using EBP. [Ghafari et al. \[2018\]](#) correlated the statistical models (index: RMSD and CC; baseline: day 1) to the compressive strength of different cementitious materials using 50-mm cubes. [Su et al. \[2019\]](#) correlated the RMSD to the strength gain of cementitious materials from 4 hours using 50-mm cubes. The samples were demolded carefully for very early-age testing. [Su et al. \[2020\]](#) investigated the shift of  $f_{PZT}$  regarding the changes in the modulus of elasticity of cementitious materials at the

hardening stage using SBP and concrete cubes. The results demonstrated a high correlation between these two parameters. [Lu et al. \[2020\]](#) correlated the resonant frequencies of the ‘Miniature Prism’ to the dynamic modulus and strength of the cementitious (mortar) using SBP and EMI techniques. Their results were presented with good repeatability and were more effective than the conventional rebound tests. [Pan and Huang \[2020\]](#) investigated relationships between RMSD (baseline: final setting time) and compressive strength of the mortar using EBP and cubes. Their discussion showed that RMSD in a higher frequency region, such as that higher than 800 kHz, can promote the reliability of mortar strength monitoring. [Li et al. \[2021\]](#) correlated the changes in the  $f_{PZT}$  to the compressive strength of recycled aggregate concrete. Linear relationships were regressed between the early-age strength of the recycled aggregate concrete and the increment of the  $f_{PZT}$ .

In summary, the applications of the EMI techniques in the characterization of concrete/cementitious materials are popular. However, several issues have not been addressed yet. The first one is the effect of the bonding/coating layer.  $f_{PZT}$  was commonly employed as the main index. However, it is sensitive to the status of the bonding/coating layers geometrically (i.e., thickness) and mechanically (i.e., modulus of elasticity). The second one is that there is no unified theory to extend the existing results, limiting the application scenarios of the EMI techniques.

Table 2.12 Summaries of applications of the EMI techniques for predicting the properties of concrete/cementitious materials

Reference	PZT size (mm)	Sensor type	Index	Frequency range (kHz)	Baseline status	Specimen size	Strength range (MPa)
Soh and Bhalla [2005]	10×10×0.3	SBP	$f_{PZT}$	0–1000	Free PZT	150 mm cube	10–100
Shin et al. [2008]	10×10×0.2	SBP	$\Delta f_{PZT}$	100–400	Day 3	Φ 100 mm × 200 mm	<27.73
Tawie and Lee [2010]	10×10×0.5	SBP	$\Delta f_{PZT}$	100–400	Day 3	150 mm cube	<45
Jothi Saravanan et al. [2017]	10×10×0.3	EBP	RMSD	10–500	Day 1	150 mm cube	<40
Ghafari et al. [2018]	10×10×0.2	SBP	RMSD CC	2–500	Day 1	50 mm cube	56.27–71.97
Su et al. [2019]	10×10×0.2	SBP	RMSD	100–500	4 hours	50 mm cube	2.6–33.5
Su et al. [2020]	10×10×0.2	SBP	$f_{PZT}$	5–1000	Free PZT	50 mm cube	1.1–27.3
Lu et al. [2020]	10×10×0.3	SBP	$f_{struc}$	3–350	-	250×15×10 mm <sup>3</sup>	40–65
Pan and Huang [2020]	Φ12×1.8	EBP	RMSD	72–2000	Final setting time	50 mm cube	10–40
Li et al. [2021]	Φ10×1.0	EBP	$\Delta f_{PZT}$	100–500	Day 2	150 mm cube	9.3–26.6

#### 2.3.5.2 Concrete Hydration Monitoring

Concrete is an aging material that transforms from a plastic (fluid) to a solid state, and the solid gains strength over time. The maturity and hydration monitoring were highly desired for the construction site. The EMI technique was considered an alternative tool to monitor the evolution of concrete properties at early ages. Embedded sensors were preferred since they can monitor the evolution of concrete from the beginning of the hydration process. The piezoceramic sensors were protected in advance to avoid failure. In these application scenarios, the shift of the first resonance

peak was employed as the index rather than the statistical model since the baseline data was hard to select.

Table 2.13 summarizes the EMI technique for hydrating concrete monitoring. Narayanan et al. [2017] embedded a PZT patch into a mortar cube and conducted 28-day monitoring. The shift of the  $f_{PZT}$  was utilized to evaluate the evolutions. The results showed that very rapid changes were observed within 24 hours, and the change rate decreased after 10 days. The concrete evolutions were also monitored using the EBP within the first 28 days after casting [Bharathi Priya et al. 2018; Kocherla and Subramaniam, 2020]. The evolution pattern was the same as that of the mortar. The amplitude of the PZT resonance peak decreased while the PZT resonant frequency  $f_{PZT}$  increased rapidly at the same time from 3 to 9 hours after casting. The changes during the first 24 hours of hydration were rapid, with a progressively decreasing change rate up to the 10-day curing age. After a 10-day curing age, peak amplitude and frequency changes were minimal. Fan et al. [2021] utilized an embedded spherical to monitor the hydration of concrete in the first 10 hours and compare it with traditional path-based EBP. Their results were evaluated using RMSD and showed that the spherical PZT shell was more sensitive and suitable for the hydration change. Hu et al. [2024] utilized an embedded sensor to monitor the evolution of concrete in the first 6 hours. The fabricated sensors were embedded on a construction site in advance, and their monitoring evaluations using  $f_{PZT}$  were consistent with the bar-dropping test procedure.

In summary, some attempts have been conducted to monitor the evolution of concrete at early ages using the EMI technique and EBP. Currently, the first resonance peak of the PZT sensor has been utilized for evaluation. Although the signal changes have proved effective, they will not directly correlate to the concrete properties.

Table 2.13 Summary of the EMI techniques for hydrating concrete monitoring

Reference	PZT size (mm)	Index	Frequency range (kHz)	Baseline status (hour)	Specimen size	Curing age
<a href="#">Narayanan et al. [2017]</a>	20×20×1.0	$\Delta f_{PZT}$	10–150	0	100 mm cube	0–28 day
<a href="#">Bharathi Priya et al. [2018]</a>	10×10×0.3	$\Delta f_{PZT}$	10–500	0	150 mm cube	0–28 day
<a href="#">Kocherla and Subramaniam [2020]</a>	20×20×1.0	$\Delta f_{PZT}$	10–500	0	150 mm cube	0–28 day
<a href="#">Fan et al. [2021]</a>	Spherical shell Outer radius: 10 Inner radius: 9.25	RMSD	50–200	1	Cylinder: 250 mm×324 mm	1–10 hour
<a href="#">Hu et al. [2024]</a>	Φ20×0.2	$\Delta f_{PZT}$	40–200	0.5	Concrete field	0–6 hour

#### 2.3.5.3 Damage Detection

Damage detection is the most popular application of EMI techniques. Different types of damage were introduced to concrete specimens and structures. This subsection discusses different types of damage, including loading-induced damage and artificial damage.

##### *Loading-induced Damage*

Concrete specimens, such as slabs and beams, with bending-induced damage, were widely investigated using the EMI technique. [Soh et al. \[2000\]](#) conducted a monitoring study during the destructive loading testing of a prototype RC bridge ( $5250 \times 1000 \times 250 \text{ mm}^3$ ) instrumented with SBP ( $10 \times 10 \times 0.3 \text{ mm}^3$ ). Their result showed the signals of the patches located in the vicinity of the damage were significantly affected, while those farther away were less affected. RMSD was used to quantify the damage. [Ai et al. \[2018\]](#) investigated the monitoring of the tension/compression stress-induced damage using SBP ( $10 \times 10 \times 0.5 \text{ mm}^3$ ) and an RC beam ( $2000 \times 220 \times 150 \text{ mm}^3$ ) subjected to a four-point bending test. The damages were evaluated through RMSD using raw



signals and compared to those of non-stressed SBP. The results showed that an increase in tension and compression stress leads to a decrease and increase in resonant frequency and peak amplitude, respectively. Meanwhile, RMSD indices displayed gradual growth with an increase in structural stress. [Ai et al. \[2019\]](#) extended their work to a pre-stressed RC beam using SBP and found that RMSD and its rate could not only offer a higher sensitivity in comparison with conventional sensors (i.e., strain gauges and displacement) but also detect concrete cracking and reinforcement yielding in advance. [Balamonica et al. \[2020\]](#) utilized a multi-sensing technique, which connected the SBPs ( $10 \times 10 \times 0.3 \text{ mm}^3$ ) in series and parallel to speed up the data retrieval process in an RC beam ( $1500 \times 240 \times 150 \text{ mm}^3$ ) subjected to a three-point bending test. [Ai et al. \[2023\]](#) investigated flexure-induced damage in an RC beam ( $2000 \times 400 \times 200 \text{ mm}^3$ ) using EBPs (sensor size:  $10 \times 10 \times 0.5 \text{ mm}^3$ ). Their results showed that EBPs were superior to visual inspection and SBP in identifying concrete cracking and that those located in the compressive zone were more effective in predicting the forthcoming yield and final failure of the RC beam.

Seismic-induced damage in concrete frames was also investigated using the EMI technique. [Bhalla and Soh \[2003\]](#) reported a damage diagnosis study conducted on an RC frame model (420 mm width and 580 mm height) subjected to ground motions on a shaking table. The  $Z_{\text{stru}}$  was extracted from the raw signal recorded by SBP ( $10 \times 10 \times 0.2 \text{ mm}^3$ ) and evaluated with RMSD to quantify the damage. This evaluation method performed better than the low-frequency vibration modes and the raw-signals-based quantitative EMI technique. [Yang et al. \[2008\]](#) conducted a sensitivity analysis for damage detection of an RC frame (3000 mm width and 3750 mm height) subjected to ground motions on a shaking table using SBP ( $10 \times 10 \times 0.2 \text{ mm}^3$ ). RMSD was utilized to evaluate the raw signals and extracted structural mechanical impedance. Their evaluation showed that the real parts of the  $Z_{\text{stru}}$  were more sensitive to damage than the imaginary parts. Based on this index, the sensing region of the PZT sensor was determined to be 70-90 cm for the concrete material, while the sensing region was only

40-60 cm for the raw signals.

Uniaxial loading on the standard concrete specimens was another topic regarding the EMI technique-based damage evaluation. [Narayanan and Subramaniam \[2016\]](#) investigated the concrete cubes ( $150 \times 150 \times 150 \text{ mm}^3$ ) with SBP ( $20 \times 20 \times 1.0 \text{ mm}^3$ ) at loaded (i.e., uniaxial compressive stress) and unloaded conditions using the EMI technique. Their results showed that the indices  $f_{PZT}$  and RMSD were insensitive to the damage at a low-stress ratio at loaded conditions. Only at a high-stress ratio could the damage be detected well in the RMSD values in both loaded and unloaded conditions. [Wang et al. \[2018\]](#) employed EMI techniques to study the axial load effects on the steel fiber concrete using concrete cubes ( $150 \times 150 \times 150 \text{ mm}^3$ ) and EBP ( $15 \times 15 \times 1.0 \text{ mm}^3$ ). Their results showed that axial loads can be well correlated to the normalized RMSD values, considering RMSD values with and without loading conditions. [Zhao et al. \[2020a\]](#) utilized the EMI technique to assess the damages of concrete cubes ( $150 \times 150 \times 150 \text{ mm}^3$ ) with EBP (circular patch) under uniaxial compressive stress. RMSD indices were considered effective in detecting the damage and correlated to the damage volume ratio of the concrete. [Zhao et al. \[2020b\]](#) extended their conclusions to concrete cubes with embedded spherical PZT sensors, which are more sensitive than the traditional circular patch. [Liu et al. \[2023\]](#) presented that EBP ( $10 \times 10 \times 0.5 \text{ mm}^3$ ) placed along the loading direction had better sensitivity than that placed normal to the loading direction in concrete cubes ( $100 \times 100 \times 100 \text{ mm}^3$ ) when using the RMSD index.

#### *Artificial Damage*

Artificial damage, such as cutting, was preferred to be introduced to concrete specimens to quantitatively assess the damage in terms of location and severity using the EMI technique. [Tseng and Wang \[2004\]](#) investigated the ability of the qualitative EMI technique (i.e., RMSD was used) to estimate the location and extent of damages introduced by artificial cutting using plain concrete prisms ( $500 \times 100 \times 100 \text{ mm}^3$ ) and SBP (diameter and thickness equal to 12 mm and 0.35 mm, respectively). Their results

demonstrated that RMSD could detect the increase in damage extent as the damage approached the SBP on the surface and in the depth of the concrete prism. Wang et al. [2013] investigated the ability of the qualitative EMI technique (i.e., CC was used) to detect the location and severity of damages introduced by artificial cutting using plain concrete beam ( $2000 \times 200 \times 100 \text{ mm}^3$ ) and SBP ( $26.5 \times 13.5 \times 0.5 \text{ mm}^3$ ). Their results showed that the values of the CC index from one sensor decreased gradually with the increase in damage severity. Meanwhile, the values of the CC index decreased with the distance to the damage decrease, ensuring the ability to estimate the damage location. Hu et al. [2014] extended the investigation of damage detection of the artificial cutting to the plain concrete slab ( $600 \times 300 \times 40 \text{ mm}^3$ ) using the qualitative EMI technique and SBP ( $10 \times 10 \times 0.5 \text{ mm}^3$ ) and compared the statistical index of RMSD, CCD, and  $R_y/R_x$ . The results showed that a new damage index,  $R_y/R_x$ , was effective for detecting the damage location and extent.

Kim et al. [2019] investigated the ability of the model-free EMI technique (i.e., RMSD, MAPD, CoV, and CCD were used) to assess the crack (introduced by artificial cutting) repair in plain concrete specimens ( $250 \times 125 \times 150 \text{ mm}^3$ ) using SBP ( $25 \times 25 \times 0.2 \text{ mm}^3$ ). Their results showed that RMSD, MAPD, and CCD could be used as effective indices to assess damage severity and its recovery in the optimal frequency range of 50-99.9 kHz. Lan et al. [2024] extended the application of crack repair assessment using model-free EMI techniques (i.e., RMSD, MAPD, and CCD) from SBP to two types of EBP in concrete cubes ( $200 \times 200 \times 200 \text{ mm}^3$ ), including traditional PZT patches and spherical PZT sensors. Their results showed that the spherical PZT sensor performed better in sensitivity and stability during the evaluation.

## 2.4 Summary and Remarks

Although it is the most used material in civil engineering, concrete has not been sufficiently investigated at the current stage. Regarding testing targets in the laboratory, current NDT can only be implemented on specific geometry shapes (such as prisms with certain length-to-width ratios), while some commonly used shapes of concrete

specimens and members, such as cubic shape specimens, cannot be measured. Regarding the measurement of the material properties, accurate determination of the elastic constants is still challenging because the existing methods do not examine the impacts of the two fundamental assumptions: (a) concrete material is considered isotropic; (b) concrete material is assumed to be homogenous.

Regarding the delamination detection in concrete structures, current NDT methods aim to roughly detect large-size defects outdoors, such as on the exterior walls of high-rise buildings and bridge decks; there is no practical method to detect delamination for indoor problems, such as the bottom side of concrete slabs in buildings with considerably smaller size of delamination.

Considering the development of the EMI technique, it provides a promising solution to address some critical problems in the concrete field. Compared to other acoustic methods, the EMI technique has numerous advantages. From the mechanism perspective, the actuation can be well controlled and designed, and sweeping from low to high-frequency range can be easily and quickly achieved. From the implementation perspective, only one sensor and one device are needed, leading to ease of operation outside the laboratory. [Figure 2.12](#) compares the working frequency and dimension ranges of the reviewed mechanical wave-based techniques. From the working frequency range of the perspective, the impulse-response method covers the low-frequency range (1-800 Hz), the impact-echo method works in the middle-frequency range from hundreds of hertz to forty kilohertz, and the RUS method utilizes the response in the high-frequency range from seventy kilohertz to seven megahertz. From the dimension range perspective, the RUS method is only suitable for small specimens (smaller than 10 mm), while the impact echo method can detect a thickness dimension of up to 1.4 m. EMI technique can cover a wide frequency range from 2 kHz to 2 MHz from the literature, ensuring it can cover the dimension range from 10 mm to 1000 mm. The working frequency range and dimension range of the EMI technique indicate that the EMI technique can not only be used to characterize the material properties but also

to detect damage or monitor structures in actual practice. The simple features of the EMI technique ensure that it is easy to conduct in laboratories and on construction sites.

However, some issues should be addressed for the EMI techniques when effectively implemented in the concrete field. A baseline-free method should be proposed for concrete specimens and structures, considering the effects of the bonding layer and sensor itself. Currently, the baseline-free EMI technique is only suitable for beams and plates under axial and bending vibrations. They cannot be directly extended to the existing concrete specimens. For example, the mode shapes of a cube are complicated and need to be studied and selected carefully. Moreover, the fundamental frequencies of the axial and bending modes of large concrete beams and slabs are too low for piezoelectric sensors, whose effective frequency range is greater than 2 kHz when no amplifier is used.

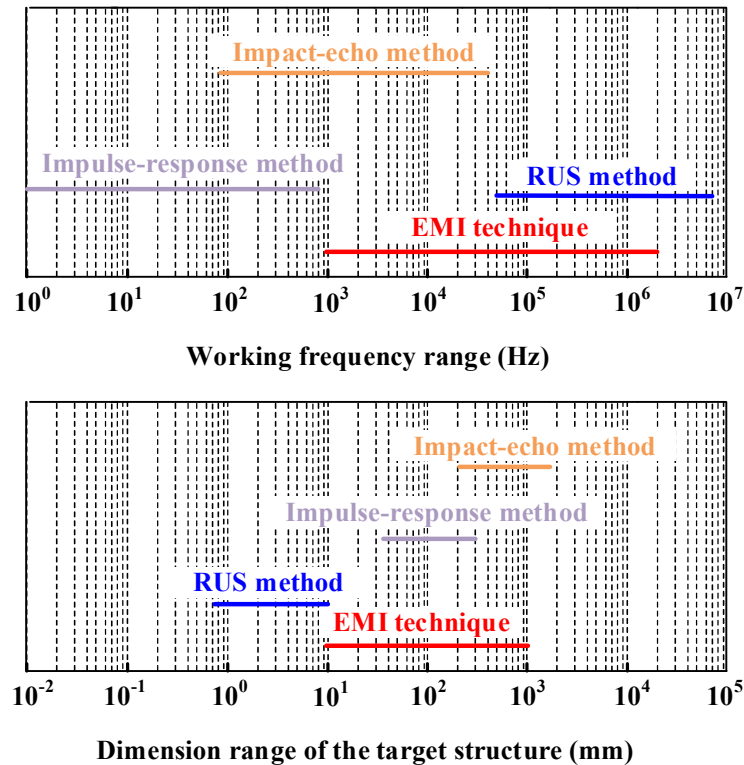


Figure 2.12 Comparison of the working frequency dimension ranges of the reviewed techniques

To bridge the above-mentioned knowledge gaps, this thesis presents systematic investigations of the EMI techniques for material characterization and delamination

detection in concrete. The knowledge gaps addressed in this thesis are listed as follows:

- (1) Existing NDT methods for material characterization are established in terms of standard cylinders/prisms. Standard concrete cubes, commonly used on construction sites and in laboratories, are not covered in the existing NDT methods. The EMI technique is promising to fill this gap. However, the physical meaning of the signal spectra of the EMI technique using concrete cubes is unclear.
- (2) The measurement of the modulus of elasticity of concrete by using NDT methods is extensive and well-established. By contrast, measurement of Poisson's ratio is challenging in concrete because of its anisotropic and inhomogeneous properties. Standard static and dynamic testing methods present dispersive evaluations on Poisson's ratio. NDT methods that can accurately, stably, and rapidly measure Poisson's ratio are absent.
- (3) The material properties of very-early-age concrete are desired on construction sites. Existing NDT methods are qualitatively correlated to concrete strength in this stage and cannot measure the elastic constants in this stage because (a) dramatic changes in Poisson's ratio make the accurate evaluation of elastic constants difficult, and (b) the high damping ratio of concrete at this stage leads to difficulties in measurement.
- (4) The existing baseline-free EMI techniques still focused on small-scale beam-like specimens using the fundamental resonance modes at free-free boundary conditions. However, beam-like structures in concrete are large and may have more complicated boundaries. An effective strategy is desirable to extend the EMI technique in actual practice.
- (5) Existing NDT methods cannot effectively cover small-size concrete delamination in indoor structures (e.g., slab structures). The EMI technique has shown the ability to detect this type of damage. However, the EMI technique employs baseline-dependent signal processing methods and fixed sensors in

the existing concrete studies, which cannot achieve large-area inspections and limits the actual applications. The EMI technique, which utilizes a detachable sensor, is highly desired for detecting delamination in indoor concrete structures.

The solutions presented in this thesis for the abovementioned research gaps are as follows:

- (1) Find the signal characteristics that are highly related to the target structures and insensitive to the sensory system (i.e., material properties and geometric size of piezoelectric sensors and adhesive layers) in the EMI signal spectrum. Structural resonance peaks are physically expressed, extracted, and used to measure the modulus of elasticity of standard concrete cubes.
- (2) Study and select the vibration modes that show special behavior. With the understanding of the vibration modes of the specimens and structures, special vibration modes can be utilized to overcome difficulties mentioned in the research gaps. In cube specimens, two types of vibration modes are studied and used: (a) vibration modes without direction bias, which may show superiority to measure elastic constants of weak anisotropic material; (b) vibration modes that are only related to shear modulus, which ensures the evaluation accuracy independent of the variation of Poisson's ratio. In prism specimens, special modes that are insensitive to the length in the middle-frequency range are studied and selected to achieve more general measurements. These length-insensitive modes further benefit the measurement under more complex boundary conditions.
- (3) Design proper installation methods for extracting target modes: After knowing the characteristics of the vibration modes in each scenario, appropriate sensors, actuation mechanisms, and bonding materials can be designed to (a) extract the target modes with the concept of symmetry for material characterization, (b) extract local resonance modes with the concept of local vibration behavior

for damage detection. Fixed (including SBP and EBP) and detachable sensors are used to achieve target extraction for material characterization and damage detection. Corresponding signal processing and evaluation methods are established numerically.



## CHAPTER 3 MEASURE MODULUS OF ELASTICITY OF CONCRETE CUBES USING SBP

The thesis begins with establishing a framework for the baseline-free EMI techniques using SBP, considering SBP is the most widely used installation strategy for piezoelectric sensors and can be operated easily. As one of the most tested standard specimens, concrete cubes are employed to ensure the proposed method can be easily accepted by engineers and directly applied on construction sites. Signal characteristics with high reproducibility, repeatability, and stability are required to generalize the proposed baseline-free method. Therefore, signal characteristics should meet the criteria as follows: (a) reproducible in different concrete materials and test specimens; (b) repeatable in different sizes of sensor and thicknesses of bonding layer; (c) stable regarding the temperature change.

The EMI technique can easily capture a series of the resonant frequencies of the tested cubes using sweeping frequencies. In this chapter, these resonant frequencies are examined numerically and experimentally regarding the abovementioned three criteria, showing suitability as the target signal signatures. Then, a framework to utilize these resonant frequencies to measure the modulus of elasticity of concrete cubes is presented.

Experiments show that the proposed baseline-free EMI technique can quickly, conveniently, and accurately measure the modulus of elasticity of 28-day-age concrete, compared with the traditional destructive testing method.

### 3.1 Introduction

As reviewed in [Section 2.1](#), two essential material properties, namely, compressive strength ( $f'_c$ ) and modulus of elasticity ( $E_c$ ), are inevitably used in the design of concrete structures. These two properties are highly related to concrete mix design, handling, compaction, and curing conditions [[Neville and Brooks, 2010](#)].

As reviewed in [Section 2.2](#), various NDT methods, such as UPV measurements and resonance methods, have been proposed to estimate  $E_c$  of concrete and monitor

concrete structures.

As reviewed in [Section 2.3](#), baseline-dependent EMI techniques are widely used in concrete specimens to correlate the signal changes (i.e., changes of the PZT peak or structural peaks) obtained by the SBP to the development of the strength or modulus of elasticity of concrete through statistical indices. However, the evaluations of the baseline-dependent EMI techniques are sensitive to the selection of the PZT sensor and adhesive materials, as well as the variation of the ambient environment. In comparison, baseline-free EMI techniques based on the frequency shift of structural resonance peaks were developed recently for different materials. Several attempts have been made to measure  $E_c$  in prism and cylinder specimens in small sizes. The results showed the promising application of the EMI technique in predicting the physical parameters of a host structure. By contrast, concrete cubes, as the most used standard specimen in the concrete field, have not been covered by the baseline-free EMI technique, which motivated the research in this chapter.

The abovementioned research concludes that the baseline-dependent approaches are highly sensitive to the status of the sensor system, leading to the inconvenient and complex implementations of the EMI techniques. Meanwhile, a baseline-free signal processing method utilizing the resonance of the host structure has promising application scenarios in concrete structures and has not been extended to concrete cubes. The following research gaps relevant to this chapter can be identified in the existing studies: (1) Reproducible characteristics of the signatures (i.e., resonant frequencies of cubes) that are highly related to the properties of concrete cubes and insensitive to the status of the sensor system are needed. (2) The physical meanings of cube resonance peaks for specific host structures (e.g., standard cubes commonly tested in the field of concrete materials) need to be understood to achieve quantitative evaluation. (3) A quick and convenient assessment employing the selected characteristics is demanded for concrete monitoring, which has the potential to be extended to different types of concrete structures.

To this end, this chapter presents the first baseline-free framework for measuring the modulus of elasticity of concrete using the EMI technique and concrete cubes installed with SBP. Standard concrete cubes with SBP are investigated numerically and experimentally to bridge the abovementioned gaps, thereby shedding light on future research on the monitoring of concrete curing, degradation, and damage. The rest of this chapter is organized as follows: Reproducible features in the EMI spectrum of cubes installed with different sizes of SBP are discussed and extracted through a numerical model first. Then, the stability of the extracted features is analyzed by considering the effects of dimensions and thermal effects on PZT patches and bonding layers. Correlations between the concrete material properties and selected features are established. Finally, the accuracy of measurement, signal repeatability, and temperature effects are investigated and validated experimentally.

## **3.2 Numerical Investigations on Suitable EMI Indicators**

### **3.2.1 Numerical Simulation Setup**

Although 1D and 2D interactions between a PZT transducer and a host structure have been derived previously [Liang et al., 1994; Zhou et al., 1995; Zagri and Giurgiutiu, 2002], similar derivation in 3D structures is challenging. The finite element method (FEM) can simplify the analyses of such 3D problems. In comparison, conventional analytical models can hardly accurately investigate the bonding layer effects. Therefore, FEM is an effective tool for simulating dynamic interactions in EMI techniques [Ai et al., 2020; Tang et al., 2020; Narayanan et al., 2018; Zhao et al., 2020]. Commercial FEM software, ANSYS, is used in the present chapter for multiphysics harmonic analysis in the coupled electromechanical field. The detailed principle for the piezoelectric analysis in ANSYS can be found in Yang et al. [2008a, 2008b] and Ai et al. [2020].

A standard concrete cube (100 mm in width), widely used in concrete-related codes, is simulated as a host specimen whose modulus of elasticity is to be measured. In practical laboratory tests, cubes can provide at least four surfaces for sensor bonding,

facilitating the validation of test repeatability. A square-section PZT patch is bonded to the surface center by using an adhesive material. The shape of the adhesive material is assumed as a cuboid with its width equal to that of the PZT patch. Taking advantage of the model symmetry, only a quarter model is numerically simulated to save computation time, as shown in [Figure 3.1](#). Solid5, a coupled field solid element with eight nodes, is used to model the PZT patch. Solid45 is used for adhesive and concrete materials. The mechanical and piezoelectric properties of the PZT materials used in this chapter are listed in [Table 3.1](#), which were given by the factory. The material properties of epoxy and concrete are listed in [Table 3.2](#), which are consistent with those measured in the experimental section. The interface between the PZT layer and the adhesive layer is assumed to be fully bonded. The top surface of the concrete layer is picked as the target area by using Target170 element. The bottom surface of the adhesive layer is set as the contact area by using the Contact174 element. The PZT patch is excited by a sinusoidal voltage of 1 V in the polarization directions (i.e., between the top and bottom surfaces) within a wide frequency range of 0.5–250 kHz (step size: 0.5 kHz) to obtain the EMI signatures. After a convergence analysis of element sizes, an element mesh size of 0.05 mm is selected for the PZT and adhesive materials, and a mesh size of 1.25 mm is selected for the concrete, both satisfying the relationship between the element size and the minimum wavelength [[Zhao et al., 2020](#)]. Free boundary conditions are employed in the models of the target samples [[Zagri and Giurgiutiu, 2002](#)], considering the concrete cubes were put on a table with low stiffness and friction in the experiments in [Section 3.3](#).

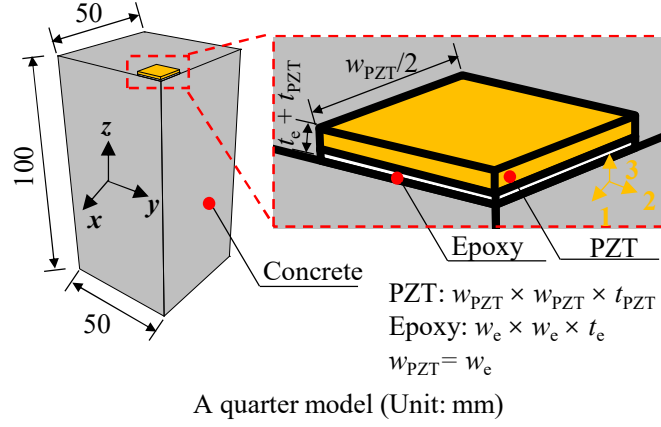


Figure 3.1 A quarter-model adopted for simulations

Table 3.1 Material properties of PZT used in simulations

Parameters	Values
Relative permittivity $\epsilon^S$ under constant strain (F/m)	$\epsilon_{11}^S = \epsilon_{22}^S = 1310$ $\epsilon_{33}^S = 810$
Piezoelectric strain coefficients $d$ ( $10^{-12}$ m/V)	$d_{31} = d_{32} = -255$ $d_{33} = 400$ $d_{52} = d_{61} = 650$
Compliance $s^E$ under short circuit ( $10^{-12}$ m <sup>2</sup> /N)	$s_{11}^E = s_{22}^E = 16$ $s_{33}^E = 19$ $s_{12}^E = -5.13$ $s_{13}^E = s_{23}^E = -6.46$ $s_{44}^E = s_{55}^E = 45$ $s_{66}^E = 41$
Density, $\rho_{PZT}$ (kg/m <sup>3</sup> )	7600
Dielectric loss factor, $\tan \delta$	0.02
Damping ratio, $\xi_{PZT}$	0.024

Table 3.2 Material properties of epoxy and concrete used in simulations

Material	Parameters	Values
Epoxy	Density, $\rho_e$ (kg/m <sup>3</sup> )	1100
	Modulus of elasticity, $E_e$ (GPa)	3.0
	Poisson's ratio, $\mu_e$	0.38
	Damping ratio, $\xi_e$	0.024
Concrete	Density, $\rho_c$ (kg/m <sup>3</sup> )	2408
	Modulus of elasticity, $E_c$ (GPa)	30
	Poisson's ratio, $\mu_c$	0.20
	Damping ratio, $\xi_c$	0.008

In literature, conductance ( $G$ ) (i.e., the real part of the admittance) is often considered more sensitive to the changes of host structures (e.g., hardening and damage) than susceptance ( $B$ ) (i.e., the imaginary part of the admittance). However, presenting  $G$  spectra only and neglecting the changes of the  $B$  spectra results in information loss. These two physical quantities obtained in the tests highly depend on the piezoelectric material properties. In practice, a dimensionless physical quantity is always preferred to improve the generalizability for piezoelectric materials of different properties. The phase,  $\arctan(B/G)$ , consisting of the conductance and susceptance can provide promising evaluation results [Su et al., 2020]. Since the  $B$  value is considerably larger than  $G$ , the shapes of the phase and conductance spectra tend to be mirror-symmetric, i.e., the peaks in the  $G$  spectra correspond to the valleys in the phase spectra. Therefore, the present chapter adopts a new physical quantity, i.e.,  $\arctan (G/B)$ , which is the complementary angle of the phase. Its peak frequencies are consistent with those peaks in the conductance spectra. Signals obtained by the SBP of different dimensions are simulated and analyzed directly in the following sections.

### 3.2.2 Repeatable Signature for Different Sizes of PZT Patches

Although the EMI signals in a high-frequency range may be more sensitive to the changes in the status of the host concrete specimens (e.g., modulus of elasticity), they are also heavily affected by the PZT and epoxy dimensions [Yang et al., 2008a]. It is a crucial task to search for signal characteristics that are sensitive to concrete property changes but insensitive to the properties of the PZT and adhesive materials.

Figure 3.2 shows  $\arctan (G/B)$  spectra in two frequency ranges, namely, 10–250 kHz and 10–70 kHz. Three different dimensions of PZT patches,  $20 \times 20 \times 1.0 \text{ mm}^3$ ,  $10 \times 10 \times 1.0 \text{ mm}^3$ , and  $10 \times 10 \times 0.5 \text{ mm}^3$  (denoted as L-PZT, S-PZT, and ST-PZT, respectively) are simulated to consider two different widths and thicknesses of PZT patches. All these PZT patch sizes are frequently used and commercially available. The thickness of the adhesive layer is assumed to be 0.25 mm in this baseline case. As shown in Figure 3.2(a), the signals collected from the bonded PZT patches show that the

dominant PZT resonant frequency in the  $\arctan(G/B)$  spectra for L-PZT, S-PZT, and ST-PZT is 120, 192.5, and 220 kHz, respectively, indicating that the PZT patch with thin thickness and small width is associated with a high frequency of the first PZT resonant mode. From this perspective, the first PZT resonant frequency cannot be used directly to evaluate the changes in concrete cubes, if the PZT patches cannot be standardized in practical applications. Different dimensions of PZT patches should be analyzed separately, with varying material properties being considered simultaneously. In comparison, Figure 3.2(b) plots the signal spectra from 10–70 kHz, mainly including the cube resonance peaks of the host structure [Tang et al., 2020; Lu et al., 2020; Lim et al., 2021]. Almost the same peak frequencies can be obtained by different sizes of the PZT patches but in different magnitudes, as shown in Figure 3.2(b). It should be noted that Figure 3.2(b) has double y axes since the magnitude of these curves differ significantly. The curves of ST-PZT and S-PZT correspond to left y-axis, while the curve of L-PZT corresponds to the right y-axis.

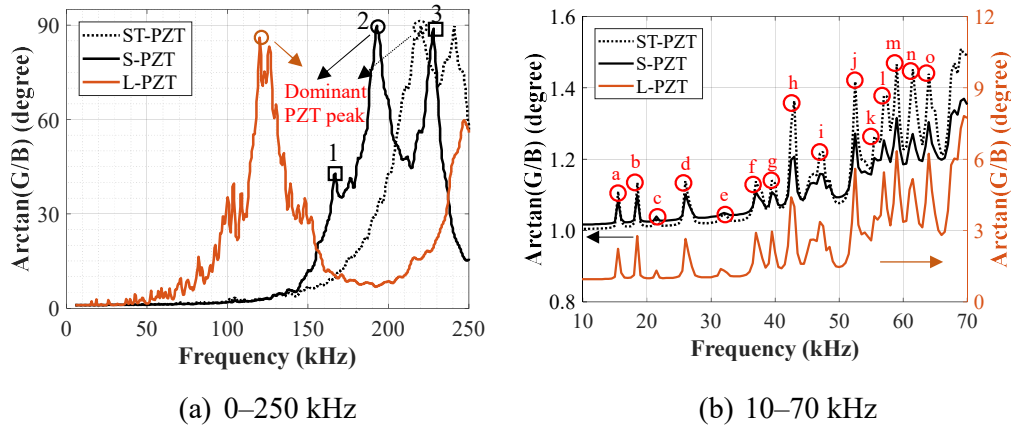


Figure 3.2 Effect of PZT size on different frequency ranges

The sensitivity with respect to the size of the PZT patch can be evaluated by comparing the peak amplitudes. The spectra obtained by the L-PZT show larger responses than the other two small PZT patches in the standard concrete cubes. The sensitivity of the ST-PZT is slightly higher than that of the thick one (S-PZT). For instance, the magnitude of peak a is around 0.1 (from 1.0 to 1.1) obtained by ST-PZT & S-PZT and around 1.3 (from 1.5 to 2.8) obtained by L-PZT. Therefore, the sensitivity

order to capture the cube resonance peaks in 10–70 kHz is  $L\text{-PZT} > S\text{-PZT} > ST\text{-PZT}$ . Despite the obviously different peak amplitudes, reproducible cube resonance peak can be captured by different sizes of the PZT patches in 10–70 kHz.

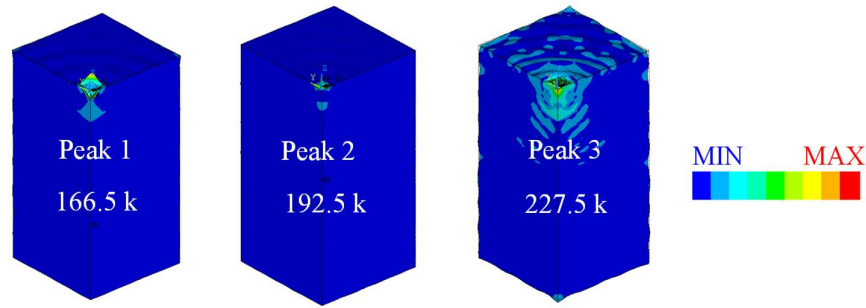
### 3.2.3 Vibration Modes of Interested Peaks

Based on the above description, different vibration modes of the concrete cube can be excited and recorded by the PZT sensor with sweeping frequencies. This section discusses the behavior of the different peaks in different frequency ranges. [Figure 3.3](#) shows the deformation of different vibration modes when the cube is excited by the S-PZT patch, wherein the vibration modes are classified into two groups, the PZT resonance peaks and cube resonance peaks in 100–250 kHz and the cube resonance peaks in 10–70 kHz. Each vibration mode corresponds to one peak labeled by a circle in [Figure 3.2](#). Peaks 1 to 3 in [Figure 3.3\(a\)](#) show the main deformation concentrated in the field near the PZT sensor, implying that the frequency changes of the corresponding peaks highly depend on the PZT sensor property, adhesive layer, and nearby concrete.

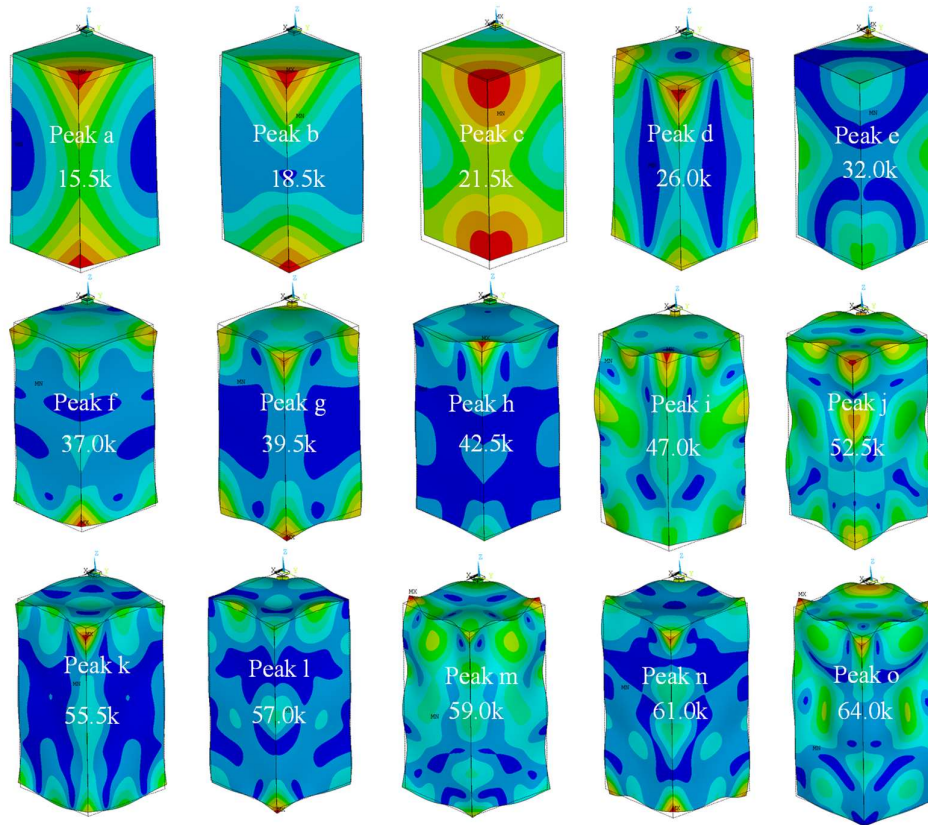
In terms of the 15 peaks (i.e., peaks a to o) shown in [Figure 3.3\(b\)](#), the deformation is distributed in the entire concrete cube structure, which explains why they are referred to as cube resonance peaks. For example, peak a shows a bending mode, in which the top (the face bonded with the PZT sensor) and bottom surfaces bend in the same direction. The minimum displacement in blue occurs at the middle center of the side surface, whereas the maximum displacement in red color is observed at the corners in the same direction (along z-axis). For peak b, the top and bottom surfaces bend in the opposite direction, with the minimum transformation observed at the middle point of the sideline. Peak c presents a breathing vibrating mode, in which the maximum displacements are seen on the corners of the top and bottom surfaces, which are in the opposite trends. The signal spectra in [Figure 3.2](#) shows peak c amplitude is much lower than those of other modes. At peak d, the side surfaces show shear deformation, and the vibration mode of the corners and the middle points of the sideline are in opposite directions. Peak e also has a weak response and cannot be observed directly in the signal



of the S-PZT. Peaks i to h correspond to high-order vibration modes excited, wherein the main deformations occur at the top and bottom surfaces.



(a) Vibration modes of distinct cube and PZT resonance peaks



(b) Vibration modes corresponding to cube resonance peaks in 10–70 kHz

Figure 3.3 Summary of vibration modes

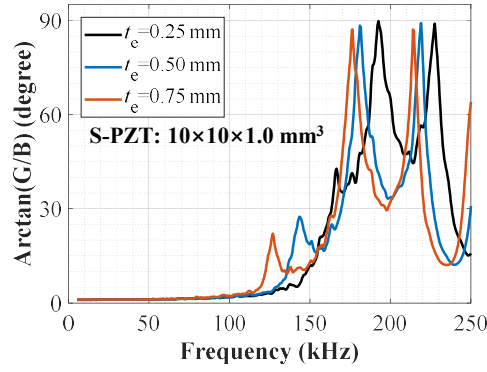
### 3.2.4 Repeatability of Signal Characteristics with Different Thickness of Adhesive Layer

This section presents parametric analyses regarding the adhesive layer thickness  $t_e$ . Three values  $t_e = 0.25$ ,  $0.50$ , and  $0.75$  mm are considered, all of which can be implemented easily in practice. Figure 3.4 shows the effect of the adhesive layer

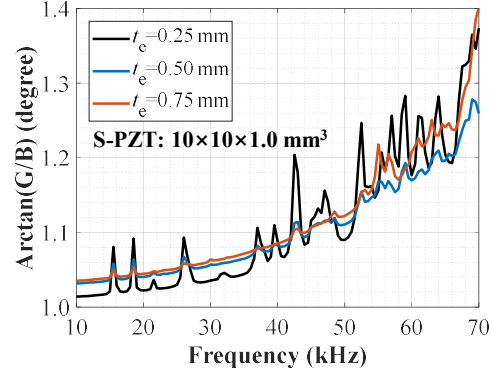
thickness on the obtained signals. As shown in Figure 3.4(a), the first PZT resonance peak of all the SBP shifts leftward with the increases of  $t_e$ , which agrees with the observations by other researchers [Yang et al., 2008b; Qing et al., 2006]. Considering the thickness  $t_e$  can hardly be controlled accurately, the first PZT resonance peak cannot be practically applied in a baseline-free method.

In comparison, in 10–70 kHz, the signal baseline shifts upward with the increase of  $t_e$ . However, the frequencies of the cube resonance peaks are not affected, although the magnitude decreases with the increase of  $t_e$ . In the signal spectra obtained from S-PZT, the relatively weak peaks (e.g., peaks c and e) are hardly observed when a thick adhesive layer is used. The frequencies of the peaks larger than 45 kHz obtained by S-PZT with  $t_e = 0.75$  mm are inconsistent with the other two working conditions, as shown in Figure 3.4(b). Some peaks in this frequency range (i.e., 45–75 kHz) disappear, whereas others shift leftward. Therefore, the epoxy thickness for the S-PZT patch is suggested not to exceed 0.5 mm, which is practically achievable. Although some peaks weaken or even disappear in the spectra of ST-PZT, the frequencies of those observable peaks do not change in the whole 10–70 kHz, as shown in Figure 3.4(c). For the L-PZT shown in Figure 3.4(d), similar phenomena can be observed. The peaks weaken with the increase of  $t_e$ , and only peak e becomes hard to catch. The peaks obtained by L-PZT show the slightest reduction in the peak magnitudes with the increase of the  $t_e$ , whereas the signals obtained by S-PZT are the most influenced.

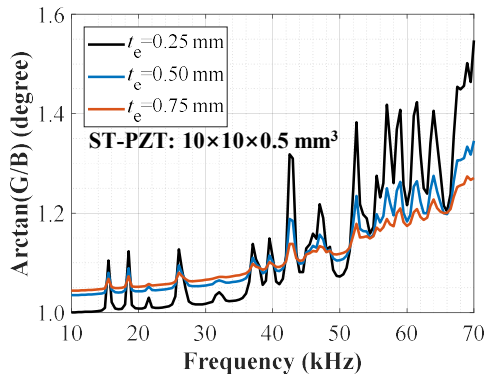
The discussion above indicates that the effect of the adhesive thickness  $t_e$  in the frequency range of 10–70 kHz is quite smaller than that in the high-frequency range. The frequencies of the first several peaks (peaks a to h) are maintained nearly constant given the dimensional changes of epoxy. In the following numerical parts, S-PZT is set as the default PZT patch, and 0.25 mm is used for  $t_e$ .



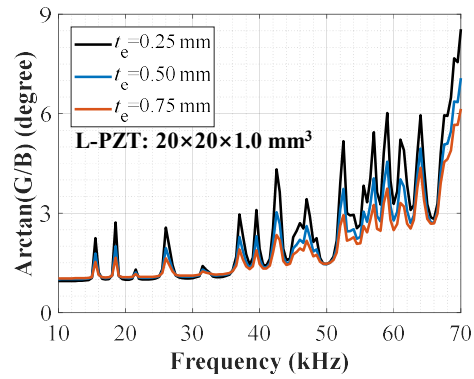
(a) 0–250 kHz of S-PZT



(b) 10–70 kHz of S-PZT



(c) 10–70 kHz of ST-PZT



(d) 10–70 kHz of L-PZT

Figure 3.4 Effect of thickness of the adhesive layer on different frequency ranges

### 3.2.5 Repeatability of Signal Characteristics at Different Temperatures

Temperature influences both the mechanical properties of the adhesive materials and the mechanical and piezoelectric properties of the PZT materials, thereby leading to the changes in the frequencies of the resonant peaks of the PZT patches. Table 3.3 summarizes the temperature dependence of the material coefficients of PZT materials [Sabat et al., 2007] and typical adhesive materials [Ai et al., 2020].

The temperature effect on the PZT and adhesive materials causes considerable changes in the signals that are highly related to the adhesive and PZT materials. However, the changes in signal characteristics corresponding to the properties of the host structures should be minimal. Figure 3.5 shows the  $\arctan(G/B)$  signal spectra concerning the changes in the temperature in two frequency ranges (0–250 kHz and 10–70 kHz). The properties at room temperature (RT) are regarded as the control group.

The thermal effects are applied only to the PZT and adhesive materials; and thus, the properties of PZT materials and adhesive materials vary with the temperature, whereas the concrete properties are fixed.

Table 3.3 Temperature dependence of material coefficients

Material	Coefficient	Symbol	Rate ( $\pm 15$ °C)
PZT	Piezoelectric strain coefficients	$ d_{31} $	$\pm 6\%$
		$d_{33}$	$\pm 6\%$
		$d_{15}$	$\pm 1\%$
	Dielectric permittivity	$\varepsilon_{11}$	$\pm 10\%$
		$\varepsilon_{33}$	$\pm 3\%$
	Compliance coefficients	$s_{11}$	$\pm 1.5\%$
		$ s_{12} $	$\pm 1.6\%$
		$ s_{33} $	$\pm 0.8\%$
		$ s_{55} $	$\pm 2.0\%$
	Modulus of elasticity	$E_c$	$\pm 9\%$
Epoxy	Poisson's ratio	$\mu_c$	$\pm 0.02$

The parameters listed in Table 3.3 are used in the simulations. Figure 3.5(a) shows that the frequencies of the first PZT resonance peak vary with temperature changes, indicating that complex temperature-related modifications are needed to remove the temperature effect from the monitoring results. In contrast, the interested signal spectra in 10–70 kHz shift upward with the temperature increase from RT-20 °C to RT+20 °C; however, no frequency changes of peaks occur, as shown in Figure 3.5(b). Therefore, the selected characteristics of the  $\arctan(G/B)$  signal spectra in this frequency range are not affected by the thermal effects on the piezoelectric and adhesive materials. The changes in the adhesive layer (hardening or deterioration) will not lead to the frequency changes of the selected peaks, guaranteeing stability in a quick measurement and long-term monitoring.

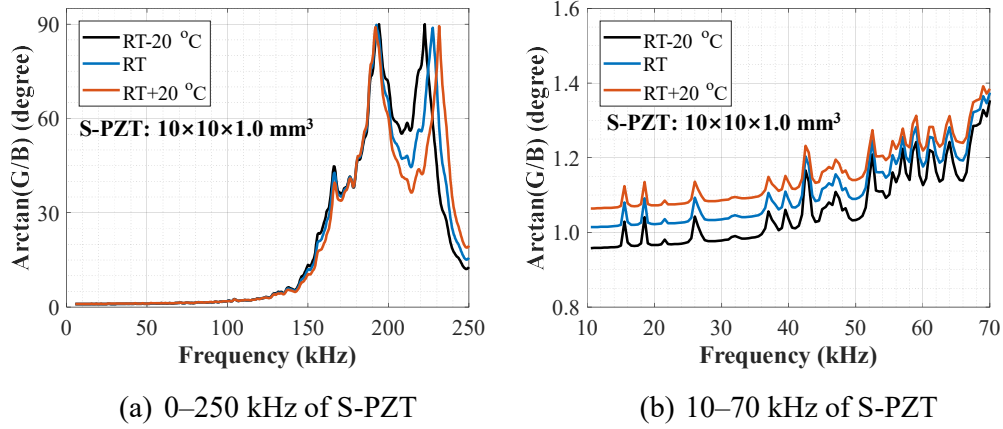


Figure 3.5 Temperature-induced changes in the PZT and adhesive materials

### 3.2.6 Correlations between Signal Characteristics and Concrete Properties

The discussion above indicates that the frequencies of the peaks in 10–70 kHz are insensitive to the dimensional and thermal changes of the PZT and adhesive materials, particularly for the first several cube resonance peaks. In this section, the selected peaks are further investigated to build correlations with the properties of the concrete materials.

Zhou et al. [1994, 1995] and Zagrai et al. [1995] derived a dynamic model for a bonded PZT actuator integrated with a 2D structure (e.g., a thin plate) using the EMI technique. The theoretical formula implies that for different vibration modes (e.g., the in-plane and bending vibration modes), linear relationships exist between the modal frequencies and the square root of the modulus of elasticity of the structure divided by the density, i.e.,  $\sqrt{E/\rho}$ , when  $\mu_c$  and dimensions of the host structure are fixed. This chapter considers concrete after 28 days of curing age; thus,  $\mu_c$  can be regarded as stable and is often set as 0.2 for concrete materials. Therefore,  $E_c$  and  $\rho_c$  are two important parameters that determine the frequencies of different vibration modes of a concrete cube. In addition, the damping ratio of concrete materials,  $\xi_c$ , is also studied parametrically. The modulus of elasticity is set from 15 GPa to 55 GPa with an interval of 2.5 GPa. The density of the concrete varies from 2308 kg/m<sup>3</sup> to 2508 kg/m<sup>3</sup> with an

interval of 100 kg/m<sup>3</sup>. The damping ratio of the concrete cubes typically varies from 0.8% to 2.1% [Ai et al., 2020]; thus, three damping ratios (0.8%, 1.6%, and 2.4%) are considered in the parametric study.

Figure 3.6 shows the typical effects of the concrete properties on the interested frequency range. Only three spectra showing the effects of the modulus of the elasticity are plotted in Figure 3.6(a) for clarity. The frequencies corresponding to peaks a to d are summarized in Table 3.4. All the peaks shift rightward with the increases in the modulus of elasticity. In general, the peaks at higher frequencies shift larger horizontal distances. Similar trends can be observed in the effect of the density. All the peaks shift leftward with respect to the increases in density, as shown in Figure 3.6(b). In contrast, changes in the damping ratio in the selected range do not lead to any frequency changes in the selected peaks, as shown in Figure 3.6(c). But some peaks with small magnitudes disappear or become difficult to identify with the increases in the damping ratio (e.g., Peaks c, e, and g).

The discussion above indicates that the frequencies of the selected peaks can be correlated to the values of  $E_c$  and  $\rho_c$ . The value of  $\sqrt{E_c/\rho_c}$  (unit: m/s) is used to fit a linear relationship, as shown in Equation (3.1).

$$f_i = \kappa_i \sqrt{\frac{E_c}{\rho_c}}, \quad (3.1)$$

where  $f_i$  (unit: Hz) is the frequency of the  $i$ th vibration mode, and  $\kappa_i$  (unit: m<sup>-1</sup>) refers to the slope for a specific vibration mode.

Figure 3.6(d) shows the regression results between  $\sqrt{E_c/\rho_c}$  and the frequencies corresponding to cube resonance peaks a to d. The  $R^2$  values show that the linear relationships fit the simulation results extremely well. Among these four peaks, Peak d has the largest slope of 7.4166 m<sup>-1</sup>; the slopes of peaks a, b, and c are equal to 4.4245, 5.2273, and 6.0950 m<sup>-1</sup>, respectively. In general, a higher-order vibration mode has a larger slope  $\kappa$ .

Based on these regression results,  $E_c$  of the concrete can be evaluated directly.

After identifying the frequencies of the first four peaks from the  $\arctan(G/B)$  spectra in the selected frequency range,  $\sqrt{E_c/\rho_c}$  can be calculated. The density of concrete cubes is easy to be measured or estimated in practice. Consequently,  $E_c$  can be calculated on the basis of these peaks. Finally,  $E_c$  values from different peaks can be averaged to reduce the errors caused by different vibration modes.

Therefore, the frequencies of the first several peaks in the  $\arctan(G/B)$  spectra of the EMI signals in the frequency range of 10-70 kHz are suggested as the indexes to quantify the modulus of elasticity of concrete. The numerically obtained regression formulas shown in Figure 3.6(d) will be directly applied (without any modification) in the following experimental validations.

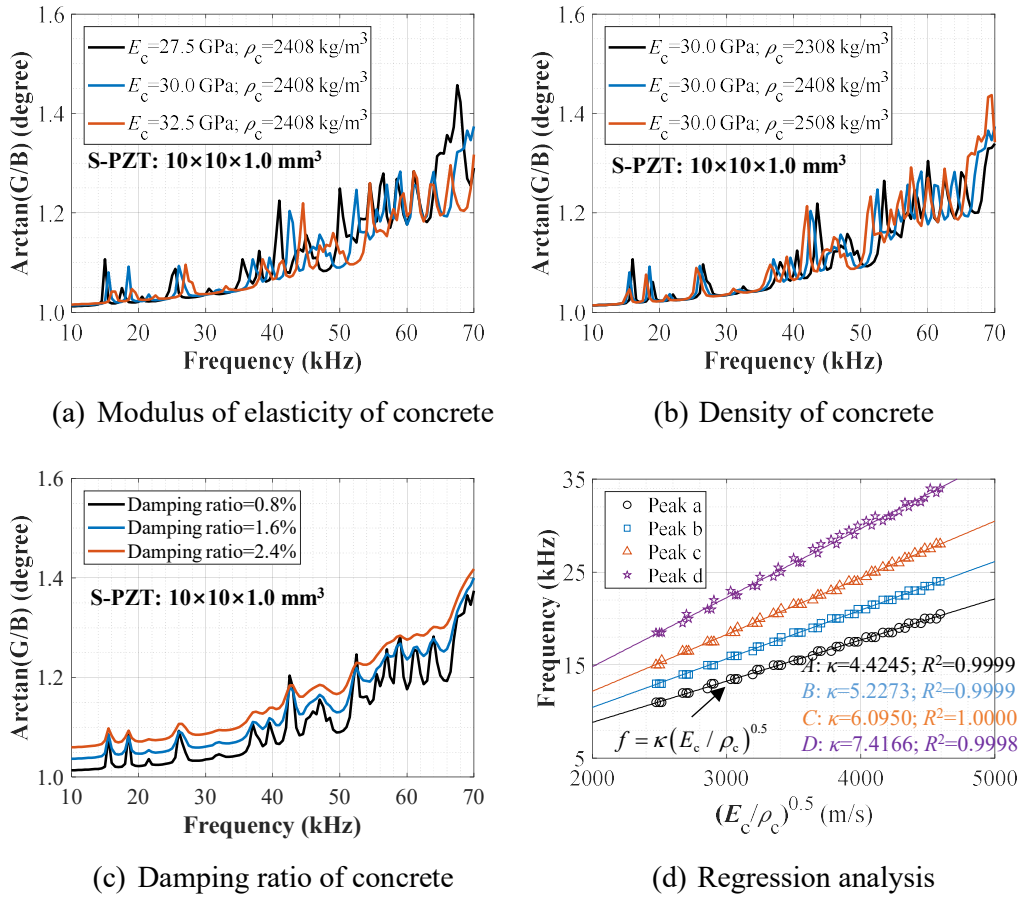


Figure 3.6 Effect of the properties of concrete material and regression results of the peaks

Table 3.4 Summary of the simulation results of peaks a to d

$E_c$ (GPa)	Frequency (kHz)											
	$\rho_c = 2308 \text{ kg/m}^3$				$\rho_c = 2408 \text{ kg/m}^3$				$\rho_c = 2508 \text{ kg/m}^3$			
	a	b	c	d	a	b	c	d	a	b	c	d
15.0	11.5	13.5	15.5	19.0	11.0	13.0	15.0	18.5	11.0	13.0	15.0	18.0
17.5	12.0	14.5	17.0	20.5	12.0	14.0	16.5	20.5	11.5	14.0	16.0	19.5
20.0	13.0	15.5	18.0	21.5	13.0	15.0	17.5	21.0	12.5	15.0	17.0	21.5
22.5	14.0	16.5	19.0	23.0	13.5	16.0	18.5	22.5	13.5	15.5	18.5	22.0
25.0	14.5	17.0	20.0	25.0	14.5	17.0	19.5	23.5	14.0	16.5	19.0	24.0
27.5	15.5	18.0	21.0	25.5	15.0	17.5	20.5	25.5	14.5	17.5	20.0	25.0
30.0	16.0	19.0	22.0	26.5	15.5	18.5	21.5	26.0	15.5	18.0	21.0	25.5
32.5	16.5	19.5	23.0	27.5	16.5	19.0	22.5	27.0	16.0	19.0	22.0	26.5
35.0	17.0	20.5	23.5	28.5	17.0	20.0	23.0	28.0	16.5	19.5	23.0	27.5
37.5	18.0	21.0	24.5	29.5	17.5	20.5	24.0	29.0	17.0	20.0	23.5	28.5
40.0	18.5	22.0	25.5	30.5	18.0	21.5	25.0	30.0	17.5	21.0	24.5	29.5
42.5	19.0	22.5	26.0	31.5	18.5	22.0	25.5	31.0	18.0	21.5	25.0	31.0
45.0	19.5	23.0	27.0	32.5	19.0	22.5	26.5	32.5	18.5	22.0	26.0	31.0
47.5	20.0	23.5	27.5	33.5	19.5	23.0	27.0	32.5	19.5	23.0	26.5	32.0
50.0	20.5	24.5	28.5	35.0	20.0	24.0	28.0	33.5	20.0	23.5	27.0	33.0
52.5	21.0	25.0	29.0	35.0	20.5	24.5	28.5	34.5	20.0	24.0	28.0	34.5
55.0	21.5	25.5	30.0	36.0	21.0	25.0	29.0	36.0	20.5	24.5	28.5	34.5

### 3.3 Experimental Validations

The experimental measurements of  $E_c$  of concrete cubes were conducted to validate the methods proposed in the last section and examine the repeatability of the proposed indexes in temperature effects.

#### 3.3.1 Measurement of Modulus of Elasticity

Three batches of concrete cubes, using seawater sea-sand concrete (SSC) and high-strength concrete (HSC) with different densities and strengths, were cast to measure the modulus of elasticity. The corresponding material proportions of concrete are summarized in [Table 3.5](#). Each batch contained three cubes (100 mm in width) and three cylinders (150 mm diameter and 300 mm height), where three cubes were used for the measurements using the proposed EMI technique and three cylinders were for the conventional destructive compressive tests according to [ASTM C39/C39M \[2020\]](#). A minimum curing period of 28 days was implemented. For each concrete cube, a PZT



patch with dimensions of  $10 \times 10 \times 1.0 \text{ mm}^3$ , corresponding to the S-PZT case in the FEM simulation, was bonded at the center point of the surface. Five-minute-fast epoxy (Devcon 14270) was used as the adhesive material. The thickness of the adhesive layer ranged approximately 0.10–0.35 mm, satisfying the requirement recommended above.

Table 3.5 Mix proportions of the tested concrete materials

Batch	Material	Mix proportion by weight	Density (kg/m <sup>3</sup> )	Curing days
I	SSC	C: SW: SS: CA: FA: PFA: SP <sup>a</sup> = 1:0.333:0.5:2.212:1.712:1.409:0.008	2370	28
II	HSC	C: W: S: CA: FA: SP <sup>b</sup> = 1:0.199:1.149:1.017:0.680:0.018	2450	28
III	HSC	C: W: S: CA: FA: SP = 1:0.199:1.149:1.017:0.680:0.018	2450	90

<sup>a</sup>C = cement; SW = seawater; SS= sea-sand; CA = 20 mm aggregate; FA = 10 mm aggregate; PFA = pulverized fuel ash.

<sup>b</sup>W = water; S = sand.

Figure 3.7 shows the test setup for the measurement. The EMI signal measurement system consisted of an LCR meter (Keysight E4980AL) and a laptop for recording. EMI spectra were obtained by applying a voltage of 1 V across the terminals of the PZT patch over a frequency range of 0.5–250 kHz at 0.5 kHz intervals. The concrete cubes were placed on a wooden table with low stiffness and friction, whose boundary constraint effects are negligible according to the results of trial tests and simulations. The room temperature for measurement was around 20 °C.

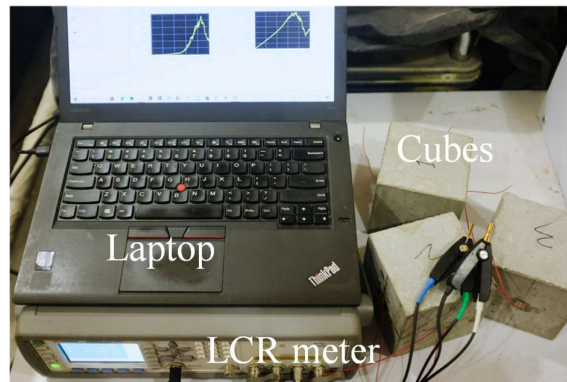


Figure 3.7 Test setup for measurement

Meanwhile, conventional compressive tests were conducted to obtain concrete

strength  $f'_c$ . Although both concrete cubes and cylinders are used to obtain the compressive strength in different standards, there are no widely acceptable equations for accurately estimating the modulus of elasticity from the cube strength. Therefore, compressive strength of standard cylinders was tested in this chapter. Three identical standard cylinders for each batch were tested according to [ASTM C39/C39M \[2020\]](#). The tests were performed by positioning the samples in a uniaxial loading device (340 tons). The average values of the compressive strength at 28-day curing age for batch I, batch II and batch III were 46.1, 94.3 and 95.4 MPa, respectively; the corresponding coefficients of variation were 0.01, 0.02 and 0.03, respectively. The moduli of elasticity of these three different batches were subsequently estimated according to [ACI-318 \[ACI, 2019\]](#), as shown in Equation (3.2).

$$E_{cs} = 0.043\rho_c^{1.5}\sqrt{f'_c} \quad (\text{in MPa}) \quad (3.2)$$

Consequently, the  $E_{cs}$  values were calculated as 33685, and 50638 and, 50931 MPa for batch I, batch II and batch III, respectively, by substituting the corresponding value. The estimated moduli of elasticity were employed here, as the results can also be extended to correlate the strength of concrete and EMI signals. Although estimated indirectly, the modulus of elasticity determined using the above code equation, originally proposed by [Pauw \[1960\]](#), has been proven acceptable for most applications over the past years [\[ACI, 2019\]](#). For example, [Vakhshouri \[2018\]](#) compared the estimation accuracies of the moduli of elasticity of concrete in 35 design codes and 19 empirical models and concluded that the code equation in [ACI-318 \[ACI, 2019\]](#) was relatively compatible with the randomly selected experimental results with a great variety of aggregates, curing conditions, and testing methods and standards. In this chapter, the main goal is to illustrate the good repeatability and stability of the proposed methods. Furthermore, the comparison between the modulus of elasticity measured by EMI methods and static tests is presented in [Section 4.4](#).

[Figure 3.8](#) plots the experimental  $\arctan(G/B)$  spectra obtained from the EMI tests of both batches. In the high-frequency range of 0.5–250 kHz, the first PZT resonance

peak and the cube resonance peaks showed low repeatability in Figures 3.8(a) and 3.8(c); whereas reproducible signal spectra could be seen in the 10–70 kHz range, particularly for the first several peaks, as shown in Figures 3.8(b) and 3.8(d). The peaks at frequencies higher than 45 kHz showed relatively lower repeatability, but repeatable peaks from a to d could be observed in both batches, as shown in Figures 3.8(b) and 3.8(d). Peak c in batch I was not obvious; but in batch II, peak c could be identified easily.

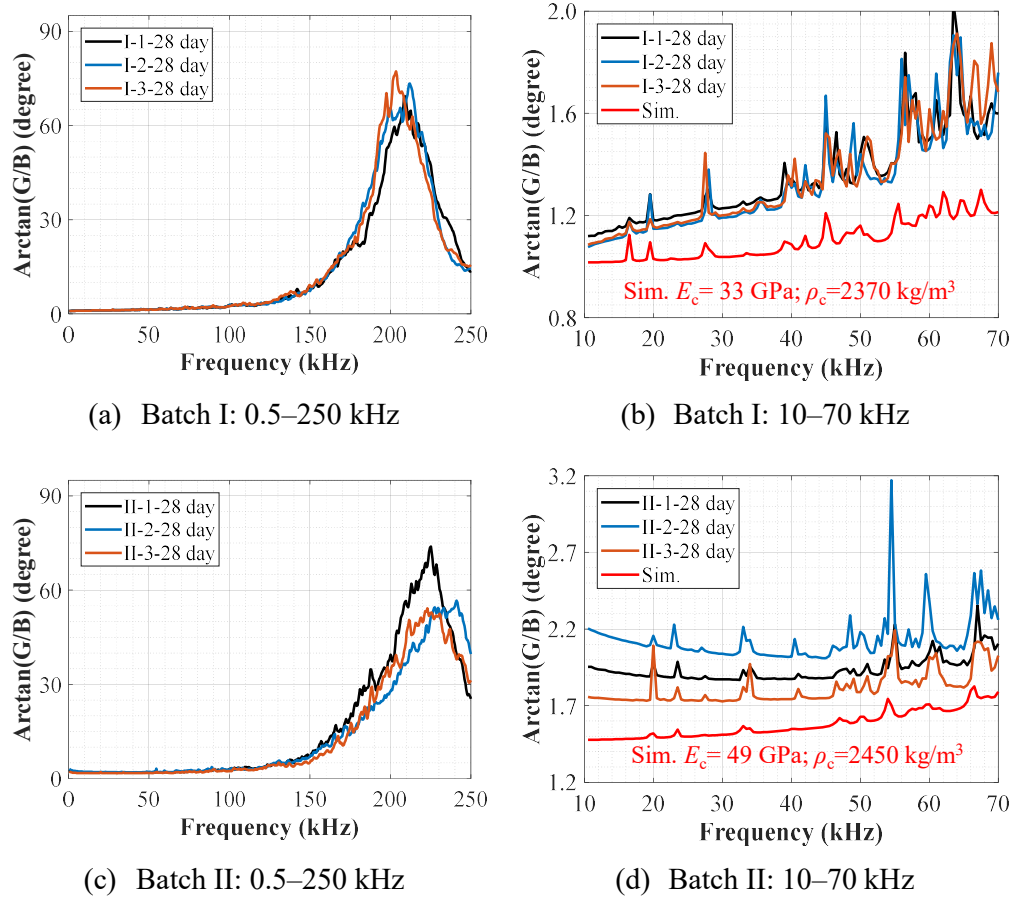


Figure 3.8 The measured  $\arctan(G/B)$  spectra for two batches of concrete

Hence, only peaks a, b, and d that could be easily identified in the experimental results were selected to calculate the modulus of elasticity for each cube. The frequencies of the peaks were extracted first. Then,  $E_{ce}$  were calculated using the regression relationships presented Figure 3.6(d). The comparison of the compressive tests and SBP tests were plotted in Figure 3.9 and summarized in Table 3.6. The largest

error here was approximate  $-3.9\%$ , which was small enough for concrete measurement. The mean errors for batch I and batch II were only  $-1.7\%$  and  $-3.0\%$ , respectively, proving that the proposed method is accurate in measuring the modulus of elasticity of concrete cubes. The proposed method could be extended to different sizes of concrete cubes or other concrete specimens by selecting suitable cube resonance peaks and calibrating the corresponding slopes  $\kappa$ .

Table 3.6 Experimental results for  $E_c$  measurement

Specimen <sup>†</sup>	Compressive test		SPB-based EMI test		Relative difference in $E_c$	
	$f'_c$ (MPa)	$E_{cs}$ (MPa) <sup>#</sup>	Peaks a / b / d (kHz)	$E_{ce}$ (MPa) <sup>*</sup>	in MPa	in %
I-1	46.1 (0.01) <sup>^</sup>	33685	16.5 / 19.5 / 28.0	33240	445 MPa	$-1.3\%$
I-2			16.5 / 19.5 / 28.0	33240	445 MPa	$-1.3\%$
I-3			16.5 / 19.5 / 27.5	32842	843 MPa	$-2.5\%$
II-1	94.3 (0.02)	50638	20.0 / 23.5 / 33.0	49361	1277 MPa	$-2.5\%$
II-2			20.0 / 23.0 / 33.0	48666	1972 MPa	$-3.9\%$
II-3			20.0 / 23.5 / 33.0	49361	1277 MPa	$-2.5\%$

<sup>\*</sup>Values are SBP estimations and calculated by averaging the results obtained by all three peaks.

<sup>^</sup>Values in the bracket are the coefficients of the variations.

<sup>#</sup>Values are calculated by the results of the compressive tests.

<sup>†</sup>The name of the specimen is defined as “batch No. – sample No.”

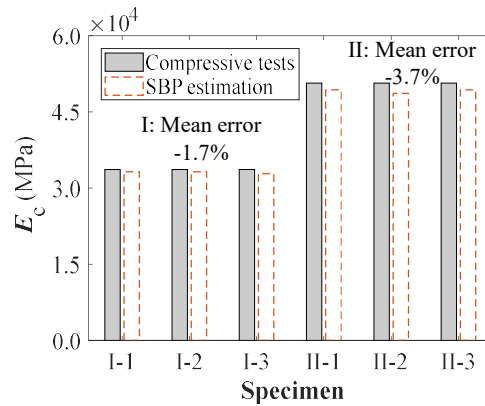


Figure 3.9 Test setup for measurement

Notably, the material properties obtained from low-strain nondestructive tests are sometimes called “dynamic” constants [Kolluru et al., 2000]. The complex

relationships between “dynamic” and static moduli of elasticity remain ambiguous, as dynamic moduli of elasticity may depend on different resonant modes selected [Bassim and Issa, 2020]. More experimental tests need to be conducted to clarify an accurate relationship, which is out of the major scope of this chapter. Therefore, the estimated moduli of elasticity were directly compared with the static counterparts in this chapter, given the relatively small differences between them.

The simulated signal spectra were also plotted in Figures 3.8(b) and 3.8(d) using the calculated results for each batch. Good agreements of frequencies could be observed in the peaks at a relatively low frequency (i.e., <40 kHz), which justifies the effectiveness of the major conclusions obtained in Section 3.3.2. At 40–70 kHz, however, the simulation results deviated from the experimental results. The differences might be attributed to the nonhomogeneous material properties of concrete that were not simulated in the FEM model. Real concrete materials consist of aggregates, sand, cement, and void, which involve complicated interfaces between different phases and affect the signals in a high-frequency range easily, whereas the numerical model for concrete is assumed as homogenous in this chapter.

### 3.3.2 Repeatability Tests for Different Types of Sensor Systems

Repeatable signal indexes are essential for the practical applications of EMI techniques. The numerical analyses in Section 3.2 indicated that the three selected sizes of PZT patches presented the same characteristic frequencies in the selected frequency range, but the signals obtained from L-PZT presented the highest sensitivity. Therefore, experiments using L-PZT and S-PZT were conducted to validate the results from numerical analyses. Three concrete cubes (batch III) were cast with the same material proportions as HSC and used for validation and further temperature tests. The tests were conducted after 90 days of curing age. For each concrete cube in batch III, an L-PZT ( $20 \times 20 \times 1.0 \text{ mm}^3$ ) and an S-PZT ( $10 \times 10 \times 1.0 \text{ mm}^3$ ) were bonded simultaneously to the opposite sides of the same cube by using a five-minute-fast epoxy (Devcon 14270), as shown in Figure 3.10(a). The thickness of the adhesive layers was around

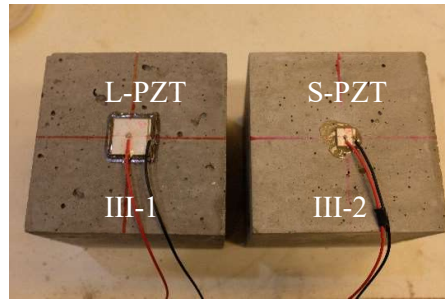
0.2–0.3 mm. The signal from 10–70 kHz was measured with a small interval of 0.1 kHz to present clear movements of the signals.

Figure 3.10(b) shows the typical signals (Specimen III-1) from L-PZT and S-PZT. At 10–70 kHz, both sizes of PZT sensors could capture almost the same frequencies of the selected peaks. This experimental observation confirmed the conclusions obtained in the numerical analyses. The first four peaks were selected to calculate the  $E_{ce}$ . As shown in Figure 3.10(d), the results from L-PZT and S-PZT showed a minimal difference (i.e., –0.3%). Figure 3.10(b) shows the magnitude of the peaks obtained by the S-PZT patch was smaller than that obtained by the L-PZT patch. For example, the peak C recorded by S-PZT was hard to capture, whereas L-PZT can easily identify this peak. The noise level in the S-PZT spectra was close to small peak magnitudes in Figure 3.10(b), which might present some difficulty in peak selections and misunderstandings in the analyses. According to the experience gained in the experiments, the noise might be attributed to the welding quality, which had more influence on S-PZT. Therefore, large-size PZT patches, which can provide strong and clear signal characteristics for analyses, are recommended for future tests.

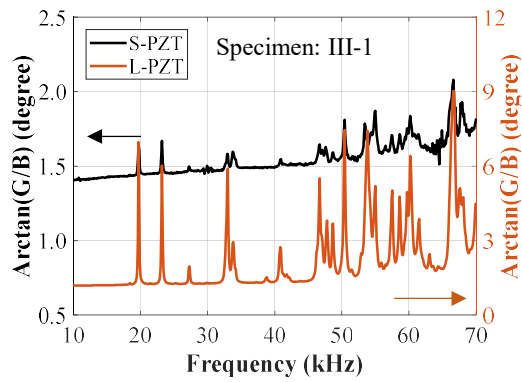
The hardening time of the epoxy was another crucial factor in the practical applications of the proposed methods because the hardening time at the measurement moment influences the modulus of elasticity of the epoxy. A quick hardening process is beneficial for capturing the spectra peaks with sufficient repeatability and magnitude as early as possible. The signals recorded by the L-PZT were used to investigate the effect of the hardening time of the adhesive layer. Figure 3.10(c) plots the recorded signals at 10 min, 100 min, and 36 h after bonding. The increases in the hardening time (from 10 min to 100 min) of the epoxy resulted in the downward shift of the spectra with apparently observed peaks. Given the selected adhesive materials, even the spectrum recorded by L-PZT at 10 min could clearly show those peaks of interest. The spectrum recorded at 36 h showed nearly the same resonant frequencies as the other two sets of data. Among the first four peaks, peaks c and d of the signals recorded at 36 h shifted

leftward by 100 Hz, leading to  $-0.3\%$  differences compared with the other two sets of data, as summarized in Table 3.7. The difference of  $E_c$  between 10 min and 36 h was  $0.3\%$ .

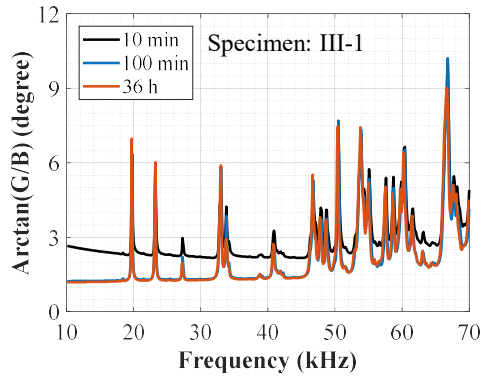
The comparisons of the abovementioned two tests were plotted in Figure 3.10(d). The differences induced by different PZT sensors and different hardening time of bonding were small enough. The largest difference in this specimen was only 163 MPa (i.e.,  $0.3\%$ ), proving that the proposed EMI technique can provide repeatable and accurate results.



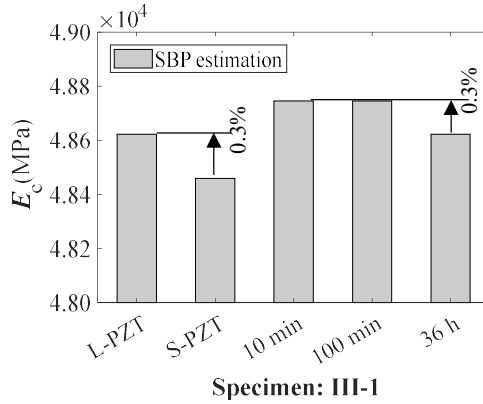
(a) Cubes of batch III



(b) PZT size effect



(c) Effect of hardening of the epoxy



(d) Comparison of  $E_c$

Figure 3.10 Experimental validation of the repeatability of the signals

Table 3.7 Results of repeatability of the indexes

Specimen	PZT size	Hardening	a / b / c / d (kHz)	$E_{cc}$ (MPa)	Difference
		time of epoxy			
III-1	S-PZT	36 h	19.7 / 23.2 / 27.2 / 32.9	48459	-0.3%
	L-PZT		19.7 / 23.2 / 27.3 / 33.0	48622	/
		10 min	19.8 / 23.2 / 27.3 / 33.0	48745	0.3%
	L-PZT	100 min	19.8 / 23.2 / 27.3 / 33.0	48745	0.3%
		36 h	19.7 / 23.2 / 27.3 / 33.0	48622	/

Note:  $E_c$  is calculated by averaging the results obtained based on all four peaks; differences are calculated by comparing them with the status of L-PZT at 36 h.

### 3.3.3 Temperature Tests

After the abovementioned tests, the concrete cubes of batch III were tested with the ambient temperature ranging from 5°C to 45°C to validate the effectiveness of this EMI-based method in varying temperature conditions. Figure 3.11 shows the experimental setup for the temperature tests. The concrete cubes were placed inside an environmental chamber (MKF 115). The measurement was conducted every 20 min after temperature loading was applied. The data collection setup was the same as that described in Section 3.3.2. Once the RMSD of the  $\arctan(G/B)$  spectra between every two consecutive measurements was smaller than 0.005, the temperature condition was considered stable.

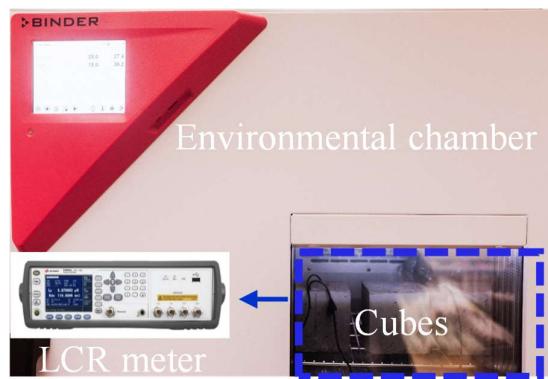


Figure 3.11 Test setup for temperature effects

Considering the conclusion in Section 3.2.5 shows that the homogenous FEM model may not capture the peaks accurately at a relatively high-frequency range, only the first four cube resonance peaks (peaks a to d) were selected to investigate the



temperature effect. Figure 3.12 shows the experimental results of the temperature effects. The selected peaks shifted leftward with the increasing temperature. Meanwhile, the entire spectrum of the signals shifted upward, leading to small magnitudes of the peaks, when the temperature reached 45 °C. The same phenomenon could be obtained for all three specimens of batch III as shown in Figures 3.12(a–c). The frequencies of peaks a to d are summarized in Table 3.8. Elevating the temperature from 25°C to 45°C would lead to larger differences in  $E_c$  than elevating the temperature from 5°C to 25°C, as shown in Figure 3.12(d). Compared with 25°C, the average differences for  $E_c$  at 5°C and 45°C were 1.9% and 3.4%, respectively. Notably, the modulus of elasticity of concrete may change by 1.5–6.1% for every 20°C temperature change [Shoukry et al., 2011; Bahr et al., 2013]. Therefore, the proposed method can capture small changes in concrete properties induced by environmental temperature variations. Compared with traditional destructive compressive tests, the proposed method provides an efficient, nondestructive, and *in situ* technique for monitoring the material properties of concrete, helping save human and material costs.

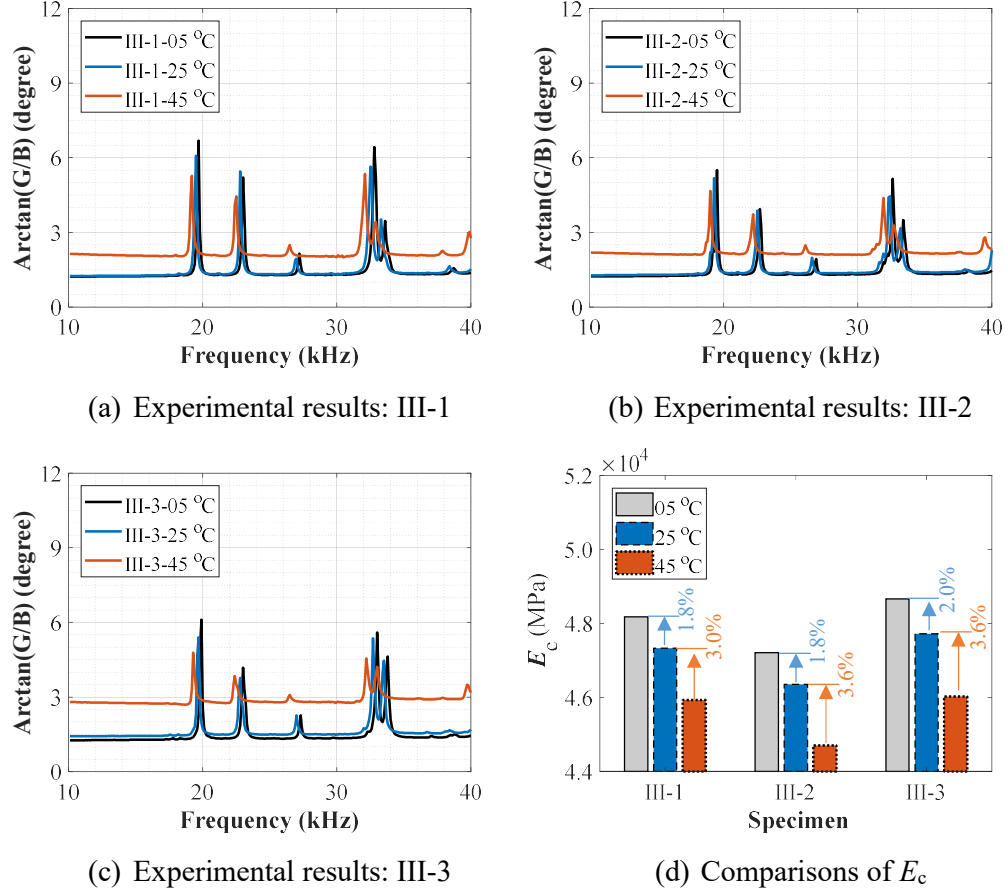


Figure 3.12 Temperature effects on signals and evaluation results

Table 3.8 Temperature tests on the measurement results

Specimen	Degree (°C)	A / B / C / D (kHz)	$E_c$ (MPa)	Difference
III-1	05	19.7 / 23.0 / 27.2 / 32.8	48178	1.8%
	25	19.5 / 22.8 / 27.0 / 32.5	47331	/
	45	19.2 / 22.5 / 26.5 / 32.1	45934	-3.0%
III-2	05	19.5 / 22.7 / 26.9 / 32.6	47212	1.8%
	25	19.3 / 22.5 / 26.6 / 32.4	46358	/
	45	19.0 / 22.0 / 26.1 / 31.9	44707	-3.6%
III-3	05	19.9 / 23.0 / 27.3 / 33.0	48662	2.0%
	25	19.7 / 22.8 / 27.0 / 32.7	47721	/
	45	19.3 / 22.4 / 26.5 / 32.2	46026	-3.6%

Note:  $E_c$  is calculated by averaging the results obtained by all four peaks; differences are calculated by comparing them with the status of 25 °C for each specimen.

### 3.4. Summary

A baseline-free EMI technique for measuring the modulus of elasticity of concrete

was proposed for the first time in this chapter on the basis of a series of numerical and experimental studies. The repeatable signatures in the proposed  $\arctan(G/B)$  spectra were identified through the numerical simulations of the standard concrete cubes (100 mm in width) with SBP. Subsequently, a series of experiments were conducted to examine the accuracy and repeatability of the proposed baseline-free EMI technique method. Some major conclusions are summarized as follows:

1. The selected cube resonant frequencies can be obtained consistently by different sizes of the PZT patches, indicating that these signature frequencies are highly related to the concrete properties but insensitive to the sizes of PZT patches. Among the studied PZT patches, the PZT patches with large width and thin thickness show the highest sensitivity and thus are recommended in practical applications.
2. The majority of the selected cube resonance peaks are insensitive to both the adhesive layer thickness and the thermal effects on the sensor system. Given a certain PZT patch, a small thickness of the adhesive layer leads to high sensitivity. It is recommended that the thickness of the adhesive layer should not exceed 0.5 mm, which is easily achievable in practice.
3. The correlations between the frequencies of the selected cube resonance peaks and  $\sqrt{E_c/\rho_c}$  were established numerically. The slopes for the first four peaks were obtained through numerical regression analyses. The experiments on two batches of concrete cubes (SSC and HSC) indicate that the regression formulas can accurately estimate  $E_c$  of the concrete cubes.
4. The repeatability of the signature frequencies obtained by different sizes of patches and the effects of the ambient temperature were validated both numerically and experimentally.
5. The proposed method offers an efficient and nondestructive technique to accurately capture small changes in  $E_c$  of concrete.

Although this chapter mainly focuses on measuring the modulus of elasticity of

standard concrete cubes that are commonly tested on construction sites, the proposed framework can be extended to assess other material properties (e.g., compressive strength) of concrete cubes or other concrete specimens with different shapes and sizes, which presents a promising research direction in the future.

## CHAPTER 4 MEASURE ELASTIC CONSTANTS OF CONCRETE CUBES USING SBPS

[Chapter 3](#) presented the successful measurement of the modulus of elasticity of the concrete cube using baseline-free EMI technique and SBP at/after 28-day age. In this chapter, the baseline-free EMI technique is further improved to measure one more elastic constant of concrete, i.e., Poisson's ratio, which is difficult to accurately measure using traditional testing methods (i.e., including dynamic and static methods) because of anisotropy of concrete and wall effect. Standard concrete cubes and SBPs are employed to ensure the proposed method can be directly transferred to existing research and application scenarios.

The enabling methodology of this chapter is mode selection. Different mode shapes of concrete cubes are carefully discussed regarding their deformation and symmetric types. Vibration modes with special deformation patterns and symmetric types are selected, and a corresponding sensor installation strategy for extracting the target modal frequencies is designed, considering the ease of identification and accessibility. The selected special modes are found to be insensitive to anisotropy and skin effects of concrete cube through numerical investigation. Based on these special modes, the method to measure the two elastic constants of concrete cubes is proposed.

Experiments demonstrate the proposed method works well at different curing ages (i.e., the first 28-day and 400-day ages) and outperforms the traditional dynamic resonance method in terms of accuracy, stability, and reproducibility.

### 4.1 Introduction

As reviewed in [Sections 2.1](#) and [2.2](#), two essential elastic constants, namely, modulus of elasticity ( $E_c$ ) and Poisson's ratio ( $\mu_c$ ), are crucial properties for concrete design in laboratories and on construction sites. Measuring  $E_c$  plays a significant role in making decisions on formwork removal in building construction and early opening of newly paved roadway sections to traffic [[Lim et al., 2021](#); [Bassim and Issa, 2020](#)].

$\mu_c$  is important for assessing the shear stiffness of concrete structures [Carrillo et al., 2019] and the long-term serviceability of prestressed concrete structures [Aili et al., 2016]. Viscoelastic Poisson's ratio, an important parameter for describing creep behavior, can be estimated from elastic Poisson's ratio [Aili et al., 2016]. Moreover,  $\mu_c$  has been proven to be a promising damage index in composite materials because it is more sensitive to damage than  $E_c$  [Smith and Wood, 1990; Van Paepegem et al., 2010] and does not rely on the absolute strain values [Yilmaz et al., 2016].

As presented in Tables 2.2 and 2.3, in most of the existing resonance methods for measuring the elastic constants of concrete, the resonant frequencies of concrete specimens (i.e., prisms, slabs, and standard cylinders) at free-free status are recorded under impulse excitations using accelerometers. The frequencies of fundamental vibration modes, such as combining a torsional mode with either a longitudinal or bending mode or combining the first two longitudinal modes, are employed to directly or indirectly derive  $\mu_c$ .

Carrazedo et al. [2020] showed that the average coefficient of variation (CoV) of  $E_{cd}$  evaluated by using the first bending and longitudinal resonant frequencies was less than 3%, indicating the low dispersion of the method. However, evaluating  $\mu_{cd}$  based on fundamental bending, longitudinal, and torsional resonant frequencies of prisms/cylinders are sensitive to the anisotropy of concrete [Swamy, 1971]. Researchers have observed anisotropy in concrete strength [Hughes and Ash, 1970; Leshchinsky, 1990; Hansen et al., 2018] and elastic constants [Haach et al., 2020] after casting, which is called initial anisotropy of concrete [Bertolodo et al., 2020]. The anisotropy of concrete is highly related to mix proportions (e.g., the fraction of aggregate, maximum aggregate size, and water-cement ratio) and casting direction. Meanwhile, the difficulty in measuring the anisotropy ratio of concrete hinders the development of correction methods to obtain reliable  $\mu_{cd}$  values. In addition to material anisotropy, the heterogeneity of concrete also challenges accurate measurement. Krejiger [1984] demonstrated that the outer part of a concrete sample, called the skin of concrete, was

weaker than the core part. When aggregate sizes are non-negligible compared with the mold, the compaction of concrete and the uniformity of aggregate distribution are affected by the mold wall, which is the so-called wall effect. Overlooking the wall effect may result in an inaccurate evaluation of the mechanical properties of concrete specimens [Zheng et al., 2003]. However, this wall effect is also difficult to quantify. Therefore, an NDT technique insensitive to the material anisotropy and the skin effect is highly desirable for reliably and stably measuring the dynamic elastic constants of concrete, especially for  $\mu_{cd}$ , to bridge the abovementioned research gaps.

Chapter 3 presented that the proposed EMI technique can easily, stably, and accurately capture the high-order resonant modes, showing its potential for selecting the anisotropy-insensitive and wall-effect-insensitive modes, assuring reliable measurement results. Moreover, Chapter 3 has extended the baseline-free EMI techniques to measure  $E_c$  of concrete cubes, widely used standard specimens in the concrete field, in which, however,  $\mu_c$  of concrete cubes were assumed to be 0.2 and could not be accurately assessed. Moreover, the assessment method was usually performed by assuming that concrete materials were isotropic and homogeneous. Thus, the baseline-free EMI technique on concrete cubes must be improved by eliminating the assumption regarding  $\mu_c$  and examining the assumptions regarding isotropy and homogeneity.

In summary, the traditional dynamic methods cannot measure  $\mu_c$  of concrete accurately and stably, and the existing baseline-free EMI techniques cannot really measure  $\mu_c$  of concrete cubes so far. Inaccurately measured or assumed  $\mu_c$  may adversely affect the assessment of the modulus of elasticity of concrete as well. In view of this research gap, this paper presents an improved EMI-R technique that can simultaneously measure Poisson's ratio and modulus of elasticity of concrete. Moreover, the proposed method is insensitive to the anisotropy and wall effect of concrete, guaranteeing the measured reliability and stability of properties. Tests on standard concrete cubes using the proposed EMI-R technique are performed numerically and

experimentally to address the abovementioned research gap. In this chapter, the diverse vibration modes of concrete cube specimens are discussed first, and some special modes are subsequently identified. A series of numerical analyses are conducted using isotropic and homogenous models to design sensor installation strategies and their corresponding evaluation methods. Afterward, the proposed methods regarding their sensitivity to anisotropy and skin effects of concrete are examined. Finally, the measurement accuracy, stability, and reproducibility of the proposed EMI-R technique are validated experimentally.

## **4.2 Principle and Assessment Procedure of the Improved Method**

### **4.2.1 Vibration Modes Selection**

Ayorinde and Yu [1999, 2005] showed the advantage of mode selection in the elastic constants identification for thin composite plates, in which the diagonal modes of a square composite plate led to considerably better results for the predicted elastic constants. This finding may inspire a potential solution for evaluating elastic constants of concrete cubes. Therefore, the vibration modes of a cube are investigated first. A 150 mm cube without piezoelectric sensors under free boundary conditions is simulated for modal analyses by using ANSYS. Solid45 elements are employed to model the concrete cube. The element mesh size is set to 3 mm after convergence analysis. The concrete material is assumed to be isotropic and homogenous. The  $E_c$ ,  $\mu_c$ ,  $\rho_c$ , and  $\xi_c$  are 30 GPa, 0.2, 2300 kg/m<sup>3</sup>, and 0.8%, respectively.

Figure 4.1 plots the nine symmetric planes and axes of the cube to describe the mode shapes. The red, blue, and purple dots represent the center of the cube, the centers of the surfaces, and the middle points of the edges, respectively. The nine symmetric planes can be classified as three parallel planes (blue color, parallel with surfaces of cubes) and six (i.e., three pairs) diagonal planes (purple color).



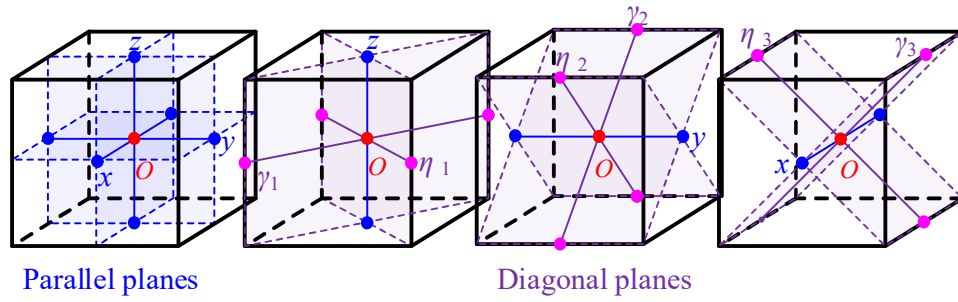


Figure 4.1 Nine symmetric planes for a cube

Figure 4.2 presents vibration modes of the concrete cube from an isotropic model. The first 73 elastic vibration modes of the concrete cube are presented by excluding the first six rigid-body modes. The 73 modes can be classified into 18 modes in triplets, 7 in pairs, and 5 singly. The triplet and single modes have obvious physical interpretations. The triplet modes can be explained as the same mode along the  $x$ -axis,  $y$ -axis, and  $z$ -axis. The single modes are those with no directional bias [Smith and Kidger, 1991]. The modes appearing in pairs are contrary to the intuitive expectations for 3D elements. Smith and Kidger [1991] indicated that the pair modes represent motion in polar coordinates such that nodes move in planes tangential to the circumscribing sphere. The pair modes are just two orthogonal forms of a set of three fundamental forms in which each is a linear combination of the other two.

These modes were classified into four groups by their deformation types, namely, torsion (e.g., mode A), dilation (e.g., modes E and H), shear (e.g., mode C), and flexure (e.g., modes B and D) [Demarest, 1971]. The shear and flexural groups are basically triplet modes; the torsional and dilation groups are basically pair modes; However, single modes (e.g., modes F, I, L, S, and Z) are not explicitly considered in this classification. Therefore, this chapter classified these unique single modes as the fifth group.

The differences among these five mode groups can be reflected by the symmetric types of the corresponding mode shapes, which are summarized in Table 4.1. For mode A from the torsional group, the deformation is anti-symmetric about three parallel

planes and two pairs of diagonal planes and is symmetric about one pair of diagonal planes (i.e., planes  $\gamma_{10z}$  and  $\eta_{10z}$ ). For mode H from the dilation group, the deformation is symmetric about three parallel planes and one pair of diagonal planes and is anti-symmetric about the other two pairs of diagonal planes. Modes C and D from the shear and flexure groups, respectively, present different vibrating behavior regarding the parallel planes. Both have one pair of symmetric diagonal planes, but mode C and mode D have one and two symmetric parallel planes, respectively. Notably, only selected modes, instead of all the modes, are presented in [Table 4.1](#). For modes in triplets or in pairs, only one of them is described in [Table 4.1](#).

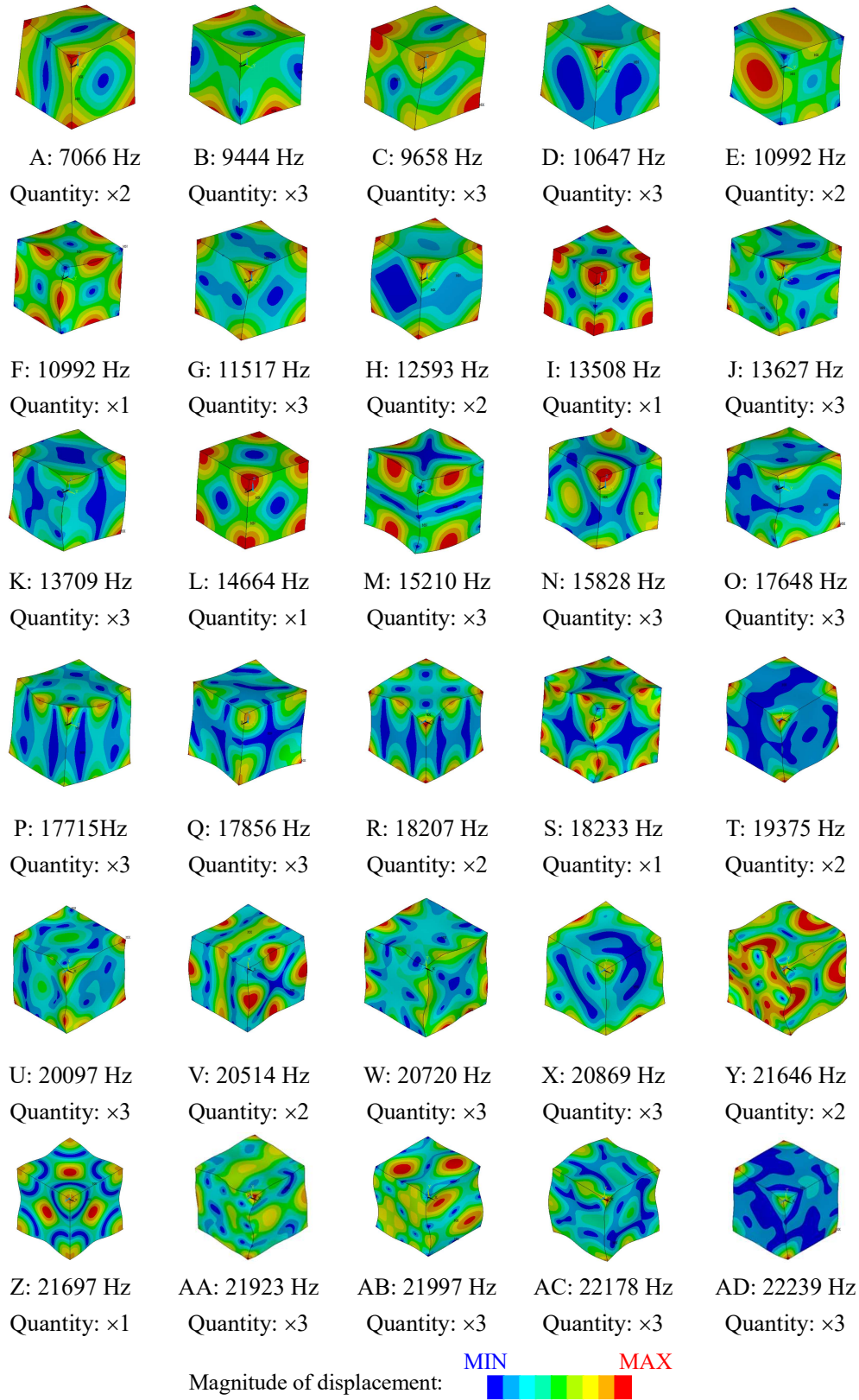


Figure 4.2 First 73 vibration modes of a concrete cube from an isotropy model

In terms of the single mode group, all six surfaces vibrate in the same pattern. Figure 4.3 presents the first five single modes of a cube, labeled from SM-1 to SM-5 according to the frequency from low to high. Modes SM-2, SM-3, and SM-5 are symmetric about the three pairs of diagonal planes, whereas modes SM-1 and SM-4 are anti-symmetric about all the diagonal planes. Modes SM-3 and SM-5 are symmetric about all three parallel planes, whereas mode SM-2 is anti-symmetric about the three parallel planes. Modes SM-1, SM-2, and SM-3 are the so-called twist mode, star mode [Smith and Kidger, 1991], and breathing mode [Ekstein and Schiffman, 1956], respectively.

As will be discussed in Sections 4.3.2 and 4.3.3 the single modes with three pairs of symmetric diagonal planes promise selections for measuring elastic constants of concrete cubes because of their insensitivity to anisotropy and skin of concrete caused by the wall effect. With these modes, two independent elastic constants may be directly calculated.

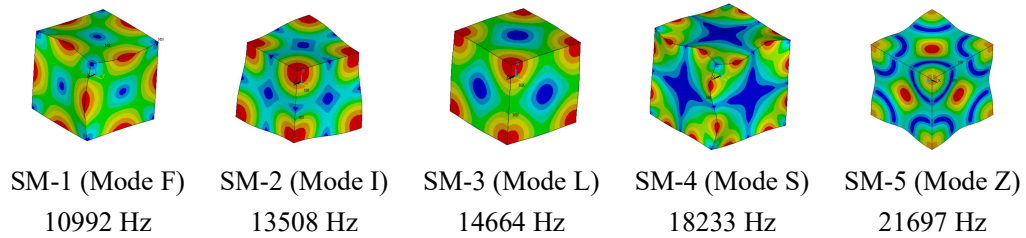


Figure 4.3 First five equivalent isotropic vibration modes

Table 4.1 Symmetric type of for different types of modes

Group	Mode	Parallel planes			Diagonal planes					
		$xoy$	$xoz$	$yoz$	$\gamma_{1oz}$	$\eta_{1oz}$	$\gamma_{2oy}$	$\eta_{2oy}$	$\gamma_{3ox}$	$\eta_{3ox}$
Torsion	A	<i>AS</i>	<i>AS</i>	<i>AS</i>	<i>AS</i>	<i>AS</i>	<i>S</i>	<i>S</i>	<i>S</i>	<i>S</i>
Shear	C	<i>AS</i>	<i>AS</i>	<i>S</i>	<i>S</i>	<i>S</i>	<i>AS</i>	<i>AS</i>	<i>AS</i>	<i>AS</i>
Flexure	D	<i>AS</i>	<i>S</i>	<i>S</i>	<i>S</i>	<i>S</i>	<i>AS</i>	<i>AS</i>	<i>AS</i>	<i>AS</i>
Dilation	H	<i>S</i>	<i>S</i>	<i>S</i>	<i>S</i>	<i>S</i>	<i>AS</i>	<i>AS</i>	<i>AS</i>	<i>AS</i>
Single modes	SM-1	<i>S</i>	<i>S</i>	<i>S</i>	<i>AS</i>	<i>AS</i>	<i>AS</i>	<i>AS</i>	<i>AS</i>	<i>AS</i>
	SM-2	<i>AS</i>	<i>AS</i>	<i>AS</i>	<i>S</i>	<i>S</i>	<i>S</i>	<i>S</i>	<i>S</i>	<i>S</i>
	SM-3	<i>S</i>	<i>S</i>	<i>S</i>	<i>S</i>	<i>S</i>	<i>S</i>	<i>S</i>	<i>S</i>	<i>S</i>
	SM-4	<i>AS</i>	<i>AS</i>	<i>AS</i>	<i>AS</i>	<i>AS</i>	<i>AS</i>	<i>AS</i>	<i>AS</i>	<i>AS</i>
	SM-5	<i>S</i>	<i>S</i>	<i>S</i>	<i>S</i>	<i>S</i>	<i>S</i>	<i>S</i>	<i>S</i>	<i>S</i>

*AS*: Anti-symmetric plane; *S*: Symmetric plane.

### 4.2.2 Sensors Installation Strategies for Identifying Selected Modes

Given the characteristics of the single modes of concrete cubes identified in [Section 4.2.1](#), strategies for extracting target modes are designed accordingly. Modes SM-3 and SM-5 have nine symmetric planes. Installing a piezoelectric sensor at one surface center introduces a simple way with multiple symmetric planes, called installation strategy EMI-I in [Figure 4.4\(a\)](#). EMI-I represents a very common sensor installation strategy. A PZT patch, a common type of piezoelectric sensor, is employed because of its lightweight, cost-effectiveness, and high sensitivity [[Lim et al., 2021](#)]. Three yellow axes (namely, 1-axis, 2-axis, and 3-axis) describe the orientation of the PZT sensor. The PZT patch is polarized along the thickness, i.e., 3-axis. The bottom surface of the PZT patch is bonded to the surface center of the concrete via adhesive materials (e.g., epoxy). Alternating voltage with a sweeping frequency is applied to the bottom and top surfaces of the PZT patch during the measurement, resulting in oscillating deformation along the 1-axis and 2-axis simultaneously. [Figure 4.4\(b\)](#) plots the actuation mechanism of this installation strategy. The PZT patch generates two perpendicular sets of forces on the surface of the cube [[Zagrai and Giurgiutiu, 2002](#)], introducing two parallel (i.e., planes  $xoz$  and  $yoz$ ) and two diagonal symmetric planes (i.e., planes  $\eta_{10z}$  and  $\gamma_{10z}$ ) for the cubic sample.

The finite element model of the concrete cube with the PZT patch is also built in ANSYS, and harmonic analyses are conducted to obtain the signal spectra. The simulated size of the PZT patch is  $20 \times 20 \times 1.0 \text{ mm}^3$ . The bonding layer is 0.5 mm thick, and its area is the same as that of the PZT patch. The material properties of the PZT material are listed in [Table 3.1](#). The concrete parameters and settings are the same as in [Section 4.2.1](#). The modulus of elasticity, Poisson's ratio, density, and damping ratio of the adhesive material are 3 GPa, 0.38, 1100 kg/m<sup>3</sup>, and 2.4%, respectively. Solid45 and Solid5 are used for the adhesive and PZT materials, respectively, and their mesh sizes are both 0.25 mm, determined after convergence analysis. The interfaces between the different materials are fully bonded. Free-free boundaries are employed for

the cube model. The applied voltage and the frequency interval are 1 V and 50 Hz, respectively.

Figure 4.4(c) presents the simulated signal spectra corresponding to the installation strategy EMI-I, in which six modes are labeled, including the two target single modes (i.e., SM-3 and SM-5) and modes D, H, P, and R shown in Figures 4.2 and 4.3. Although the amplitudes of modes SM-3 and SM-5 are smaller than those of the other modes, they can still be identified easily. Further observations reveal that all the other identified modes (i.e., modes D, H, P, and R) are symmetric about four symmetric planes of the PZT patch; while their deformations can be either symmetric or anti-symmetric about the other symmetric planes of the concrete cube (e.g., parallel plane  $xoy$  and diagonal planes  $\gamma_{2oy}$ ,  $\eta_{2oy}$ ,  $\gamma_{3ox}$ , and  $\eta_{3ox}$ ).

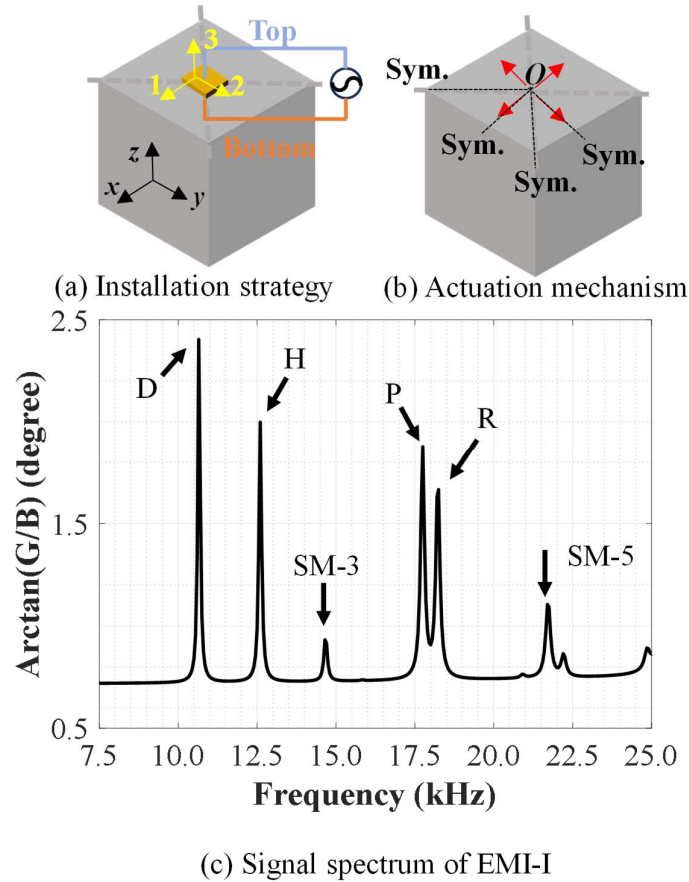


Figure 4.4 Installation strategy EMI-I and its corresponding signal spectra

Notably, mode SM-2 cannot be excited by the installation strategy EMI-I in Figure 4.4, because the sensor in EMI-I is symmetric about four planes  $xoz$ ,  $yoz$ ,  $\eta_{1oz}$  and  $\gamma_{1oz}$ ,

while mode SM-2 is symmetric about two diagonal planes  $\eta_{10z}$  and  $\gamma_{10z}$  and anisymmetric about parallel planes  $xoz$  and  $yoz$ . Figure 4.5 presents an alternative strategy EMI-II for capturing SM-2, wherein two PZT patches, which are electrically connected in parallel, are bonded along the diagonal lines of the concrete surface and are only symmetric about two diagonal planes  $\eta_{10z}$  and  $\gamma_{10z}$ , as depicted in Figure 4.5(a). The corresponding actuation forces are also symmetric about these two planes, as shown in Figure 4.5(b).

Figure 4.5(c) plots the simulated signal spectra corresponding to strategy EMI-II. The single modes SM-2, SM-3 and SM-5 can be captured. The effects of the sensor distance on the recorded signal spectra are investigated (i.e., Distance= $\sqrt{2}L/4$ ,  $\sqrt{2}L/2$ , and  $3\sqrt{2}L/4$ , where  $L$  is the length of the cube, and  $\sqrt{2}L$  is the length of the diagonal line). With the changes in sensor distance, the change trends of the modes SM-2 and SM-3 are opposite, while mode SM-5 is relatively difficult to identify. At the sensor distance of  $\sqrt{2}L/4$ , the peak of mode SM-2 is weak, whereas that of SM-3 is strong. At the sensor distance of  $3\sqrt{2}L/4$ , although the responses of modes SM-2 and SM-3 are acceptable for identification, the amplitudes of modes D and H are comparable, which increases the difficulties in differentiating them. Based on the discussions, the optimal sensor distance is selected as  $\sqrt{2}L/2$ , ensuring that modes SM-2 and SM-3 can be easily extracted.

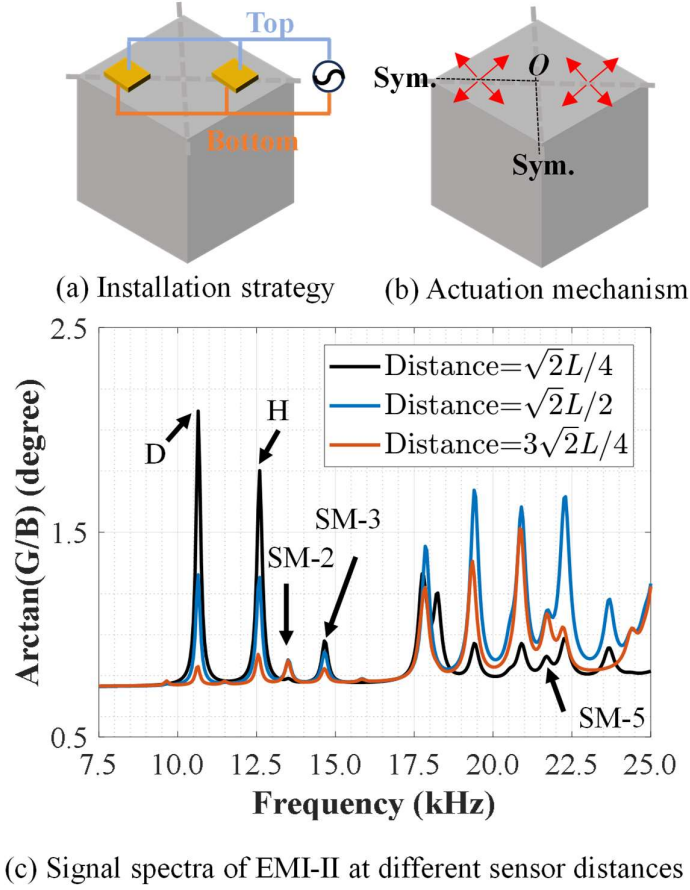


Figure 4.5 Strategy EMI-II and its corresponding signal spectra

#### 4.2.3 Evaluate Elastic Constants from Selected Modes

The elastic constants of concrete cubes will be evaluated on the basis of the excited target modes.  $\mu_c$  can be evaluated using the frequency ratio of two modes. Then, the modulus of elasticity can be calculated using analytical equations.

For isotropic materials in cubic shapes, analytical equations have been derived for two specific vibration modes: the lowest torsional mode and the Mindlin–Lamé mode [Mindlin, 1956; Lee et al., 2000], which correspond to mode A and mode SM-1, respectively, in Figure 4.2. Their corresponding frequencies can be expressed

$$f_{\text{torsion}} = \frac{\sqrt{2}}{\pi L_c} \sqrt{\frac{G_c}{\rho_c}} = \frac{1}{2L_c} \frac{2}{\pi \sqrt{1 + \mu_c}} \sqrt{\frac{E_c}{\rho_c}}, \quad (4.1)$$

$$f_{\text{SM-1}} = \frac{1}{\sqrt{2}L_c} \sqrt{\frac{G_c}{\rho_c}} = \frac{1}{2L_c} \frac{1}{\sqrt{1 + \mu_c}} \sqrt{\frac{E_c}{\rho_c}}, \quad (4.2)$$



where  $L_c$  is the length of the cube edge, and  $G_c$  is the shear modulus of the material. The frequency ratio of these two modes can be expressed as a function of Poisson's ratio.

However, it is difficult to derive analytical equations for other resonance modes of a cube. Numerical methods (e.g., the Rayleigh–Ritz method and finite element method) are usually adopted to calculate their frequencies [Demarest, 1971; Li et al., 2012]. Table 4.2 presents the simulated  $\mu_c$  and frequencies of the labeled peaks in strategies EMI-I and EMI-II in a variety of cases. The results are generated via the FEM using the same setting as that in Section 4.2.1. Discrete values of  $\mu_c$  ranging from 0.00 to 0.45 are used, assuring the applicability of the regression formula in the concrete field.

Assume the empirical equation of each frequency can be decomposed into two parts:  $1/(2L_c)\sqrt{E_c/\rho_c}$  and a function of Poisson's ratio, similar to Equations (4.1–4.2). Then, the frequency ratio between any two modes can be expressed as a function of  $\mu_c$ . Considering that mode SM-3 can be extracted from both installation strategies EMI-I and EMI-II in Section 4.2.2, this mode is used as a reference mode to normalize all other modes to calculate the frequency ratios. Consequently,  $\mu_c$  can be estimated from the regression formulas that correlate  $\mu_c$  and the frequency ratio

$$\mu_c = g\left(\frac{f_i}{f_{\text{SM-3}}}\right), i = A, B, \dots, \quad (4.3)$$

where  $f_i$  and  $f_{\text{SM-3}}$  refer to the frequencies of the arbitrary mode  $i$  and mode SM-3, respectively; and  $g(\cdot)$  is the function of a frequency ratio. The regression formulas obtained on the basis of the simulation results in Table 4.2 are as follows:

$$\begin{aligned} \mu_c = & 231.4054 \left(\frac{f_{\text{SM-2}}}{f_{\text{SM-3}}}\right)^6 - 1343.6748 \left(\frac{f_{\text{SM-2}}}{f_{\text{SM-3}}}\right)^5 + 3235.1581 \left(\frac{f_{\text{SM-2}}}{f_{\text{SM-3}}}\right)^4 \\ & - 4134.51 \left(\frac{f_{\text{SM-2}}}{f_{\text{SM-3}}}\right)^3 + 2958.3874 \left(\frac{f_{\text{SM-2}}}{f_{\text{SM-3}}}\right)^2 \\ & - 1124.6458 \left(\frac{f_{\text{SM-2}}}{f_{\text{SM-3}}}\right) + 178.0221, \quad R^2 = 1 \end{aligned} \quad (4.4)$$

$$\begin{aligned}
\mu_c = & 38672.36 \left( \frac{f_D}{f_{SM-3}} \right)^6 - 170245 \left( \frac{f_D}{f_{SM-3}} \right)^5 + 311585.5 \left( \frac{f_D}{f_{SM-3}} \right)^4 \\
& - 303480 \left( \frac{f_D}{f_{SM-3}} \right)^3 + 165905.9 \left( \frac{f_D}{f_{SM-3}} \right)^2 \\
& - 48268.9 \left( \frac{f_D}{f_{SM-3}} \right) + 5839.729, \quad R^2 = 0.9997
\end{aligned} \tag{4.5}$$

$$\begin{aligned}
\mu_c = & 20515.77 \left( \frac{f_H}{f_{SM-3}} \right)^6 - 107422 \left( \frac{f_H}{f_{SM-3}} \right)^5 + 233856.8 \left( \frac{f_H}{f_{SM-3}} \right)^4 \\
& - 270936 \left( \frac{f_H}{f_{SM-3}} \right)^3 + 176184.9 \left( \frac{f_H}{f_{SM-3}} \right)^2 \\
& - 60973.2 \left( \frac{f_H}{f_{SM-3}} \right) + 8774.137, \quad R^2 = 0.9991
\end{aligned} \tag{4.6}$$

$$\begin{aligned}
\mu_c = & 48.088 \left( \frac{f_P}{f_{SM-3}} \right)^6 - 368.156 \left( \frac{f_P}{f_{SM-3}} \right)^5 + 1168.488 \left( \frac{f_P}{f_{SM-3}} \right)^4 \\
& - 1968.07 \left( \frac{f_P}{f_{SM-3}} \right)^3 + 1855.446 \left( \frac{f_P}{f_{SM-3}} \right)^2 \\
& - 929.06 \left( \frac{f_P}{f_{SM-3}} \right) + 193.5921, \quad R^2 = 1
\end{aligned} \tag{4.7}$$

$$\begin{aligned}
\mu_c = & 65.2808 \left( \frac{f_R}{f_{SM-3}} \right)^6 - 510.74 \left( \frac{f_R}{f_{SM-3}} \right)^5 + 1657.084 \left( \frac{f_R}{f_{SM-3}} \right)^4 \\
& - 2853.91 \left( \frac{f_R}{f_{SM-3}} \right)^3 + 2751.932 \left( \frac{f_R}{f_{SM-3}} \right)^2 \\
& - 1409.38 \left( \frac{f_R}{f_{SM-3}} \right) + 300.0834, \quad R^2 = 0.9999
\end{aligned} \tag{4.8}$$

Table 4.2 Resonant frequency related to the changes in  $\mu_c$ 

$E_c$ (GPa)	$\rho_c$ (kg/m <sup>3</sup> )	$L_c$ (mm)	$\mu_c$	Frequency (Hz)						
				D	H	SM-2	SM-3	P	R	SM-5
5	2400	150	0.00	4044	4812	5733	4812	7582	7691	8756
			0.05	4098	4863	5648	5021	7442	7575	8710
			0.10	4152	4917	5564	5260	7313	7468	8674
			0.15	4205	4973	5481	5537	7192	7369	8656
			0.20	4255	5033	5399	5860	7080	7276	8671
			0.25	4302	5093	5318	6233	6975	7191	8749
			0.30	4346	5155	5240	6640	6876	7112	8964
			0.35	4384	5215	5164	7022	6783	7039	9470
			0.40	4417	5273	5090	7288	6695	6973	10604
			0.45	4444	5327	5019	7425	6611	6913	11493
30	2300	150	0.00	10126	12044	14359	12044	19008	19272	21962
			0.05	10263	12171	14147	12566	18657	18983	21843
			0.10	10398	12306	13935	13166	18332	18714	21752
			0.15	10530	12449	13726	13861	18029	18464	21708
			0.20	10657	12598	13520	14671	17748	18233	21743
			0.25	10776	12750	13319	15605	17484	18018	21937
			0.30	10885	12904	13123	16630	17236	17820	22473
			0.35	10982	13057	12932	17593	17002	17638	23739
			0.40	11066	13204	12747	18270	16781	17472	26621
			0.45	11135	13340	12568	18619	16571	17322	28936
55	2500	100	0.00	19721	23460	27962	23460	37005	37524	42748
			0.05	19987	23707	27549	24478	36322	36961	42518
			0.10	20250	23970	27138	25646	35688	36438	42342
			0.15	20508	24248	26730	26999	35100	35952	42256
			0.20	20754	24538	26330	28575	34552	35501	42326
			0.25	20985	24835	25938	30393	34038	35083	42705
			0.30	21197	25134	25557	32385	33556	34698	43749
			0.35	21386	25430	25185	34257	33101	34344	46216
			0.40	21548	25715	24825	35569	32671	34022	51801
			0.45	21682	25980	24476	36243	32263	33729	56249

Figure 4.6(a) presents the regression results for the frequency ratios between two single modes. A monotonical trend is observed for the ratios of  $f_{SM-2}/f_{SM-3}$ , and the sixth-order polynomial formulas in Equation (4.4) have perfect  $R^2$  for the regression results. In contrast, the ratios of  $f_{SM-5}/f_{SM-3}$  are unsuitable for assessing  $\mu_c$  because the corresponding trend is not monotonic in the given range.

When Strategy EMI-I is designed, modes D, H, P, and R can be used to evaluate Poisson's ratios, and the average value can be calculated subsequently. The corresponding regression formulas presented in Equations (4.5–4.8) have nearly perfect  $R^2$ .

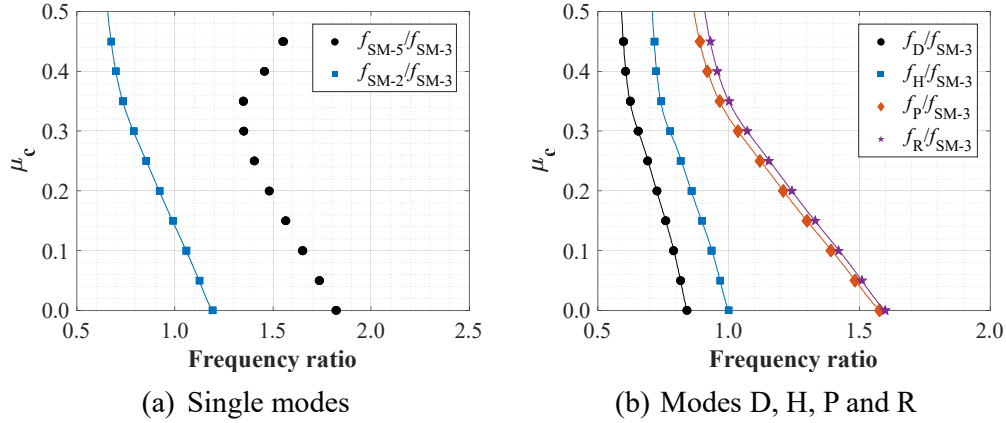


Figure 4.6 Regression results for calculating  $\mu_c$

Given the estimated  $\mu_c$ , the modulus of elasticity can be determined subsequently. By drawing on the form of Equations (4.1–4.2), the equation for the reference mode SM-3 can be directly regressed as shown in Equation (4.9), where  $F_{SM-3}(\mu_c)$  is a complicated function of Poisson's ratio for mode SM-3. The regressed  $F_{SM-3}(\mu_c)$  is presented in Equation (4.10) with perfect  $R^2$ .

$$f_{SM-3} = F_{SM-3}(\mu_c) \frac{1}{2L_c} \sqrt{\frac{E_c}{\rho_c}} \quad (4.9)$$

$$F_{SM-3}(\mu_c) = -25.0759\mu_c^4 + 15.3786\mu_c^3 - 1.1876\mu_c^2 + 0.9183\mu_c + 1.0002, \quad R^2 = 1.000 \quad (4.10)$$

where  $F_{SM-3}(\mu_c)$  is a function of  $\mu_c$  for mode SM-3. The regressed function  $F_{SM-3}(\mu_c)$  in Equation (4.10) shows perfect  $R^2$ .

The abovementioned regression formulas prepare for calculating two elastic constants. The calculation steps for the evaluations are as follows:

- (a) Determine of PZT sensor installation strategy (EMI-I or EMI-II).
- (b) Select modes and extraction of the corresponding frequencies (i.e., strategy EMI-I: modes D, H, P, and R; strategy EMI-II: mode SM-2).

- (c) Calculate  $\mu_c$  using the frequency ratio(s) between the selected modes and reference mode (i.e., mode SM-3) via Equations (4.4–4.8). Use the average value if appropriate.
- (d) Calculate  $E_c$  of the selected modes by substituting the estimated  $\mu_c$  into Equations (4.9–4.10) and use the average value if appropriate.

Although Strategies EMI-I and EMI-II are presented in parallel, the traditional Strategy EMI-I is presented for comparison to illustrate the advantages of the novel Strategy EMI-II in this chapter. The material properties evaluated by using the proposed EMI strategies are denoted as  $E_{ce}$  and  $\mu_{ce}$  hereinafter to differentiate from other methods.  $E_{ce,I}$  and  $\mu_{ce,I}$  are used for strategy EMI-I, while  $E_{ce,II}$  and  $\mu_{ce,II}$  are used for strategy EMI-II.

### 4.3 Accuracy and Stability Considering Multiple Influencing Factors

This section examines the accuracy and stability of the recommended strategy (i.e., EMI-II) by considering multiple practical influencing factors, such as edge imperfection, anisotropic properties, and wall effect. Strategy EMI-I and the traditional dynamic resonance method introduced in Table 2.3 are also compared to study the advantages of the proposed strategy.

#### 4.3.1 Modification Regarding Imperfect Edge Dimensions

Most of the concrete cubes are not perfect cubes. The effect of slight edge differences, called edge dimension imperfection, is discussed in this subsection, and a corresponding modification method is proposed to improve the accuracy of the proposed EMI technique.

Figure 4.7(a) shows the dimension labels of a concrete cube. The average edge length,  $L_{eq}$ , is defined as the edge of a cube whose volume is equal to that of the rectangular parallelepiped [Ekstein and Schiffman, 1956],

$$L_{eq} = (h_c w_c l_c)^{\frac{1}{3}}, \quad (4.11)$$

where  $h_c$  is the edge length perpendicular to the sensor installation surface (i.e., along  $z$ -axis), and  $w_c$  (i.e., along  $x$ -axis) and  $l_c$  (i.e., along  $y$ -axis) are the other two edge lengths of the sensor installation surface. The first imperfection parameter,  $\delta_1$ , is defined as the average difference between section edges and the average edge, as shown in Equation (4.12). The second imperfection parameter,  $\delta_2$ , is defined as the ratio between  $h_c$  and the average edge, as presented in Equation (4.13).

$$\delta_1 = \frac{\left( \left| \frac{w_c - L_{eq}}{L_{eq}} \right| + \left| \frac{l_c - L_{eq}}{L_{eq}} \right| \right)}{2} \quad (4.12)$$

$$\delta_2 = \frac{h_c}{L_{eq}} \quad (4.13)$$

These imperfection parameters (i.e.,  $\delta_1$  and  $\delta_2$ ) consider slight edge variations in the section and height, respectively, because the captured modes are highly dependent on the actuation direction. [Table 4.3](#) presents the effect of edge imperfections on the captured frequencies and evaluated elastic constants of the two installation strategies, wherein the concrete properties are the same as those in the aforementioned isotropic model. The true elastic constants are  $E_c = 30$  GPa and  $\mu_c = 0.2$ . The evaluation results by strategy EMI-I are highly related to imperfections ( $\delta_1$  and  $\delta_2$ ) because the employed vibration modes are dependent on vibration directions. As imperfection  $\delta_1$  increases from 0 to 0.064,  $\mu_c$  evaluated by strategy EMI-I increase from 0.198 to 0.223, leading to the largest differences of 11.5% and 3.9% in the estimated  $\mu_c$  and  $E_c$ , respectively. By contrast, the maximum differences in the estimated  $\mu_c$  and  $E_c$  by strategy EMI-II are only 3.5% and 0.2%, respectively. As height  $h_c$  increases from 141 mm to 159 mm (i.e.,  $\delta_2$  increases from 0.94 to 1.06), the evaluated  $\mu_c$  by strategy EMI-I decreases from 0.223 to 0.183, and the evaluated  $E_c$  increases from 28829 MPa to 31685 MPa. By contrast, the evaluated elastic constants by strategy EMI-II remain unchanged, showing high stability in evaluation.

From the preceding discussion, modification considering edge imperfections is needed for strategy EMI-I, but such modification equations may not be necessary for strategy EMI-II whose results show high stability against edge imperfection and can be

used directly in most cases. However, the modification formulas are still presented for both EMI-I and EMI-II strategies, as shown in Equations (4.14–4.17).

$$\begin{aligned} \frac{\mu_{ce,I}^{\text{modified}}}{\mu_{ce,I}^{\text{measured}}} &= -17.21 - 5.588\delta_1 + 34.93\delta_2 + 22.79\delta_1^2 + 4.956\delta_1\delta_2 \\ &\quad - 16.72\delta_2^2, \quad R^2 = 0.9985 \end{aligned} \quad (4.14)$$

$$\begin{aligned} \frac{E_{ce,I}^{\text{modified}}}{E_{ce,I}^{\text{measured}}} &= 10.35 + 2.563\delta_1 - 17.99\delta_2 - 9.175\delta_1^2 - 2.636\delta_1\delta_2 \\ &\quad + 8.641\delta_2^2, \quad R^2 = 0.9988 \end{aligned} \quad (4.15)$$

$$\begin{aligned} \frac{\mu_{ce,II}^{\text{modified}}}{\mu_{ce,II}^{\text{measured}}} &= 1.371 + 2.501\delta_1 - 0.7912\delta_2 - 13.94\delta_1^2 - 2.245\delta_1\delta_2 \\ &\quad + 0.4206\delta_2^2, \quad R^2 = 0.9998 \end{aligned} \quad (4.16)$$

$$\begin{aligned} \frac{E_{ce,II}^{\text{modified}}}{E_{ce,II}^{\text{measured}}} &= 1.013 + 0.1148\delta_1 - 0.02759\delta_2 - 0.6401\delta_1^2 \\ &\quad - 0.08953\delta_1\delta_2 + 0.01494\delta_2^2, \quad R^2 = 0.9995 \end{aligned} \quad (4.17)$$

Table 4.3 Effect of edge imperfections on the evaluation results of the proposed strategies

$h_c \times w_c \times l_c$ (mm <sup>3</sup> )	Frequency differences (Hz)						$\mu_{ce}$		$E_{ce}$ (MPa)		
	D	H	SM-3	P	R	SM-2	SM-3	EMI-I	EMI-II	EMI-I	EMI-II
150×150×150	0	0	0	0	0	0	0	0.198	0.200	29957	29908
147×150×153	-150	50	50	-200	-150	0	0	0.208	0.200	29525	29900
144×150×156	-300	150	100	-400	-250	0	50	0.215	0.202	29196	29908
141×150×159	-450	250	150	-650	-350	0	150	0.223	0.207	28829	29931
150×147×153	50	50	50	0	-25	0	0	0.199	0.200	30089	29900
150×144×156	200	25	100	50	300	0	50	0.196	0.202	30541	29908
150×141×159	400	75	150	100	500	0	150	0.190	0.207	31105	29931
153×150×147	200	-50	50	250	150	0	0	0.194	0.200	30491	29900
156×150×144	400	-100	100	450	300	0	50	0.190	0.202	30987	29908
159×150×141	650	-100	150	700	450	0	150	0.183	0.207	31685	29931



### 4.3.2 Effect of Anisotropy

The determination of the dynamic elastic properties of concrete from impact resonance measurements [ASTM C215, 2019] usually assumes isotropic behavior, leading to limitations of resonance methods in evaluating Poisson's ratio [Swamy, 1971]. Although anisotropy corrections can be introduced theoretically, measuring the anisotropy of each specimen is practically difficult. Consequently, it is important to examine and understand the sensitivity of the evaluation results to anisotropy. The orthotropic material model, including nine independent constants for the material [Bažant, 1983], was recommended for investigating anisotropic material properties of concrete [Haach et al., 2020]

$$[D] = \begin{bmatrix} (E_x)^{-1} & -\mu_{yx}(E_y)^{-1} & -\mu_{zx}(E_z)^{-1} & 0 & 0 & 0 \\ -\mu_{xy}(E_x)^{-1} & (E_y)^{-1} & -\mu_{zy}(E_z)^{-1} & 0 & 0 & 0 \\ -\mu_{xz}(E_x)^{-1} & -\mu_{yz}(E_y)^{-1} & (E_z)^{-1} & 0 & 0 & 0 \\ 0 & 0 & 0 & (G_{yz})^{-1} & 0 & 0 \\ 0 & 0 & 0 & 0 & (G_{zx})^{-1} & 0 \\ 0 & 0 & 0 & 0 & 0 & (G_{xy})^{-1} \end{bmatrix}, \quad (4.18)$$

where  $[D]$  is the stiffness matrix, and  $E_x, E_y, E_z, \mu_{yz}, \mu_{zx}, \mu_{xy}, G_{yz}, G_{zx}$ , and  $G_{xy}$  are the independent elastic constants.

The anisotropy in  $E_c, \mu_c$ , and  $G_c$  will be considered separately in this subsection. Haach et al. [2020] showed that when concrete was evaluated under the hypothesis of orthotropic material model, the CoVs were not higher than 6% for three longitudinal moduli of elasticity (i.e.,  $E_x, E_y$ , and  $E_z$ ) and 13% for three transverse moduli of elasticity (i.e.,  $G_x, G_y$ , and  $G_z$ ). Bertoldo et al. [2020] presented that the CoVs were not higher than 7%, 6%, and 21% for longitudinal moduli of elasticity, transverse moduli of elasticity, and Poisson's ratios, respectively. Therefore, the relative differences are set to 10%, 30%, and 30% for  $E_c, G_c$ , and  $\mu_c$ , respectively, in the simulated isotropic and anisotropic cases in Table 4.4. The isotropic case has elastic constants as  $E_x = E_y = E_z = 30.0$  GPa,  $\mu_{yz} = \mu_{zx} = \mu_{xy} = 0.2$ ,  $G_{yz} = G_{zx} = G_{xy} = 12.5$  GPa. The labels express the anisotropic directions of elastic constants. For example, the anisotropic case 0.9-1.0-1.1 for the longitudinal moduli of elasticity  $E_c$  means that  $E_x, E_y, E_z$  are equal to  $E_c$  multiplied by 0.9, 1.0, and 1.1, respectively, where the values of  $\mu_c$  and  $G_c$  remain the same in three directions in this case.

In addition to concrete cubes, prisms of  $150 \times 150 \times 300 \text{ mm}^3$  are also simulated to investigate the anisotropy effect on the traditional dynamic resonance methods in [ASTM C215](#) for comparison. In practical operation, an accelerometer is utilized to record the signals induced by an impactor. In this subsection, the resonant frequencies are directly simulated through modal analyses, and the evaluation method is the same as that reported by [Chen and Leon \[2019\]](#), who evaluated elastic constants by using the fundamental bending and torsional modes directly and avoided iteration. [Figure 4.7\(b\)](#) shows the dimension labels of the investigated prisms.

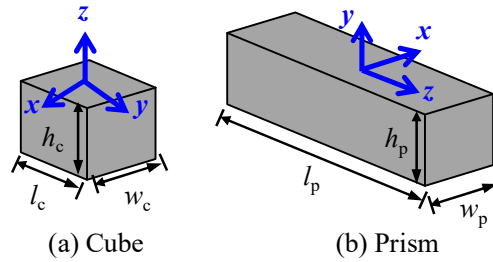


Figure 4.7 Dimension labels of the tested samples

[Figure 4.8](#) plots the anisotropic effect on the signal spectra of the concrete cubes, in which [Figures 4.8\(a\), 4.8\(c\), and 4.8\(e\)](#) show the spectra with three different anisotropies measured by strategy EMI-I, and [Figures 4.8\(b\), 4.8\(d\), and 4.8\(f\)](#) show the measurement by strategy EMI-II. The corresponding frequencies of the peaks considering the effects of anisotropy are summarized in [Table 4.4](#). For strategy EMI-I, the movement of different modes varies with different types of anisotropy, except for mode D which presents similar changes in each anisotropy. Mode H splits into two peaks for  $E_c$  and  $\mu_c$  anisotropies, while it is insensitive to  $G_c$  anisotropy. The average frequency of mode H can be used in real practice. Mode P is sensitive to  $G_c$  anisotropy only and will split into two peaks. Mode R is sensitive to  $E_c$  and  $G_c$  anisotropies but insensitive to  $\mu_c$  anisotropy. Mode SM-3 has minimal movement compared with other modes, indicating mode SM-3 reflects average elastic constants and is insensitive to the anisotropy effect. For strategy EMI-II, mode SM-2 is insensitive to  $E_c$  and  $\mu_c$  anisotropies and has ignorable changes with  $G_c$  anisotropy. Notably, each cube has three pairs of faces. High sensitivity to anisotropy implies that different resonant frequencies will be captured when the

PZT sensor is installed on three different orthogonal faces of a cube with anisotropy.

The different behaviors of the abovementioned modes may be caused by the classification of mode shapes. Root-mean-square error (RMSE) compared with the isotropic case is used to assess the variation induced by anisotropy. Among all the modes, modes SM-2 and SM-3 have the lowest normalized total RMSE, indicating the most stable results of strategy EMI-II against anisotropy. Given the three different anisotropies, strategy EMI-II shows smaller RMSE values in the evaluations of both elastic constants than strategy EMI-I. The values of normalized mean RMSE for EMI-II are 1.2% and 0.6% for  $E_c$  and  $\mu_c$ , respectively.

The anisotropy effects on the traditional dynamic resonance method recommended by [ASTM C215](#) are summarized in [Table 4.5](#). The fundamental bending mode splits into two due to the anisotropy, denoted by the 1-B-1 and 1-B-2. These two bending modes are sensitive to  $E_c$  and  $G_c$  anisotropies, while the torsional mode (1-T) is sensitive to  $G_c$  anisotropy only. The elastic constants can be evaluated using one of the bending modes and the first torsional mode. Therefore, two groups of elastic constants can be evaluated:  $\mu_{cd1}$  and  $E_{cd1}$  correspond to the evaluations by using the 1-B-1 and 1-T frequencies, and  $\mu_{cd2}$  and  $E_{cd2}$  correspond to the evaluations by using the 1-B-2 and 1-T frequencies. In general, the anisotropies in  $E_c$  and  $G_c$  cause large errors in the evaluated elastic constants; especially, the normalized mean RMSE for Poisson's ratio is as large as 37.6% and 55.1%.

[Figure 4.9](#) further illustrates the evaluation errors induced by three different types of anisotropy. Corresponding to the anisotropies of 10% $E_c$ , 30% $\mu_c$ , and 30% $G_c$ , [Figure 4.9\(a\)](#) shows the results for strategy EMI-I, where the maximum errors in the evaluated  $\mu_c$  are 7.5%, 7.5%, and 4.0%, respectively, while the evaluation errors in  $E_{cc}$  are less than 3%. Regarding strategy EMI-II shown in [Figure 4.9\(b\)](#), the anisotropy of Poisson's ratio has minimal effects on the evaluation results with negligible errors. Considering all the types of anisotropy, the maximum errors in the evaluated  $\mu_c$  and  $E_c$  are 5.5% and 0.9%, respectively, which are smaller than those of strategy EMI-I.

[Figure 4.9\(c\)](#) shows the evaluation results by the traditional dynamic resonance method using modes 1-B-1 and 1-T. Compared with the results of the EMI strategies, the evaluation

errors caused by  $E_c$  and  $G_c$  anisotropies are quite significant. The maximum errors are larger than 56% and 7.8% for the evaluated  $\mu_c$  and  $E_c$ , respectively. The numerical results showed that both the EMI strategies (especially strategy EMI-II) can reliably assess  $\mu_c$  of concrete cubes with anisotropy and outperform the traditional dynamic resonance method recommended by [ASTM C215](#).

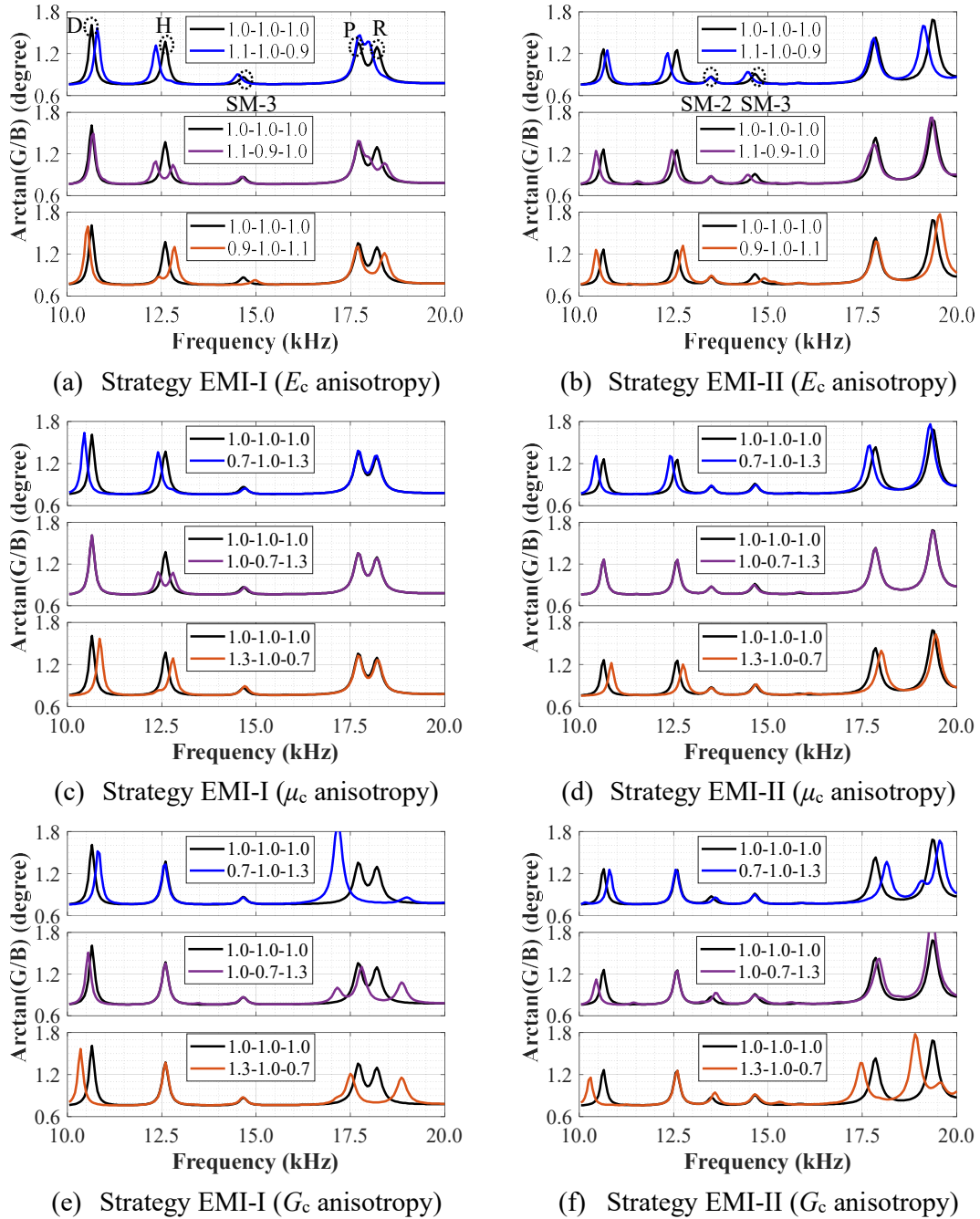


Figure 4.8 Effect of anisotropy on the signal spectra of two proposed strategies

Table 4.4 Summary of assessment of the proposed methods regarding different anisotropy statuses

Case	Label	Frequencies of each mode (Hz)							$\mu_{ce}$		$E_{ce}$ (MPa)	
		EMI-I					EMI-II		EMI-I	EMI-II	EMI-I	EMI-II
		D	H	SM-3	P	R	SM-2	SM-3				
Isotropy	1.0-1.0-1.0	10650	12600	14650	17700	18200	13500	14650	0.198	0.200	29927	29908
$E_c$ anisotropy	1.1-1.0-0.9	10800	12350	14500	17750	17950	13500	14450	0.193	0.190	29706	29776
	1.1-0.9-1.0	10700	12580	14600	17700	18400	13500	14450	0.193	0.190	30126	29776
	0.9-1.0-1.1	10550	12850	15000	17700	18400	13500	14900	0.215	0.211	30229	30065
	RMSE <sup>1</sup>	108	204	222	29	218	0	218	0.010	0.010	227	187
$\mu_c$ anisotropy	0.7-1.0-1.3	10450	12400	14700	17700	18200	13500	14700	0.211	0.202	29276	29940
	1.0-0.7-1.3	10650	12600	14700	17700	18200	13500	14650	0.202	0.200	29920	29908
	1.3-1.0-0.7	10850	12800	14700	17700	18200	13500	14700	0.192	0.202	30582	29940
	RMSE <sup>1</sup>	163	163	50	0	0	0	41	0.008	0.002	538	72
$G_c$ anisotropy	0.7-1.0-1.3	10800	12600	14650	17150	19000	13600	14650	0.192	0.195	30373	30282
	1.0-0.7-1.3	10550	12600	14650	17475	18850	13600	14650	0.197	0.195	30044	30282
	1.3-1.0-0.7	10350	12600	14650	17500	18850	13600	14650	0.202	0.195	29722	30282
	RMSE <sup>1</sup>	202	0	0	362	704	100	0	0.005	0.005	270	282
Mean RMSE		158	122	91	130	307	33	86	0.008	0.006	345	180
Normalized mean RMSE		1.5%	1.0%	0.6%	0.7%	1.7%	0.2%	0.6%	4.0%	3.0%	1.2%	0.6%

Note: 1. RMSE: root-mean-square error, where error is computed in comparison with the isotropy case.

Table 4.5 Summary of the assessment by the prism regarding different anisotropy statuses

Label		Frequency (Hz)			$\mu_{cd1}$	$E_{cd1}$ (MPa)	$\mu_{cd2}$	$E_{cd2}$ (MPa)
		1-B-1	1-B-2	1-T				
Isotropy	1.0-1.0-1.0	3946.7	-	3565.6	0.205	30023	-	-
$E_c$ anisotropy	0.9-1.0-1.1	4097.1	4099.5	3565.5	0.318	32837	0.320	32883
	0.9-1.1-1.0	3944.8	3948.5	3565.4	0.204	29985	0.206	30052
	1.0-1.1-0.9	3780.5	3781.8	3565.5	0.088	27118	0.089	27140
	RMSE	129.4	129.8	0.1	0.094	2335	0.094	2345
$\mu_c$ anisotropy	0.7-1.0-1.3	3942.5	3949.7	3564.3	0.203	29947	0.208	30078
	1.0-0.7-1.3	3938.3	3952.1	3564.1	0.200	29872	0.210	30122
	1.3-1.0-0.7	3941.4	3948.1	3563.9	0.202	29929	0.207	30050
	RMSE	6.2	3.7	1.5	0.002	90	0.008	88
$G_c$ anisotropy	0.7-1.0-1.3	3945.6	4035.3	3785.5	0.046	29368	0.102	30954
	1.0-0.7-1.3	3783.0	4035.2	3395.2	0.224	27651	0.431	32322
	1.3-1.0-0.7	3782.9	3945.5	3235.2	0.375	28202	0.525	31275
	RMSE	133.7	72.3	249.4	0.135	1746	0.237	1626
Mean RMSE		89.8	68.6	83.7	0.077	1390	0.113	1353
Normalized mean RMSE		2.3%	1.7%	2.3%	37.6%	4.6%	55.1%	4.5%

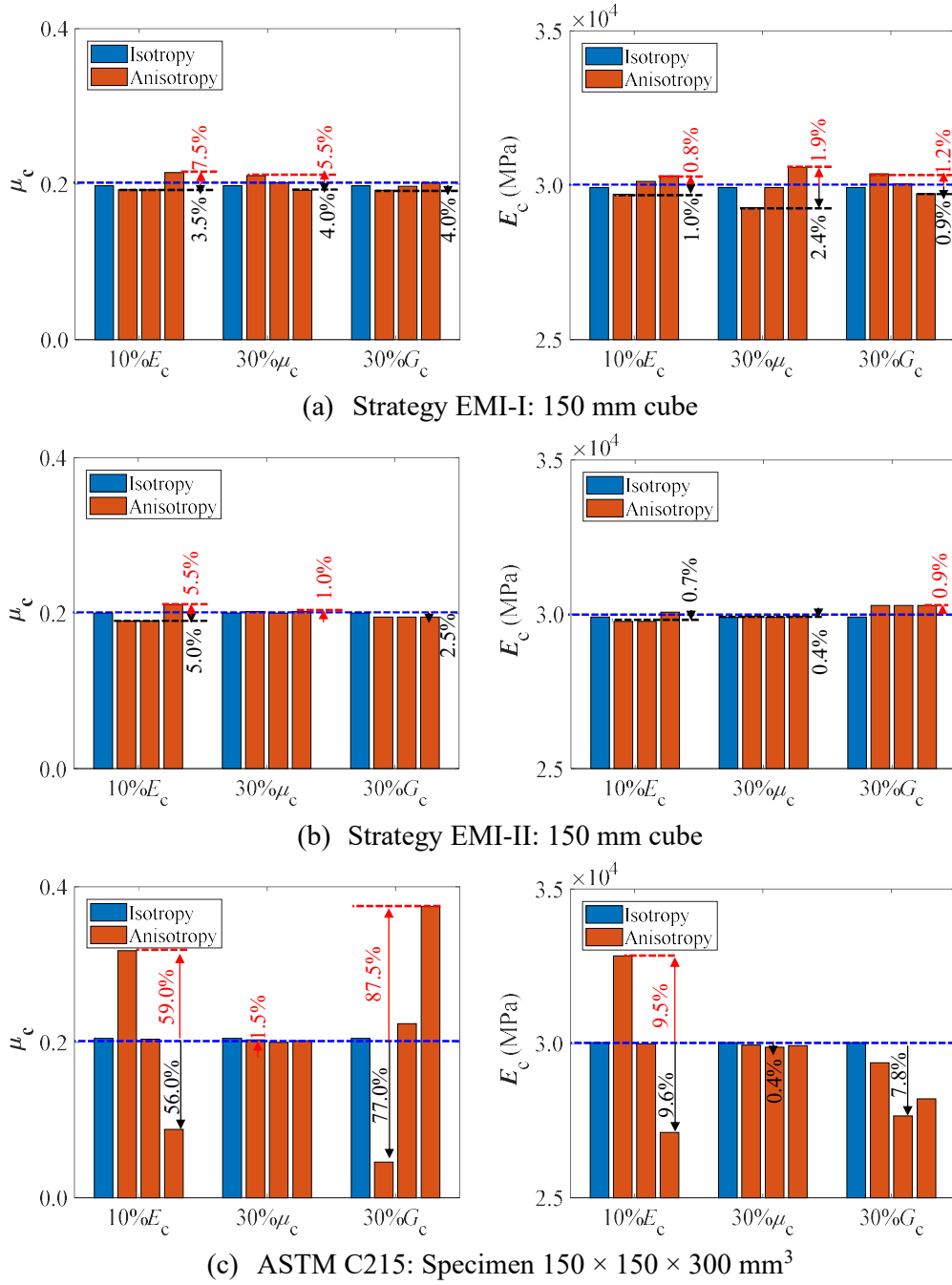


Figure 4.9 Anisotropy-induced evaluation errors with different methods

### 4.3.3 Effect of Concrete Skin

In addition to material anisotropy, the heterogeneity of concrete also challenges accurate measurement. Krejiger [1984] demonstrated that the outer part of a concrete sample, called the skin of concrete, was weaker than the core part. When aggregate sizes are non-negligible compared with the mold, the compaction of concrete and the uniformity of aggregate

distribution are affected by the mold wall, which is the so-called wall effect. Overlooking the wall effect may result in an inaccurate evaluation of the mechanical properties of concrete specimens [Zheng et al., 2003].

Concrete is inherently a heterogeneous composite [Huang et al., 2022]. As mentioned in Section 4.1, when the aggregate size is non-negligible compared with the mold size, the mold wall effect influences the compaction of concrete and the distribution of aggregate particles [Zheng et al., 2003]. Krejiger [1984] investigated the skin of concrete geometrically and physically. Geometrically, the outer layer of concrete is 0.1 mm thick cement paste, and the middle layer is around 5 mm thick mortar. Physically, the porosity of the mortar layer is much larger than the concrete layer. Moreover, the modulus of elasticity of the concrete core is at least twice that of the mortar layer. Wetzel et al. [2015] made a similar observation in ultra-high-performance concrete: the hardness of the outer layer was almost one-third of that of the core part. Czarnecki and Sadowski [2022] demonstrated that the thickness of the cement paste layer was from 0.06 mm to 1.13 mm, depending on the material type of the formwork, as measured using a 3D laser scanning method. Huang et al. [2022] observed through CT scanning that the aggregate density gradually increased with increasing distance from the surface and remained stable at the deep zone, and the thickness of the weak zone was around 4.7–9.5 mm. Based on the discussion above, overlooking the wall effect may result in an inaccurate evaluation of the elastic properties of concrete [Zheng et al., 2003]. Therefore, this subsection examines the effect of the skin of concrete cubes on the performance of the proposed EMI-II method in comparison with the EMI-I and traditional dynamic resonance methods.

The concrete specimens are considered to have two parts, namely skin and core, as shown in Figure 4.10. Both parts are regarded as isotropic and homogeneous in this subsection. The sizes of cubes and prisms are the same as those in Section 4.3.1. Modal analyses are conducted to obtain resonant frequencies. The material properties of the core are the same as those of concrete in Section 4.2.1 (i.e.,  $E_c = 30$  GPa,  $\rho_c = 2300$  kg/m<sup>3</sup>,  $\mu_c = 0.2$ ). The skin thickness ( $t_s$ ) is assumed to be the same at each face, and its modulus of elasticity is assumed to be half of the core part (i.e., 15 GPa). Poisson's ratio, density, and damping ratio of the skin are 0.3, 1500



kg/m<sup>3</sup>, and 0.8%, respectively, consistent with those of normal cement paste.

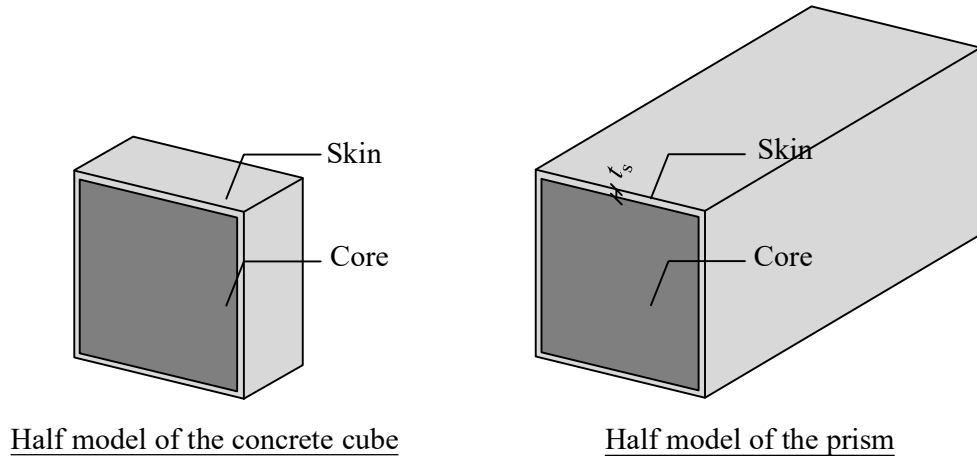


Figure 4.10 Schematics of the skin of the concrete for different samples

Tables 4.6 and 4.7 summarize the effect of skin thickness on the EMI methods and traditional dynamic resonance method, respectively. Notably, the density of the entire cube would decrease because of the skin effect. Under this situation, the decreased or unchanged frequencies (such as modes D, H, P, and R, as shown in Table 4.6) would result in underestimated elastic constants according to Equation (4.9). Similar trends can be found in the frequencies of transverse and torsional modes presented in Table 4.7. By contrast, the frequencies of modes SM-2 and SM-3 increase as the thickness of the skin layer increases.

Table 4.6 Effect of the skin of concrete on the proposed methods

$t_s$ (mm)	Density (kg/m <sup>3</sup> )	Frequencies of each mode (Hz)						$\mu_{ce}$		$E_{ce}$ (MPa)	
		D	H	SM-3	P	R	SM-2	EMI -I	EMI -II	EMI -I	EMI -II
0	2300	10647	12593	14664	17715	18207	13508	0.199	0.200	29923	29948
3	2208	10668	12544	14814	17552	17999	13631	0.213	0.201	28430	29282
6	2123	10644	12441	14952	17337	17704	13742	0.229	0.201	26822	28629

Table 4.7 Effect of the skin of concrete on the traditional testing methods

$t_s$ (mm)	Density (kg/m <sup>3</sup> )	Frequency (Hz)		$\mu_{cd}$	$E_{cd}$ (MPa)
		1-B	1-T		
0	2300	3945.7	3564.1	0.205	30006
3	2237	3914.6	3531.7	0.209	28735
6	2150	3880.5	3494.9	0.214	27160

Figure 4.11 compares the evaluation results of different methods regarding the impact of

varying skin thicknesses. In general, the evaluation differences increase with the thickness of the skin layer. Strategy EMI-II presents a perfect performance for evaluating  $\mu_c$  (Figure 4.11(a)), in which almost no difference occurs in the studied cases. Strategy EMI-I and the traditional dynamic resonance method show relatively poor evaluation performance, and their measured  $\mu_c$  is higher than that of strategy EMI-II for cases  $t_s=3$  mm and 6 mm. Although all the methods underestimate  $E_c$ , strategy EMI-II shows a smaller error than the other two methods (Figure 4.11(b)). The measured  $E_c$  by strategy EMI-I and the dynamic resonance method are smaller than by strategy EMI-II. Although  $E_c$  of the core part can be more accurately estimated by compensating for the skin effect, the implementation is difficult because the mechanical properties of the skin are typically unknown. Nevertheless, the discussion is still informative for knowing the relative differences between the actual and measured  $E_c$ .

In summary, strategy EMI-II outperforms the other two methods, showing higher accuracy in evaluating elastic constants, which is mainly attributed to the careful selection of unique vibration modes that are insensitive to edge imperfection, material anisotropy, and concrete skin effect.

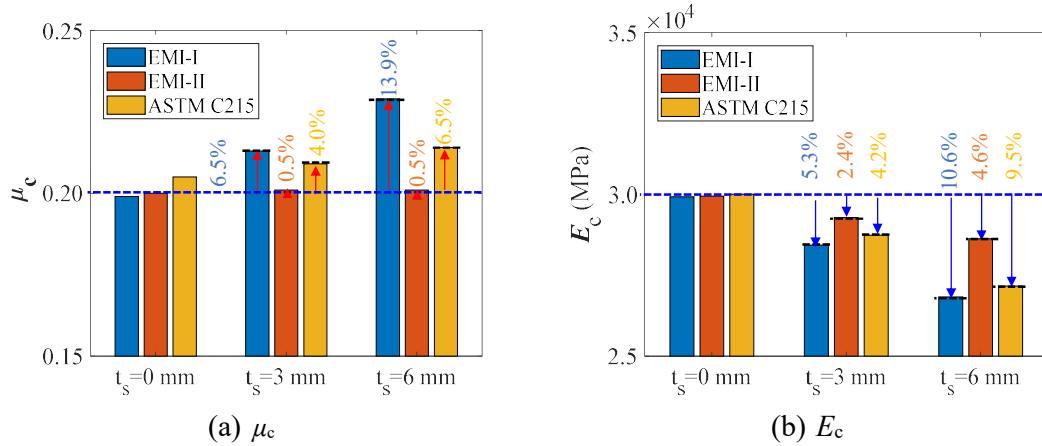


Figure 4.11 Effect of the skin of concrete on different methods

## 4.4 Experimental Validations

Experimental investigations on the measurement of elastic constants (i.e.,  $E_c$  and  $\mu_c$ ) of concrete cubes were conducted to validate the proposed EMI method. The evaluation results were compared with the results of standard static [ASTM C469/C469M, 2022; GB/T 50081, 2019] and dynamic [ASTM C215, 2019] testing methods. Three tasks presented in this section

aimed to: (a) evaluate the effectiveness of the proposed strategy EMI-II in comparison with the ASTM C215 method; (b) validate the advantage of the mode selection of strategy EMI-II in comparison with strategy EMI-I; (c) correlate the dynamic elastic constants measured by strategy EMI-II to the static elastic constants measured by standard destructive tests.

#### 4.4.1 Measurement of Elastic Constants at 400 Days

The experimental validation started with the measurement of concrete specimens with stable material properties. Figure 4.12 presents the specimens prepared for different testing methods, namely, the dynamic resonance, static, and EMI-R methods. Ten concrete prisms were cast in one batch for the measurement (Figure 4.12(a)). Six of them had a size of  $100 \times 100 \times 300 \text{ mm}^3$  and were labeled P-S, while the remaining four had a size of  $150 \times 150 \times 300 \text{ mm}^3$  and were labeled P-L. The corresponding mix proportions of concrete are summarized in Table 4.8. Plastic formwork was used. The curing age was 400 days at the moment of measurement.

All prisms were tested in accordance with ASTM C215 [2019] using the 1<sup>st</sup> bending and 1<sup>st</sup> torsional modes to obtain the dynamic elastic constants first (Figure 4.12(b)). A compact data acquisition system (NI-9230) having a maximum sampling rate of 12.8 kS/s, and a high-fidelity triaxial accelerometer (PCB 356b18) were used for the measurement. Then, the ten specimens were evenly divided into groups A and B. Each group had three P-S specimens and two P-L specimens. The accurate information for each specimen is summarized in Table 4.9.

Figure 4.12(c) presents the specimens for the proposed EMI-R and static tests. After the traditional dynamic resonance tests, the prisms in group A were cut into cubic shapes for the EMI-R measurement. The P-S and P-L prisms with 100 mm and 150 mm widths were cut into three and two cubes, respectively. The cutting section is plotted in Figure 4.12(a). The PZT patches were bonded to the cutting surface using a quick-hardening epoxy (Devcon 14270). Small ( $10 \times 10 \times 1.0 \text{ mm}^3$ ) and large ( $20 \times 20 \times 1.0 \text{ mm}^3$ ) PZT patches were used for 100 mm and 150 mm specimens, respectively, both of which have the same material properties as shown in those used in the simulation, as shown in Table 3.1. An LCR meter (Keysight E4980 AL) was employed. The scanning frequency range and interval were 1–50 kHz and 25 Hz,

respectively. The applied voltage was 1 V. The tested specimens were placed on a foam to achieve negligible boundary constraint effects.

After the dynamic resonance tests, the prisms in group B were tested in accordance with [GB/T 50081 \[2019\]](#) to obtain static elastic constants. Two transverse and two vertical strain gauges were installed on the left and right surfaces of the specimens, respectively. The tests were conducted in a 340-ton uniaxial compression test machine. The room temperature for measurement was around 20 °C.

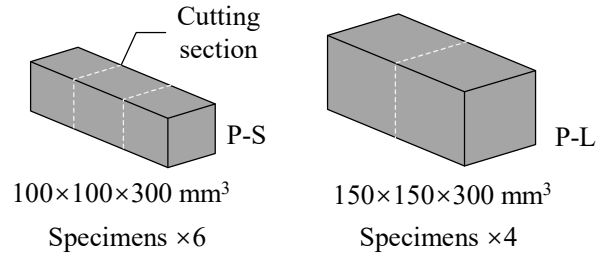
Table 4.8 Material proportions of the adopted concrete materials

Type	Mix proportion, by weight	Density (kg/m <sup>3</sup> )
Normal Concrete	C: W: S: CA: FA: SP <sup>a</sup> =1:0.375:1.659:1.561:0.780: 0.006	2368

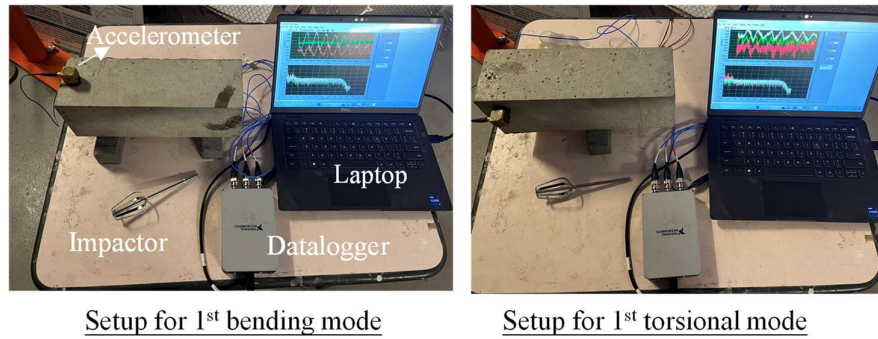
<sup>a</sup>C= cement; W= water; S= sand; FA= 10 mm aggregate; CA= 20 mm aggregate; SP= superplastic

Table 4.9 Experimental results of prisms from the traditional dynamic resonance and static tests

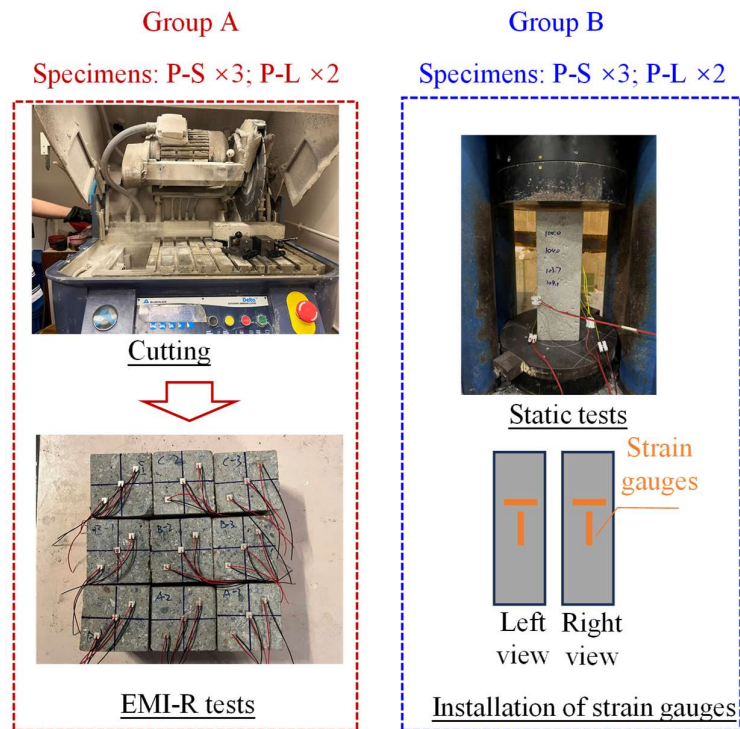
Group	Specimen	$h_p$ (mm)	$w_p$ (mm)	$l_p$ (mm)	Density (kg/m <sup>3</sup> )	Frequency (Hz)		Dynamic Tests		Static Tests	
						1-B	1-T	$\mu_{cd}$	$E_{cd}$ (MPa)	$\mu_{cs}$	$E_{cs}$ (MPa)
A	P-S-1	99.4	102.5	300.0	2265	3356	3825	0.175	33096	-	-
	P-S-2	99.4	101.9	300.0	2289	3392	3859	0.184	34094		
	P-S-3	99.5	104.4	300.0	2229	3339	3762	0.201	32218		
	P-L-1	149.9	153.3	300.0	2268	4319	3912	0.214	34495		
	P-L-2	149.7	151.2	300.0	2254	4229	3815	0.198	34256		
B	P-S-4	99.9	102.5	300.0	2258	3372	3769	0.187	33174	0.165	28280
	P-S-5	100.0	104.1	300.0	2259	3396	3852	0.189	33588	0.170	28451
	P-S-6	100.0	103.9	300.0	2250	3372	3792	0.203	33084	0.169	27371
	P-L-3	147.0	151.5	300.0	2329	4255	3845	0.224	37084	0.212	31824
	P-L-4	150.1	150.7	300.0	2263	4292	3862	0.203	33846	0.191	28069



(a) Ten specimens used in this test



(b) Experimental setup for the dynamic resonance method



(c) Specimens for EMI-R and static tests

Figure 4.12 Experimental design for the measurement of the elastic constants by different methods

Comparisons of the evaluation results between the different testing methods are summarized and presented in Table 4.10 and Figure 4.13, respectively. The detailed experimental results from the traditional tests and proposed EMI-R tests are presented in Tables 4.9 and 4.11. As each test was conducted on multiple specimens, CoV was computed to quantitatively assess the dispersion of the results.

Regarding the  $\mu_c$  evaluation, strategy EMI-II presented the most stable performance with the smallest CoV value of 3.2%, followed by strategy EMI-I with a CoV value of 3.7%, both of which are much smaller than those of the traditional dynamic resonance (7.4%) and static method (11.0%). The mean values were normalized by the results from the static method to compare different methods. The  $\mu_c$  from the traditional dynamic resonance method was around 109.4% of static  $\mu_{cs}$ ; while  $\mu_{ce}$  from the EMI strategies EMI-I and EMI-II are 102.2% and 98.3% of static  $\mu_{cs}$ , respectively, which are almost equal. These correlations are consistent with the hypothesis from Anson and Newman [1966], who predicted that static  $\mu_{cs}$  and dynamic  $\mu_{cd}$  tend to converge when the curing age is very long.

Table 4.10 Comparison of different testing methods

Method	Specimen	Specimen Nos.	$\mu_c$			$E_c$		
			Mean	CoV (%)	Normalized ratio	Mean (MPa)	CoV (%)	Normalized ratio
EMI-I	Cube	13	0.185	3.7	1.022	33477	3.1	1.162
EMI-II	Cube	13	0.178	3.2	0.983	34225	2.9	1.188
Dynamic: ASTM C215	Prism	10	0.198	7.4	1.094	33894	3.9	1.177
Static: GB/T 50081	Prism	5	0.181	11.0	1.000	28799	6.0	1.000

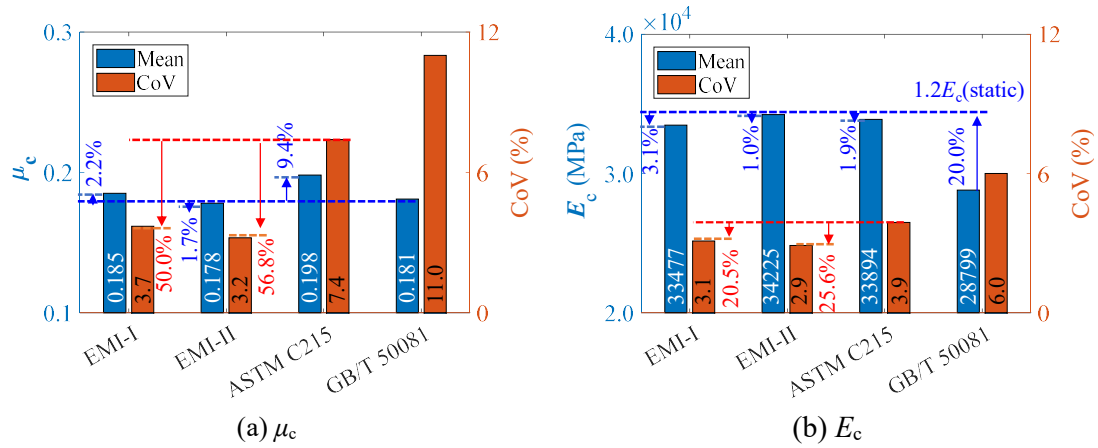


Figure 4.13 Comparison of different methods on evaluations

Regarding the evaluation of  $E_c$ , all the methods indicated relatively smaller CoVs than the evaluations of  $\mu_c$ . All three dynamic methods showed better stability than the static method. The proposed EMI methods showed improved stability performance beyond 20% compared with the traditional dynamic resonance method. The normalized ratios by the value from the static method were from 1.162 to 1.188, which are consistent with the findings by [Lydon and Balendran \[1986\]](#), who suggested that  $E_{cd} \approx 1.20E_{cs}$ .

This subsection presents experimental investigations of the accuracy and stability of the proposed strategy EMI-II for measuring elastic constants at 400-day age. The results showed that the proposed strategy EMI-II can present a more accurate Poisson's ratio than the traditional dynamic resonance method, and the measured dynamic modulus of elasticity can be directly correlated with static values. Meanwhile, the proposed strategies EMI-I and EMI-II showed better stability than the ASTM C215 method, especially for Poisson's ratio.

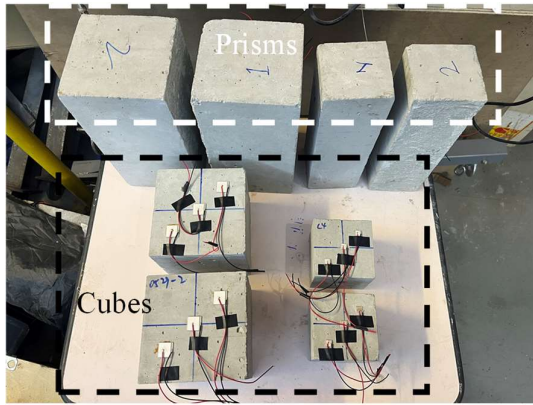


Table 4.11 Experimental results from the EMI-R methods

Specimen	$h_c$ (mm)	$w_c$ (mm)	$l_c$ (mm)	Density (kg/m <sup>3</sup> )	Frequency (Hz)						$\mu_{ce}$		$E_{ce}$ (MPa)		
					EMI-I					EMI-II		EMI-I	EMI-II	EMI-I	EMI-II
					D	H	SM-3	P	R	SM-2	SM-3				
P-S-1a	99.9	102.0	99.4	2267	16550	19675	22525	27700	28838	21600	22550	0.180	0.173	32850	33633
P-S-1b	94.4	103.3	99.3	2257	16600	20400	23350	27825	28950	22075	23100	0.180	0.174	33702	33731
P-S-1c	98.5	102.2	99.4	2269	16650	19850	22750	27975	28875	21800	22775	0.180	0.173	33400	34094
P-S-2a	97.4	102.3	99.4	2316	16575	20000	22825	28300	29125	22050	22875	0.175	0.168	34124	34906
P-S-2b	97.4	102.6	99.3	2265	17125	20400	23350	28575	29600	22275	23325	0.176	0.175	35123	35290
P-S-2c	98.4	100.9	99.4	2280	16850	20125	23075	28350	29125	22225	23100	0.183	0.170	33791	35000
P-S-3a	97.5	105.1	99.8	2215	16225	19488	22500	27050	28225	21400	22500	0.184	0.177	31812	32523
P-S-3b	98.2	104.2	99.3	2230	16675	19825	22875	27600	28225	21575	22900	0.188	0.184	32587	33152
P-S-3c	98.0	103.9	99.5	2219	16400	19650	22775	27425	28225	21525	22775	0.191	0.182	31929	32835
P-L-1a	148.9	153.0	149.8	2289	11275	13200	15450	18625	19325	14575	15425	0.194	0.182	33346	34289
P-L-1b	147.0	153.6	150.0	2280	11125	13325	15475	18588	19575	14700	15500	0.190	0.180	33701	34783
P-L-2a	147.0	151.0	149.8	2283	11450	13475	15750	19100	19650	14875	15750	0.192	0.183	34553	35461
P-L-2b	147.5	151.3	149.5	2259	11400	13550	15800	19100	19600	14850	15800	0.196	0.186	34285	35226

#### 4.4.2 Measurement of Elastic Constants in the First 28 Days

After validating the stability and accuracy in [Section 4.1](#), the proposed strategy EMI-II was further examined in the first 28-day curing age, a period when elastic constants changed dramatically. Another concrete batch was cast using the same mix proportions shown in [Table 4.8](#). [Figure 4.14](#) presents the specimens used for various testing methods at different curing ages. Four cubes (two of them were in  $100 \times 100 \times 100 \text{ mm}^3$ , and the other two were in  $150 \times 150 \times 150 \text{ mm}^3$ ) were prepared for EMI-R tests, and four prisms (two of them were in  $100 \times 100 \times 300 \text{ mm}^3$  and the other two were in  $150 \times 150 \times 300 \text{ mm}^3$ ) were prepared for dynamic resonance tests. The EMI-R and traditional dynamic resonance tests were conducted on days 1, 2, 3, 5, 7, 14, 21, and 28, as shown in [Figure 4.14\(a\)](#). Six standard cylinders with a height of 300 mm and a diameter of 150 mm were cast for the static tests in accordance with [ASTM C469/C469M](#), as illustrated in [Figure 4.14\(b\)](#), and were tested on days 2 and 28. The test setups for the dynamic and static tests were the same as those described in [Section 4.3.1](#). All the specimens were cast using plastic formwork.



(a) Specimens for the EMI tests and the dynamic testing methods



(b) Specimens for the static method

Figure 4.14 Specimens for various methods at different curing ages

[Table 4.12](#) and [Figure 4.15](#) present the overall comparison among the traditional dynamic resonance, static, and proposed EMI-R methods, in which both the mean values and CoVs are given. The detailed experimental results for the measured elastic constants are presented in [Tables 4.13–4.15](#). Regarding the Poisson's ratio, as the curing age increased,  $\mu_{ce,II}$  from the EMI-II method decreased, and the corresponding evolution curve was quite smooth ([Figure](#)

4.15(a)). By contrast, the traditional dynamic resonance methods and the EMI-I testing method provided fluctuating evolution curves of  $\mu_{cd}$  and  $\mu_{ce,I}$ , respectively. The evolution trend of  $\mu_{cs}$  differed from that of the dynamic counterparts. The static Poisson's ratio ( $\mu_{cs}$ ) increased with the curing age, which is consistent with the results presented for concrete in the existing literature [Anson and Newman, 1966; Persson, 1999]. But at the 28-day curing age, the mean value of  $\mu_{ce,II}$  was almost equal to that of  $\mu_{cs}$ , confirming that static and dynamic Poisson's ratios of concrete tend to converge with an increase in curing age. Moreover, the proposed strategies EMI-I and EMI-II showed more stable evaluation results of  $\mu_c$  than the traditional dynamic resonance methods (Table 4.12). The CoVs for the proposed EMI strategies were smaller than 2.8% across different tested specimens, whereas the CoVs for the traditional dynamic resonance method could have a maximum value of up to 14.5%, comparable to that of the standard static method.

The evolution trends of different  $E_c$  curves are the same (Figure 4.15(b)). The values of  $E_{ce,II}$  were slightly higher (around 2%–6%) than those of  $E_{ce,I}$  and  $E_{cd}$  at the same curing age, while the values of  $E_{ce,I}$  and  $E_{cd}$  were very close. These differences in the  $E_c$  values will be discussed in the following subsection (i.e., Section 4.3). Differences between the  $E_{cd}$  and  $1.2E_{cs}$  were small (i.e., 0.1%) at the 28-day curing age, and the error bars on the  $1.2E_{cs}$  could almost cover the range of the evaluated  $E_c$  from the other three methods. But differences became significant (i.e., 21.7%) at the 2-day curing age, suggesting that the relationship of  $E_{cd} \approx 1.20E_{cs}$  is not satisfied at the early age of concrete. Regarding the stability of evaluating  $E_c$ , the CoV values of the proposed strategies were smaller than 2.1%, whereas those of the traditional dynamic resonance method could be up to 4.9%. Nevertheless, the latter one is still considered acceptable for measuring  $E_c$ .

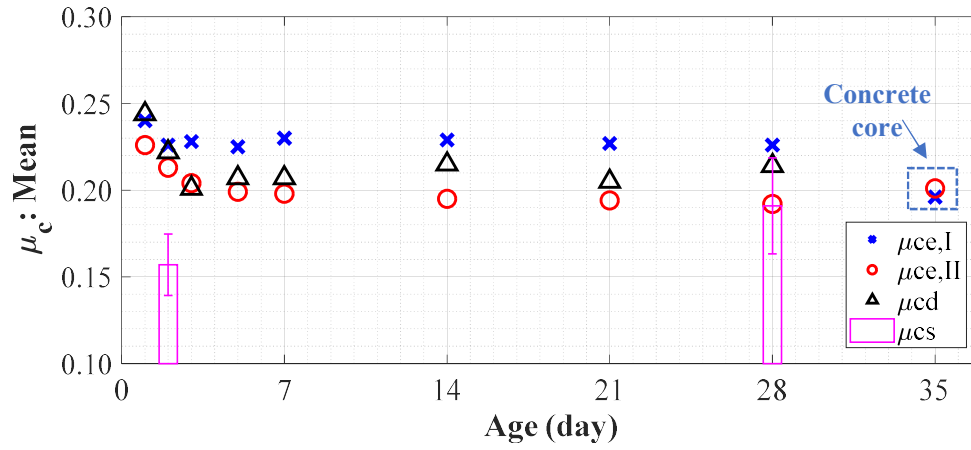
In summary, strategy EMI-II indicates its superiority in the measurement of elastic constants at different ages compared with the traditional dynamic resonance method and strategy EMI-I. The small CoV values of strategies EMI-I and EMI-II were likely attributed to their insensitivity to material anisotropy. By contrast, the maximum CoV value of the dynamic resonance method might be as large as that of static destructive tests. The good agreement of

Poisson's ratios between strategy EMI-II and the static method at 28-day and 400-day ages in Sections 4.4.1 and 4.4.2 indicated strategy EMI-II could provide rapid and accurate evaluations of Poisson's ratio in real practice.

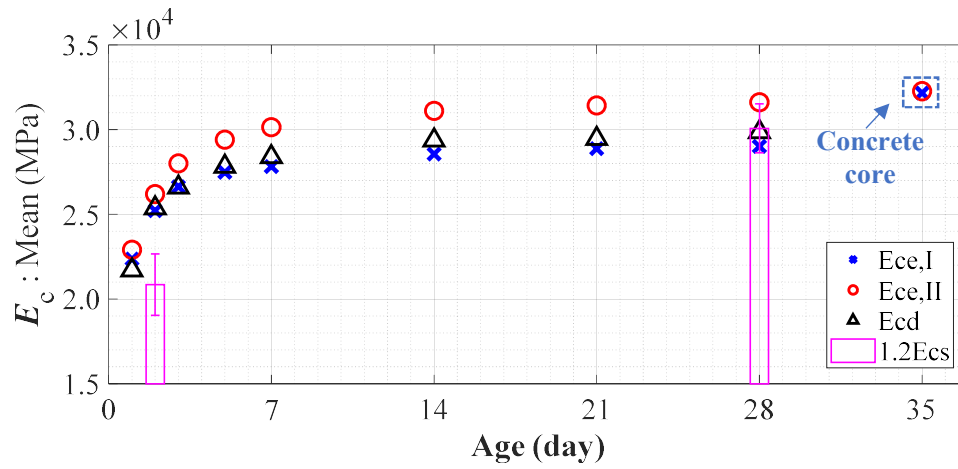
Table 4.12 Comparison of various methods at different curing age

Age (day)	$\mu_c$				$E_c$ (MPa)			
	$\mu_{ce,I}$	$\mu_{ce,II}$	$\mu_{cd}$	$\mu_{cs}$	$E_{ce,I}$	$E_{ce,II}$	$E_{cd}$	$E_{cs}$
1	0.240 (2.5)	0.226 (1.5)	0.244 (1.3)	-	22353 (1.9)	22915 (2.1)	21691 (4.0)	-
2	0.226 (1.5)	0.213 (1.5)	0.222 (7.5)	0.157 (11.3)	25213 (0.5)	26202 (1.3)	25370 (3.5)	17373 (8.7)
3	0.228 (2.8)	0.204 (1.5)	0.201 (13.4)	-	26629 (1.2)	28000 (1.1)	26593 (4.9)	-
5	0.225 (1.5)	0.199 (1.5)	0.207 (9.2)	-	27483 (0.9)	29407 (1.0)	27820 (2.3)	-
7	0.229 (1.5)	0.198 (1.8)	0.207 (14.4)	-	27824 (1.0)	30140 (0.9)	28386 (4.3)	-
14	0.227 (1.0)	0.195 (1.9)	0.215 (13.6)	-	28549 (1.3)	31111 (0.4)	29362 (4.8)	-
21	0.227 (0.5)	0.194 (1.8)	0.205 (5.1)	-	28876 (1.1)	31436 (0.2)	29458 (3.8)	-
28	0.226 (0.6)	0.192 (2.1)	0.214 (6.6)	0.191 (14.5)	29015 (1.3)	31615 (0.3)	29866 (3.1)	25064 (4.8)

Note: Values outside and in parentheses are the mean values and coefficient of variations in %, respectively.



(a)  $\mu_c$  (Mean)



(b)  $E_c$  (Mean)

Figure 4.15 Comparison of various methods at different curing age

Table 4.13 Experimental results from the traditional dynamic resonance method at different curing age

Specimen	$h_p$ (mm)	$w_p$ (mm)	$l_p$ (mm)	Density (kg/m <sup>3</sup> )	Age (day)	Frequency (Hz)		ASTM C215	
						1-B	1-T	$\mu_{cd}$	$E_{cd}$ (MPa)
P-S-7	99.6	101.5	300.5	2234	1	2690	2990	0.246	21228
					2	2900	3277	0.200	24560
					3	2947	3370	0.168	25285
					5	3072	3437	0.228	27635
					7	3103	3471	0.228	28197
					14	3142	3513	0.229	28906
					21	3112	3530	0.190	28261
					28	3153	3540	0.218	29084
P-S-8	99.5	100.1	299.9	2242	1	2661	2960	0.240	20724
					2	2908	3255	0.223	24707
					3	2971	3361	0.194	25714
					5	3057	3439	0.209	27266
					7	3044	3474	0.170	26930
					14	3093	3513	0.183	27840
					21	3143	3537	0.208	28819
					28	3167	3541	0.226	29313
P-L-5	149.8	152.3	299.8	2278	1	3431	3059	0.247	22572
					2	3710	3315	0.241	26369
					3	3826	3428	0.232	28010
					5	3882	3506	0.209	28752
					7	3951	3539	0.233	29878
					14	4034	3595	0.249	31208
					21	4015	3619	0.215	30779
					28	4037	3634	0.219	31130
P-L-6	149.7	149.5	300.0	2259	1	3416	3048	0.244	22240
					2	3687	3311	0.225	25843
					3	3798	3428	0.210	27362
					5	3823	3485	0.182	27627
					7	3882	3522	0.195	28538
					14	3945	3572	0.201	29494
					21	3976	3595	0.205	29975
					28	3977	3610	0.194	29939

Table 4.14 Experimental results from the EMI-R methods at different curing age

Specimen	$h_c$ (mm)	$w_c$ (mm)	$l_c$ (mm)	Density (kg/m <sup>3</sup> )	Age (day)	Frequency (Hz)					$\mu_{ce}$		$E_{ce}$ (MPa)			
						EMI-I					EMI-II		EMI-I	EMI-II	EMI-I	EMI-II
						D	H	SM-3	P	R	SM-2	SM-3				
C100-1	100.0	101.5	99.8	2247	1	14050	16450	20100	22775	23725	17950	20125	0.240	0.222	22203	23401
					2	14975	17400	21100	24425	25225	19200	21225	0.229	0.213	25209	26658
					3	15325	17725	21600	25175	25850	19875	21550	0.229	0.199	26413	28395
					5	15575	17975	21950	25700	26463	20350	21950	0.227	0.196	27384	29719
					7	15650	18000	22175	25775	26638	20600	22175	0.233	0.194	27559	30434
					14	15800	18200	22375	26025	26938	20900	22375	0.231	0.191	28142	31271
					21	15875	18325	22450	26250	27088	20975	22425	0.229	0.190	28513	31482
					28	15925	18375	22450	26275	26975	21050	22450	0.228	0.188	28582	31681
C100-2	100.0	101.4	100.1	2265	1	14050	16450	20000	22950	23575	17750	20000	0.236	0.226	22463	23134
					2	14950	17300	20900	24525	25100	18975	20925	0.222	0.211	25385	26262
					3	15200	17625	21500	25150	25800	19650	21450	0.229	0.204	26432	28076
					5	15538	17900	21825	25675	26150	20200	21850	0.226	0.198	27422	29584
					7	15638	17975	22075	25675	26300	20450	22050	0.232	0.195	27624	30290
					14	15813	18188	22275	26075	26600	20725	22300	0.229	0.194	28324	31090
					21	15900	18300	22325	26225	26775	20850	22375	0.226	0.192	28685	31439
					28	15925	18350	22350	26300	26850	20900	22325	0.225	0.189	28831	31541

Table 4.14 Experimental results from the EMI-R methods at different curing age (*Continued*)

Specimen	$h_c$ (mm)	$w_c$ (mm)	$l_c$ (mm)	Density (kg/m <sup>3</sup> )	Age (day)	Frequencies of peaks for each strategy (Hz)							$\mu_{cc}$		$E_{cc}$ (MPa)	
						EMI-I					EMI-II		EMI-I	EMI-II	EMI-I	EMI-II
						D	H	SM-3	P	R	SM-2	SM-3				
C150-1	150.5	150.3	150.8	2261	1	9225	10900	13150	15125	15600	11650	13100	0.235	0.224	21867	22307
					2	9850	11575	13900	16275	16775	12600	13900	0.225	0.211	25055	25941
					3	10150	11925	14500	16838	17325	13050	14275	0.235	0.205	26598	27754
					5	10350	12125	14550	16813	17413	13400	14575	0.227	0.201	27283	29212
					7	10425	12175	14750	17275	17775	13575	14750	0.228	0.201	27977	29970
					14	10600	12375	14975	17600	17975	13825	14975	0.228	0.199	28881	31053
					21	10650	12425	15050	17725	18100	13925	15050	0.227	0.197	29198	31482
					28	10675	12475	15075	17700	18175	13975	15075	0.227	0.196	29350	31689
C150-2	150.3	150.3	150.2	2228	1	9525	11500	13800	15450	15825	11875	13475	0.248	0.230	22878	22817
					2	10025	11675	14150	16550	16925	12700	14150	0.230	0.218	25205	25948
					3	10350	12175	14475	17075	17425	13175	14425	0.219	0.206	27075	27776
					5	10550	12200	14700	17425	17775	13500	14700	0.220	0.202	27844	29114
					7	10625	12250	14875	17525	17900	13675	14875	0.226	0.201	28135	29864
					14	10775	12400	15075	17750	18100	13950	15100	0.226	0.198	28850	31029
					21	10825	12450	15150	17850	18175	14025	15150	0.227	0.197	29111	31343
					28	10850	12500	15175	17900	18225	14075	15175	0.225	0.195	29295	31548



Table 4.15 Experimental results from the standard static method at different curing age

ID	Density (kg/m <sup>3</sup> )	Age (day)	$\mu_{cs}$	$E_{cs}$ (MPa)	$f'_c$ (MPa)
Cylinder-1	2300	2	0.141	17555	20.8
Cylinder-2	2294	2	0.176	15786	23.5
Cylinder-3	2277	2	0.154	18779	22.4
Mean	/	/	0.157	17373	22.2
CoV (in %)	/	/	11.3	8.7	6.1
Cylinder-4	2282	28	0.223	25477	41.1
Cylinder-5	2271	28	0.175	26012	39.5
Cylinder-6	2293	28	0.175	23704	38.0
Mean	/	/	0.191	25064	39.5
CoV (in %)	/	/	14.5	4.8	3.9

#### 4.4.3 Measurement of Elastic Constants of Concrete Cores

To investigate the effect of the skin of concrete, two 100 mm cubes (i.e., specimens C-100-1 and C-100-2) were cut for further measurement. The thickness of the weak skin zone was around 4.7–9.5 mm for a 100 mm cube [Huang et al., 2022]. Therefore, the specimens were cut into cubes around 70 mm by removing the skin. Figure 4.16 shows the concrete core of specimens C100-1 and C100-2. Because of the limitations of the cutting machine, the specimens were cut into nearly cubic parallelepiped. The same surfaces tested at intact status were selected to install PZT patches ( $10 \times 10 \times 1.0 \text{ mm}^3$ ) and evaluated by strategies EMI-I and EMI-II at the same time. The setups of the tests were the same as those in Section 4.2. The tests were conducted at the 35-day curing age. Compared with the 28-day results, the 7-day difference for the tests is acceptable, given that the elastic properties became nearly converged, as shown in Figure 4.15. The details of the concrete core are summarized in Table 4.16.

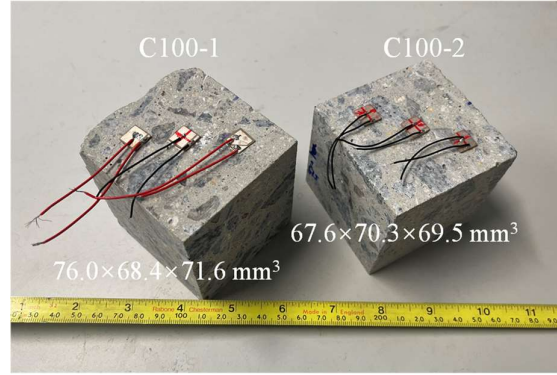


Figure 4.16 Concrete core of the specimens C100-1 and C100-2

Table 4.17 summarizes the evaluation results of different methods for original and core cubes. Poisson's ratio and modulus of elasticity, as measured by strategy EMI-II, have minimal differences between these two concrete cubes (i.e., 0.001 for  $\mu_c$  and 486 MPa for  $E_c$ ). Meanwhile, strategy EMI-I presents very close evaluations of  $\mu_c$  and  $E_c$  for these core cubes compared with strategy EMI-II, as shown in Figure 4.15. The differences in  $E_c$  and  $\mu_c$  between these two EMI strategies are 0.0% and 2.5%, respectively, indicating that the values evaluated by strategy EMI-II for the concrete core cubes can be considered the actual values for this batch. Compared with this actual value of  $E_c$ , the values obtained by strategy EMI-I and the traditional dynamic resonance method for the original cube specimens were underestimated by around 10% due to the skin effect, whereas strategy EMI-II presented very accurate evaluations (i.e., the error was only -2.0%) on the original cubes. Compared with the actual value of  $\mu_c$ , strategy EMI-II for the original cube specimens indicated an error of only -6.5%, which was small enough and better than those of the other methods.

In summary, the proposed strategy EMI-II is insensitive to the skin effect of concrete cubes and can provide highly accurate results of the elastic constants of concrete cores, validating the advantage of the mode selection proposed in this chapter. By contrast, strategy EMI-I and the traditional dynamic resonance method are apparently affected by the skin effect.

Table 4.16 Experimental results for the specimen C-100-1 and specimen C-100-2 before and after cutting

Specimen	$h_c$ (mm)	$w_c$ (mm)	$l_c$ (mm)	Density (kg/m <sup>3</sup> )	Frequency (Hz)						$\mu_{cc}$		$E_{cc}$ (MPa)		
					EMI-I					EMI-II		EMI-I	EMI-II	EMI-I	EMI-II
					D	H	SM-3	P	R	SM-2	SM-3				
C-100-1-Original	100.0	101.5	99.8	2247	15925	18375	22450	26275	27213	21050	22425	0.226	0.187	28834	31653
C-100-1-Core	76.0	68.4	71.6	2270	24775	27538	32100	38725	40150	29525	32100	0.189	0.201	32671	32492
C-100-2-Original	100.0	101.4	100.1	2265	15925	18363	22325	26325	26875	20900	22325	0.223	0.189	28992	31526
C-100-2-Core	67.6	70.3	69.5	2274	23475	28400	33075	38925	40663	30475	33100	0.202	0.200	31668	32006

Table 4.17 Evaluation results of different methods for the intact and core cubes

Status	Methods	Specimen used	$\mu_c$			$E_c$ (MPa)		
			Value	Mean	Error (%)	Value	Mean	Error (%)
Original	EMI-I	C100-1	0.226	0.225	11.9	28834	28913	-10.3
		C100-2	0.223			28992		
	EMI-II	C100-1	0.187	0.188	-6.5	31653	31590	-2.0
		C100-2	0.189			31526		
Core	EMI-I	C100-1	0.189	0.196	-2.5	32671	32170	0.0
		C100-2	0.202			31668		
	EMI-II	C100-1	0.201	0.201	-	32492	32249	-
		C100-2	0.200			32006		

Note: Error was calculated by comparing with the mean value of the core part from strategy EMI-II.

## 4.5 Summary

An improved EMI-R technique, which actuates special vibration modes by employing a new PZT sensor installation strategy (i.e., strategy EMI-II), was proposed for measuring the elastic constants of concrete cubes and validated through a series of numerical and experimental studies. A series of numerical simulations were conducted to investigate vibration mode selection, effective sensor installation, evaluation formulas, and the corresponding evaluation accuracy and stability. Subsequently, experiments were conducted to examine the accuracy, reproducibility, and stability of the proposed method. Some major conclusions are summarized as follows:

1. The proposed sensor installation strategy EMI-II offers an efficient, easy, and rapid NDT technique for accurately measuring the elastic constants of concrete cubes.
2. In measuring the dynamic elastic constants (i.e.,  $\mu_c$  and  $E_c$ ) of standard concrete cubes at different curing ages in the presence of anisotropy and skin effect, the proposed strategy EMI-II outperforms the traditional dynamic resonance method suggested by ASTM C215 in terms of stability and accuracy. Strategy EMI-I may be another acceptable alternative, which can offer reasonable evaluations of elastic constants.
3. The measured dynamic Poisson's ratio by strategy EMI-II can be directly used to replace the static Poisson's ratio from the standard destructive tests after 28-day curing. Meanwhile, the measured dynamic modulus of elasticity by strategy EMI-II can be converted to estimate the static modulus of elasticity after 28-day curing.
4. The proposed strategy EMI-II can provide highly accurate evaluations on the dynamic modulus of elasticity of the core part of concrete cubes, whereas the traditional dynamic resonance method suggested by ASTM C215 and strategy EMI-I may underestimate it by 10% because of the effect of concrete skin.

Although this chapter mainly focuses on measuring the elastic constants of standard concrete cubes that are widely tested on construction sites, the proposed NDT method can be easily extended to other materials in cubic shapes, presenting a

promising future research direction. Moreover, accurate measurements of elastic properties warrant some further investigation of the microstructures of concrete materials. Moreover, the correlations between the dynamic and static values in the first 28 days (especially in the first 7 days) need to be established in the future to completely replace the standard static tests for concrete at early ages.

## CHAPTER 5 MEASURING ELASTIC CONSTANTS OF VERY-ERLY-AGE CONCRETE CUBES USING EBP

[Chapters 3](#) and [4](#) proposed the baseline-free EMI techniques to measure elastic constants (i.e.,  $E_c$  and  $\mu_c$ ) using concrete cubes and SBPs after demolding of specimens. However, SBP cannot work before the demolding of the specimen. In this chapter, the baseline-free EMI technique is further extended to monitor the evolution of concrete at very early ages (i.e., the first 24 hours) using standard concrete cubes. In this stage, no effective NDT methods can continuously assess the elastic constants of the concrete because of the difficulties in implementation of sensors, the high  $\zeta_c$  of materials, and dramatic changes in  $\mu_c$ .

To tackle the implementation challenges, EBP is adopted in this chapter to ensure that the monitoring can start immediately after the casting, as mentioned in [Chapters 1](#) and [2](#). To solve the difficulties induced by the high  $\zeta_c$  and dramatic changes in  $\mu_c$  in very-early-age concrete, vibration modes that are only directly related to the shear modulus and have strong responses are selected and studied. After designing the corresponding installation strategies and establishing the assessment methods, modifications regarding the imperfection in dimensions of specimens and unmatched properties between the EBP and host concrete material are developed.

Experiments show the effectiveness of the proposed method at very early ages of concrete. The assessment accuracy is validated by comparing it to the traditional resonance method after demolding. The assessment shows the proposed method can evaluate the elastic constants (i.e.,  $G_c$  and  $\mu_c$ ) of the concrete cubes as early as two hours after casting, providing a new tool to investigate the mechanical behavior of the concrete.

### 5.1 Introduction

Accelerated construction schedules, driven by the pursuit of economic gains, have resulted in tragic failures during construction due to inadequate knowledge of concrete

properties at early ages [Oluokun et al., 1990]. Meanwhile, the long-term performance of concrete structures is significantly influenced by the properties and behavior of concrete at curing stages [Nehdi and Soliman, 2011]. Therefore, acquiring the early-age properties of concrete is essential from a serviceability perspective [Mesbah, et al. 2002]. Compared with the traditional point-in-time destructive tests, NDT methods can provide continuous or regular measurement of concrete properties starting from an early age. For example,  $E_c$  or  $G_c$  can be used to estimate the compressive strength of concrete [Venkateela et al., 2013], which is helpful in determining the optimal demolding time.

The NDT methods measuring the early-age elastic properties of concrete in the existing literature are summarized in Table 5.1. The impact resonance (IR) and UPV methods using accelerometers and ultrasonic transducers, respectively, are commonly employed to measure the elastic constants of concrete, as reviewed in Section 2.2. The earliest time for applying the IR and UPV methods to measure the elastic constants is usually 5.0 and 6.5 hours after casting, respectively. However, the reliability of the UPV has not been rated by any standards [Komlos et al., 1996], and the IR method is recommended to obtain the dynamic elastic constants of concrete materials using concrete prisms or cylinders [ASTM C215, 2019]. Notably, IR methods in Table 5.1 had to be applied after demolding concrete specimens. Special measures were taken to remove molds as early as possible.

Based on the discussion, the prevailing NDT methods, especially dynamic resonance methods, struggle to measure the elastic properties of concrete at very-early ages. The major challenges are listed as follows: (a) from the experimental perspective, the resonance method cannot be conducted before demolding because accelerometers or other vibration sensors cannot be installed at the fluid status; (b) from the signal perspective, the damping ratio is large, which can be up to 15% [Dandapat et al., 2018], when concrete coverts from the fluid to the solid status, resulting in rapid signal attenuation and difficulties in mode identification; (c) from the evaluation perspective, dramatic changes of  $\mu_c$  occurred in the first several hours [Krauß and Hariri, 2006],

decreased from 0.5 to approximately 0.3, resulting in inaccurate evaluation results for the modulus of elasticity using the existing evaluation methods. For example, the ASTM C215 method assumed a fixed Poisson's ratio for the evaluation when using the fundamental transverse mode [Kolluru et al., 2000].

As reviewed in [Section 2.3.5.2](#), embedding PZT transducers into cementitious materials (e.g., concrete) has been investigated to continuously monitor the changes in material from hydration to the hardening stage in laboratories and on construction sites using EMI techniques. However, no research measures the elastic constants of concrete using the baseline-free EMI techniques at this stage. Baseline-dependent signal processing methods (i.e., statistical indices and changes of the 1<sup>st</sup> resonant mode of PZT sensor) were utilized to qualitatively assess the changes in concrete.

[Chapter 4](#) has presented a framework for  $E_c$  and  $\mu_c$  evaluations using standard concrete cubes and SBPs from 1-day age. The baseline-free EMI technique using SBPs struggles to directly extend to earlier ages of concrete because SBPs can only be installed after demolding, limiting its further applications to measure properties at a very-early age. Moreover, the dramatical changes of Poisson's ratio in very-early-age concrete increase the difficulties in selecting the modes adopted in [Chapter 3](#).

Based on the review above, the existing studies on measuring the elastic constants of concrete have the following gaps: (1) An effective NDT method that can measure the elastic constants of concrete specimens at very-early ages is still lacking, especially for the time before demolding; (2) EMI-R methods that do not rely on assumptions about Poisson's ratio are currently unavailable for use with embedded PZT transducers and standard concrete cubes. Accordingly, this chapter presents a novel EMI-R method for measuring the elastic properties of very-early-age concrete cubes (i.e., within 12 hours after casting) using EBP for the first time to address these research gaps.



Table 5.1 Summary of the NDT methods for measuring the elastic constants of concrete at early ages

Ref.	Method	Sensor type	Demolding	Starting hour	Constants	Concrete and specimen
Nagy [1997]	IR	ACC	Yes	5.0	$E_{cd}$	NC; Prism: 40×40×160 mm <sup>3</sup>
Lee et al. [1997]	IR	ACC	Yes	6.0	$E_{cd}$	HSC; Cylinder: 100 mm×200 mm
Mesbah et al. [2002]	UPV	UT	No	9.0	$E_{cd}$	HSC; Cylinder: 100 mm×200 mm
Krauß and Hariri [2006]	UPV	UT	No	6.5	$E_{cd}, \mu_{cd}$	HSC; Cylinder: 100 mm×200 mm
Venkiteela et al. [2013]	IR	ACC	No	12.0	$G_{cd}$	NC; Prism: 50×75×230 mm <sup>3</sup> 100×150×300 mm <sup>3</sup>
Ahmed [2018]	IR	ACC	No	7.0	$E_{cd}, \mu_{cd}, G_{cd}$	HSC; Prism: 160×100×800 mm <sup>3</sup>

Note: IR denotes the impact resonance method; UPV denotes the ultrasonic pulse velocity method; ACC refers to the accelerometer; UT refers to the ultrasonic transducer;  $E_{cd}$ ,  $\mu_{cd}$ , and  $G_{cd}$  denote dynamic modulus of elasticity, Poisson's ratio, and shear modulus, respectively; NC refers to normal concrete; HSC refers to high-strength concrete.

## 5.2 Vibration Modes Related to Shear Modulus

Previous research on cube-shaped solids has shown that some special modes (e.g., torsion mode) are independent of Poisson's ratio [Ekstein and Schiffman, 1956]. Smith and Kidger [1991] also presented that, in the first 60 vibration modes of an isotropic cube, 11 modes are independent of bulk modulus, but they all depend on shear modulus. The advantage of measuring  $G_c$  is that the dramatic changes of  $\mu_c$  at very-early ages of concrete would not result in difficulties in the accurate assessment. Meanwhile, researchers have exerted efforts to correlate the dynamic shear modulus to the compressive strength of normal concrete at early ages (i.e., from 12 to 72 hours after casting) [Venkateela et al., 2013], motivating the further extension to the very-early age (i.e., within 12 hours after casting).

Smith and Kidger [1991] named the first four vibration modes only related to shear modulus as torsion, contra-shear, star, and box, and the corresponding mode shapes are shown in Figure 5.1. The symmetric type of each mode should be analyzed in advance to facilitate the actuation and extraction of these modes. Nine symmetric planes of a cube, including three parallel symmetric planes (i.e., planes  $xoy$ ,  $xoz$ , and  $yoz$ ) and six diagonal symmetric planes (i.e., planes  $\gamma_1oz$ ,  $\eta_1oz$ ,  $\gamma_2oy$ ,  $\eta_2oy$ ,  $\gamma_3ox$ , and  $\eta_3ox$ ), are presented in Figure 4.1 for better discussion, where a parallel symmetric plane refers to a plane parallel to a pair of faces of the cube. The symmetric types of these four modes are summarized in Table 5.2. In the torsion mode, the deformations are anti-symmetric about all three parallel planes and symmetric about a pair of diagonal planes. In contra-shear mode, the deformation is symmetric about one parallel plane and a pair of diagonal planes. The deformation of the box mode is symmetric about all three parallel planes and a pair of diagonal planes. In star mode, the deformation is anti-symmetric about all three parallel planes and symmetric about all three pairs of diagonal planes.

The EBP generates planar forces inside a concrete cube. This feature implies that the sensor cannot actuate a highly anti-symmetric mode because the planar actuation forces themselves are symmetric about two planes. Therefore, torsion and star modes

are hardly actuated using a single EBP. By contrast, the highly symmetric modes are more easily obtained, indicating that the contra-shear and box modes are preferred. In the following part, these two modes are intentionally actuated for further evaluation.

Table 5.2 Symmetric type of the vibration modes only related to the shear modulus

Mode	Parallel planes			Diagonal planes					
	$xoy$	$xoz$	$yoz$	$\gamma_{10z}$	$\eta_{10z}$	$\gamma_{20y}$	$\eta_{20y}$	$\gamma_{30x}$	$\eta_{30x}$
Torsion	<i>AS</i>	<i>AS</i>	<i>AS</i>	<i>S</i>	<i>S</i>	<i>AS</i>	<i>AS</i>	<i>AS</i>	<i>AS</i>
Contra-shear	<i>AS</i>	<i>AS</i>	<i>S</i>	<i>S</i>	<i>S</i>	<i>AS</i>	<i>AS</i>	<i>AS</i>	<i>AS</i>
Box	<i>S</i>	<i>S</i>	<i>S</i>	<i>S</i>	<i>S</i>	<i>AS</i>	<i>AS</i>	<i>AS</i>	<i>AS</i>
Star	<i>AS</i>	<i>AS</i>	<i>AS</i>	<i>S</i>	<i>S</i>	<i>S</i>	<i>S</i>	<i>S</i>	<i>S</i>

*AS*: anti-symmetric plane; *S*: symmetric plane.

Moreover, isotropic materials have two independent elastic constants. Therefore, using two resonant frequencies are theoretically enough to directly determine the two elastic constants of isotropic concrete cubes [Li et al., 2012]. Given that the EMI techniques can capture many modes more easily than traditional resonance methods, one more mode can be selected to derive the other elastic constants (i.e.,  $\mu_c$  or  $E_c$ ).

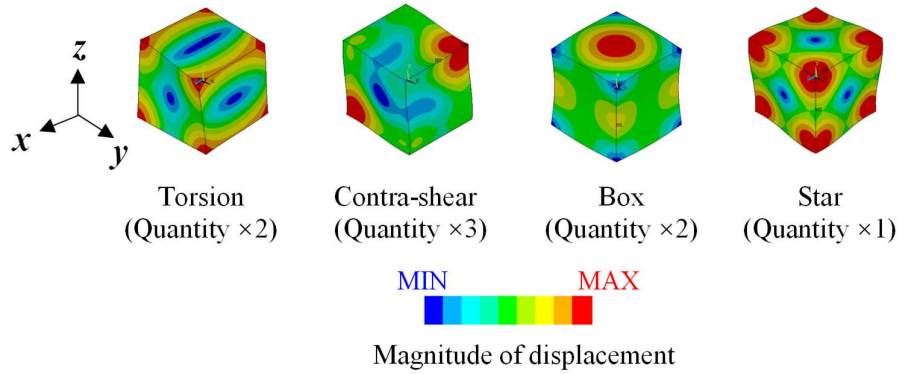


Figure 5.1 Vibration modes only related to the shear modulus

## 5.3 EBP Design and Installation Strategies

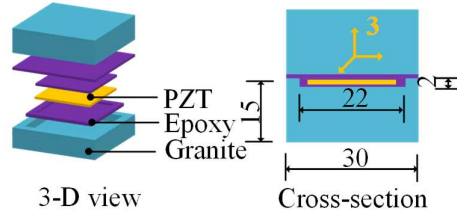
### 5.3.1 EBP Configuration

Based on the discussion above, the sensors are preferred to be embedded at the center of the cube so that high-symmetric actuation can be achieved and very-early-age concrete properties can be captured. Figure 5.2(a) presents the detailed configuration of the embedded package, consisting of a PZT patch, packaging layers, and adhesive

layers. A PZT patch in  $20 \times 20 \times 1.0 \text{ mm}^3$  is selected, polarized along the thickness (i.e., 3-axis shown in yellow). This size of the PZT patch is well-commercialized and can provide high sensitivity in resonant frequency range of a cube, as shown in [Chapter 3](#). The PZT patches with wrapping electrode (i.e., the electrode of the bottom surface is wrapped to the top surface) are selected to ensure the flatness of the bonding interface because unexpected rotations would increase the difficulties in analyses. The PZT properties are provided by the suppliers and listed in [Table 3.1](#). The PZT patch is encapsulated in the center of the package to ensure installation accuracy. The entire package is in a cubic shape with a 30-mm width. A pair of granite blocks are selected as the protection packaging layers. One of the granite blocks is cut with a groove in advance to accommodate the PZT patch. The epoxy is used to bond each part into a whole. The properties of the granite and epoxy are provided by the suppliers and listed in [Table 5.3](#).

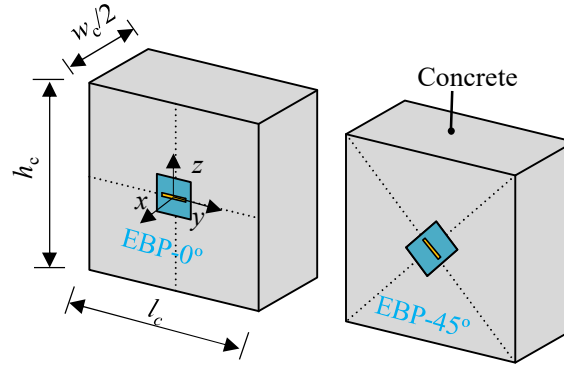
Table 5.3 Material properties of epoxy and concrete for simulation

Material	Parameters	Unit	Values
Epoxy	Density, $\rho_e$	kg/m <sup>3</sup>	1600
	Modulus of elasticity, $E_e$	GPa	4
	Poisson's ratio, $\mu_e$	-	0.38
	Damping ratio, $\zeta_e$	-	0.012
Granite	Density, $\rho_g$	kg/m <sup>3</sup>	2710
	Modulus of elasticity, $E_g$	GPa	57
	Poisson's ratio, $\mu_g$	-	0.30
	Damping ratio, $\zeta_g$	-	0.008
Concrete	Density, $\rho_c$	kg/m <sup>3</sup>	2300
	Modulus of elasticity, $E_c$	GPa	20
	Poisson's ratio, $\mu_c$	-	0.25
	Damping ratio, $\zeta_c$	-	0.02



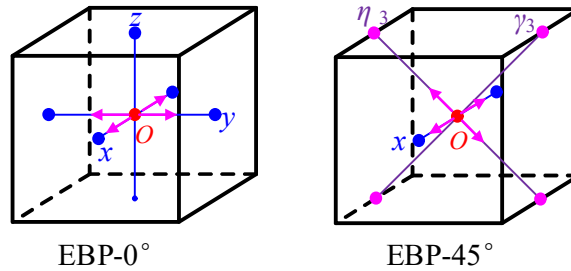
Whole structure of the embedded package: Unit (mm)

(a) Details of the embedded package



Presented in half models

(b) Proposed sensor installation strategies (presented in half model)



(c) Actuation mechanisms (planar forces are colored in pink)

Figure 5.2 Proposed sensor installation strategy and their actuation mechanism

### 5.3.2 Installation Strategies

Figure 5.2(b) shows two types of placement locations and orientations of the PZT patch using a half model of a cube. These two installation strategies are labeled as EBP-0° and EBP-45°. Here, EBP refers to the embedded PZT sensor, while 0° and 45° denote that the angles between the orientation of the PZT patch and the plane  $xoy$  is 0 and 45 degrees, respectively.

Figure 5.2(c) shows the corresponding actuation mechanisms. In the case of EBP-

0°, the planar forces generated by the PZT patch are along the plane  $xoy$ , resulting in five symmetric planes (i.e., planes  $xoy$ ,  $xoz$ ,  $yoz$ ,  $\gamma_{10z}$ , and  $\eta_{10z}$ ) in the tested concrete cube, including three parallel planes and one pair of the diagonal planes. Meanwhile, in the case of EBP-45°, the planar forces vibrate along the plane  $xo\eta_3$ , which means that three symmetric planes (i.e., planes  $xo\eta_3$ ,  $xo\gamma_3$ , and  $yoz$ ) are in the tested concrete cube, including one parallel plane and one pair of the diagonal planes. EBP-0° and EBP-45° strategies are designed for actuating the box and contra-shear modes, respectively.

## 5.4 Numerical Investigations of the Proposed EMI-R Methods

A series of numerical investigations were presented in this section to illustrate the feasibility and effectiveness of the proposed method and establish its framework to evaluate the elastic constants of concrete cubes using the proposed EMI-R methods.

### 5.4.1 Numerical Modeling of Concrete Cubes with EBPs

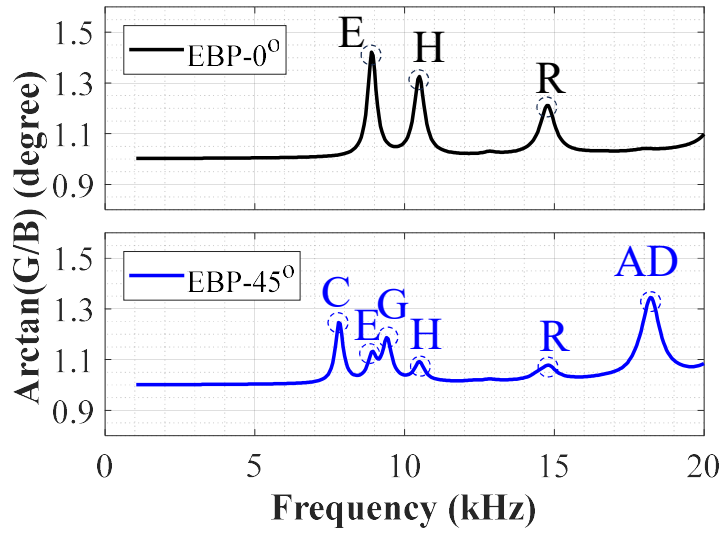
ANSYS is used in this chapter for multi-physics harmonic analysis to compute electromechanical behavior in the electromechanical coupled field. A standard concrete cube (150 mm in width) is modeled as the host specimen for the simulation because it is widely used in the standardized concrete-related tests (e.g., compressive strength) in many European and Asian countries [Narayanan, 2024]. The mechanical and piezoelectric properties of the PZT materials used in the simulation are listed in Table 3.1. The properties of the coating layer and the epoxy are listed in Table 5.3. All the properties are provided by the suppliers.

In terms of the element type, Solid5, a coupled field solid element with eight nodes, is used to model the PZT patch, while Solid45 is selected for adhesive, granite, and concrete materials. The interfaces between any two materials are assumed to be fully bonded. Within a wide frequency band of 1–20 kHz (step size: 0.05 kHz), the PZT patch was excited by a sinusoidal voltage of 1 V in the polarization directions (between the top and the bottom surfaces) to obtain the EMI signatures. In terms of the mesh size, 0.25 mm is selected for the elements of PZT and epoxy, satisfying the relationship between the element size and the minimum wavelength of incident waves in a

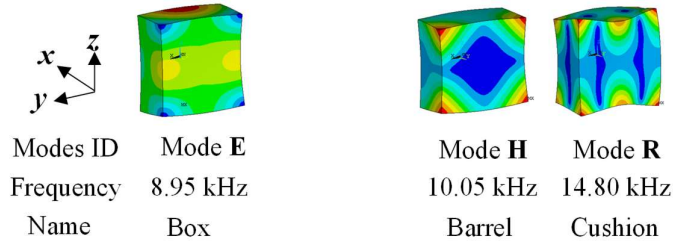
frequency as high as 20 kHz [Zhao et al., 2020]. After the trial convergence tests, 1 and 3 mm are used as the mesh sizes for the packaging and concrete materials, respectively. The geometric information of the numerical model is the same as those shown in Figures 5.2(a) and 5.2(b). The complementary angle of the phase, i.e.,  $\arctan(G/B)$ , is used to present the signal spectrum, which has been proven effective in studying the signal changes, as shown in Chapter 3.

#### 5.4.2 Signal Spectra and Captured Vibration Modes

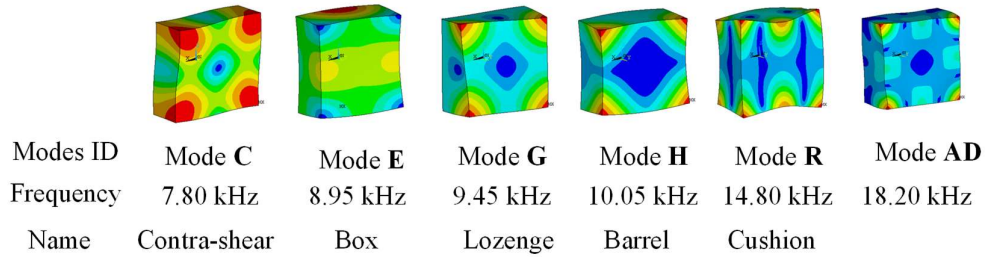
Before analyzing the signal spectra under a large damping ratio, the pattern of the signal spectra is presented under the low damping ratio in this subsection to compare the two adopted sensor installation strategies. Figure 5.3 presents the signal spectra from two different sensor installation strategies and the corresponding extracted vibration modes. The material properties of concrete are summarized in Table 5.3. In this case, a low damping ratio (i.e.,  $\zeta_c$  equals 0.02) is selected to show the peaks in the signal spectrum of each installation strategy. Figure 5.3(a) presents the signal spectra of the two adopted installation strategies, in which EBP-0° and EBP-45° have three and six peaks, respectively. The mode shapes of five extracted modes are plotted in Figure 5.3(b). The modes are labeled the same as those in Figure 4.2. Modes C, E, G, H and R are also named contra-shear, box, lozenge, barrel, and cushion, respectively, by Smith and Kidger [1991]. These two strategies share three modes (i.e., modes E, H, and R) in the signal spectra with different amplitudes. In particular, contra-shear and box modes in Figure 5.1 are captured, while torsion and star modes in Figure 5.1 are not.



(a) Signal spectra of the adopted two installation strategies



(i) Mode shapes from EBP-0°



(ii) Mode shapes from EBP-45°

(b) Vibration modes

Figure 5.3 Recorded EMI signals and the corresponding vibration modes

The numbers of the symmetric planes of the two actuation strategies cause a difference in the identified mode numbers. In general, the identified mode numbers would decrease with increases in the symmetric planes [Evensen, 1976]. The peaks are not uniformly distributed in the given frequency range. The first four peaks (i.e., modes



C, E, G, and H) of EBP-45° are close to each other. Meanwhile, the peaks in EBP-0° are sparser because the modes C and G are not captured. In terms of the amplitudes of the common modes (i.e., modes E, H and R), EBP-0° can present larger amplitudes than EBP-45°. For example, mode H has relative amplitudes of 0.31 and 0.05 degrees from EBP-0° and EBP-45°, respectively.

### 5.4.3 Effect of Damping Ratio and Corresponding Signal Processing

The modulus of elasticity increased within the curing age of concrete. However,  $\zeta_c$  is also dramatically changed at a very-early age and has not been discussed yet. Damping ratios are very high at the early age of concrete, especially in the fluid status. As discussed in [Section 5.1](#), the damping ratio can be up to 15% when concrete converts from the fluid to the solid status [[Dandapat et al., 2018](#)]. Thereafter,  $\zeta_c$  decreases as the curing time increases. [Xi et al. \[2021\]](#) showed that  $\zeta_c$  of the concrete specimens at 28-day curing age ranged from 2.3% to 3.3%. For concrete specimens in laboratories, such as manufactured cubes,  $\zeta_c$  ranged from 0.8% to 2.1% [[Ai et al., 2020b](#)]. The changes in the damping ratio may significantly affect the signal spectra, resulting in difficulties in mode identifications. Therefore, the effect of the damping ratio must be carefully discussed with the evolution of concrete.

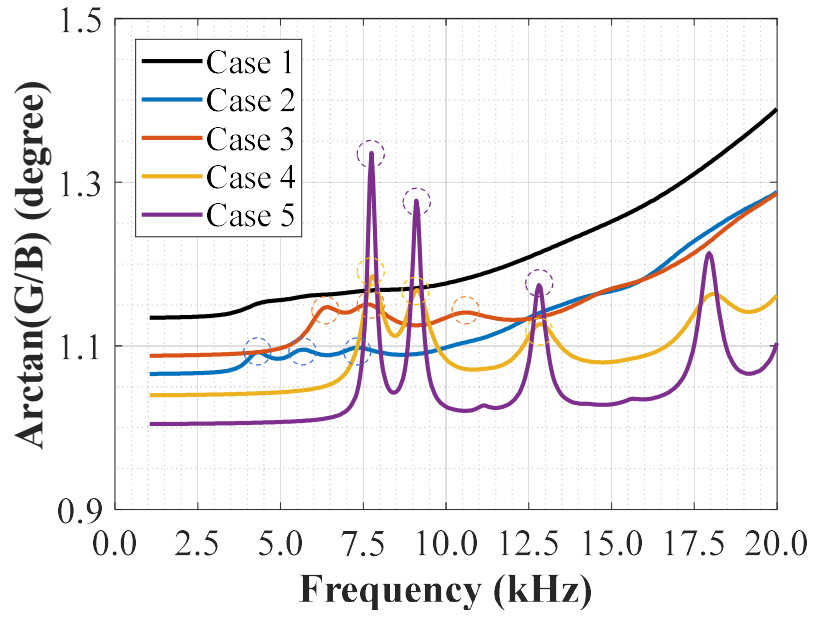
[Table 5.4](#) presents the five different cases for simulating early-age concrete, considering different  $E_c$ ,  $\mu_c$ , and  $\zeta_c$ . The material properties are assumed to be isotropic and homogeneous. The values in these cases are selected to simulate the evolution of the hardening stage of the concrete. Consequently,  $E_c$  increases from 5 GPa to 15 GPa with increases in the case number.  $\mu_c$  and  $\zeta_c$  decrease from 0.45 to 0.25 and from 20% to 2% with increases in the case number, respectively. The frequency range studied here also ranges from 1 kHz to 20 kHz. The  $\zeta_c$  equal 20% and 10% are considered as high and middle damping levels, respectively, according to the value of  $\zeta_c$  (i.e., 15%) reported by [Dandapat et al. \[2018\]](#). By contrast, the damping ratios equal 5%, and 2% are considered low damping levels. The difference between Case 1 and Case 2 is the damping ratio. The differences between Case 2 and Case 3 are elastic constants. The

material properties of Case 4 and Case 5 are close to the status of a 12-hour age in Venkiteela et al. [2013].

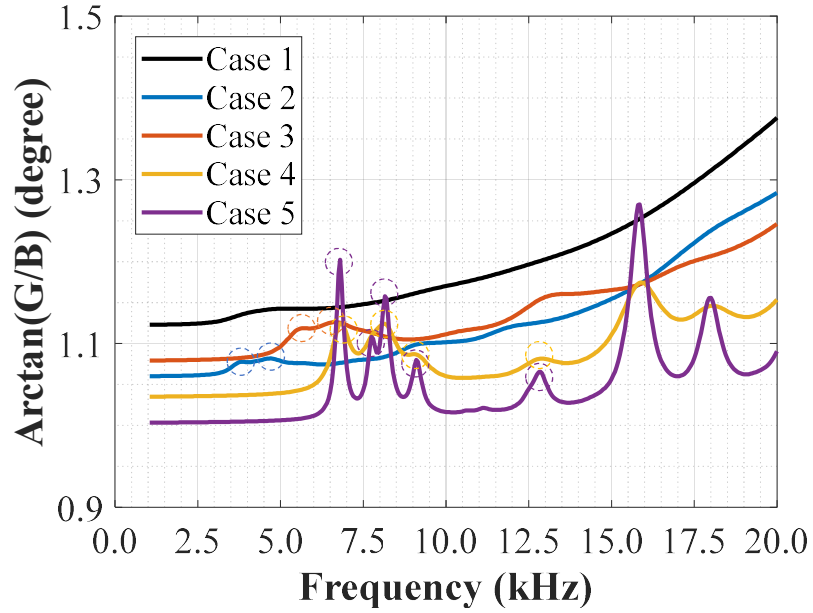
Table 5.4 Details of the different cases for simulating evolutions of concrete at early ages

Case no.	$E_c$ (GPa)	$\rho_c$ (kg/m <sup>3</sup> )	$\mu_c$	$\xi_c$ (%)	Damping level
Case 1	5	2300	0.45	20	High
Case 2	5	2300	0.45	10	Middle
Case 3	10	2300	0.30	10	Middle
Case 4	15	2300	0.25	5	Low
Case 5	15	2300	0.25	2	Low

Figure 5.4 shows the simulated signal spectra with the evolution of the concrete properties at an early age. Figure 5.4(a) presents the simulated behaviors for EBP-0°. At a high damping level (i.e., Case 1), the signal spectrum is quite smooth, and the peaks can hardly be identified. After  $\xi_c$  is reduced to 10% (i.e., Case 2), three peaks can be identified in the frequency range of 3.5–7.5 kHz. However, the amplitudes of these three peaks are still low. In contrast with Case 2, the three peaks moved rightward to the frequency range of 6.5–11.0 kHz in Case 3. However, no evident improvements are observed in the mode identification. In Case 4, the peaks move rightward. The peaks in the signal spectra are more distinct compared with those in Case 2, enabling easy mode identification, which is mainly attributed to the reduction of the damping ratio. The peak amplitude significantly increases with the reduction of the damping ratio to only 2% in Case 5. Meanwhile, some small peaks can be found in the signal spectra. The two peaks in Case 5 correspond to modes E and H, which are helpful in further evaluations. Besides the changes in the peaks, the signal trend line also changes with the material properties of the concrete, especially the damping ratio of concrete. Overall, the signal trend line would move downward with decreases in the damping ratio. When the damping ratio is the same (i.e., Cases 2 and 3), the trend line at the low-frequency range (1–13 kHz) is also affected by the elastic constants of concrete. However, the two trend lines become close at a higher frequency range.



(a) EBP-0°



(b) EBP-45°

Figure 5.4 Simulated behaviors of the signal spectra with concrete hardening

Similar behaviors can be found for EBP-45° (Figure 5.4(b)). From the perspective of the mode identification, at a high damping level (i.e., Case 1), the peaks cannot be found in the signal spectrum. With a reduction of  $\zeta_c$  in Case 2, two peaks can be found in the frequency range of 3.5 to 5.0 kHz. In Case 3, the peaks move rightward compared with Case 2 because of the increases in  $E_c$ . In Cases 4 and 5, the peaks are easier to be

identified. Two identifiable modes at the middle and high damping levels are modes C and G, respectively. The trend lines show the same behaviors as EBP-0°.

Based on the discussion regarding Figure 5.4, direct identification of the modes from the signal spectrum at a very-early age is challenging, potentially hindering the application of the EMI-R methods. Therefore, a signal processing method for extracting the target modes in the middle and high damping levels is introduced here to overcome the abovementioned difficulties. Given that the peaks are superimposed on the signal trend line, the signal spectrum is detrended firstly in the given frequency to remove a second-degree polynomial trend in the target spectrum. Relative arctan ( $G/B$ ) is used to present the spectrum after detrending. Afterward, the processed signal spectrum (i.e., from 1 kHz) is smoothed using a 250-Hz moving average filter to improve the signal-to-noise ratio in practice. Figure 5.5 shows the signal spectra after detrending processing. Although the peaks still cannot be identified at a high damping level (i.e., Case 1), the corresponding peaks become clearer and easier to extract at the middle damping level (i.e., Case 2). The first three peaks are clearly captured in Case 2 of EBP-0° (Figure 5.5(a)). The peaks of Case 3 are also easier to identify and extract. Similarly, the amplitudes of the peaks become more distinct after detrending in EBP-45° (Figure 5.5(b)). It can be found that at the middle damping level (i.e., Cases 2 and 3), the captured peaks in EBP-0° are modes E and H, while those in EBP-45° are modes C and G, respectively. EBP-45° can show clear peaks representing modes E and H only when the damping level is low (i.e., Case 4). Moreover, the relative amplitudes of modes E and H in EBP-0° are larger than those in EBP-45° in Case 4, indicating that EBP-0° is more suitable for extracting modes E and H.

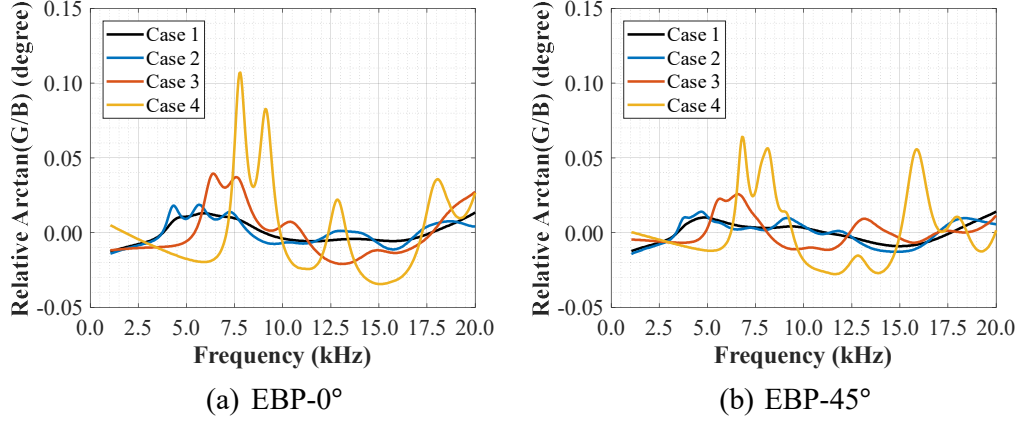


Figure 5.5 Signal spectra after detrending processing

#### 5.4.4 Determination of Elastic Properties

After extracting the target modes from the processed signal spectra, the correlations between the elastic properties of concrete and the modal frequencies must be established. Analytical equations for vibration modes of a cube at a free-free status are rarely available, except for torsion and Mindlin-Lamé modes (i.e., the box mode or mode E) [Li et al., 2012],

$$f_{\text{torsion}} = \frac{\sqrt{2}}{\pi L_c} \sqrt{\frac{G_c}{\rho_c}}, \quad (5.1)$$

$$f_{\text{ml}} = \frac{1}{2L_c} \sqrt{\frac{E_c}{(1 + \mu_c)\rho_c}} = \frac{1}{\sqrt{2}L_c} \sqrt{\frac{G_c}{\rho_c}}, \quad (5.2)$$

where  $f_{\text{torsion}}$  and  $f_{\text{ml}}$  are the frequencies of the torsional and Mindlin-Lamé modes, respectively;  $L_c$  is the edge length of the cube; and  $G_c$  refers to the shear modulus. These two equations are derived from the isotropic and homogenous cases. However, as explained in Section 5.2, torsion modes cannot be actuated because of the actuation symmetric type of EBP. In contrast, the Mindlin-Lamé mode (i.e., mode E) can be actuated and observed in Figure 5.3.

Table 5.5 presents the variations of the target frequencies with changes in Poisson's ratio, dimension, and modulus of elasticity, where the frequencies are obtained from the modal analyses in the ANSYS. The element type of concrete and mesh size are the same as in Section 5.3.3.  $\mu_c$  changes from 0.20 to 0.45, covering the range of  $\mu_c$  at early ages

of concrete. Meanwhile, the frequencies of mode E were also calculated using Equation (5.2). The differences between the analytical equation and the numerical results for mode E are small enough, with a maximum difference of only 3 Hz. This mode E can be used as an important reference mode because its frequency is independent of  $\mu_c$  and can directly reflect  $G_c$ . Considering that  $\mu_c$  of concrete varies dramatically at a very-early age, this mode presents a great advantage in evaluating very-early-age elastic properties of concrete by avoiding the uncertainties in the estimated  $\mu_c$ . Subsequently, the frequency ratios between other modes and mode E can be used to quantify  $\mu_c$  [Li et al., 2012; Chen and Leon, 2019].

Table 5.5 Frequencies of the target modes regarding the variation of Poisson's ratio

$L_c$ (m)	$\rho_c$ (kg/m <sup>3</sup> )	$E_c$ (GPa)	$\mu_c$	Frequencies (Hz)					
				Eq. (5.2)	FEM				
					E	C	E	G	H
0.15	2300	10	0.45	5772	5096	5774	6460	7695	9987
			0.40	5874	5182	5876	6501	7617	10074
			0.35	5982	5273	5984	6540	7534	10169
			0.30	6096	5369	6097	6577	7447	10274
			0.25	6217	5470	6218	6614	7358	10388
			0.20	6345	5576	6346	6649	7270	10512
0.15	2300	30	0.45	9998	8826	10001	11189	13328	17299
			0.40	10174	8976	10177	11259	13194	17449
			0.35	10361	9133	10364	11327	13049	17614
			0.30	10559	9299	10561	11392	12898	17795
			0.25	10768	9474	10770	11456	12745	17993
			0.20	10990	9658	10992	11517	12593	18207
0.10	2300	5	0.45	6122	5408	6126	6854	8167	10603
			0.40	6231	5499	6234	6897	8083	10695
			0.35	6345	5596	6348	6938	7994	10796
			0.30	6466	5697	6469	6978	7901	10907
			0.25	6594	5804	6597	7017	7807	11028
			0.20	6730	5917	6733	7055	7713	11160

Figure 5.6 presents the normalized frequencies as a linear function of  $\mu_c$ , where various frequencies are normalized by the frequency of mode E. Notably, all the data points in Table 5.5 are shown in Figure 5.6, and many data points are with the same  $\mu_c$  overlapped with one another. The normalized frequencies of mode C are almost

independent of  $\mu_c$ , which is attributed to the shear transformation. Accordingly, the frequency of mode C can be directly expressed by multiplying Equation (5.2) by 0.88, as shown in Equation (5.3).

$$f_c = \frac{0.88}{\sqrt{2}L_c} \sqrt{\frac{G_c}{\rho_c}} \quad (5.3)$$

In the other three modes, the normalized frequencies of mode H have the largest slope, indicating that it is more sensitive to  $\mu_c$  and a good candidate for evaluating  $\mu_c$ . Meanwhile, modes G and R show similar slopes. All trends can be fitted using linear equations with high determination of coefficients (i.e.,  $R^2 > 0.98$ ), as shown in Figure 5.6.

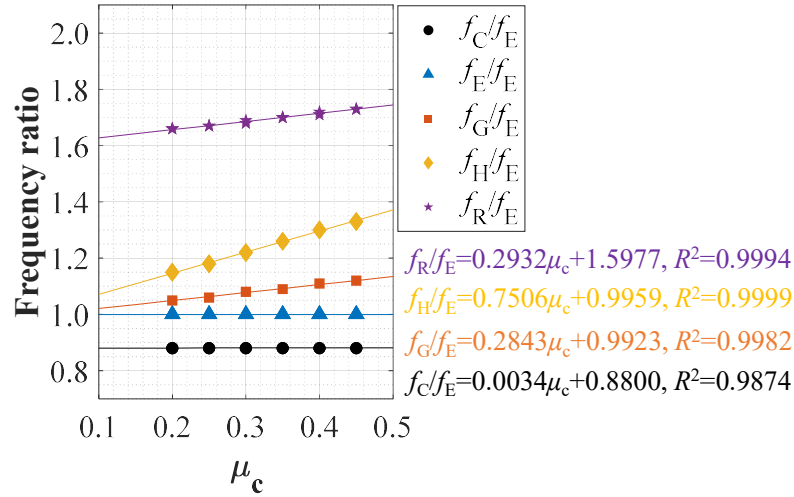


Figure 5.6 Normalized frequencies by mode E as a linear function of  $\mu_c$

Based on the discussion in this subsection,  $G_c$  can be directly determined using modes C and E for EBP-45° and EBP-0°, respectively. Thereafter,  $\mu_c$  can be obtained by using the frequency ratios and regression formulas shown in Figure 5.6. If necessary,  $E_c$  can be evaluated through  $E_c = 2G_c(1+\mu_c)$ .

In summary, this subsection presents the proposed evaluation procedure, in which at least two modes are used to evaluate both  $G_c$  and  $\mu_c$ . But the shear modulus can be determined alone as early as when only one peak is detected (i.e., mode E in EBP-0° or mode C in EBP-45° will appear first in the spectrum because of the large amplitude).

Meanwhile, at least two peaks (i.e., modes E and H are used for EBP-0°, and modes C and G are utilized for EBP-45°.) are needed to determine  $\mu_c$  of concrete materials. The measured  $G_c$  and  $\mu_c$  by EMI-R methods are denoted as  $G_{ce}$  and  $\mu_{ce}$ , respectively, to differentiate them from those measured by other methods.

## 5.5 Modification of the Proposed Methods

The general evaluation methods were established in the previous subsection. However, further discussions are needed to improve the evaluation accuracy by considering two influencing factors, including the effects of edge dimension imperfection and volumetric ratio of EBP.

### 5.5.1 Effect of Edge Dimension Imperfection

Usually, the molds for casting cubes have equal edges. However, the dimension along the cast direction, denoted as  $w_c$ , may have inevitable imperfections in practice. Accordingly, modification is needed to consider the effect of such imperfection in cube dimensions. The definition of the edge has been presented in [Figure 5.2\(b\)](#). The equivalent average length was utilized to discuss the effect [\[Ekstein and Chiffman, 2004\]](#), as shown in Equation (5.4).

$$L_{eq} = (l_c h_c w_c)^{\frac{1}{3}} \quad (5.4)$$

[Table 5.6](#) presents the frequency variations of the target modes with different cube imperfections. The imperfection on  $w_c$  is from -4.0% to 4.0%. Modes E and H are affected by imperfections in  $w_c$ , while mode C has little changes (where the maximum difference equals 3 Hz). Therefore, the measured  $G_{ce}$  and  $\mu_{ce}$  need modifications by considering the real dimension parameter (i.e.,  $w_c/L_{eq}$ ). The modified equations are presented from Equations (5.5–5.8), where  $G_{ce,mea}$  and  $G_{ce,mod}$  refer to the measured shear modulus before and after modification, respectively; and  $\mu_{ce,mea}$  and  $\mu_{ce,mod}$  denote the measured Poisson's ratio before and after modification, respectively. The superscripts EBP-0° and EBP-45° refer to the values evaluated for EBP-0° and EBP-45°, respectively. In general, the regression results (in terms of  $R^2$ ) for EBP-0° are better than those for EBP-45° for both  $G_c$  and  $\mu_{ce}$ .



$$\frac{G_{ce,mod}^{EBP-0^\circ}}{G_{ce,mea}^{EBP-0^\circ}} = 0.9334 \frac{w_c}{L_{eq}} + 0.0666, R^2 = 0.9982 \quad (5.5)$$

$$\frac{\mu_{ce,mod}^{EBP-0^\circ}}{\mu_{ce,mea}^{EBP-0^\circ}} = -3.6072 \frac{w_c}{L_{eq}} + 4.6086, R^2 = 0.9291 \quad (5.6)$$

$$\frac{G_{ce,mod}^{EBP-45^\circ}}{G_{ce,mea}^{EBP-45^\circ}} = -0.9567 \frac{w_c}{L_{eq}} + 1.9551, R^2 = 0.9679 \quad (5.7)$$

$$\frac{\mu_{ce,mod}^{EBP-45^\circ}}{\mu_{ce,mea}^{EBP-45^\circ}} = 252.05 \left( \frac{w_c}{L_{eq}} \right)^2 - 486.92 \frac{w_c}{L_{eq}} + 235.87, R^2 = 0.8676 \quad (5.8)$$

Table 5.6 Frequency of the target modes with cube imperfection

Material properties	$l_c$ (mm)	$h_c$ (mm)	$w_c$ (mm)	Frequency (Hz)			
				C	E	G	H
$E_c=10$ GPa, $\mu_c=0.3$ , $\rho_c=2300$ kg/m <sup>3</sup>	150	150	144	5371	6256	6792	7518
			147	5370	6176	6681	7480
			150	5369	6097	6577	7447
			153	5367	6019	6479	7416
			156	5366	5942	6386	7390
$E_c=10$ GPa, $\mu_c=0.3$ , $\rho_c=2300$ kg/m <sup>3</sup>	100	100	96	8061	9386	10191	11282
			98	8059	9267	10025	11224
			100	8057	9149	9869	11174
			102	8055	9031	9721	11129
			104	8052	8914	9582	11089
$E_c=5$ GPa, $\mu_c=0.45$ , $\rho_c=2300$ kg/m <sup>3</sup>	150	150	144	3606	4190	4716	5501
			147	3605	4136	4640	5470
			150	3603	4083	4568	5441
			153	3602	4030	4500	5415
			156	3600	3979	4436	5392
$E_c=30$ GPa, $\mu_c=0.2$ , $\rho_c=2300$ kg/m <sup>3</sup>	150	150	144	9661	11272	11891	12707
			147	9659	11133	11698	12645
			150	9658	10992	11517	12593
			153	9656	10850	11345	12548
			156	9654	10707	11184	12511

### 5.5.2 Modification for inclusion of EBP

Because of the contrast in material properties between the concrete and packaging material, embedding sensors inside concrete introduces a certain level of inhomogeneity to concrete cubes. The package size of an EBP cannot be too small

because the large PZT patch is preferred to ensure high sensitivity, especially in scenarios with a high damping ratio. In addition, a large package size helps position sensors at the target locations. In this chapter, the package of the EBP is 30 mm in width, slightly larger than the aggregate size (i.e., 20 mm) used for building structures. The whole package has stable material properties, whereas dramatic changes occur in concrete at an early age. Consequently, an unignorable volume ratio effect due to unmatched material properties must lead to evaluation errors without modifications. The volumetric ratio  $R_{vol}$ , and velocity ratio  $R_{vel}$  are used to discuss the effect of the embedded package,

$$R_{vol} = \frac{V_{EP}}{V_{cube}} \times 100\%, \quad (5.9)$$

$$R_{vel} = \sqrt{\frac{G_{ce,mea}}{\rho_c}} / \sqrt{\frac{G_{EP}}{\rho_{EP}}} \quad (5.10)$$

where  $V_{EP}$  and  $V_{cube}$  are the volumes of the embedded package and the concrete cube, respectively; and  $G_{EP}$  and  $\rho_{EP}$  are the shear modulus and density of the packaging layer, respectively. [Table 5.7](#) summarizes the effect of the embedded package on the frequencies of the target modes. Four volumetric ratios (0.1%, 0.8%, 2.7%, and 6.4%) and four different material properties, are simulated as the packaging layers. Although granite is used as the packaging material in this chapter, a wider range of the modulus of elasticity is simulated to make the conclusions more general. The concrete cube is 150 mm in width, indicating that the four volumetric ratios for the embedded sensors representing the width of embedded packing are 15, 30, 45, and 60 mm, respectively. The numerical model used in this subsection is the same as the EBP-0° in [Figure 5.2](#). Here, only package materials and concrete were included to simplify the model. The material properties of the concrete are the same as those in Case 3, as shown in [Table 5.4](#). Given that the volumetric ratio of the PZT patch ( $20 \times 20 \times 1.0 \text{ mm}^3$ ) inside EBP is only 0.01% in the numerical model and has an equal size as the normal aggregate, it was not considered in the analyses in this subsection. The unmatched properties between the packaging and the concrete materials have an increased influence with the

increases in the volumetric ratio, resulting in underestimation or overestimation of the shear modulus. For example, when  $E_{EP}$  and  $R_{vol}$  equal 57 GPa and 2.7%, respectively, the measured shear moduli from EBP-45° and EBP-0° in Case 3 are 10% and 13.5% larger than the actual values. With regard to the errors in evaluating Poisson's ratio, the unmatched properties also affect the measured values, which can introduce errors of up to 50%. Therefore, the modifications of the shear modulus and Poisson's ratio are important for evaluations, and the regression equations for the modifications are presented in Equations (5.11–5.14). The fitting results of these four equations show good determination of the coefficients ( $R^2 > 0.8175$ ).

$$\frac{G_{ce,raw}^{EBP-0^\circ}}{G_{ce,mea}^{EBP-0^\circ}} = 0.9959 - 8.049R_{vol} + 0.002684R_{vel} + 26.5R_{vol}^2 + 6.132R_{vol}R_{vel}, R^2 = 0.9860 \quad (5.11)$$

$$\frac{\mu_{ce,raw}^{EBP-0^\circ}}{\mu_{ce,mea}^{EBP-0^\circ}} = 1.0012 + 6.221R_{vol} - 0.02679R_{vel} - 149.9R_{vol}^2 + 1.056R_{vol}R_{vel} + 0.0104R_{vel}^2 + 910.8R_{vol}^3 + 34.04R_{vol}^2R_{vel} - 3.608R_{vol}R_{vel}^2, R^2 = 0.8976 \quad (5.12)$$

$$\frac{G_{ce,raw}^{EBP-45^\circ}}{G_{ce,mea}^{EBP-45^\circ}} = 0.9949 - 5.995R_{vol} + 0.003385R_{vel} + 15.94R_{vol}^2 + 4.701R_{vol}R_{vel}, R^2 = 0.9896 \quad (5.13)$$

$$\frac{\mu_{ce,raw}^{EBP-45^\circ}}{\mu_{ce,mea}^{EBP-45^\circ}} = 1.052 + 7.859R_{vol} - 0.1013R_{vel} - 225R_{vol}^2 + 5.546R_{vol}R_{vel} + 0.0336R_{vel}^2 + 673.4R_{vol}^3 + 102R_{vol}^2R_{vel} - 7.205R_{vol}R_{vel}^2, R^2 = 0.8175 \quad (5.14)$$

Table 5.7 Combinations in simulations for considering the package of the EBP

Values of $G_{EP}$	$\rho_{EP}$	Values of $G_c$	$\rho_c$	$R_{vol}$	Range of $R_{vel}$
1.92 GPa;	2710 kg/m <sup>3</sup>	0.86 GPa;	2300 kg/m <sup>3</sup>	0.0%;	From 0.195 to 2.760
11.54 GPa;		1.72 GPa;		0.1%;	
21.92 GPa;		2.78 GPa;		0.8%;	
26.92 GPa;		3.85 GPa;		2.7%;	
		4.81 GPa;		6.4%;	
		5.88 GPa;			
		8.00 GPa;			
		10.41 GPa;			
		12.50 GPa;			

Note: A total of 180 combinations are simulated.  $E_{EP}$  is from 5 GPa to 70 GPa, and  $\mu_{EP}$  is equal to 0.30;  $E_c$  is from 2.5 GPa to 30 GPa, and  $\mu_c$  is from 0.20 to 0.45.

In summary, this section presents the modifications of the evaluation results to extend the proposed strategies to more general application scenarios. The measured elastic constants can be modified using the obtained equations to reduce errors. In actual practice, these two factors (i.e., edge dimension imperfection and unmatched material properties) may appear simultaneously. Accordingly, the effect of the edge dimension imperfections is recommended to be modified first, followed by those of the unmatched properties between the concrete and the package of the EBP. According to the regression results of each strategy, EBP-0° shows better  $R^2$  than EBP-45° in evaluating Poisson's ratio, while both strategies show good regression results in evaluating shear modulus.

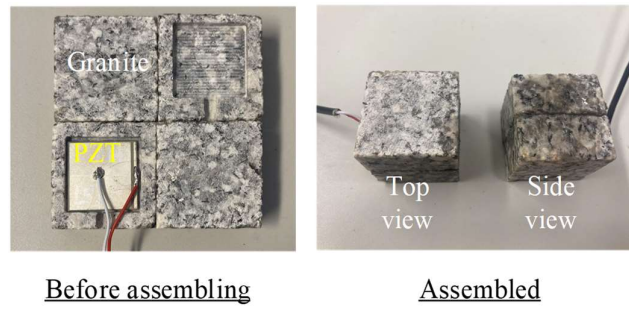
## 5.6 Experimental Validations

This section presents the experimental validations of the proposed framework. The early age refers to the first few hours or days after casting and is characterized by two main processes: setting (progressive loss of fluidity) and hardening (gaining strength). However, the early-age period of concrete lacks a universally accepted definition [Nehdi and Soliman, 2011]. In this section, the concrete properties within 48 hours and 10 hours were investigated as follows: (1) Two sizes of concrete cubes installed with the EBP were tested in the first 48 hours using the proposed EMI-R technique; thereafter, they were compared with the traditional dynamic and static testing methods to demonstrate the effectiveness of the proposed technique; (2) Continuous monitoring

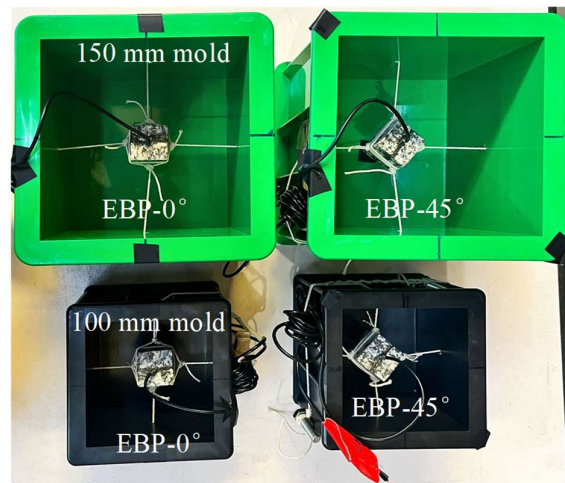
was performed using the two proposed installation strategies to observe the evolution of the elastic constants in the first 10 hours after casting.

### 5.6.1 Experimental Preparation and Setup

The configuration of EBP is described in [Section 5.3.1](#). [Figure 5.7\(a\)](#) shows the details of the sensor fabrication. Three steps are required to finish the fabrication. First, the welded PZT patch was bonded to the granite block ( $30 \times 30 \times 15 \text{ mm}^3$ ) with a groove (groove dimensions:  $22 \times 22 \times 2 \text{ mm}^3$ ) through epoxy (Araldite 2014-1) with a thickness of approximately 0.25 mm. Thereafter, the block with the PZT patch is sealed with epoxy. Afterward, the sealed block and an intact granite block ( $30 \times 30 \times 15 \text{ mm}^3$ ) are assembled using a 0.25 mm thick epoxy. After assembling the whole package, an additional two days are required to allow the hardening of the epoxy and obtain stable signals.



(a) Fabrication of the sensor



(b) Installation of the embedded sensor

Figure 5.7 Details of the sensor fabrication and installation

After the assembly, the sensors were placed at the center of the mold in different

placement orientations ([Figure 5.7\(b\)](#)). The molds were made of plastic and pre-drilled with four holes (2 mm in diameter) at the center of the four side faces. Four pieces of rope (1 mm in diameter) were secured with joints around the assembled sensor. Thereafter, tension was applied to the ropes to ensure that the sensor could be stably suspended in the center of the molds and placed in the desired orientations (i.e.,  $0^\circ$  and  $45^\circ$ ). Two sizes of molds (100 mm and 150 mm in widths) were utilized to validate the effectiveness of the proposed methods. The plastic molds were brushed with oils in advance to reduce friction on the interfaces that may provide certain constraints to the concrete cubes.

The mix proportions of the concrete are listed in [Table 4.8](#). Three batches of concrete were cast with the same mix proportions for two different objectives: (a) the first batch (i.e., Batch I) was used to validate the effectiveness of the proposed method; (b) the other two batches (i.e., Batches II and III) were used to monitor the concrete properties continuously. [Table 5.8](#) summarizes the types and numbers of the specimens used in this section. The specimens were named by Installation Strategy-Batch No.-Length. For example, EBP- $0^\circ$ -I-L100 indicates that the sensor was installed according to EBP- $0^\circ$ , and the specimen was cast in Batch I and had a size of 100 mm.

In the first batch, two 150 mm cubes and two 100 mm cubes were prepared for the EMI-R techniques. Two of these cubes were installed with EBP- $0^\circ$ , and the other two cubes were installed with EBP- $45^\circ$ . These cubes were tested at 5-hour, 7-hour, 9-hour, 24-hour, 48-hour, and 672-hour (i.e., 28-day) curing ages using the proposed EMI-R techniques. In addition, two large prisms (i.e.,  $150 \times 150 \times 300 \text{ mm}^3$ ) and two small prisms (i.e.,  $100 \times 100 \times 300 \text{ mm}^3$ ) were prepared for the standard dynamic resonance tests according to [ASTM C215 \[2019\]](#) and tested at 1-day, 2-day and 28-day curing ages. The shear modulus and Poisson's ratio measured by the standard dynamic resonance tests are denoted  $G_{cd}$  and  $\mu_{cd}$ , respectively. Moreover, six standard cylinders (i.e., with a diameter of 150 mm and height of 300 mm) were prepared for the standard static destructive tests according to [ASTM C469/C469M \[2022\]](#) at 2-day and 28-day

curing ages. The shear modulus and Poisson's ratio measured by the standard static tests are denoted  $G_{cs}$  and  $\mu_{cs}$ , respectively.

In the second and third batches, each batch included one 150 mm cube and three standard cylinders, where the former was used for continuous monitoring using the EMI-R techniques and the latter were used for standard static destructive tests at 28-day ages.

Table 5.8 Summary of the type and numbers of the specimens in this chapter

Batch	EMI-R tests				Dynamic resonance tests		Static destructive tests
	150 mm cube		100 mm cube		Prism		Cylinder
					Small	Large	
	EBP-0°	EBP-45°	EBP-0°	EBP-45°	-	-	
I	1	1	1	1	2	2	6
II	1	-	-	-	-	-	3
III	-	1	-	-	-	-	3
Total	2	2	1	1	2	2	12

Figure 5.8 shows the measurement setup in the EMI-R test. The EMI signal measuring system consisted of an LCR meter (Keysight E4980AL) and a laptop for recording. The EMI signatures were obtained by applying a voltage of 1 V across the terminals of the embedded sensor over a frequency range of 2–50 kHz at 0.05 kHz intervals. The room temperature for measurement was around 20 °C. The concrete cube specimens were tested in the mold directly before demolding. The demolding times of the specimens were 24, 15, and 10 hours after casting for Batches I, II, and III, respectively. Given that changes in early-age curing are dramatic, frequent measurements must be conducted during the first 24 hours of the curing process. Therefore, continuous monitoring was conducted for Batches II and III. The specimens were placed on a wooden table for measurements after demolding, which can be regarded as the free–free boundary conditions.

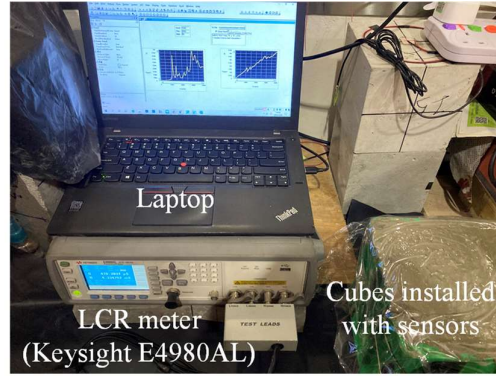


Figure 5.8 Test setup for the concrete monitoring

Figure 5.9 presents the experimental test setup for the standard dynamic resonance and static destructive tests. The test setup for dynamic resonance testing was prepared in accordance with ASTM C215 [2019], which included one laptop, one compact data acquisition system (NI-9230) with a maximum sampling rate of 12.8 kS/s, and a high-fidelity triaxial accelerometer (PCB 356b18) (Figure 5.9(a)). As previously mentioned, this type of testing can only be applied after demolding the specimen (i.e., 1-day age in this chapter). The frequencies of the first bending and torsional modes were obtained to calculate the corresponding material properties of concrete. The details of the specimens and testing results are summarized in Table 5.9, while the evaluation results are summarized in Table 5.10. The evaluation process followed that of Chen and Leon [2019], which can directly obtain the Poisson's ratio without iteration, ensuring a more reasonable evaluation of the results from the ASTM C215 method.

Standard static tests were conducted at a 340-ton uniaxial compression test machine (Figure 5.9(b)). Two transverse and two vertical strain gauges were installed to measure the deformation of the standard cylinders. The room temperature for the dynamic and static measurements was around 20 °C. Table 5.11 presents the modulus and strength obtained by standard static destructive tests [ASTM C469/C469M, 2022]. In each batch, three standard concrete cylinders were tested for the properties. The details of each cylinder are summarized in Table 5.12.



Table 5.9 Summary of test information of the standard dynamic tests

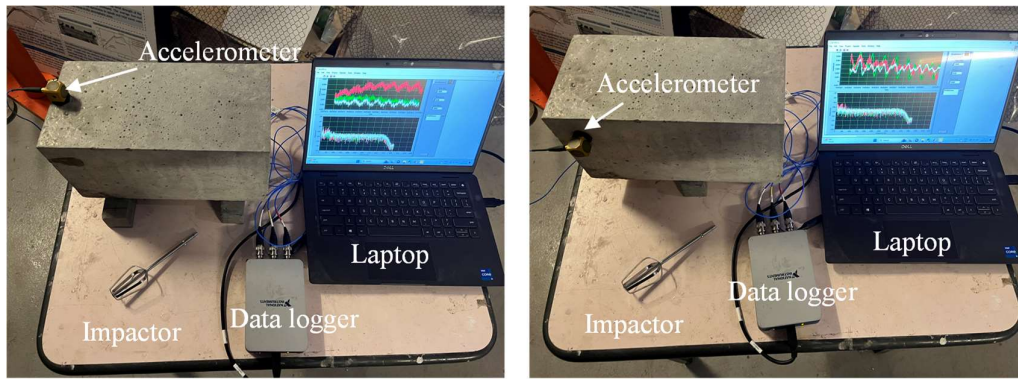
ID	$h_p$ (mm)	$w_p$ (mm)	$l_p$ (mm)	Mass (g)	Age (day)	1-B (Hz)	1-T (Hz)
Small Prism-1	99.6	101.5	300.5	6787	1	2690	2990
					2	2900	3277
					28	3153	3540
Small Prism-2	99.5	100.1	299.9	6696	1	2661	2960
					2	2908	3225
					28	3167	3541
Large Prism-1	149.8	152.3	299.8	15579	1	3431	3059
					2	3710	3315
					28	4037	3634
Large Prism-2	149.7	149.5	300.0	15166	1	3416	3048
					2	3687	3311
					28	3977	3610

Note: 1-B and 1-T refer to the first bending and torsional modes, respectively.

Table 5.10 Material properties of concrete from the first batch based on standard dynamic resonance tests

Age (day)	$E_{cd}$ (MPa)	$\mu_{cd}$	$G_{cd}$ (MPa)
1	21691	0.244	8716
	(1.3)	(4.0)	(3.8)
2	25370	0.222	10378
	(3.5)	(7.5)	(2.4)
28	29866	0.214	12301
	(3.1)	(6.6)	(3.4)

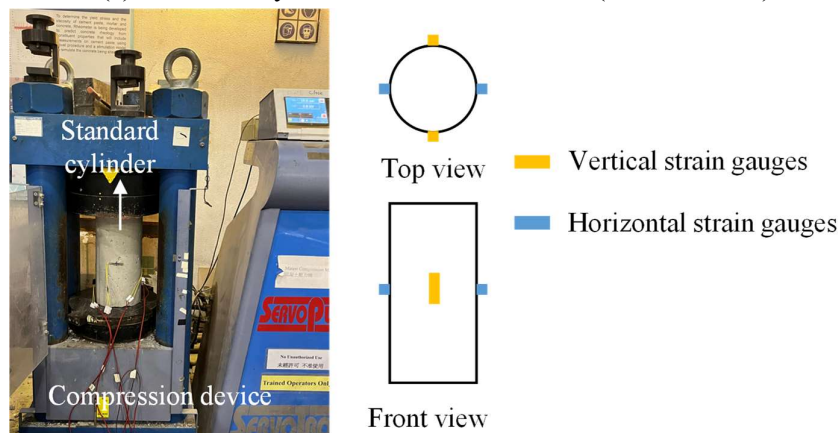
Note: The values outside and in parentheses are the mean values and coefficient of variation (CoV) in %, respectively. Each value is obtained from the four specimens in each test.



Test setup for the first bending mode

Test setup for the first torsional mode

(a) Standard dynamic resonance method (ASTM C215)



(b) Standard static tests (ASTM C469)

Figure 5.9 Test setup for standard dynamic and static tests

Table 5.11 Material properties of concrete from three batches based on the standard static tests

Batch No.	Age (day)	$E_{cs}$ (MPa)	$\mu_{cs}$	$f'_c$ (MPa)	$G_{cs}$ (MPa)
I	2	17373 (8.7)	0.157 (11.3)	22.2 (6.1)	7514 (9.7)
I	28	25064 (4.8)	0.191 (14.5)	39.5 (3.9)	10524 (4.8)
II	28	31425 (2.7)	/	42.0 (3.9)	/
III	28	29241 (6.8)	/	42.0 (2.8)	/

Note: Values outside and in parentheses are the mean values and coefficient of variation in %, respectively. Each value is obtained from three specimens from one batch.

Table 5.12 Summary of test information of the standard static tests

Batch	Age (day)	Cylinder	$\mu_{cs}$	$E_{cs}$ (MPa)	$f'_c$ (MPa)
I	2	Specimen-A	0.141	17555	20.8
		Specimen-B	0.176	15786	23.5
		Specimen-C	0.154	18779	22.4
I	28	Specimen-D	0.223	25477	41.1
		Specimen-E	0.175	26012	39.5
		Specimen-F	0.175	23704	38.0
II	28	Specimen-G	-	32382	43.8
		Specimen-H	-	31048	41.7
		Specimen-I	-	30844	40.6
III	28	Specimen-J	-	31224	42.2
		Specimen-K	-	27222	40.7
		Specimen-L	-	29277	43.0

### 5.6.2 Spectral Evolution in the First 48 Hours

Figure 5.10 presents the experimental EMI signal spectra in the first 24 hours when the cubes are in the plastic molds. The relative signal spectra from the 150 mm cubes are presented using the same y-axis range as that in Figure 5.5, while those from 100 mm cubes are illustrated utilizing a wider range for the y-axis to better discuss the signal results. The raw signals were first detrended and then smoothed using a 250 Hz span to improve the signal-to-noise ratio. In specimen EBP-0°-I-L150, only one peak could be found in the frequency range of 2.5–5.0 kHz at a 5-hour curing age (Figure 5.10(a)). Subsequently, the peak amplitude increased as the curing age progresses. Unlike the simulation results, only mode E could be easily identified in this specimen, while mode H was relatively weak at the beginning. Consequently, only the shear modulus could be measured at the 5-hour age. In specimen EBP-0°-I-L100, the peaks at the same curing age had larger responses with amplitudes almost twice those in EBP-0°-I-L150, indicating that a higher sensitivity was achieved in the small-size cube (Figure 5.10(b)). The reason is that the same actuation forces from the same PZT patch could result in larger responses for the small-size cubes. Both modes E and H could be identified in the signal spectra at a 5-hour curing age. Thereafter, the peaks moved rightward and became stronger as the curing age increased. The actual behaviors of the evolution of

the signal spectra in the 24 hours were consistent with the simulated behaviors in [Figure 5.5\(a\)](#). When the damping level was high, mode identification was difficult. The damping ratio decreased as the curing age increased, resulting in stronger responses of the target peaks, which helped mode identification. Mode identification could be achieved from a 5-hour age for both sizes of cubes. This time was shorter than the initial setting time for normal concrete, which was approximately 6 hours [[Sant et al., 2009](#)].

In specimen EBP-45°-I-L150, only one peak (i.e., mode C) was identified at the 5-hour age, while two modes (i.e., modes C and G) could be determined from the 7-hour curing age ([Figure 5.10\(c\)](#)). Then, the peaks became stronger and moved rightward. The relative amplitudes of the peaks were relatively smaller in specimen EBP-45°-I-L150 than in specimen EBP-0°-I-L150, indicating the lower sensitivity of this installation strategy. The peaks in specimen EBP-45°-I-L100 also showed larger responses at the 5-hour age and became stronger and moved rightward with the increases in the curing age, compared with those in specimen EBP-45°-I-L150 ([Figure 5.10\(d\)](#)).

[Figure 5.11](#) compares the experimental EMI signal spectra at 24 and 48 hours, wherein both the EMI spectra before and after demolding at 24 hours are plotted for better comparison. In specimen EBP-0°-I-L150, the responses of the peaks became larger after demolding; mode H became easier to identify, as shown in [Figure 5.11\(a\)](#). Meanwhile, very slight differences in the frequencies could be observed for the target peaks. For example, the frequencies of mode E with and without mold were 9375 and 9500 Hz, respectively, with a 1.3% difference only. Meanwhile, the peaks at the 48-hour age were stronger than those at the 24-hour age because the damping ratio continued to decrease. Similarly, the peaks in specimen EBP-45°-I-L150 presented larger responses after demolding and continued to move rightward as curing age increases ([Figure 5.11\(b\)](#)). The differences in the frequencies of modes C and G with and without molds are only 0.3% and 0.2%, respectively. The results shown in [Figure 5.11](#) illustrate that the effect of the plastic mold on the target frequencies can be ignored,

but it affects the peak amplitudes of the target modes, similar to an added damping effect on the concrete cubes.

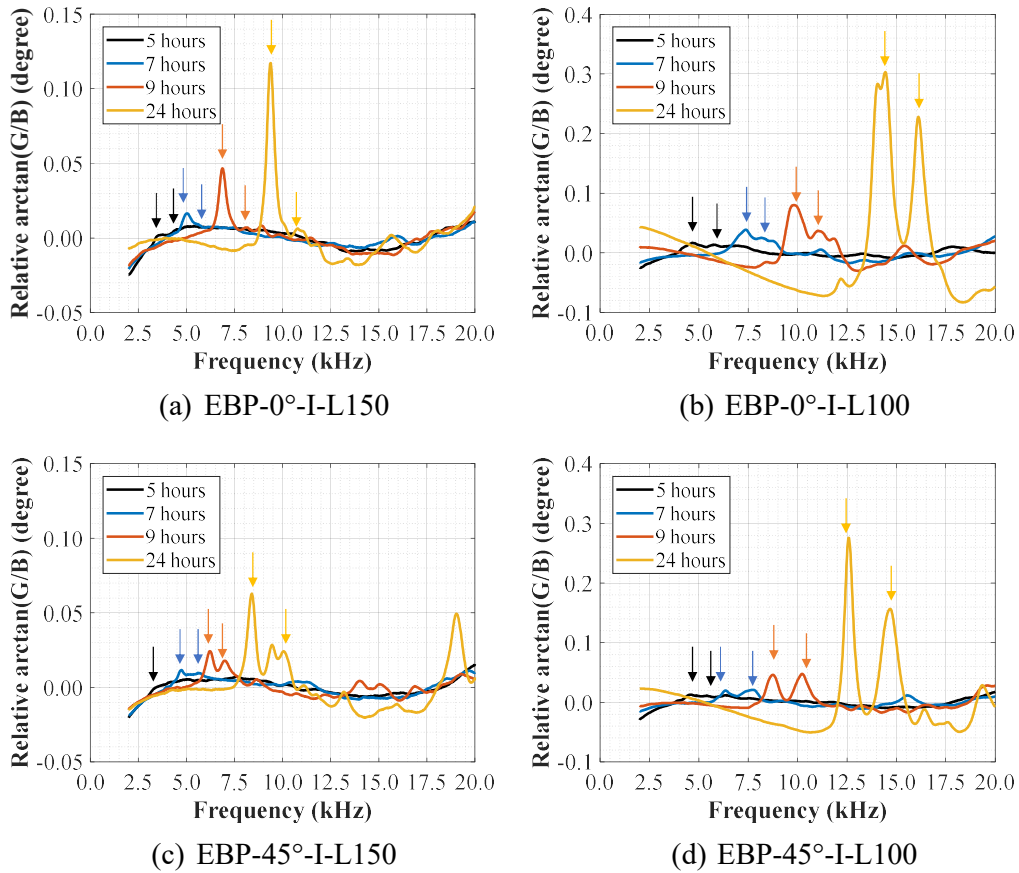


Figure 5.10 Experimental EMI signals in the first 24 hours as cubes with plastic molds

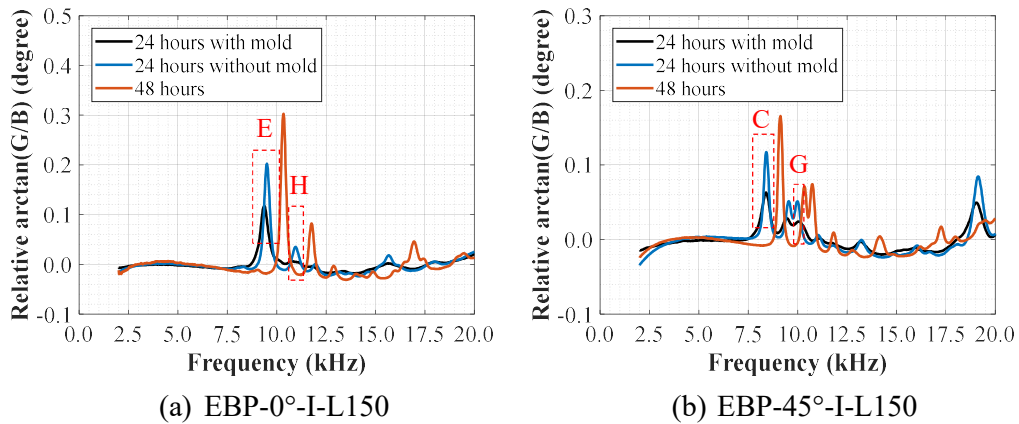


Figure 5.11 Experimental EMI signals at 24 and 48 hours as cubes demolded

### 5.6.3 Comparison with Different Testing Methods

Given the experimental signal spectra, the elastic properties of the concrete cubes could be evaluated subsequently. The details of the tested cubes are summarized in Table 5.13. Figure 5.12 presents the evaluation results with and without modification. The evaluation results from the 24-hour age were selected. Regarding  $G_{ce}$ , the initially measured values were higher than the modified values, indicating the overestimation of the initially measured results (Figure 5.12(a)). The measured values using the 100 mm cubes ( $R_{vol}=2.7\%$ ) caused larger overestimations (up to 9.4%) compared with the 150 mm cube ( $R_{vol}=0.8\%$ ). These results showed that modifications are needed when the unmatched properties between the packaging materials and the concrete exist, especially when the volumetric ratio of the EBP is large.

Regarding  $\mu_{ce}$ , the modified values were higher than the initially measured values, as shown in Figure 5.12(b). The measured values using 100 mm cubes without modification caused larger errors. Although modification has been conducted, the measurements of  $\mu_{ce}$  by EBP-45° show great variability, indicating that strategy EBP-45° may not be proper for evaluating  $\mu_c$ .

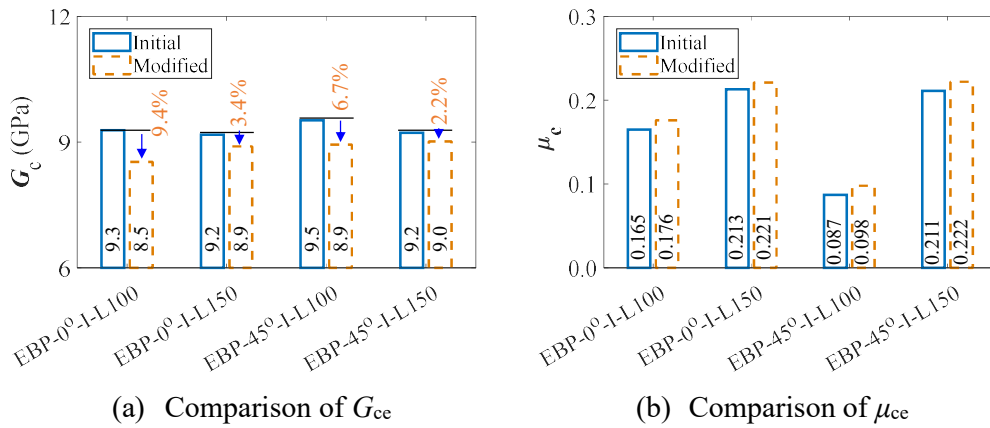


Figure 5.12 Comparison of the evaluation results with and without modification regarding package effect (24-hour age of Batch I)

Table 5.13 Dimensions and mass of the tested concrete cubes

Specimen ID	Mass (g)	$h_c$ (mm)	$w_c$ (mm)	$l_c$ (mm)
EBP-0°-I-L100	2265	100.4	99.8	100.4
EBP-0°-I-L150	7645	150.2	149.0	150.2
EBP-45°-I-L100	2306	100.5	100.5	100.5
EBP-45°-I-L150	7664	150.2	151.4	150.3
EBP-0°-II	7846	150.0	149.0	150.0
EBP-45°-III	7838	150.0	150.0	150.0

Figure 5.13 compares the evaluation results from the different testing methods. Regarding  $G_{ce}$ , the evaluation results from EBP-0° present profound agreement with those from ASTM C215 (Figure 5.13(a)). Compared with ASTM C215, the differences in the evaluated  $G_c$  at 1-day (i.e., 24-hour age), 2-day (i.e., 48-hour age), and 28-day ages were 0.0%, 0.0%, and 4.9%, respectively. Meanwhile, EBP-45° also presented consistent evaluations with differences ranging from 2.9% to 5.7%. The shear moduli  $G_{cs}$  from the static results are also presented for discussion. At 28-day age,  $G_{cd}$  and  $G_{ce}$  were approximately 1.2 times  $G_{cs}$ . This observation demonstrated good consistency with the classic relations between dynamic and static moduli of elasticity, i.e.,  $E_{cd} \approx 1.2E_{cs}$  [Lydon and Balendran, 1986]. However, at 2-day age,  $G_{cd}$  and  $G_{ce}$  were close to 1.4 times  $G_{cs}$ , implying that the above relation may be unsuitable for early-age concrete. But coefficient 1.4 is still in the  $E_{cd}/E_{cs}$  range of 0.9 to 1.5 for concrete with a compressive strength of 30 MPa [Carrazedo, et al. 2018].

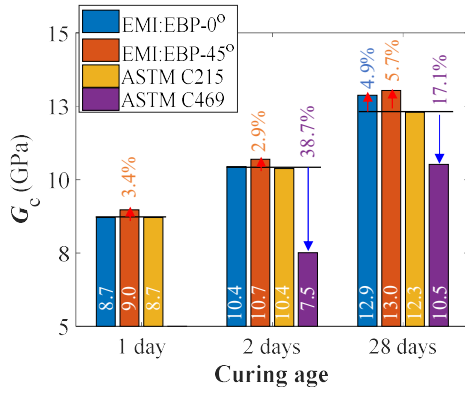
Regarding the stability of  $G_{ce}$  evaluated by the proposed EMI techniques, both EBP-0° and EBP-45° presented smaller coefficient of variation (CoV) values than the traditional dynamic and static testing methods, indicating high stability for evaluating shear moduli (Figure 5.13(b)). The CoV value is the ratio of the standard deviation value to the mean value, calculated based on the measurement results from different samples shown in Table 5.8. The maximum CoV in these three ages is 3.0% for the proposed EMI-R techniques.

Regarding  $\mu_c$ , both the proposed EMI-R techniques present lower evaluations than the results from the ASTM C215. The maximum differences from EBP-0° and EBP-45°

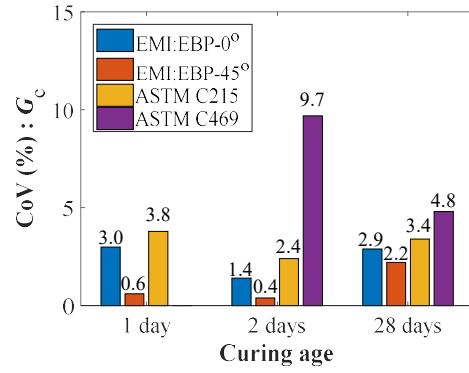
are 24.0% and 65.7% in the first two days, indicating that the proposed methods have relatively large differences in measuring  $\mu_{cd}$  compared with the traditional dynamic testing methods (Figure 5.13(c)). The differences become large at 28-day age, up to 89.3% and 267% for EBP-0° and EBP-45°, respectively. The evaluation differences are induced by the anisotropic properties of concrete in real practice, resulting in difficulties in evaluating the Poisson's ratio using dynamic methods that use isotropic assumption [Swamy, 1971]. Bertoldo et al. [2020] measured  $\mu_{cd}$  from 0.09 to 0.32 at 28-day age. ASTM C215 [2019] presented that the measured  $\mu_{cd}$  of concrete normally varies between 0.10 and 0.25 for the dry and saturated specimens, respectively. Meanwhile, the correlations between  $\mu_{cd}$  and  $\mu_{cs}$  have not been well investigated in the concrete field. In this test, the difference between  $\mu_{cd}$  and  $\mu_{cs}$  becomes smaller with the increases in the curing age.

In terms of the stability in evaluating  $\mu_c$ , the traditional dynamic method presents the highest stability among these four methods. By contrast, EBP-45° presents unacceptable stability with CoVs larger than 46.4%, (Figure 5.13(d)). EBP-0° presents relatively good stability in evaluating  $\mu_c$ , with comparable CoVs with static methods.

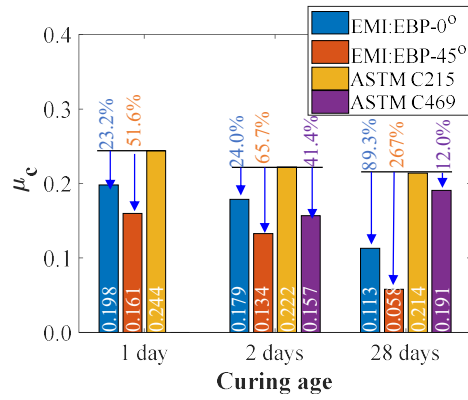




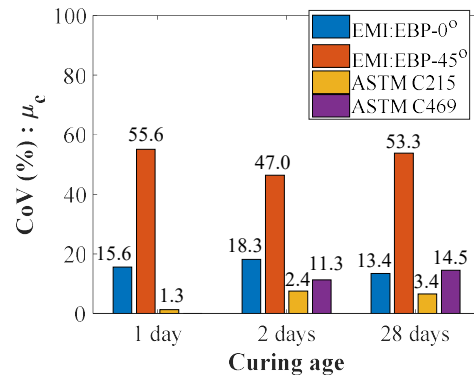
(a) Comparison of the mean value of  $G_c$



(b) Comparison of the CoV of  $G_c$



(c) Comparison the mean value of  $\mu_c$



(d) Comparison the CoV of  $\mu_c$

Figure 5.13 Comparisons of the evaluation results from the different testing methods

Considering the ignorable effects of the plastic molds (Figure 5.11), the proposed strategies can be directly used to measure the shear modulus of concrete before demolding. Figure 5.14 presents the evaluation results of the tested four cubes using the proposed EMI-R techniques in this batch when the cubes are inside the molds. The two EMI-R methods present similar evolution trends of the measured shear modulus (Figure 5.14(a)). The measured shear modulus increases as the curing age increases. The differences between the two EMI-R methods are relatively small, and the maximum absolute difference between the mean values is 518 MPa at the 5-hour age. Figure 5.14(b) presents the evolution of Poisson's ratio evaluated by the two strategies. EBP-0° presents a more reasonable trend, in which the dynamic Poisson's ratio decreases as the curing age increases [Anson and Newman, 1966; Swamy, 1971], while no trend is

observed in the evaluated  $\mu_c$  by EBP-45°.

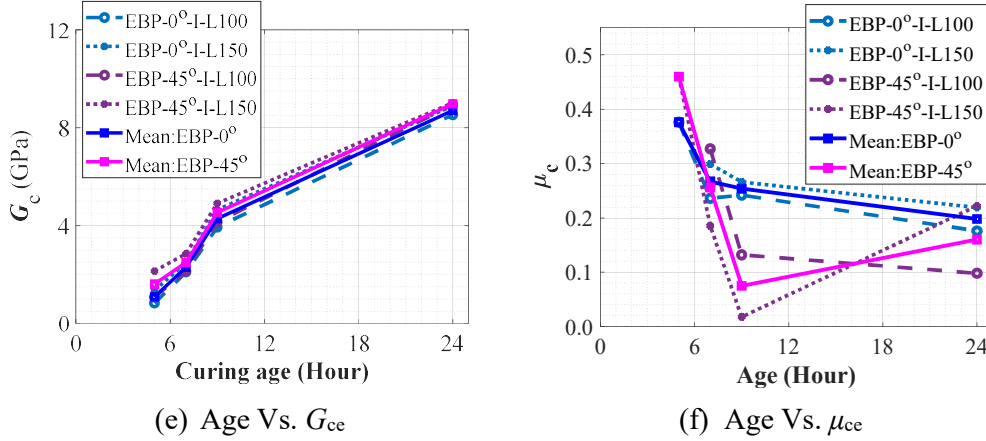


Figure 5.14 Evaluation results using the proposed EMI-R methods for the cubes with molds

This subsection presents the evaluation results of the proposed methods in the first 48 hours and compares them with the traditional dynamic and static methods. In summary, the proposed EMI-R technique using both installation strategies can provide accurate evaluation results of the shear modulus. By contrast, EBP-0° can provide reasonable evaluation results on the Poisson's ratio, and EBP-45° is not recommended to measure Poisson's ratios. Notably, given the estimated shear modulus and Poisson's ratio, the modulus of elasticity can be derived indirectly. So only EBP-0° is recommended if estimating the modulus of elasticity is also necessary.

#### 5.6.4 Continuous Monitoring in First 10 Hours

The potential capability of the proposed method was further investigated in this subsection by performing continuous monitoring to investigate the earliest time that the elastic constants can be measured and the evolution behaviors of the elastic constants in the first 10 hours. The testing interval for the EMI-R methods was 0.5 hours within the first hour and became 1 hour after the 1-hour age. Two 150 mm cubes were used because the size is most commonly utilized in real practice. The experimental setup and test information have been introduced in [Section 5.5.1](#). The signal processing methods were the same as those in [Section 5.5.2](#). The details of the concrete, which were the normal concrete, can be found in [Tables 4.8](#) and [5.11](#).

Figure 5.15 presents the signal spectra of two tested cubes in the continuous monitoring in the first 10 hours. Figures 5.15(a) and (c) present the curing ages from 0.5 to 4 hours after casting, while Figures 5.15(b) and (d) present the behaviors from 4 to 10 hours. In EBP-0°-II-L150, no peaks could be identified in the signal spectra in the first two hours because of the high damping ratio (Figure 5.15(a)). At 3-hour age, three peaks could be found in the frequency range of 2.5–5.5 kHz, presenting a spectrum similar to the simulated Case 2 in Figure 5.5(a). Subsequently, the peaks became much stronger at the 4-hour age. The peak responses increased with the increase in the curing age, and the peaks moved rightward (Figure 5.15(b)). In this specimen, mode H is easier to identify than specimen EBP-0°-I-L150. Meanwhile, specimen EBP-45°-III-L150 presented similar behaviors in the first 2 hours. No distinct peaks could be identified in the first hour (Figure 5.15(c)). A distinct peak could be identified at the 2-hour age in the frequency range of 3.0–3.5 kHz. Thereafter, two peaks (corresponding to modes C and G) could be identified at the 4-hour age. The two peaks in the spectrum were the same as those in the simulated Case 2 in Figure 5.5(b). The relative distance of the modes increased as the peaks moved rightward. Meanwhile, the responses of the peaks increased with the increase in the curing age (Figure 5.15(d)).

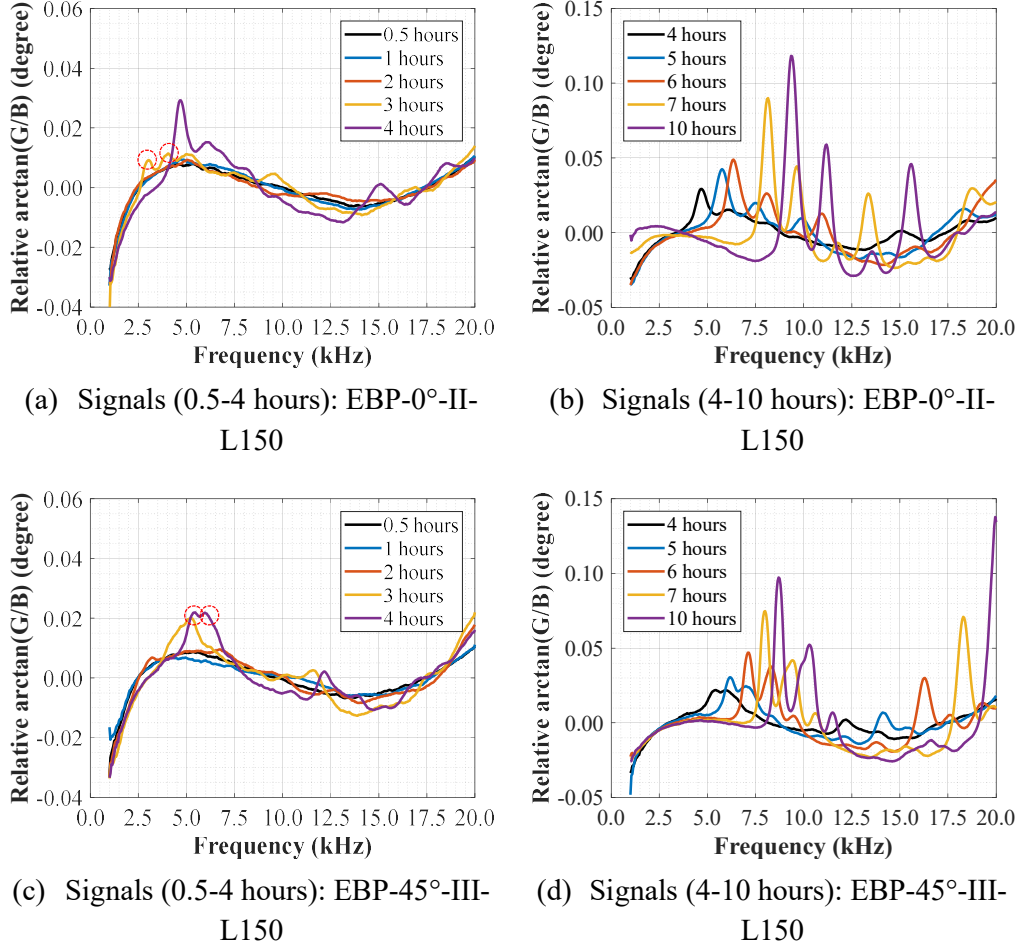


Figure 5.15 Continuous monitoring using the proposed strategies in the first 10 hours

Figure 5.16 presents continuous monitoring results using the proposed method in the first 10 hours. Figure 5.16(a) presents the evaluation results between the age and the shear moduli. The general evolution trends are the same for these two strategies, and the initial value of the shear modulus for each strategy is around 1.5 GPa. EBP-45°-III-L150 provides higher evaluations than EBP-0°-II-L150 at the same age, with differences ranging from 1.1 GPa to 1.7 GPa from 4 hours to 10 hours. Property variations between two different batches may cause the difference.

Figure 5.16(b) presents the evaluation results of Poisson's ratio. In terms of the general trend of the evolution of Poisson's ratio, EBP-0°-II-L150 offered quite reasonable evaluation results. Poisson's ratio dramatically decreased around the initial

setting time (i.e., around 6 hours after casting for normal concrete) while keeping relatively stable in the other time in the first 10 hours. By contrast, the evolution results by EBP-45°-III-L150 are not presented because they are unreliable based on the discussion in [Section 5.5.3](#).

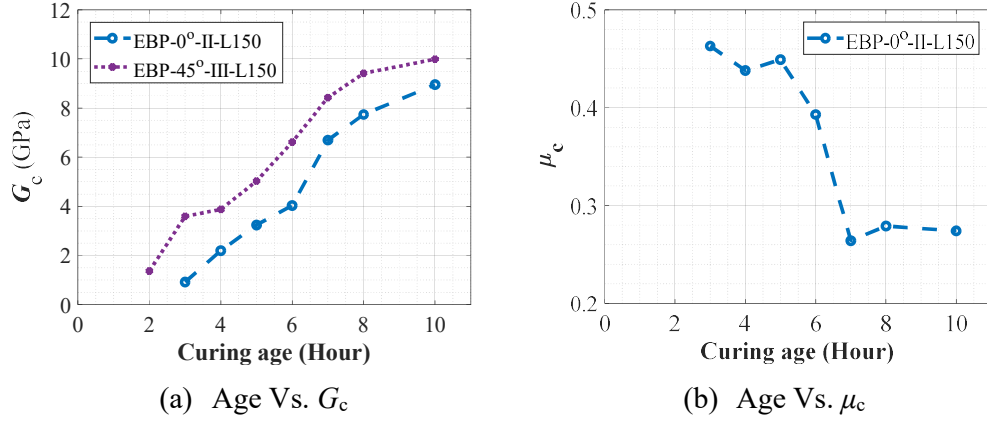


Figure 5.16 Evaluation results of continuous monitoring using the proposed EMI-based strategies in the first 10 hours

In this subsection, the behavior of elastic constants of the concrete materials in the first 10 hours is evaluated and discussed using the EMI-R methods for the first time. The strategy EBP-0° is recommended in real practice because it can provide reasonable dynamic elastic constants (i.e., shear modulus, and Poisson's ratio) at a very-early age, while EBP-45° can only offer shear modulus.

## 5.6 Summary

Novel EMI-R methods for measuring the elastic properties of very-early-age concrete cubes were proposed for the first time. Two unique vibration modes only related to the shear modulus were selected. Moreover, two corresponding sensor installation strategies (i.e., EBP-0° and EBP-45°) were designed and numerically investigated for extracting the target modes. The evaluation and modification methods of these two strategies were presented through a series of numerical investigations. Thereafter, laboratory experiments were conducted to validate the proposed methods. Some conclusions can be drawn as follows:

1. The proposed two types of sensor installation strategies can offer accurate

evaluation results in measuring the shear modulus, while only EBP-0° is recommended, when measuring the Poisson's ratio and modulus of elasticity is desirable.

2. The proposed methods can be used when concrete cubes are still in molds. The earliest time for measuring the shear modulus and Poisson's ratio using the proposed methods was 2 hours after casting, which is much earlier than the initial setting time for normal concrete (i.e., typically 6 hours after casting). This capability outperforms the traditional dynamic testing method, showing the application potential of the proposed techniques.
3. The modification formulas considering the unmatched properties between the concrete and the packaging materials (especially when  $R_{vol}$  is large) are proposed to improve the evaluation accuracy.
4. Given concrete cubes of the same size, strategy EBP-0° can provide higher sensitivity than strategy EBP-45°. Meanwhile, EBP shows higher sensitivity in a smaller cube.

Although this chapter focuses on measuring the elastic constants of the concrete material, the proposed NDT methods can be easily extended to other cementitious materials. Meanwhile, the successful measurement for very-early-age concrete makes the proposed method a promising tool for quantitatively analyzing the initial and final settings of cementitious materials in the future.

## CHAPTER 6 MEASURING MODULUS OF ELASTICITY OF CONCRETE PRISMS USING LENGTH- INSENSITIVE RESONANT MODES

[Chapters 3–5](#) measured the elastic constants using baseline-free EMI techniques and standard concrete cubes at different ages. This chapter further extends the baseline-free EMI technique from cubic specimens to beam-like specimens for a broader range of application scenarios. Fundamental resonant frequencies are widely used for beam-like specimens to characterize the elastic properties in metal and cementitious materials using the traditional resonance method. However, these fundamental resonant frequencies may be too low in long-length concrete elements/structures for piezoelectric sensors, whose working frequency range is higher than 3 kHz. Moreover, the high-damping ratio of concrete increases the difficulties of extracting the fundamental modes in the low-frequency range. Length-insensitive modes are promising and can be selected for the baseline-free EMI technique. However, length-insensitive modes may hide in the high-order global modes in the middle-frequency range, increasing the identification difficulties.

Built on the knowledge from [Chapters 4](#) and [5](#), sensor installation strategies considering symmetric planes can help reduce the modal density and extract target special modes. Taking advantage of the feasibility of the EBP, high symmetric boundary conditions can be achieved to extract the desirable length-insensitive modes. Numerical and experimental investigations show that length-insensitive modes can be easily identified by utilizing the concept of symmetry. Evaluation results show the accuracy of measuring the modulus of elasticity using length-insensitive modes compared to the fundamental modes. Moreover, a high-damping-ratio case presents the superiority of the length-insensitive modes compared to the fundamental modes (e.g., longitudinal and bending modes).

## 6.1 Introduction

As reviewed in [Section 2.3.5.3](#), baseline-dependent EMI techniques have been extensively applied in concrete structures, such as the damage detection of concrete slabs and beams using SBP and EBP. In contrast, the baseline-free EMI techniques are limited to small standard specimens (i.e., cylinders). Meanwhile, existing baseline-free techniques used fundamental modes of beam-like structures to measure the material properties, as shown in [Table 2.11](#) of [Chapter 2](#).

However, fundamental modes may not be identifiable by piezoelectric sensors in large-size concrete members because of the high working frequency range ( $>3$  kHz) of piezoelectric sensors and the high damping ratio of concrete. As capacitance-type sensors, piezoelectric sensors may not effectively capture the resonant frequencies in the low-frequency range. Extremely high voltage (a few hundred volts typically) may be required to drive the sensor because the impedance of a capacitive transducer increases with decreasing frequency and approaches infinity for a zero frequency [[Measurement Specialties, 1999](#)]. At frequencies lower than approximately 3 kHz, the sensitivity of piezoelectric sensors becomes low and may underestimate structural responses [[Jenq and Chang, 1995](#)]. [Giurgiutiu and Zagrai \[2002\]](#) recommended avoiding frequencies below 5 kHz because the peaks obtained in the EMI spectra tend to have small amplitudes. Classical fundamental modes (i.e., bending, longitudinal, and torsional modes) are highly related to the length. In practical structures, beam-like concrete members can have lengths of several meters, indicating that the frequencies of their fundamental modes are typically lower than the working frequency range of piezoelectric sensors, especially for the fundamental bending modes. Moreover, the length-dependent feature of classical fundamental modes implies that their resonant frequencies are heavily affected by the boundary conditions [[Gonçalves et al., 2007](#); [Rao, 2007](#)]. In addition, concrete has a damping ratio higher than steel materials [[Papageorgiou and Gantes, 2010](#)], causing difficulties in actuating and capturing fundamental modes of concrete members. Variations in the damping ratios are



remarkable during the early ages of concrete [Swamy and Rigby, 1971] or when it undergoes damage [Li and Xiao, 2021]. Therefore, special and identifiable modes in a higher frequency range are desired to overcome the difficulties from a practical perspective.

The above discussion highlights the following research gaps in existing studies: (a) a baseline-free EMI-R technique using modes in a middle-frequency range is desirable for beam-like concrete structures to overcome the limited frequency range of the piezoelectric sensors and high damping ratio of concrete; (b) special modes that are insensitive to member length are desired to remove the effects introduced by the length and boundary conditions at the ends for better generalizability.

To this end, the baseline-free EMI-R technique using special length-insensitive modes was explored in this chapter for the first time to overcome situations when the fundamental modes of beam-like concrete members cannot be identified. A series of numerical investigations were conducted (a) to find the length-insensitive resonant modes in beam-like concrete members, (b) to extract the target resonant modes using appropriate sensor installation strategies, (c) to show the benefits of using length-insensitive modes, and (d) to correlate the resonant frequencies to the material properties and geometric information of the beam-like concrete structures. Subsequently, experimental validations were conducted to demonstrate the accuracy and effectiveness of the length-insensitive high-order modes through a comparison with methods using the global modes (e.g., the first longitudinal mode).

## **6.2 Concept and Identification of Length-insensitive Modes of a Prism**

### **6.2.1 Concept of Length-insensitive Vibration Modes**

A continuum solid (e.g., a straight concrete beam) has infinite vibration modes. The traditional dynamic tests [e.g., ASTM C215, 2019] prefer using the fundamental modes (i.e., bending, longitudinal, and torsional modes) of rectangular prismatic specimens to measure the dynamic modulus of elasticity of concrete, in which

frequency response spectra are usually obtained using accelerometers. Sharp distinct resonance peaks in the spectra represent specific vibration modes. Only a small number of vibration modes appeared within the target frequency range, which facilitates identification [Ezvan et al., 2018]. As aforementioned, the current baseline-free EMI-R technique is unsuitable for capturing the fundamental modes in the low-frequency range ( $< 3\text{kHz}$ ). As a result, the method encounters challenges when applied to straight concrete members with long lengths.

On the other hand, the EMI-R technique has demonstrated its ability to capture many high-order resonant modes of a target structure, in addition to fundamental modes, under small strain, particularly in the medium- and high-frequency bands. Therefore, special modes in the higher frequency range can potentially be utilized to leverage this advantage of the EMI-R technique fully. Tzou et al. [1998] discussed the vibration modes of an arbitrarily shaped disk cross-section over a wide range of lengths (i.e., from a thin plate to a long beam) with free boundaries. Some resonant modes were characterized by predominantly in-plane motion, and their frequencies were relatively less affected by length-to-radius ratios. These length-insensitive modes have frequencies much higher than those of the fundamental modes (bending, longitudinal, and torsional) of beam members with large length-to-radius ratios. Some scholars attempted to study the behavior of length-insensitive modes to detect damage in concrete beams using the impact echo method, wherein accelerometers were used as sensors [Lin and Sansalone, 1992; Gassman and Zein, 2008; Zein and Gassman, 2010; Malone et al., 2023]. Moreover, another benefit of the length-insensitive modes is that some of them are uncoupled with boundary conditions at the ends [Gazis, 1959; Mindlin and Fox, 1960].

However, accurately identifying and extracting these length-insensitive modes was difficult because the recorded signal spectrum in the target frequency range presents erratic mode numbers and exhibits numerous overlapping peaks [Ezvan et al., 2018], presenting some obstacles to utilizing these modes. The spectrum in the medium-

frequency range tends to have denser modes per unit frequency than the low-frequency range [Ezvan et al., 2018]. Notably, most concrete members (e.g., beam-like members) are multi-symmetric structures (i.e., structures have multiple symmetric planes). The symmetry concept can be used to reduce the number of modes identified in the target frequency range [Evensen, 1976], facilitating mode identification and accessibility in the medium-frequency range. Taking advantage of the installation flexibility of piezoelectric sensors (such as surface-bonded or embedded sensors) in concrete members, symmetric boundary conditions can be achieved easily, ensuring the potential identification and application of special high-symmetric modes.

### 6.2.2 Modal Density Variation with Different Symmetric Boundaries

Prior to discussing the length-insensitive modes, this subsection presents a numerical investigation of how symmetric boundaries reduce modal density. Figure 6.1 shows a prism with a square section having five symmetric planes, namely, three parallel symmetric planes and two diagonal symmetric planes, where the three parallel planes are parallel with the three pairs of the faces. The pair of diagonal planes (i.e., planes  $\eta ox$  and  $\gamma ox$ ) is perpendicular to the plane  $yo z$ . The red, blue, and pink dots in Figure 6.1 refer to the center of the prism, the centers of the faces, and the midpoints of the edges, respectively. All these five symmetric planes can be reached by embedded PZT sensors. These symmetric planes were deliberately utilized in this chapter.

A standard concrete prism with a square section (i.e.,  $150 \times 150 \times 550 \text{ mm}^3$ ) was modeled and simulated to investigate the effect of the number of symmetric planes. This standard concrete prism is commonly used for measuring flexural strength and dynamic modulus of elasticity in the concrete field [Bassim and Issa, 2020; GB/T 50081, 2019]. Modal analysis was conducted using ANSYS. Solid45 was selected as the element type for the concrete. The material properties were set as follows: modulus of elasticity = 30 GPa, density =  $2300 \text{ kg/m}^3$ , Poisson's ratio = 0.2, and damping ratio = 0.8%. The mesh size was set to 2.5 mm after convergence analysis. Table 6.1 presents the number of vibration modes below 20 kHz for the simulated prism under different

symmetric conditions. The modes with different numbers of symmetric planes are obtained from the modal analyses by applying symmetric boundaries about the listed planes. For example, 0 symmetric plane indicates that the corresponding modal analyses were conducted using an entire model with free boundary conditions; and 4 symmetric boundaries indicate the corresponding modal analyses were conducted with 1/8 model with listed planes as symmetric boundaries. The frequency range was divided into four intervals (i.e., 5 kHz for each) for improved description. The five symmetric planes only have eight combinations because the symmetric plane  $xoy$  is equivalent to  $xoz$ .

Two trends can be observed in [Table 6.1](#). First, the mode number increased dramatically with increases in frequency. For example, the number of modes in the range of 10-20 kHz is approximately six times that in the range of 0-10 kHz for an entire model. The modes in the frequency range of 0-10 kHz are composed of low-order bending, torsional, and longitudinal modes. Second, the mode number decreases significantly with increases in the symmetric planes introduced. For the frequency range below 5 kHz, the mode number was reduced to only one (i.e., first longitudinal mode) as the symmetric planes increased to three. Bending and torsional modes in this frequency range disappeared because these modes have a maximum of two symmetric planes. Similar observations were made in the three other frequency ranges. When the symmetric plane increases by one, the number of modes is reduced to nearly half. For example, when two symmetric planes are applied in the frequency range of 10-20 kHz, the number of modes is reduced to approximately 28% compared with the status without symmetric planes.

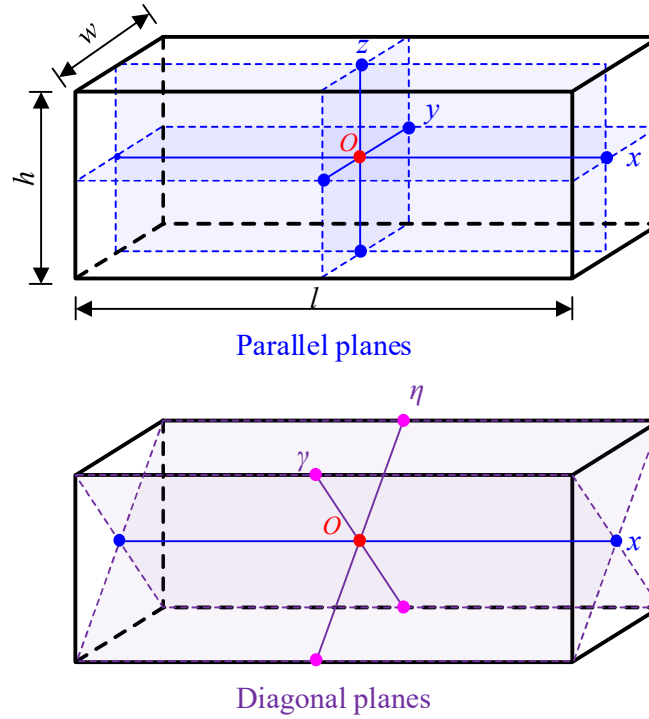


Figure 6.1 Symmetric planes of a prism

Table 6.1 Numbers of vibration modes in various frequency ranges under different symmetric boundaries (Prism specimen:  $150 \times 150 \times 550 \text{ mm}^3$ )

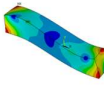
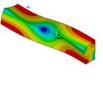
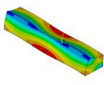
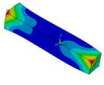
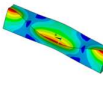
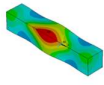
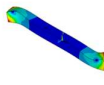
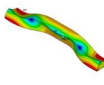
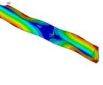
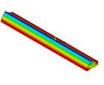
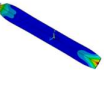
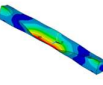
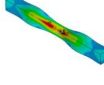
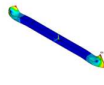
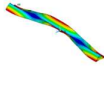
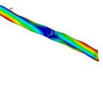


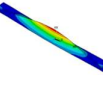
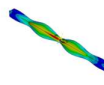





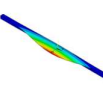
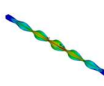
Number of symmetric boundaries	Adopted model in modal analyses	Symmetric planes	Numbers of modes			
			0~5 kHz	5~10 kHz	10~15 kHz	15~20 kHz
0	Whole model	-	7	15	59	72
1	1/2 model	$xoz$	3	6	37	37
1	1/2 model	$yoz$	4	8	32	34
2	1/4 model	$xoz, yoz$	1	2	23	18
2	1/4 model	$xoz, xoy$	2	3	20	17
3	1/8 model	$xoz, xoy, yoz$	1	1	12	9
4	1/8 model	$xoz, xoy, \eta ox, \gamma ox$	1	2	9	9
5	1/16 model	$xoz, xoy, yoz, \eta ox, \gamma ox$	1	1	4	5

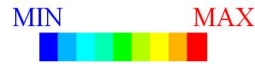
### 6.2.3 Length-insensitive Modes with High Symmetries

After demonstrating the effectiveness of reducing modal density by increasing the number of symmetric planes, this subsection further discusses highly symmetric modes in the frequency range of 10-15 kHz to identify special length-insensitive modes. [Figure 6.2](#) presents the mode shapes and corresponding frequencies of seven length-insensitive

modes with high numbers of symmetric planes. A quarter numerical model, incorporating the symmetric planes  $xoz$  and  $xoy$ , was used to illustrate the mode shapes of the prisms at different lengths, whereas the section of the prism remains the same (i.e.,  $w \times h = 150 \times 150 \text{ mm}^2$ ). The length-to-width ratio (i.e.,  $l/w$ ) varied from 3 to 20. The results from the numerical model were consistent with those in [Section 6.2.2](#). The symmetric type of each mode is also listed.

Length-insensitive modes have previously been studied in cylinders [[Gazi, 1959](#); [McNiven, 1961](#); [Wang and William, 1996](#)]. Length-insensitive modes can be categorized into in-plane modes, longitudinal shear modes [[Tzou et al., 1998](#)], and end modes [[McNiven and Shah, 1967](#)] based on their deformation patterns. The in-plane mode denotes the mode with the same deformation along the length, and its frequency remains constant for different  $l/w$ , such as mode  $D_P$  in [Figure 6.2](#). The frequencies of some modes may coalesce to the value of the in-plane mode (i.e., mode  $D_P$ ) with increases of  $l/w$ , such as modes  $B_P$  and  $C_P$  ([Figure 6.2](#)), and these modes have the same deformation on the surface of cross section but different along the length in comparison with in-plane mode [[Tzou et al., 1998](#)]. The longitudinal shear modes exhibit axial displacements (i.e., deformation along the length) that are not uniform over cross section of the member [[Tzou et al., 1998](#)]. The mode shape of longitudinal shear modes can be considered as a coupling of mode shapes of longitudinal and torsional modes [[Gazi, 1959](#)]. Their frequencies shift from high frequency to low frequency as  $l/w$  increases, such as modes  $F_P$  and  $G_P$ . The end modes have large motions at the end of the structure and diminish rapidly along the length away from its end [[Oliver, 1957](#); [McNiven, 1961](#)], such as modes  $A_P$  and  $E_P$ , and their corresponding frequencies converge quickly as  $l/w$  increases.

Label	A <sub>P</sub>	B <sub>P</sub>	C <sub>P</sub>	D <sub>P</sub>	E <sub>P</sub>	F <sub>P</sub>	G <sub>P</sub>
$l/w=3$		N/A					
	10007 Hz	N/A	10863 Hz	10991 Hz	11311 Hz	12815 Hz	13616 Hz
$l/w=6$							
	10020 Hz	10864 Hz	10956 Hz	10991 Hz	11316 Hz	12302 Hz	13170 Hz
$l/w=10$							
	10021 Hz	10942 Hz	10979 Hz	10991 Hz	11316 Hz	12263 Hz	13056 Hz
$l/w=20$							
	10021 Hz	10979 Hz	10988 Hz	10991 Hz	11311 Hz	12261 Hz	13019 Hz
Sym. planes	$xoz$ $xoy$	$xoz$ $xoy$ $yo z$	$xoz$ $xoy$	$xoz$ $xoy$ $yo z$	$xoz$ $xoy$ $\eta ox$ $\gamma ox$	$xoz$ $xoy$ $yo z$	$xoz$ $xoy$ $yo z$ $\eta ox$ $\gamma ox$
Asym. planes	$yo z$ $\eta ox$ $\gamma ox$	$\eta ox$ $\gamma ox$	$yo z$ $\eta ox$ $\gamma ox$	$\eta ox$ $\gamma ox$	$yo z$	$\eta ox$ $\gamma ox$	



Magnitude of displacement

Figure 6.2 Mode shapes and corresponding frequencies of seven length-insensitive modes of prisms with high symmetries (A quarter model is presented in this figure.)

From the perspective of symmetric types, modes A<sub>P</sub> and E<sub>P</sub> differ in symmetric types concerning their diagonal planes: the former and latter are anti-symmetric and symmetric, respectively. In addition, modes A<sub>P</sub> and E<sub>P</sub> have twin modes, which are symmetric about plane  $yo z$ . The twin modes are not presented in this figure since the differences in frequencies are minimal. For mode G<sub>P</sub>, deformation is symmetric about all mentioned planes and mainly around the center of the entire prism. Modes B<sub>P</sub>, C<sub>P</sub>, and D<sub>P</sub> are symmetric about parallel planes (i.e.,  $xoy$  and  $xoz$ ) and anti-symmetric about

diagonal planes (i.e.,  $\eta_{ox}$  and  $\gamma_{ox}$ ). However, modes  $B_P$  and  $C_P$  are symmetric and anti-symmetric about the plane  $yoz$ , respectively.

From the perspective of modal frequencies, all the selected modes converge finally. For instance, the difference between frequencies at  $l/w = 6$  and  $10$  is small enough (i.e.,  $<1\%$ ) for all the listed modes. It should be highlighted that the frequency difference of mode  $G_P$  between  $l/w = 3$  and  $6$  is relatively large ( $3.4\%$ ), as its deformation covers a relatively long dimension. In contrast, modes  $A_P$ ,  $C_P$ ,  $D_P$ , and  $E_P$  almost converge at  $l/w = 3$ . Therefore, within the range of  $l/w = 3 \sim 6$ , the effect of the length should still be considered. In general, these length-insensitive and high-symmetric modes can benefit the EMI-R technique by enabling them to be extended to larger beam-like members.

### 6.3 Capture Length-insensitive Modes of a Prism in the EMI-R Technique

In this section, the length-insensitive modes of a prism with a square section will be actuated, captured, and extracted using appropriate sensor installation strategies.

#### 6.3.1 Different Installation Strategies and Actuation Mechanism

Figure 6.3 illustrates various installation strategies for a square PZT patch in the studied standard prism to achieve different symmetric planes. Square PZT patches are commonly used piezoelectric sensors in the concrete field. These patches can be either surface-bonded or embedded in the target specimens. The yellow coordinate represents the three axes of a PZT patch. The 3-axis along the thickness direction indicates the polarization direction of the sensor. When the voltage was applied along the 3-axis, the PZT patch deforms along the 1-axis and 2-axis, generating planar force [Bhalla and Soh, 2004]. Figure 6.3 uses three terms to present the relative position and the actuation directions of the PZT patches. SBP and EBP refer to the surface bonded PZT patch and embedded PZT patch, respectively, which are installed at  $z=h/2$  and  $z=0$ , respectively. E and C indicate the eccentric ( $x=l/4$ ) and concentric ( $x=0$ ) positions of the sensors along the  $x$ -axis, respectively. The symbols  $\perp$  and  $//$  denote that the vibration directions of the PZT patch (i.e., the actuation plane) are perpendicular and parallel to the plane



$yoz$ , respectively. All PZT patches are installed at the midline of the width of the concrete prism (i.e.,  $y=0$ ). The SBP can be directly installed on one face of the concrete using adhesive materials, whereas a coating package is required to protect the EBP during concrete casting. A total of six installation strategies are investigated in this subsection, namely, SBP-C- $\perp$ , SBP-E- $\perp$ , EBP-C- $\perp$ , EBP-E- $\perp$ , EBP-C- $//$ , and EBP-E- $//$ .

Figure 6.4 and Table 6.2 summarize the schematic of the actuation type induced by different installation strategies on a concrete prism. Figure 6.4(a) illustrates the installation strategies of the SBPs. When an SBP installed on the side face of the prism is actuated, it elongates perpendicular to the planes  $yoz$  and  $xoz$ , producing two pairs of forces along the surface. The actuation forces of the PZT patches can result in width-wise and length-wise vibrations of the prism simultaneously [Yan et al., 2007]. The SBPs installed at  $x=l/4$  (i.e., SBP-E- $\perp$ ) and  $x=0$  (i.e., SBP-C- $\perp$ ) have one and two symmetric planes, respectively.

In comparison, an EBP may produce different types of actuation forces, depending on the actuation directions of the PZT patch, as shown in Figure 6.4(b). When the PZT patch is placed perpendicular to the plane  $yoz$ , it generates one pair of forces parallel to  $x$ -axis and one pair of forces parallel to  $y$ -axis at the same time. The EBP sensors installed at  $x=l/4$  (i.e., EBP-E- $\perp$ ) and  $x=0$  (i.e., EBP-C- $\perp$ ) have two and three symmetric planes, respectively. On the other hand, when the PZT patch is placed parallel to plane  $yoz$ , it generates one pair of forces along  $z$ -axis and one pair of forces along  $y$ -axis. The two pairs of actuation forces are highly symmetric about plane  $yoz$ , providing four symmetric planes at the same time. Therefore, the EBP-E- $//$  and EBP-C- $//$  have four and five symmetric planes, respectively.

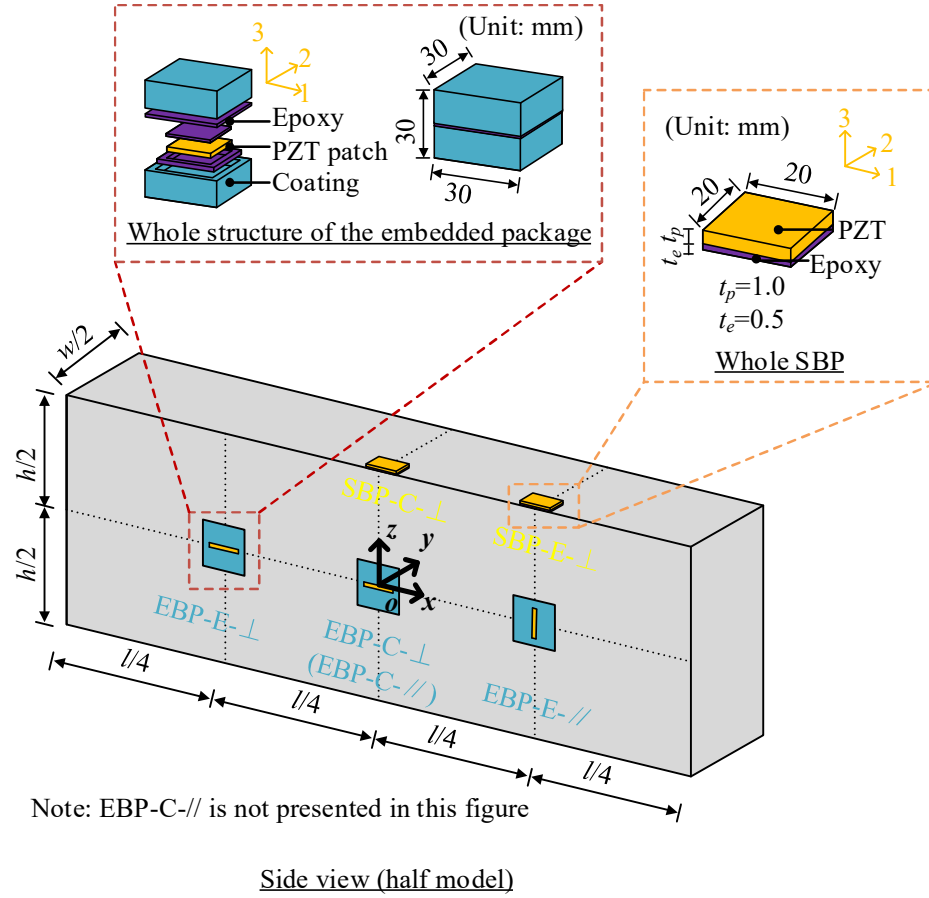


Figure 6.3 Installation strategies of the PZT sensors in the prism adopted in this study (Explain only a half model)

Table 6.2 Details of different installation strategies

Strategy ID	Location	Actuation direction	Number of symmetric planes
SBP-E-⊥	$x=l/4, z=h/2, y=0$	Perpendicular to plane $yoz$	1
SBP-C-⊥	$x=0, z=h/2, y=0$	Perpendicular to plane $yoz$	2
EBP-E-⊥	$x=l/4, z=0, y=0$	Perpendicular to plane $yoz$	2
EBP-C-⊥	$x=0, z=0, y=0$	Perpendicular to plane $yoz$	3
EBP-E-//	$x=l/4, z=0, y=0$	Parallel to plane $yoz$	4
EBP-C-//	$x=0, z=0, y=0$	Parallel to plane $yoz$	5

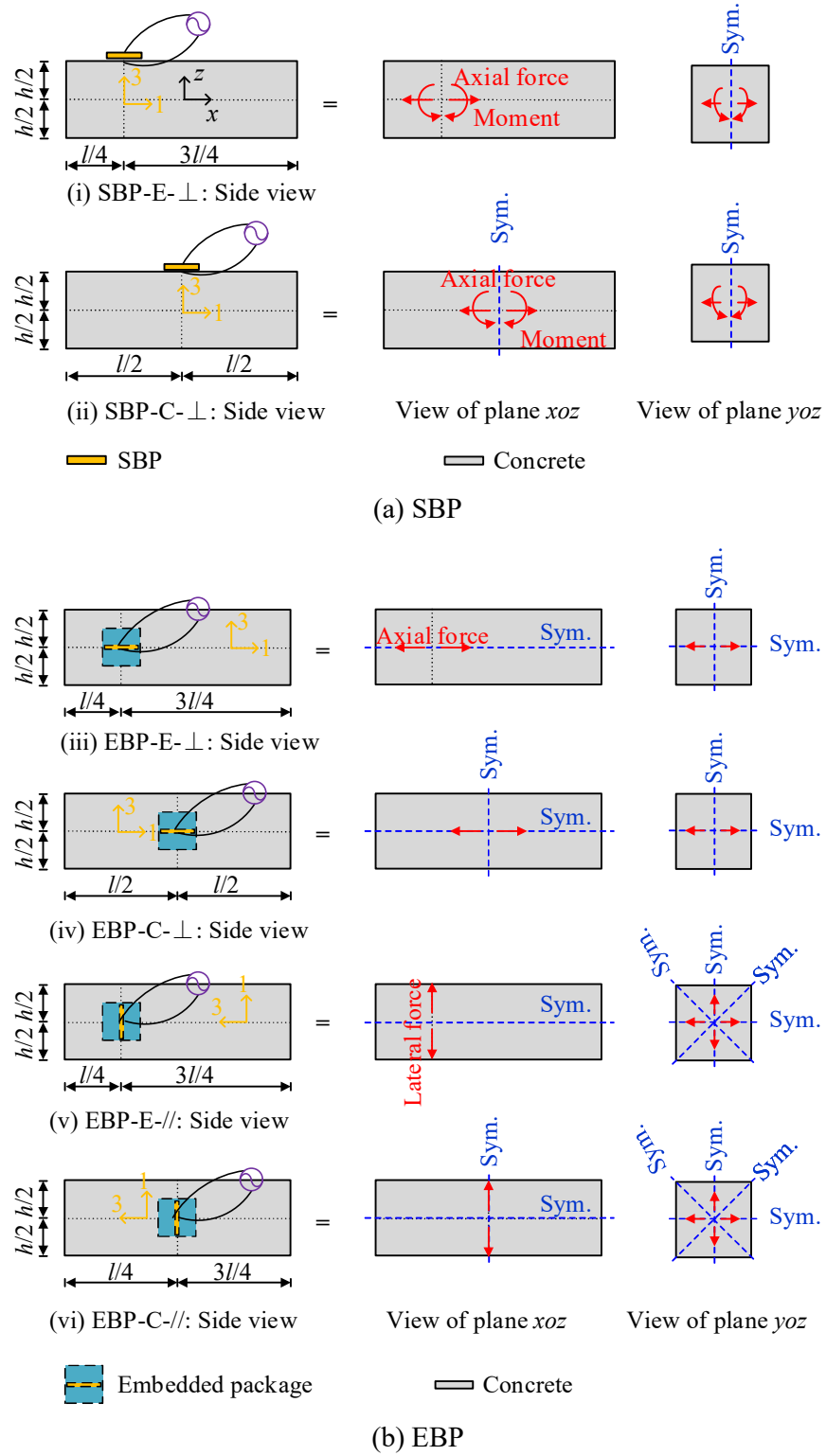


Figure 6.4 Schematic of the actuation type induced by different installation strategies on a concrete prism

### 6.3.2 Modeling of Prisms with PZT Sensors

FEM is considered an effective tool to simulate the dynamic interactions between the PZT sensors and host structures [Tang et al., 2020; Lu et al., 2020]. ANSYS is employed to investigate the collected signals by the EMI technique in this chapter. This subsection introduces the basic information of the numerical models.

The standard concrete prism (i.e.,  $150 \times 150 \times 550 \text{ mm}^3$ ) installed with PZT sensors was modeled. The layout of the six installations of PZT patches is shown in Figure 6.3. A half model was used to facilitate the calculation, given the symmetry at plane  $xoz$ . Chapter 3 has demonstrated that a large and thin PZT patch is preferred for laboratory-scale concrete members because it produces a clear spectrum (i.e., large amplitude and high signal-noise ratio). Therefore, a PZT patch, with a size of  $20 \times 20 \times 1.0 \text{ mm}^3$ , was used for simulations and experiments in the following section. The element type Solid5 was used to model the PZT patch. The properties of PZT material provided by the suppliers, including permittivity constants, piezoelectric constants, and mechanical properties, are listed in Table 3.1. A PZT patch can be directly installed on the surface of the target structure using a rigid bond (e.g., epoxy). The adhesive layer for the SBP was 0.5 mm thick, and the area was the same as the PZT patch. In contrast, a coating package is required to protect an embedded sensor. The details of the embedded sensor, including the structure of the coating, geometric dimensions, and material type, are presented in Figure 6.2 and Table 6.3.

The element type Solid45 was used for the three materials. The material properties of the adhesive layer, coating material (i.e., granite) for the EBP, and concrete are summarized in Table 6.3. The material properties of epoxy and granite were provided by the suppliers, whereas common properties were used for concrete. The PZT patch was excited by a sinusoidal voltage of 1 V along the polarization direction (i.e., along the 3-axis) in a wide frequency range of 0-20 kHz (step:0.1 kHz). The mesh size for the PZT and adhesive material was 0.25-mm. The mesh size for granite and concrete was 0.5 mm and 2.5 mm, respectively. The mesh sizes of these materials satisfy the

requirement for harmonic analyses [Zhao et al., 2020]. The interfaces between any two different materials were assumed to be fully bonded. Regarding the contact element for the interfaces, the element type Target170 was employed for target areas, whereas Contact174 was used for contact areas.

Table 6.3 Material properties of epoxy and concrete for simulation

Material	Properties			
	Density (kg/m <sup>3</sup> )	Modulus of elasticity (GPa)	Poisson's ratio	Damping ratio
Epoxy	1600	4	0.38	0.012
Granite	2710	57	0.30	0.008
Concrete	2300	30	0.20	0.008

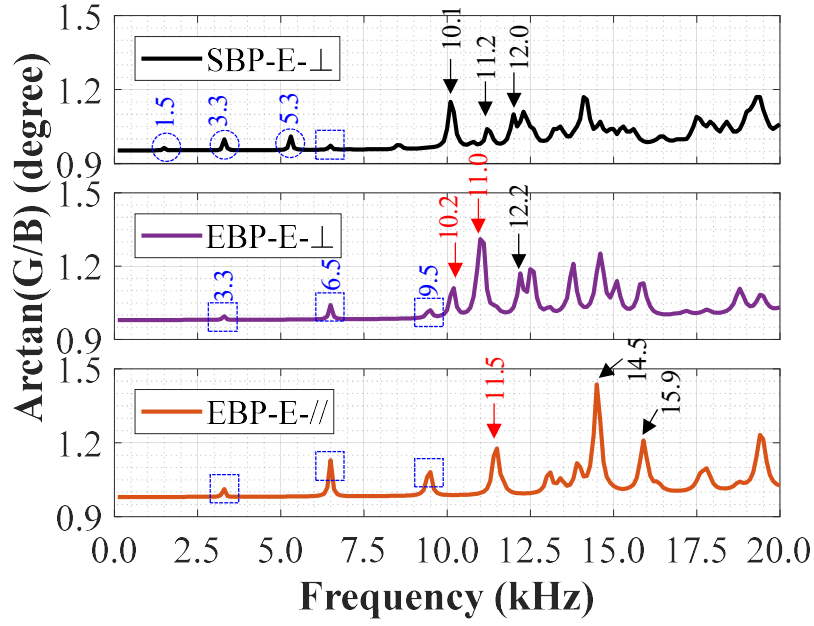
### 6.3.3 Length-insensitive Modes Captured by Proposed Installation Strategies

This subsection discusses the signal spectra, and the corresponding mode shapes from the numerical simulations. The complementary angle of the phase (i.e.,  $\arctan(G/B)$ ), which was recommended and proven effective in Chapter 3, was employed to analyze the signal spectra.

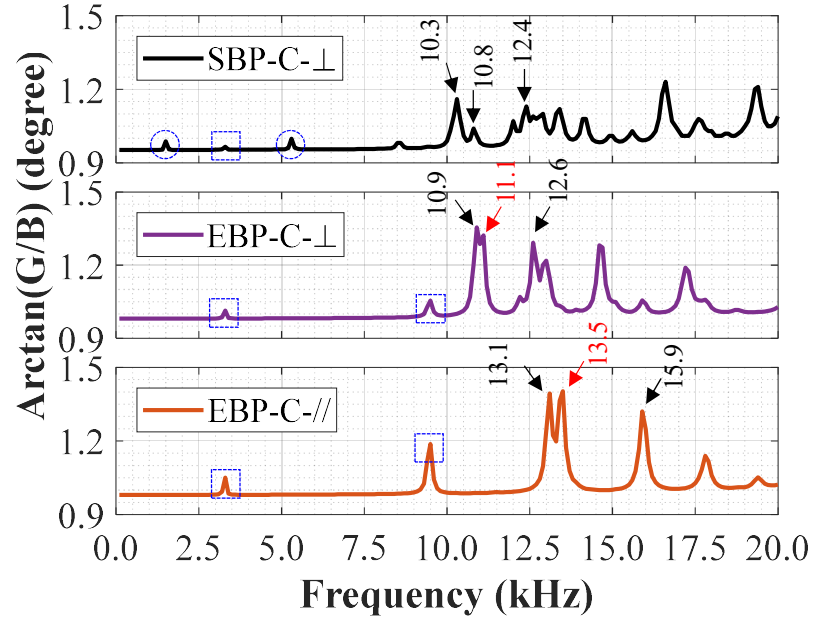
Figure 6.5 presents the simulated EMI spectra obtained from the PZT patches using six installation strategies on the concrete prism ( $150 \times 150 \times 550 \text{ mm}^3$ ). The signals are presented for different locations along the  $x$ -axis (i.e.,  $x=l/4$  and  $x=0$ ). The frequencies of the peaks of interest in each strategy are labeled in the spectra in Figure 6.5, where the values near the peaks show their frequencies. Figure 6.6 illustrates the corresponding mode shapes of the extracted classic and selected modes for each installation strategy. The EBP sensors were placed on the right of the prism at  $x=l/4$ . The labels of the mode shapes are categorized into three groups: classic low-order modes, high-order longitudinal or bending modes, and length-insensitive modes. These three groups of modes are labeled by different markers in Figure 6.5. The classic modes consist of the first three bending and longitudinal modes, marked by circle and square symbols, respectively. The number and letter in the name refer to the order and its modal type, respectively. For example, 1-B and 1-L refer to the first bending and longitudinal

modes, respectively. Black arrows mark high-order modes (longitudinal or bending). Length-insensitive modes, as mentioned in [Figure 6.2](#), are labeled by red arrows. [Figures 6.5](#) and [6.6](#) are discussed at the same time for effective description.

The peaks in the frequency range below 10 kHz are sparse and have weak amplitudes, especially below 3 kHz (e.g., the first peak in the SBP-E- $\perp$  is 1.5 kHz). By contrast, the modes are dense in the frequency range from 10 kHz to 20 kHz with some distinct peaks, as shown in [Figure 6.5\(a\)](#). As the number of symmetric planes increases from one (i.e., SBP-E- $\perp$ ) to five (i.e., EBP-C-//), the number of peaks shown in the spectra decreases significantly. For example, in the case of EBP-C-//, only five peaks are presented in the spectrum, as shown in [Figure 6.5\(b\)](#). The decreasing trends in the number of modes are consistent with the discussion in [Table 6.1](#).

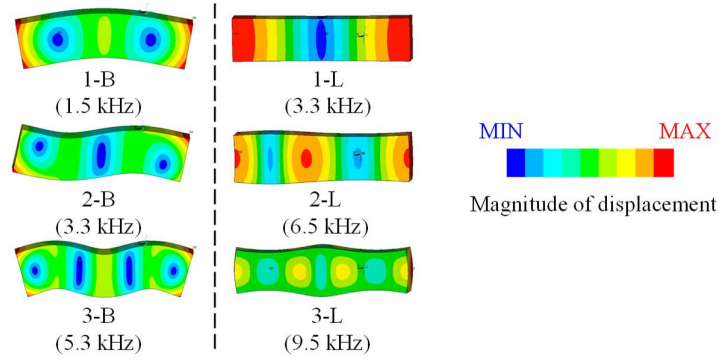


(a) Relative position:  $//4$

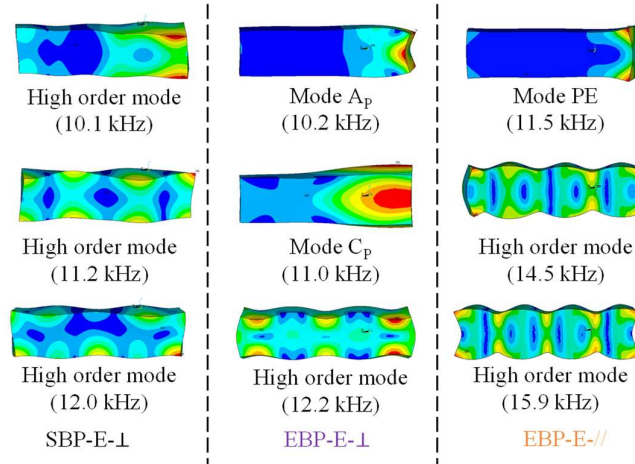


(b) Relative position:  $x=0$

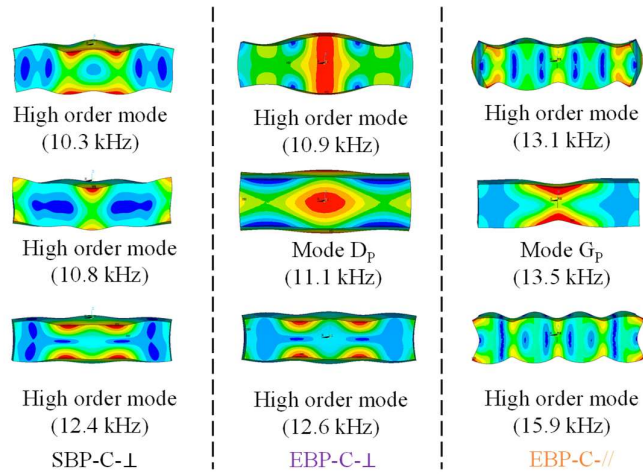
Figure 6.5 EMI peaks and the corresponding resonant modes in different relative positions (Peaks marked by circle and square symbols represent bending and longitudinal modes, respectively. Peaks labelled by black and red arrows are high-order modes and target length-insensitive modes, respectively.)



(a) Classic bending and longitudinal modes



(b) Selected modes corresponding to distinct peak at  $x=l/4$



(c) Selected modes corresponding to distinct peak at  $x=0$

Figure 6.6 Classic modes and selected modes from the different installation strategies



Meanwhile, the amplitudes of the peaks increase as the numbers of the symmetric planes increase (from the SBP to EBP). This finding will be helpful for mode identifications. For example, the relative amplitudes of mode 1-L (peak marked by the square symbol at 3.3 kHz) for the SBP-C- $\perp$ , EBP-C- $\perp$ , and EBP-C-// are 0.012 degrees, 0.061 degrees, and 0.201 degrees, respectively, as shown in [Figure 6.5\(b\)](#). Similar trends are observed for other longitudinal modes. Therefore, the installation strategy with more symmetric planes presents a higher sensitivity for the longitudinal modes. For modes larger than 10 kHz, no trend regarding the relative peak amplitudes is observed, given that different resonant modes are captured. In terms of the corresponding mode shapes, the peaks below 10 kHz correspond to bending modes (marked by blue circles) and longitudinal modes (marked by blue squares), as shown in [Figure 6.6\(a\)](#). The SBP can capture bending and longitudinal modes in small amplitude because the moment and axial force are applied simultaneously, as shown in [Figure 6.4\(a\)](#). In contrast, EBP can capture longitudinal modes only since they are placed on the neutral axis, as shown in [Figure 6.4\(b\)](#). Moreover, mode 1-L is overlapped by mode 2-B in the spectrum of SBP-E- $\perp$ .

Peaks larger than 10 kHz include the target length-insensitive modes and high-order bending and longitudinal modes. Distinct peaks are found in the frequency range of 10-20 kHz because they represent local modes that may have larger deformation around the sensor. The first three distinct peaks are labeled by arrows for each strategy, and their corresponding mode shapes are presented in [Figures 6.6\(b\)](#) and [6.6\(c\)](#). Most of the captured modes are high-order longitudinal or bending modes according to their mode deformation. But the target length-insensitive modes are also captured. For example, modes  $A_P$  and  $C_P$  are captured by the EBP-E- $\perp$ , and mode  $E_P$  is captured by EBP-E-//. These modes demonstrate that the deformation is localized on the right end where the sensor was installed. Similarly, mode  $D_P$  is captured by EBP-C- $\perp$  and mode  $G_P$  is recorded by EBP-C-//, presenting a localized deformation pattern at the center. Meanwhile, these target modes appear in the first two distinct peaks of the spectra in

the frequency range of 10-20 kHz, facilitating identification and accessibility. If the target length-insensitive mode can hardly be differentiated from the other high-order modes (e.g., 13.1 kHz and 13.5 kHz in the spectrum of EBP-C-//, as shown in [Figure 6.5\(b\)](#)), the average frequency for these two modes is recommended considering these two frequencies are extremely close.

In summary, this subsection numerically investigates the performance of various installation strategies in capturing the target length-insensitive modes. The SBP strategies are unsuitable for extracting the target length-insensitive modes, whereas EBP strategies can capture the target modes effectively.

#### **6.3.4 Effects of Lengths and Boundary Conditions on In-plane Modes**

Modes  $A_P$ ,  $C_P$ ,  $D_P$ ,  $E_P$ , and  $G_P$  were extracted in the previous subsection. End modes (i.e., modes  $A_P$  and  $E_P$ ) have been proven effective when a finite-length structure has free ends, such as mild steel rods [[McNiven and Shah, 1967](#)]. The obtained in-plane modes (such as Modes  $C_P$  and  $D_P$ ) may promise to be insensitive to the boundary conditions of two ends. Modes  $C_P$  and  $D_P$  are nearly converged at a small  $l/w$  ratio and are easier to extract in comparison with mode  $G_P$ . Therefore, this subsection discusses the behavior of mode  $C_P$  of prisms with different lengths and boundary conditions to show the advantage of utilizing length-insensitive modes.

[Figure 6.7](#) presents the behavior of mode  $C_P$  in the signal spectra with different lengths when using the installation strategy EBP-E- $\perp$ . Mode  $C_P$  (marked by red arrow) is easy to identify in the obtained EMI spectra for the lengths increased from 0.45 m to 1.50 m (i.e.,  $l/w$  is from 3 to 10). The peak amplitude is large, and the frequency of mode  $C_P$  is nearly unchanged, assuring the feasibility in actual practice. By contrast, mode 1-L is extremely sensitive to the length in terms of its frequency and amplitude. With increases in length, the frequency decreases lower than 3 kHz, and the amplitude becomes too low to identify for the piezoelectric sensor.

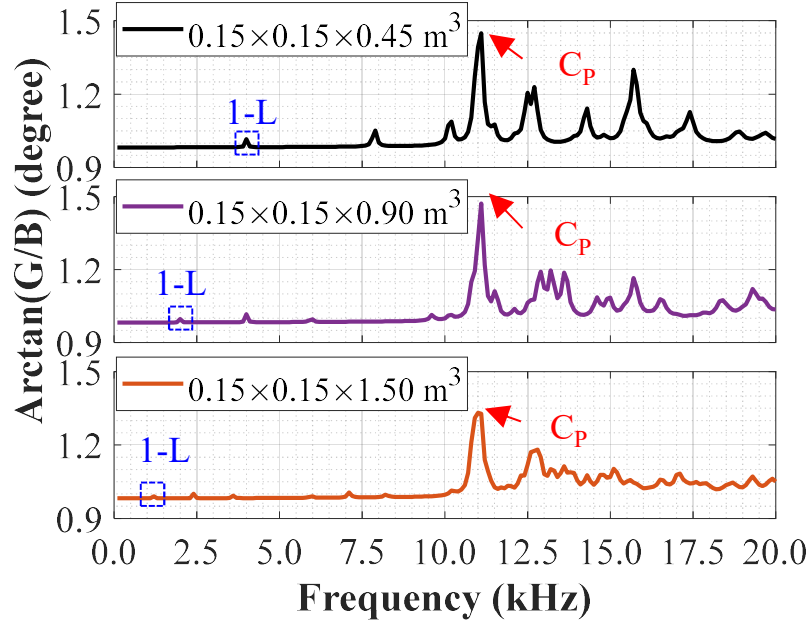
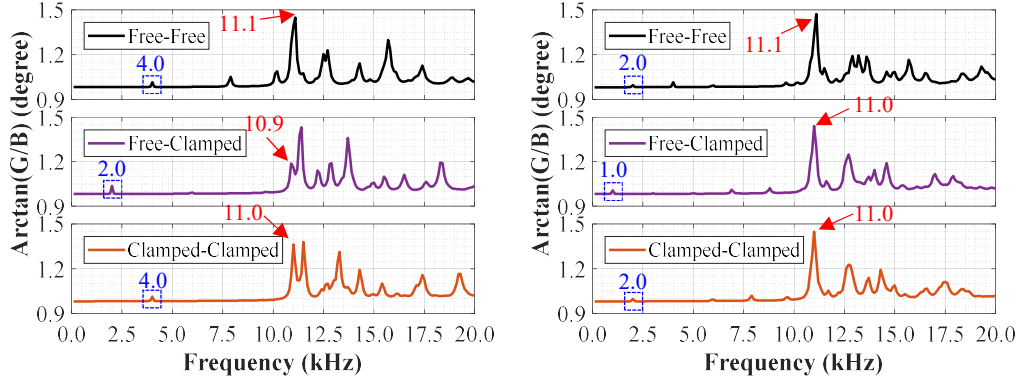


Figure 6.7 Behavior of mode  $C_P$  and mode 1-L of concrete prisms with different lengths (EBP-E- $\perp$ ;  $x=l/4$ )

Figure 6.8 presents the behavior of mode  $C_P$  under three different types of boundary conditions, namely, free-free, free-clamped, and clamped-clamped, where the first and second terms refer to the boundary conditions at two ends of the prisms. Free-clamped and clamped-clamped boundary conditions are common for concrete columns. Two sizes of the prism are used to present the results. For mode  $C_P$  (marked by red arrow), the variations of frequency at these two boundary conditions are lower than 2% (i.e., 200 Hz and 100 Hz for specimens  $0.15 \times 0.15 \times 0.45 \text{ m}^3$  and  $0.15 \times 0.15 \times 0.90 \text{ m}^3$ , respectively). On the contrary, mode 1-L (marked by a blue square) changed dramatically under these three boundary conditions. The identification of mode  $C_P$  is easy in the presented cases, except for the free-clamped boundary conditions in specimen  $0.15 \times 0.15 \times 0.45 \text{ m}^3$ , in which the peak  $C_P$  is not distinct because of the close distance from the sensor to the clamped end. These observations and discussions showed that mode  $C_P$  is promising for actual applications because it is insensitive to both element lengths and boundary conditions.



(a) Specimen:  $0.15 \times 0.15 \times 0.45 \text{ m}^3$

(b) Specimen:  $0.15 \times 0.15 \times 0.90 \text{ m}^3$

Figure 6.8 Behavior of mode  $C_P$  at different boundary conditions (EBP-E- $\perp$ ;  $x=l/4$ )

### 6.3.5 Correlations between Target Frequencies and Modulus of Elasticity

After confirming the extraction of the target modes, this subsection correlates the frequencies of length-insensitive resonant modes to geometric and material properties. The classical model to calculate the resonant frequency is typically based on the assumptions of the Euler-Bernoulli beam [Czekanski and Zozulya, 2020]. The frequency equations for the longitudinal ( $f_{n,L}$ ) modes of an elastic bar at free-free boundary conditions are presented as follows

$$f_{n,L} = \frac{n}{2l} \sqrt{\frac{E_c}{\rho_c}}, \quad n = 1, 2, 3, \dots \quad (6.1)$$

The same equation is also used in ASTM C215 [2019] for mode 1-L. Mode 1-L is sensitive to the length and boundary conditions, and it keeps decreasing with increases in length. Given the concrete properties listed in Table 6.3, when the length of the prism is equal to 600 mm,  $f_{1,L}$  will be equal to 3 kHz, close to the lower limit of the detectable frequency range of piezoelectric sensors, leading to detection difficulties in the EMI-R technique.

On the contrary, it is hard to derive the analytical equations for the target length-insensitive modes. Mindlin [1956] presented an analytical equation for a specific in-plane mode (i.e., mode  $D_P$ ), which is the so-called Mindlin-Lamé mode,

$$f_{ml} = \frac{1}{2w} \frac{1}{\sqrt{1 + \mu_c}} \sqrt{\frac{E_c}{\rho_c}} \quad (6.2)$$

where a square section is assumed (i.e.,  $w = h$ ). By substituting the information used in [Section 6.3.2](#) into the equation, the analytical frequency,  $f_{ml}$ , equals 11.0 kHz, which is very close to the numerical results.

The form in Equation (6.2) is borrowed to describe the other modal frequencies. Each generated frequencies were normalized by  $f_{ml}$  to obtain a coefficient  $\kappa$  for each mode,

$$f_i = \kappa_i f_{ml} = \frac{\kappa_i}{2w_{eq}} \frac{1}{\sqrt{1 + \mu_c}} \sqrt{\frac{E_c}{\rho_c}} \quad (6.3)$$

$$w_{eq} = \sqrt{wh} \quad (6.4)$$

where an average width,  $w_{eq}$ , was used in Equation (6.4) when the cross-section is not a perfect square.

[Table 6.4](#) summarizes the normalized frequency of the selected length-insensitive resonant modes. The frequencies were obtained through modal analyses using ANSYS, which has the same setting as in [Section 6.2](#). The modulus of elasticity, density, and Poisson's ratio of concrete was 30 GPa, 2300 kg/m<sup>3</sup>, and 0.2, respectively. The  $l/w_{eq}$  ratio ranged from 3.0 to 20.0. Prisms in two width types (i.e., 100 and 150 mm) were used for regression. Meanwhile, two cases with width (i.e., 150 mm) unequal to height (i.e., 120 and 135 mm) are included to discuss the applicable range of the proposed assessment. The coefficient  $\kappa$  for modes A<sub>P</sub>, C<sub>P</sub>, D<sub>P</sub> and E<sub>P</sub> converged rapidly after  $l/w_{eq} \geq 3.0$ , indicating that these resonant modes become insensitive to the length. The coefficient  $\kappa$  for modes F<sub>P</sub> and G<sub>P</sub> converged after  $l/w_{eq} \geq 5.0$ ; and thus,  $\kappa$  values from the linear interpolation are recommended for  $l/w_{eq} < 5.0$ . The coefficient  $\kappa$  for mode B<sub>P</sub> was not useful for  $l/w_{eq} < 5.0$  and converged after  $l/w_{eq} \geq 10.0$ . Furthermore, the deviation in the section dimensions was discussed using the studied standard prism. With variations in  $h/w$  from 1 to 0.90 (i.e., height from 150 mm to 135 mm), the maximum difference was only 2.2% for all modes. However, the maximum difference

was up to 6.6% for all modes when the  $h/w$  ratio was 0.8, indicating that the proposed assessment can only be suitable to the nearly square cross-section prism ( $0.9 \leq h/w \leq 1.0$ ).

Table 6.4 Regressed coefficients for the target length-insensitive modes

Geometric information				$\kappa$ for each target mode						
$h$ (m)	$w$ (m)	$l$ (m)	$l/w_{eq}$	A <sub>P</sub>	B <sub>P</sub>	C <sub>P</sub>	D <sub>P</sub>	E <sub>P</sub>	F <sub>P</sub>	G <sub>P</sub>
0.150	0.150	0.450	3.0	0.91	-	0.99	1.00	1.03	1.17	1.24
0.150	0.150	0.550	3.7	0.91	-	0.99	1.00	1.03	1.15	1.21
0.150	0.150	0.750	5.0	0.91	0.98	1.00	1.00	1.03	1.12	1.20
0.150	0.150	0.900	6.0	0.91	0.99	1.00	1.00	1.03	1.12	1.20
0.150	0.150	1.200	8.0	0.91	0.99	1.00	1.00	1.03	1.12	1.19
0.150	0.150	1.500	10.0	0.91	1.00	1.00	1.00	1.03	1.12	1.19
0.150	0.150	2.000	13.3	0.91	1.00	1.00	1.00	1.03	1.12	1.19
0.150	0.150	3.000	20.0	0.91	1.00	1.00	1.00	1.03	1.12	1.18
0.100	0.100	0.300	3.0	0.91	-	0.99	1.00	1.03	1.17	1.24
0.100	0.100	0.500	5.0	0.91	0.98	1.00	1.00	1.03	1.12	1.20
0.100	0.100	1.000	10.0	0.91	1.00	1.00	1.00	1.03	1.12	1.19
0.100	0.100	1.500	15.0	0.91	1.00	1.00	1.00	1.03	1.12	1.19
0.100	0.100	2.000	20.0	0.91	1.00	1.00	1.00	1.03	1.12	1.18
<b>Convergence value</b>				<b>0.91</b>	<b>1.00</b>	<b>1.00</b>	<b>1.00</b>	<b>1.03</b>	<b>1.13</b>	<b>1.18</b>
0.150	0.150	0.550	3.7	0.91	-	0.99	1.00	1.03	1.15	1.21
0.135	0.150	0.550	3.8	0.89	-	0.98	0.99	1.05	1.15	1.22
0.120	0.150	0.550	4.1	0.85	-	0.93	0.94	1.10	1.16	1.26

So far, correlations have been established between the frequencies of the target length-insensitive modes and material properties. The proposed EMI-R technique for evaluating the modulus of elasticity using prisms and length-insensitive modes is summarized as follows:

1. Measure/estimate the mass and dimension of the prism specimen.
2. Choose the sensor installation strategy. Installation strategies EBP are preferred to extract target length-insensitive modes. The four proposed EBP strategies are recommended for measuring the modulus of elasticity. In contrast, the installation strategies SBP have difficulty in extracting length-insensitive modes.
3. Measure the signal spectrum covering the target frequency range and identify

the target length-insensitive modes corresponding to the selected EBP installation strategy, as shown in [Figures 6.5–6.6](#). In EBP-E- $\perp$ , modes  $A_P$  and  $C_P$  should be used. In EBP-C- $\perp$ , mode  $D_P$  should be used. In EBP-E- $\parallel$  and EBP-C- $\parallel$ , modes  $E_P$  and  $G_P$  should be used, respectively.

Calculate the modulus of elasticity by using Equations (6.3–6.4), and the coefficient  $\kappa$  of each target mode is shown in [Table 6.4](#).

## 6.4 Experimental Validations

Seven concrete prisms were cast and tested to validate the effectiveness of the proposed EMI-R technique built on length-insensitive modes and specially designed sensor installation strategies.

### 6.4.1 Experimental Design and Preparation

The PZT patches and embedded sensors used in the experiments are presented in [Figure 6.9](#). The PZT patches with wrapping electrodes (i.e., the electrode of the bottom surface is wrapped to the top surface) were selected ([Figure 6.9\(a\)](#)). The advantage of this type of electrode is that it can ensure the flatness of the bonding interface so that the installations of the embedded sensor can be installed at target orientations. This type of PZT patch ( $20 \times 20 \times 1.0 \text{ mm}^3$ ) was used not only as SBP but also for embedded package fabrication. [Figure 6.9\(b\)](#) illustrates the embedded sensors in this study. Two types of coating, namely, granite and high-strength mortar, were used to ensure that the proposed framework can accommodate different designs of embedded PZT sensors. The structures and geometric size (i.e.,  $30 \times 30 \times 30 \text{ mm}^3$ ) of the embedded package were the same as in [Figure 6.3](#). The embedded package was assembled with two blocks and one PZT patch. The PZT patch was initially bonded to one block, which was cut with a groove for PZT patch placement, and then the remaining block was assembled using epoxy (Araldite 2014-1). The properties of the PZT, epoxy, and granite were provided by suppliers and listed in [Tables 3.1](#) and [6.3](#). The mix proportions of the high-strength mortar were from [Dawood and Ramli \[2011\]](#). The density, modulus of elasticity, and Poisson's ratio of the mortar at 28-day curing age were  $2280 \text{ kg/m}^3$ ,  $28.5 \text{ GPa}$ , and

0.02, respectively.

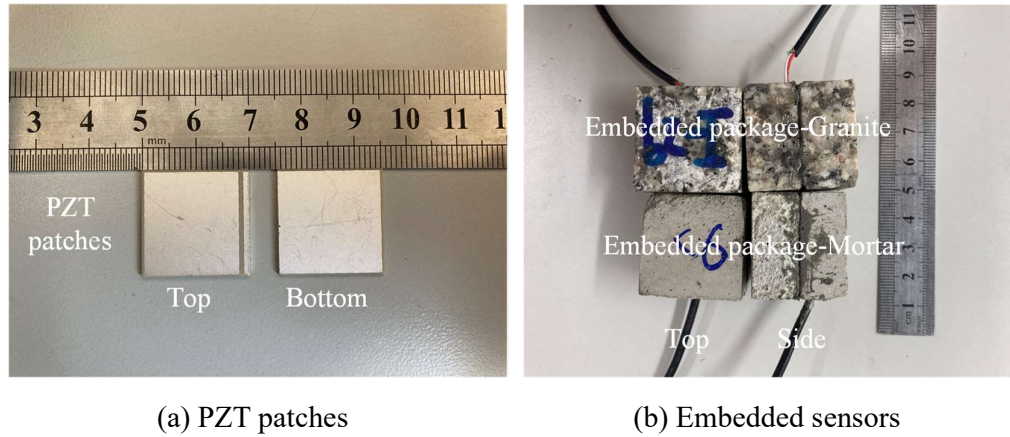


Figure 6.9 PZT patches and embedded sensors used in this chapter

Figure 6.10 presents the layout of the SBP and EBP sensors in the tested prisms. Prisms with a size of  $150 \times 150 \times 550 \text{ mm}^3$  were utilized to measure the modulus of elasticity, while prisms in the other size (i.e.,  $100 \times 100 \times 300 \text{ mm}^3$ ) were employed to study the effect of end boundary conditions. To show the sensors clearly, the figure is not drawn to the scale. In the experiments for measuring the modulus of elasticity, seven prism specimens in total were cast in four separate batches (at different dates with one-week intervals) considering the variable properties of concrete. The mix proportions of the tested normal and seawater sea-sand concrete are presented in Tables 4.8 and 6.5, respectively. All six strategies were applied in three specimens from P1 to P3. Prisms P1 and P2 installed with EBPs coated with granite cast in the same batch (i.e., Batch I) with the same sensor layout to investigate the stability of each installation strategy. The prism P3 installed with EBPs coated with mortar was cast individually (i.e., Batch II) to confirm the applicability and generality for embedded sensors with different coating packages. Because one prism only has one center point, the reproducibility of the installation strategy EBP-C-// can be studied in different prisms (i.e., P3 and P5). Prisms P4 and P5 installed with EBPs coated with granite were cast in the same batch (i.e., Batch III) to investigate the consistency of the results for one specific installation strategy of EBP in the same prism. The volumetric ratio of embedded package size to the specimen size is low (i.e., 0.22%). Thus, the influence of the selected embedded



package on the resonant frequencies in the selected frequency range is limited and can be ignored. In the experiments for investigating the effect of end boundary conditions, prisms P6 and P7 were cast in a new batch (i.e., Batch IV). The numbers and types of the sensors used in these prisms are summarized in [Table 6.6](#).

Table 6.5 Material proportions of the adopted concrete materials

Type	Mix proportion, by weight	Density (kg/m <sup>3</sup> )
Seawater sea-sand concrete	C: SW: SS: FA: PFA: SP <sup>a</sup> =1:0.374:1.851:2.404:0.275: 0.021	2390

<sup>a</sup>C= cement; SW= seawater; SS=sea-sand; FA= 10 mm aggregate; PFA=pulverized fuel ash; SP=superplastic.

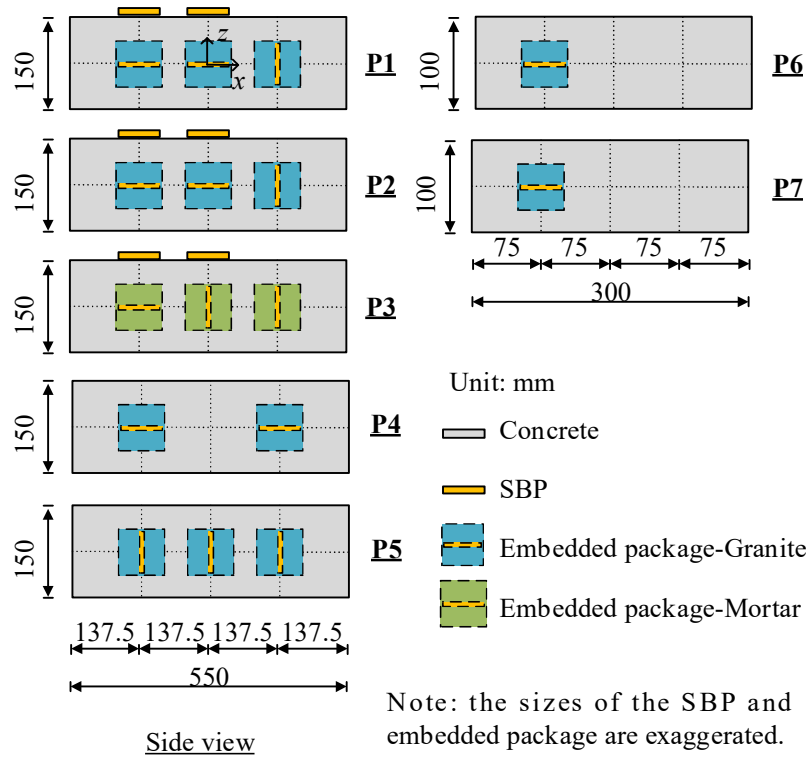


Figure 6.10 Design of layout of sensors in each specimen

Table 6.6 Summary of sensors and installation strategies for prisms P1–P7

ID	Type numbers of sensors for each installation strategy						Strategies In total	Batch
	SBP-E- $\perp$	SBP-C- $\perp$	EBP-E- $\perp$	EBP-C- $\perp$	EBP-E-//	EBP-C-//		
P1	1	1	1	1	1	0	Five	I
P2	1	1	1	1	1	0	Five	I
P3	1	1	1	0	1	1	Five	II
P4	0	0	2	0	0	0	One	III
P5	0	0	0	0	2	1	Two	III
P6	0	0	1	0	0	0	One	IV
P7	0	0	1	0	0	0	One	IV
Total	3	3	7	2	5	2	Six	-

Note: 22 sensors in total were used in the tests

In addition to the prisms, three identical standard cylinders, with a 150-mm diameter and 300-mm height, were prepared in each batch to measure the static modulus of elasticity ( $E_{cs}$ ) and compressive strength ( $f'_c$ ). [Figure 6.11](#) illustrates the standard destructive tests conducted at 28 days after casting. The tests were performed using a 340-ton uniaxial compression machine. The specimens were capped in advance to ensure the flatness of the end. Four strain gauges (Model: BX120-50AA) were bonded to each specimen to measure the axial deformation during the loading. The specimens were cured and tested at a room temperature of 20 °C. [Table 6.7](#) presents the static modulus of elasticity and strength of concrete determined according to [ASTM C469/C469M \[2020\]](#) and [ASTM C39/C39M \[2022\]](#), respectively. For the normal concrete, the coefficient of variation (CoV) for  $E_{cs}$  within each batch was 2.7%, 6.8%, and 8.3%. Compared with  $E_{cs}$ , the values of  $f'_c$  present relatively smaller CoVs within batches for normal concrete, having a maximum CoV value of 3.9% within each batch. For seawater sea-sand concrete, the values of CoV for  $E_{cs}$  and  $f'_c$  are 6.2% and 5.6%, respectively.



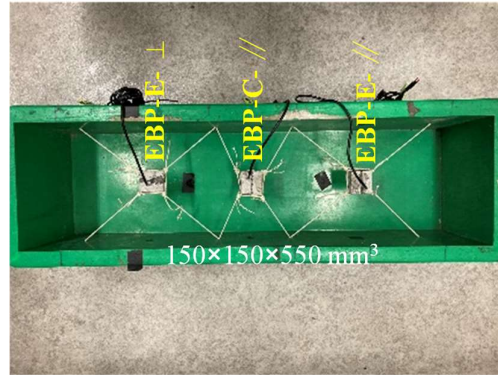
Figure 6.11 Standard static tests for the modulus of elasticity

Table 6.7 Static properties of concrete of three batches

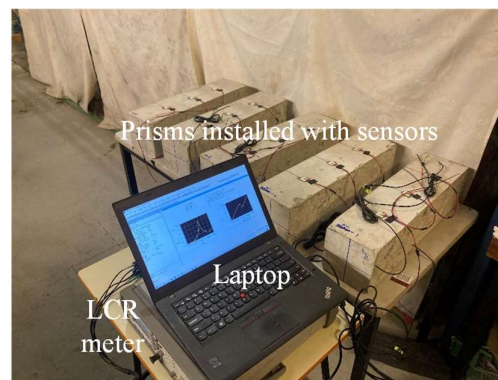
Mix	Batch	$E_{cs}$		$f'_c$	
		Mean (MPa)	CoV (in %)	Mean (MPa)	CoV (in %)
Normal concrete	I	31425	2.7	42.0	3.9
	II	29241	6.8	42.0	2.8
	III	30885	8.3	43.7	3.6
Seawater sea-sand concrete	IV	30066	6.2	40.8	5.6

Figure 6.12 presents the prism specimens for the EMI-R measurements and corresponding experimental setup. The plastic mold of standard prisms with embedded sensors is shown in Figure 6.12(a). The embedded packages were suspended using tensioned wires, which were fixed by the anchors made of steel rods. These wires maintained the embedded sensors in relatively stable positions when vibrating the concrete during the compaction. The SBP sensors were installed after demolding using a quick hardening epoxy (Devcon 14270). Figure 6.12(b) presents the experimental setup for measuring the modulus of elasticity, including a laptop for recording and an LCR meter (Keysight E4980AL) for measuring. The prisms were placed on a wooden table, where the boundary effects could be ignored. The scanning frequency ranged from 1 kHz to 25 kHz with a frequency interval of 50 Hz. The applied voltage was equal to 1 V. The EMI measurements were conducted in the laboratories at a room temperature of 20 °C. The measurements were conducted at 1-day, 7-day, and 28-day curing ages. Table 6.8 summarizes the geometric information and density for each

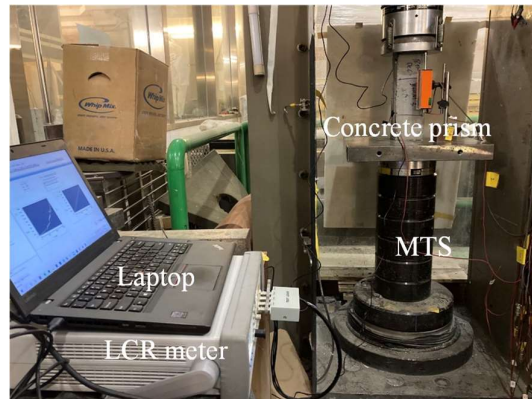
specimen for further analysis.



(a) A plastic mold installed with embedded sensors



(b) Experimental setup for the EMI measurements



(c) Experimental setup for investigating the effect of end boundary conditions

Figure 6.12 Installation of the embedded sensors and experimental setup for the EMI-R measurements

Table 6.8 Geometric information and density for each specimen

ID	Length (mm)	Width (mm)	Height (mm)	Mass (kg)	Density (kg/m <sup>3</sup> )
P1	550	151	150	29.00	2328
P2	550	150	150	28.50	2303
P3	550	150	149	28.75	2339
P4	550	143	150	28.40	2407
P5	550	146	149	28.15	2353
P6	300	99	100	7.02	2365
P7	300	100	100	7.11	2370

Note: the sectional dimension in the casting direction of the specimens is defined as width.

#### 6.4.2 Spectra of Various Installation Strategies in Different Specimens

Figures 6.13–6.15 plot the EMI signal spectra of all 20 sensors in the five prisms from 1 kHz to 25 kHz at 28-day age, where all the signal spectra were plotted using the same  $y$ -scale and  $x$ -scale. The performance of the sensors was discussed and evaluated with regard to the ease of identification (i.e., amplitude) and accessibility for the target modes. To facilitate the discussion, the bending and longitudinal modes are labeled using blue circles and rectangles, respectively, whereas the length-insensitive modes are labeled using red rectangles. The black rectangles refer to the noise in the frequency spectrum. The frequencies of the modes of interest are summarized in Table 6.9.

Figure 6.13 illustrates the EMI signal spectra of the SBP sensors from the specimens P1, P2, and P3. For the classic low-order modes, the fundamental longitudinal mode (i.e., mode 1-L) is difficult to identify in the spectra of SBP-E- $\perp$  because of the overlap by mode 2-B (Figure 6.13(a)). Meanwhile, the amplitude of mode 2-L was weaker (i.e., relative amplitude of 0.13 degrees) than the other bending modes and was overlapped by the noise in the spectrum of P3-SBP-C- $\perp$ . Moreover, the first bending mode (i.e., mode 1-B) was difficult to extract by both SBP strategies because of the low amplitude below 3 kHz and the existence of the measurement noise, indicating poor reproducibility for extracting mode 1-B. Noise was also found in the frequency range of 7-9 kHz for the sensor P3-SBP-C- $\perp$  (Figure 6.13(b)). The SBP

strategies are not discussed in the 10-25 kHz frequency range since they excite closely spaced modes, making it difficult to extract useful modal information. Therefore, the employed SBP strategies are unsuitable for extracting either fundamental resonant frequencies or length-insensitive modes of large concrete elements.

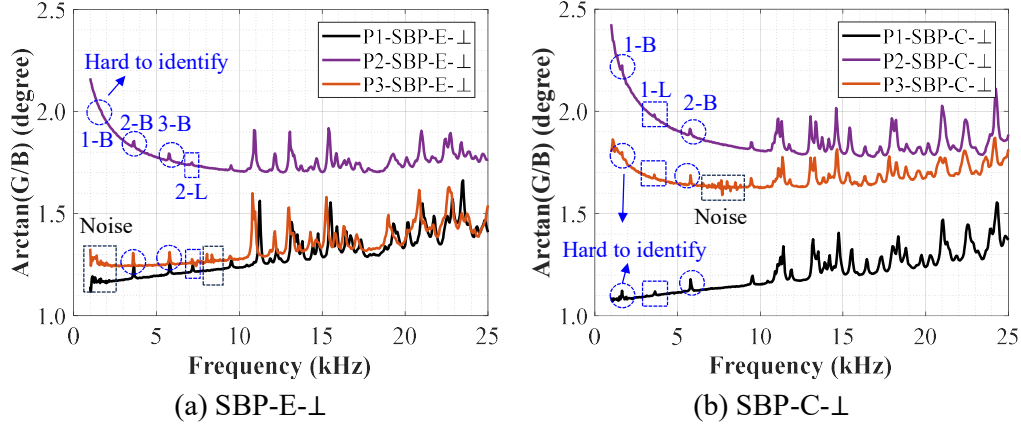


Figure 6.13 EMI Signal spectra of the SBP sensors from specimens P1, P2, and P3 at 28-day age

Figure 6.14 presents the EMI signal spectra of the EBP sensors at  $x=l/4$ . Figures 6.14(a) and 6.14(b) demonstrate the behaviors of the two strategies in different prisms. For strategy EBP-E- $\perp$ , modes 1-L and 2-L have relatively large amplitude for identification, as shown in Figure 6.14(a). Mode 3-L is extremely close to mode  $A_P$  but has a smaller amplitude. Mode  $C_P$  indicates the distinct peak in the middle frequency range. Peaks larger than 13 kHz are in relatively small amplitudes, and no distinct peaks can be found. For strategy EBP-E- $\parallel$ , modes 1-L, 2-L, and 3-L have larger amplitudes for identification compared with the previous strategies, as shown in Figure 6.14(b). Meanwhile, mode  $E_P$  has a relatively large amplitude and can be easily identified because the number of modes is greatly reduced in the frequency range of 10-15 kHz. In these prisms, two EBP-E strategies show excellent reproducibility for the target modes. Although the embedded sensors in P3 had different coating layers (i.e., high-strength mortar), they presented the same performance as the granite coating layers, indicating that the packaging materials only slightly affected the detected resonant frequencies, given that the selected size of embedded package corresponded to a small

volumetric ratio (i.e., 0.22%).

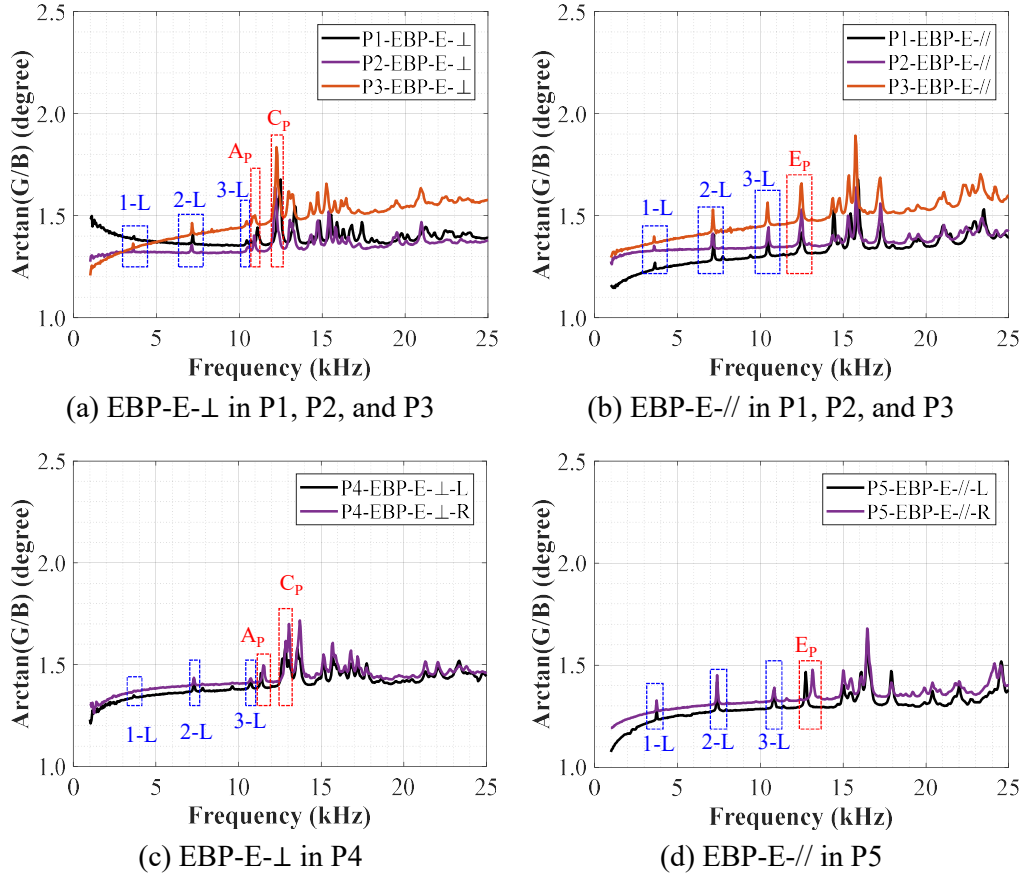


Figure 6.14 EMI Signal spectra of the EBP sensors at  $x=l/4$  at 28-day age (L and R in the name of installation strategy represents the sensor was installed on the left and right, respectively)

Figures 6.14(c-d) plot the EMI signals of EBP-E- $\perp$  and EBP-E- $\parallel$  strategies in one prism. The letters L and R in the installation strategy name in specimens P4 and P5 represent the sensors installed on the left and right sides of the prism, respectively. The global resonant peaks obtained by the two sensors aligned nearly perfectly, whereas the resonant frequencies (i.e., modes  $A_p$ ,  $C_p$ , and  $E_p$ ) varied slightly in frequencies. For example, the frequencies of mode  $E_p$  in EBP-E- $\parallel$ -L and EBP-E- $\parallel$ -R are 12750 and 13150 Hz, respectively, corresponding to a 3.1% frequency variation. Such a frequency variation is reasonable, considering that concrete is not homogeneous and EBPs only measure one side of the specimen. For example, the properties of various parts may vary because of the nonuniform distribution of aggregates induced by imperfect

compaction. This variation of the same strategies in one prism validates the target modes (i.e., modes  $A_P$ ,  $C_P$ , and  $E_P$ ) only related to the properties in a limited length.

Figure 6.15 plots the EMI signal spectra of the EBP sensors at  $x=0$ . The figure shows that the number of modes is greatly reduced in the selected frequency range. For strategy EBP-C- $\perp$ , mode  $D_P$  presents a small difference because these prisms were from the same batch (Figure 6.15(a)). For strategy EBP-C- $\parallel$ , less than 10 peaks are captured in the middle frequency range, making these modes easy to identify (Figure 6.15(b)). Mode 2-L disappeared due to its anti-symmetric property about plane  $yo$ . The EBP-C- $\parallel$  presents the largest amplitude for the classic longitudinal modes among the six strategies.

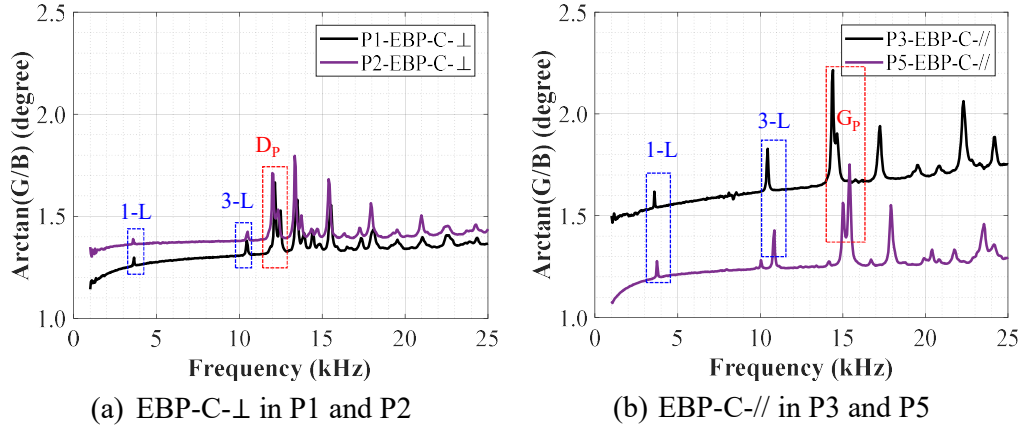


Figure 6.15 EMI Signal spectra of the EBP sensors at  $x=0$  at 28-day age

Table 6.9 Summary of the frequencies of target modes

ID	Frequency (Hz)					
	Global Mode 1-L	Target length-insensitive modes				
		EBP-E- $\perp$		EBP-C- $\perp$	EBP-E- $\parallel$	EBP-C- $\parallel$
		Mode $A_P$	Mode $C_P$	Mode $D_P$	Mode $E_P$	Mode $G_P$
P1	3650	11100	12500	12300	12500	-
P2	3600	10900	12150	12175	12500	-
P3	3600	10950	12250	-	12500	14525
P4-L	3650	11350	12950	-	-	-
P4-R	3650	11500	12900	-	-	-
P5-L	3750	-	-	-	12750	15200
P5-R	3750	-	-	-	13150	-



### 6.4.3 Evaluation Accuracy of Modulus of Elasticity

Based on the captured target length-insensitive modes of concrete prism, the evaluation accuracy of the dynamic moduli of elasticity ( $E_{cd}$ ) was examined in this subsection. Table 6.10 summarizes the evaluation results using the captured target modes by different embedded strategies. These strategies were discussed one by one and compared with the result from mode 1-L. Figure 6.16 presents the comparisons of the moduli of the elasticity using the different strategies, where the evaluation values are normalized by the  $E_{cd}$  from the global mode 1-L for each prism. Figure 6.16(a) illustrates the evaluation results from the strategy EBP-E- $\perp$ . The evaluation results from mode  $A_P$  are almost equal to those from mode 1-L. The average value for the ratio is 1.00, and the maximum error is only 3.5%. Moreover, the results from mode  $C_P$  are relatively larger than those from mode 1-L. The average value for the ratio is 1.07, and the maximum error is 10.0%. Figure 6.16(b) presents the evaluation results from EBP-E-//. Mode  $D_P$  also exhibits very consistent evaluations with Mode 1-L. The average ratio is 0.99, and the maximum error is 6.0%. Strategies EBP-C- $\perp$  and EBP-C-// present consistent average ratios compared with the evaluation results from the global mode (i.e., the average ratio is 1.02 and 0.98 for modes  $D_P$  and  $G_P$ , respectively) (Figures 6.16(c-d)). The maximum difference for the evaluation results from modes  $D_P$  and  $E_P$  is 2.1% and 3.2%, respectively, in comparison with those from mode 1-L.

These findings indicate that the length-insensitive resonant modes from each strategy provide accurate evaluations compared with the traditional dynamic evaluation, except for mode  $C_P$ , which presents a higher evaluation. In summary, EBP-E-// and EBP-C-// are optimal installation strategies considering the ease of mode identification, accessibility, and evaluation accuracy.

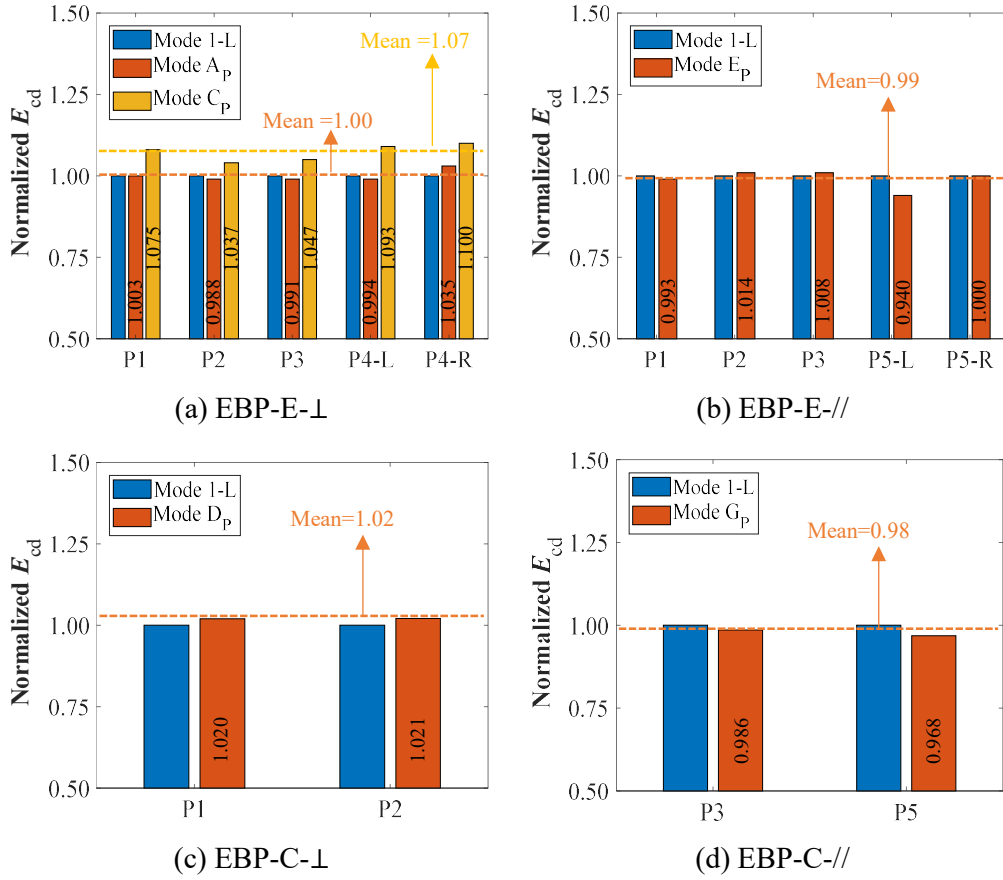


Figure 6.16 Comparisons of moduli of elasticity from different strategies (The results are normalized by  $E_{cd}$  from mode 1-L)

Table 6.10 Summary of evaluations of selected modes using different installation strategies

ID	$E_{cd}$ (MPa)					
	Global	Target length-insensitive modes				
		EBP-E-⊥		EBP-C-⊥	EBP-E-//	EBP-C-//
		Mode 1-L	Mode A <sub>P</sub>	Mode C <sub>P</sub>	Mode D <sub>P</sub>	Mode E <sub>P</sub>
P1	37528	37658	40350	38292	37277	-
P2	36115	35685	37463	36869	36632	-
P3	36679	36333	38420	-	36957	36159
P4-L	38801	38575	42429	-	-	-
P4-R	38801	40143	42679	-	-	-
P5-L	40038	-	-	-	37652	38776
P5-R	40038	-	-	-	40052	-

The comparison between the static and dynamic moduli of elasticity was also presented. The static and dynamic moduli of elasticity are listed in [Tables 6.7](#) and [6.10](#),

respectively. Lydon and Balendran [1986] suggested a linear relationship as follow

$$E_{cs} = 0.83E_{cd} \quad (6.5)$$

The dynamic moduli of elasticity were obtained by using the fundamental longitudinal mode (i.e., mode 1-L) and Equation (6.1) in this chapter. The average ratio of  $E_{cs}/E_{cd}$  for these five prisms is 0.814, which is extremely close to the empirical coefficient of 0.83, indicating the consistency of the presented evaluations. Moreover, the consistent empirical coefficient indicates that the evaluation of  $E_{cd}$  using the length-insensitive modes by the EMI-R technique can be directly used to estimate  $E_{cs}$ .

#### 6.4.4 Advantages of Length-insensitive Modes at Early Curing Age

At an early curing age, the damping ratio of concrete changes significantly [Jordan, 1980]. For example, the decrease in damping between 1-day and 7-day curing age can be as high as 50% [Swamy and Rigby, 1971]. Figure 6.17 compares the signal spectra of each EBP installation strategy at 1-day, 7-day, and 28-day curing ages. For EBP-E- $\perp$ , modes 1-L cannot be observed at 1-day age and are hardly identified at 7-day age, whereas the target modes  $A_P$  and  $C_P$  (especially for mode  $C_P$ ) are relatively easier to access. For the EBP-C- $\perp$ , although mode 1-L can be identified at the three curing ages, mode  $D_P$  presents a much larger amplitude. For EBP-E- $//$ , mode 1-L can only be captured at 28-day age, whereas mode  $E_P$  is easy to reach. The same phenomenon was observed in EBP-C- $//$ . Mode  $G_P$  has a large amplitude for identification and access at the three ages, whereas mode 1-L only works at the 28-day age. The comparison of the signal responses at the early age of concrete shows the superiority of using the target length-insensitive modes, whereas mode 1-L is likely too weak to extract at the early curing age.

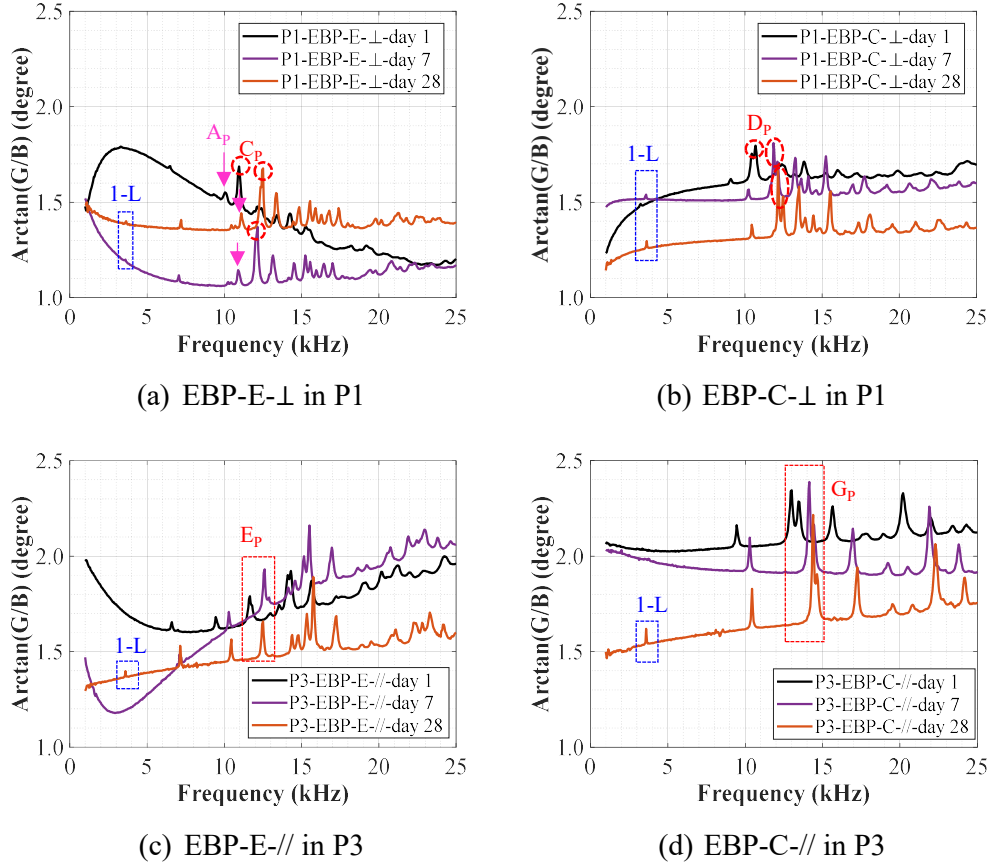


Figure 6.17 The comparison of identification and accessibility of mode 1-L and length-insensitive modes at 1-day, 7-day, and 28-day age

#### 6.4.5 Effect of End Boundary Conditions

Although mode 1-L also provided accurate evaluations in [Section 6.4.3](#), this mode is greatly affected by the element lengths and boundary conditions. Therefore, [Figure 6.12\(c\)](#) presents the experimental setup for investigating the effect of boundary conditions. The prism specimens were placed on the MTS machine during measurement, which was considered free-free boundary conditions. Then, 100 kN force was applied to the specimens to simulate clamped-clamped boundary conditions for measurement. The scanning frequency range was from 1 kHz to 40 kHz with a frequency interval of 100 Hz.

[Figure 6.18](#) presents large variations in the signal spectra under two different boundary conditions. Most peaks shift or disappear after introducing the boundary conditions. But in specimen P6, mode  $C_p$  has slight changes in frequencies (from 19.2

kHz to 19.3 kHz) and amplitudes (Figure 6.18(a)). In specimen P7, mode  $C_P$  also presents an ignorable variation in frequencies (from 18.0 kHz to 18.1 kHz) at these two boundary conditions (Figure 6.18(b)). On the contrary, mode 1-L cannot be identified in both specimens after introducing the boundary conditions. These experimental results indicated that length-insensitive modes (e.g., mode  $C_P$ ) could provide an accurate and robust assessment in complex scenarios with diverse end conditions because of their insensitivity to element lengths and boundaries, showing their superiority over classic fundamental vibration modes.

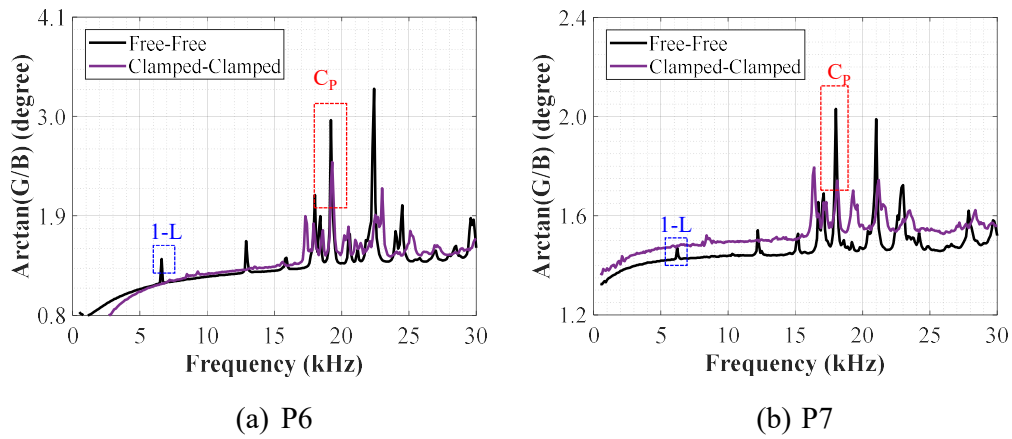


Figure 6.18 Experimental validation of mode  $C_P$  at different boundary conditions

## 6.5 Summary

This chapter presents a systemic investigation of using the length-insensitive resonant modes in the baseline-free EMI-R technique to measure the modulus of elasticity of concrete prisms, which, to the best of our knowledge, has never been reported in the literature. The major conclusions are drawn as follows:

1. The length-insensitive resonant modes of a prism can be found and easily extracted by using the symmetric concept and EBP in the EMI-R technique. At least two and up to five symmetric planes can be achieved using EBP.
2. Six installation strategies considering different interaction types, installation locations, and sensor placement orientations are discussed. The optimal sensor installation strategies (i.e., EBP-E// and EBP-C//) are recommended for

measuring moduli of elasticity in consideration of the ease of mode identification and accessibility.

3. The evaluated moduli of elasticity using the captured length-insensitive modes were consistent with those from the fundamental resonant modes, confirming the effectiveness of the proposed EMI-R technique. Moreover, length-insensitive modes show much larger sensitivity than the fundamental modes, ensuring their workability in general cases (e.g., high damping ratios and long members).
4. Some length-insensitive modes (e.g., in-plane and end modes) showed insensitivity to the boundary conditions at the two ends, providing an effective tool for investigating in-place concrete members. Suitable sensor installation strategies, such as EBP-E- $\perp$  and EBP-C- $\perp$ , are required to extract target in-plane modes.
5. For classic global fundamental modes in the low-frequency range, SBPs are suitable for bending modes, whereas EBP-C- $\parallel$  presented the largest response for the longitudinal modes, whereas EBP-E- $\parallel$  exhibited the greatest number of the longitudinal modes.

This chapter has shown the feasibility of using length-insensitive resonant modes in the baseline-free EMI-R technique, paving a new way toward more general and real-world applications. However, this chapter is only focused on concrete prisms with square sections. Further investigations are needed in the future to extend the proposed method to real concrete structural members (e.g., columns) with diverse cross-sections, boundaries, and steel reinforcement.

## CHAPTER 7 DETECT DELAMINATION OF CONCRETE COVER USING DETACHABLE SENSOR

The motivation for this chapter is that occasional casualties of residents and pedestrians were caused by falling concrete in Hong Kong. The corrosion of steel rebars typically induces concrete spalling and falling. However, there is no effective tool to detect these old buildings quickly and accurately. [Chapters 3–6](#) showed the great promise of the baseline-free EMI techniques in material characterization using fixed PZT sensors.

The EMI technique has been applied to detect delamination damage in the literature. However, fixed sensors limited the applications of the EMI technique in actual practice, especially for damage detection. In this chapter, the baseline-free EMI technique has been extended to detect the delamination of concrete cover using detachable sensors. By designing suitable sensor installation strategies and selecting proper bonding materials, (a) the sensors can be attached and detached easily and quickly, and (b) a stable and reliable EMI measurement can be achieved. Then, a corresponding assessment method is established to evaluate the delamination area through a series of numerical investigations. Laboratory experiments and on-site testing validate the robustness and effectiveness of this method in delamination detection and quick approximate assessment.

### 7.1 Introduction

As reviewed in [Section 2.2.3](#), concrete spalling is commonly observed in RC structures and is usually caused by steel rebar corrosion or freeze-thaw damage. The spalling process is typically induced by corrosion-induced expansion of steel rebars. It reduces the shear resistance of concrete members and poses a significant threat to the safety of occupants, especially in old buildings. For example, in the five years between 1996 and 2000, there were 27 reported incidents because of the concrete spalling in public areas in Hong Kong, resulting in 17 injuries and 2 deaths [[Press Releases, 2001](#)].

Concrete cover spalling often starts from near-surface delamination, typically the separation along a plane roughly parallel to and generally near the surface [Shokouhi et al., 2011]. Early detection of near-surface delamination is crucial for timely maintenance and repair. However, delamination is invisible until it is severe enough to result in surface cracking [Sajid et al., 2022].

Gucunski [2013] compared different NDT methods, including impact-echo, impulse-response, ultrasonic pulse echo, infrared thermography, and ground-penetrating radar, and reported that the impact-echo method was the best technique among them in detecting delamination defects. The impact-echo method can evaluate the condition of concrete plates (e.g., pavement slabs, bridge decks, and thick concrete walls) by analyzing the elastic waves received by displacement sensors, geophones, or accelerometers resulting from a mechanical impact. Kee and Gucunski [2016] utilized an accelerometer with an effective frequency range of up to 10 kHz to detect shallow delaminated areas larger than 254 mm × 305 mm in a concrete bridge deck. However, this large detectable size of the impact-echo method limits its applicability to indoor concrete slabs because local delamination affects areas as small as thousands of square millimeters [Shokouhi et al., 2011].

The EMI approach, as an extension of the mechanical impedance technique, has emerged as a popular damage detection method [Migot and Giurgiutiu, 2023]. Studies have proven that the EMI technique using fixed sensors can detect debonding in adhesive joints and delamination in composite plates by observing new resonance peaks in the spectra [Gresil et al., 2012; Roth and Giurgiutiu, 2017; Migot and Giurgiutiu, 2023]. Although fixed sensors can effectively detect delamination in adhesive and composite materials, using them to detect delamination in concrete structures is challenging. The detectable area of a single fixed PZT sensor is much smaller than the areas of civil engineering structures [Soh et al., 2000], and using arrays of PZT sensors to monitor the whole structure is uneconomical, if not impossible. Fixed sensors are more suitable for monitoring a small critical or repaired zone [Bois and Hochard, 2004].



Meanwhile, the baseline-dependent evaluation method is highly sensitive to sensory systems (i.e., sensors and adhesive materials) and environmental changes (e.g., temperature changes) [Yang et al., 2008a].

The following research gaps are identified from existing studies: (1) An easy-to-use mobile sensing technique that can be implemented in practice is highly desirable for detecting concrete delamination in indoor RC structures, but it has not been investigated so far. (2) A baseline-free evaluation method for quantitative assessment is needed, whose signature characteristics should be physically correlated to delamination size.

To address these research gaps, this chapter developed an innovative EMI technique to detect the delamination of concrete cover by using a detachable (i.e., moveable) PZT sensor. The feasibility of the concept was investigated numerically first by considering the process of concrete spalling. Laboratory experiments on corrosion-induced delamination were conducted to validate the proposed method. In particular, a field measurement was performed in an old building to show the practicality of the developed technique. The rest of the paper is presented as follows. First, the concept of the proposed method is introduced. Subsequently, the effectiveness of the proposed method is examined through a series of numerical investigations, followed by laboratory experimental validations. Last, the practicality of the proposed method for on-site detection is verified.

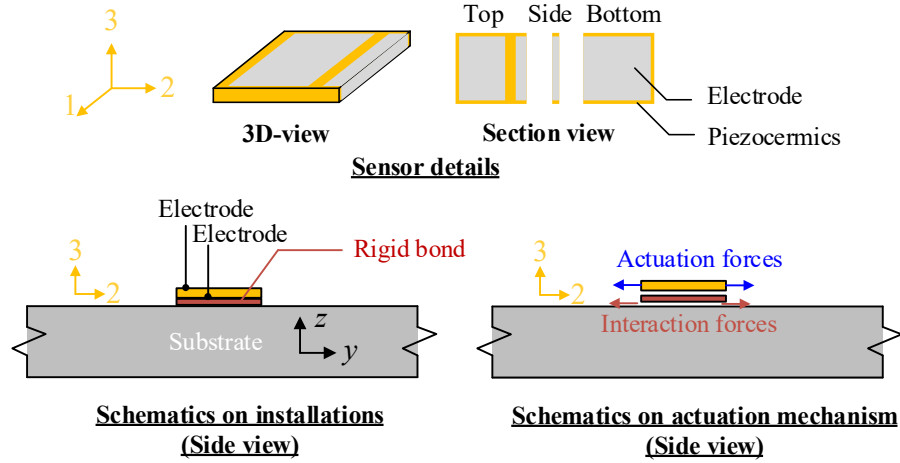
## **7.2 Concept and Principle of Detachable PZT Sensors for Delamination Detection**

### **7.2.1 Detachable PZT Sensors**

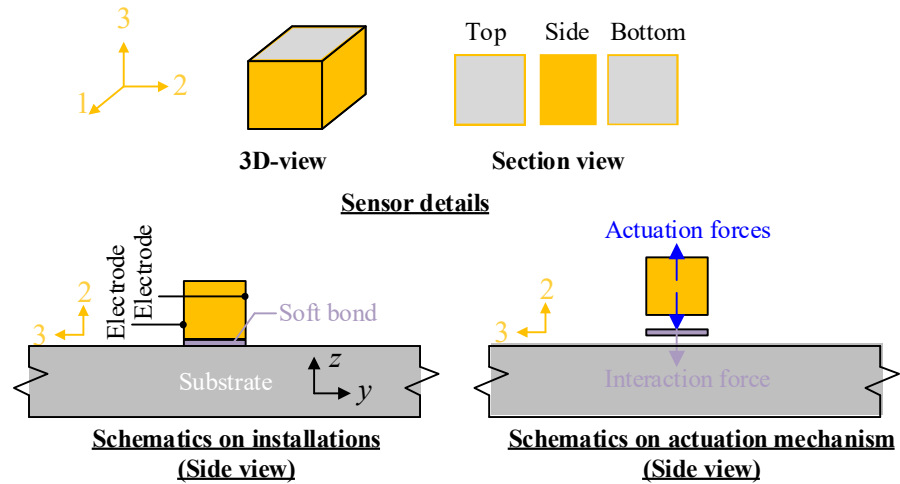
In the traditional EMI technique, patch-shaped piezoelectric sensors (also called piezoelectric wafer active sensors), polarized in the thickness direction, are commonly used for long-term monitoring and short-term NDT [Giurgiutiu, 2014]. The bottom of a patch-like sensor is bonded to a target structure (e.g., a concrete surface) by using an adhesive material (e.g., epoxy). The sensor in the  $d_{31}$  mode excites and senses the in-

plane vibration of the target structure in a wide frequency range (i.e., up to hundreds of kilohertz), as shown in [Figure 7.1\(a\)](#). This type of sensor is thin and unobtrusive when bonded to a surface [\[Roth and Giurgiutiu, 2017\]](#). The yellow coordinate in the figure defines three orthogonal axes of the PZT sensor, which is polarized along Axis-3. Traditionally, a rigid bond between the sensor and the surface is needed to provide good in-plane actuation (i.e., along Axis-1 and Axis-2 directions) [\[ASTM E650/E650M, 2017\]](#). However, a rigid bond makes the PZT sensor nonreusable and limits the mobility of the EMI technique.

Couplant and double-sided types, called soft bonds in this paper, are frequently used in acoustic emission sensor calibration and accelerometer installation for short-term measurements [\[Theobald et al., 2008; Ozman et al., 2021\]](#). They can serve as alternative bonding agents for providing mobility to the PZT sensor. However, most couplants and tapes have low viscosity, so good transmission can only be provided along the motion perpendicular to the contact surface [\[ASTM E650/E650M, 2017\]](#). Therefore, PZT sensors that can actuate perpendicular to the contact surface are desirable when soft bonds are used. A PZT sensor with a large thickness (i.e., rectangular parallelepiped and polarized along Axis-3) is employed as a detachable sensor because it provides an adequate bonding area to actuate and sense motions perpendicular to the contact surface (along the  $z$  axis), as shown in [Figure 7.1\(b\)](#).



(a) Traditional fixed PZT patch



(b) Proposed detachable PZT sensor

Figure 7.1 Actuating mechanisms of the traditional fixed PZT sensor and the proposed detachable PZT sensor (Axes 1, 2, and 3 show the coordinates of the PZT sensor, and Axis-3 is the polarization direction of the piezoceramic sensor)

Figure 7.2 presents the PZT sensor and bonding materials utilized in this chapter. The size of the PZT sensor was  $15 \times 15 \times 12 \text{ mm}^3$ . The electrode surfaces were along the Axis-3 direction (Figure 7.2(a)). Electric wires were welded on electrodes for convenient connection. One side surface without electrodes served as the contact surface. The bonding material was essentially double-sided adhesive tape (3M VHB 5608A) with a thickness of 0.8 mm (Figure 7.2(b)). Like a stethoscope, the PZT sensor can be easily detached from the structure after the measurement and moved to a new



to a rectangle. The inclined cracks (Path 1) can be viewed as a combination of horizontal and vertical cracks.

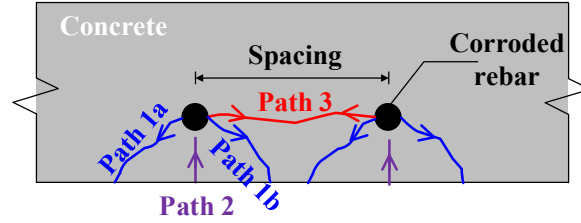


Figure 7.3 Crack types and development process of corrosion-induced spalling

### 7.2.3 Principle of Delamination Detection Using a Detachable PZT Sensor

Figure 7.4 presents the mechanism and principle of using a detachable PZT sensor to detect delamination in the cover of a concrete slab. As shown in Figure 7.1(b), the sensor connected to AC sweeping voltage applies actuation forces perpendicular to the contact surface (along the  $z$  axis). Only the resonant frequency of the attached sensor (denoted by  $f_{PZT}$ ) can be easily identified in the low-frequency range when the checked area is healthy. The attached sensor's resonance in this chapter differs from the resonance of the sensor tested in free-free status. Note that the resonant frequency of the PZT sensor adopted in this chapter is higher than 50 kHz in a free state, but the dominant resonance peak moves to around 12 kHz after being attached to the concrete surface. The low-order vibration modes of the concrete slab can hardly be captured because of the limited actuation force of the PZT sensor and the large mechanical impedance of the host structure in the frequency range below  $f_{PZT}$ . The strain of the PZT sensor induced by AC voltage is larger by at least one order of magnitude than the one induced by the responses of large structures, leading to low sensitivity [Song et al., 2013; Narayanan et al., 2018]. Some high-order structural resonant frequencies (i.e.,  $f_{struc}$ ) can be captured with relatively low amplitude in the high-frequency range above 10 kHz.

By contrast, when the near-surface delamination occurs in a localized area, the delaminated part can be considered a two-way plate with four ends fixed or simply supported. Because of its considerably smaller size than the original slab, the local

resonant vibrations of such a delaminated two-way plate can be actuated easily by the PZT sensor. Consequently, the corresponding local resonant frequencies, known as local defect resonance in composites [Tenek et al., 1993; Solodov et al., 2013; Hu et al., 2024], can be obtained. Unlike deep delamination that is dominated by the thickness stretch mode family, the spectral responses of near-surface delamination (i.e., shallow delamination) are dominated by flexural vibration modes [Kee and Gucunski, 2016]. A series of resonance peaks denoted by  $f_{\text{flex-1}}$ ,  $f_{\text{flex-2}}$ , and  $f_{\text{flex-3}}$ , corresponding to multiple flexural modes of the defect, are distinct in the low-frequency range (below  $f_{\text{PZT}}$ ) in the measured spectra and will be used for defect assessment in this chapter.

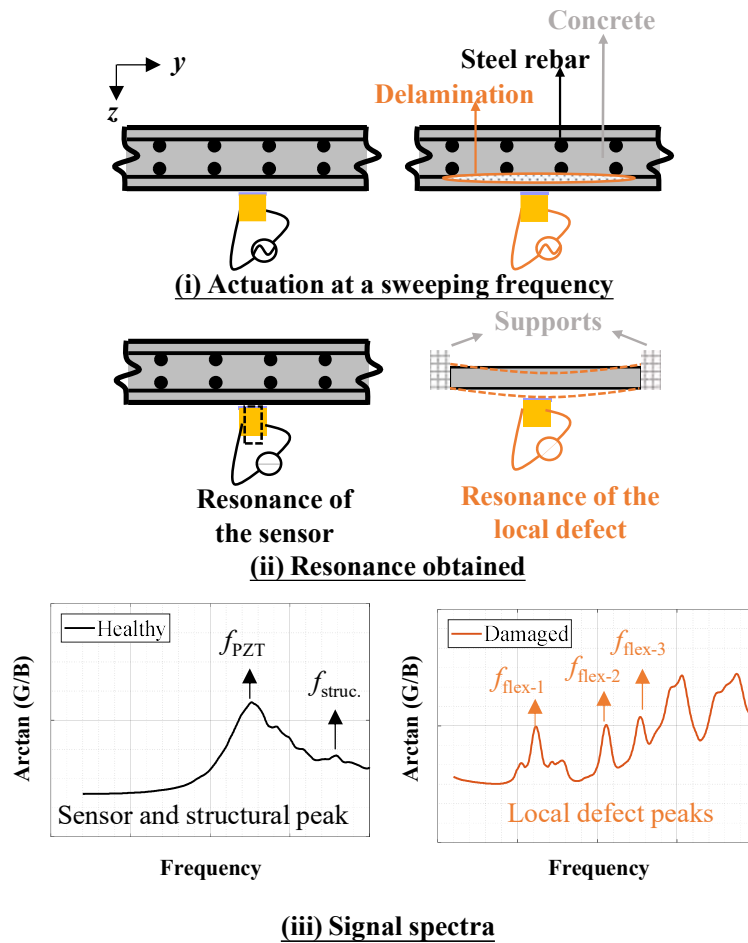


Figure 7.4 Working principle of the detachable sensor for detecting the delamination of the concrete cover of a concrete slab

## 7.3 Numerical Feasibility Study

A series of numerical analyses were conducted to examine the feasibility of the proposed method in this section. The corresponding experimental validation is presented in [Section 7.4](#).

### 7.3.1 Numerical Simulation Model

As explained in [Section 7.2.2](#), horizontal delamination and vertical/inclined cracks play important roles in spalling induced by multiple corroded rebars. Therefore, simplified numerical models were built in consideration of the propagation of the horizontal and vertical cracks using ANSYS. [Figure 7.5](#) shows the finite element model consisting of three materials: concrete, PZT, and adhesive tape materials. Steel rebars were ignored in this model, considering that they are above the delamination and have limited effects on the resonance of the delaminated layer, which was confirmed by numerical comparison. The simulated concrete slab was divided into two parts, namely, the intact and damaged parts. The damaged part was composed of five cuboid subparts. Delamination was simulated by changing the contact between the intact and damaged parts from fully bonded to unbonded interfaces. The contact interfaces were assumed to be flat for simplification, consistent with the modeling by [Li et al. \[2016\]](#), [Solodov et al. \[2013\]](#), and [Kee and Gucunski \[2007\]](#). The four sides of the delaminated part are assumed as vertical surfaces perpendicular to the slab surface.

The simulated concrete slab had the same size (length = 450 mm, width = 350 mm, and height = 120 mm) as that of the tested specimen. The slab size was considerably larger than the detectable range of the sensor, indicating that the boundary conditions can be ignored. Therefore, free boundary conditions were modeled for the concrete slab. The details of the sensor are shown in [Figure 7.2](#). The height of the PZT sensor (i.e., along the Axis-3 direction) was 12 mm, while the electrode area was  $15 \times 15 \text{ mm}^2$ . The bonding layer was modeled as a thin layer having a thickness of 0.8 mm and the same area as the sensor (i.e.,  $15 \times 12 \text{ mm}^2$ ). Most of the adopted parameters are consistent with the experiment setting in [Section 7.4](#).

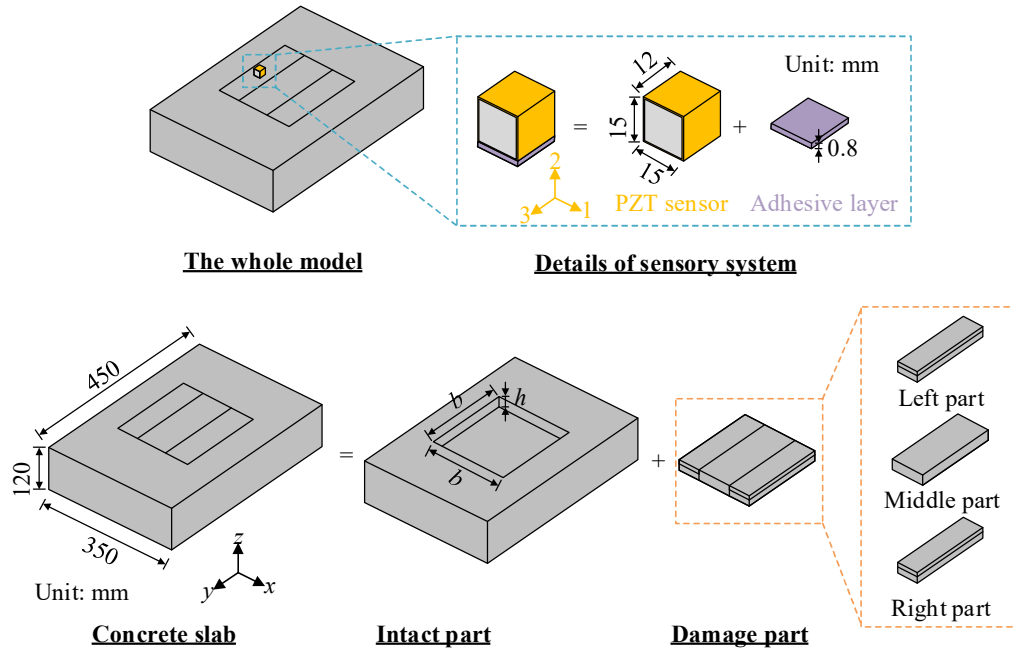


Figure 7.5 Geometric information of the numerical model

The PZT sensor was excited by a sinusoidal voltage of 1 V in the polarization directions (i.e., along the Axis-3) within a frequency range of 0–20 kHz (interval: 0.1 kHz). After a convergence analysis, element mesh sizes of 1.6 and 0.8 mm were selected for the PZT and adhesive materials, respectively; and 2.5- and 30.0-mm mesh sizes were set for the damaged and intact parts, respectively. Unlike the previous simulations in the literature, the interfaces between the PZT sensor, the adhesive layer, and the concrete are assumed to be tied only along the normal direction of the contact surface (i.e., sliding is permitted). The contact interfaces between the intact and damaged parts of the concrete are assumed to be fully bonded in a healthy status. When delamination/cracking occurs, no ties exist between two contact surfaces, and the horizontal and vertical cracks are modeled with zero thickness. [Table 7.1](#) lists the material properties of the adhesion and concrete for the tested specimen in [Section 7.4](#), where the former was provided by the factory and the latter was obtained from the laboratory tests. The PZT properties are the same as those adopted in [Table 3.1](#). The element types for selected materials and contact interfaces are the same as those in [Chapter 3](#).



Table 7.1 Material properties of adhesion and concrete

Material	Parameters	Values
Adhesive materials	Density, $\rho_e$ (kg/m <sup>3</sup> )	680
	Modulus of elasticity, $E_e$ (GPa)	0.085
	Poisson's ratio, $\mu_e$	0.49
	Damping ratio, $\zeta_e$	0.10
Concrete	Density, $\rho_c$ (kg/m <sup>3</sup> )	2368
	Modulus of elasticity, $E_c$ (GPa)	35
	Poisson's ratio, $\mu_c$	0.20
	Damping ratio, $\zeta_c$	0.02

### 7.3.2 Signal Characteristics Regarding Different Damage Level

This section correlates the signal characteristics in the EMI spectra to the different damage levels of near-surface delamination, which is a prerequisite for delamination detection. Figure 7.6 shows multiple damage levels that simulate the whole spalling process. The intact status is considered the control group, where the steel spacing of  $b = 200$  mm and the concrete cover thickness of  $h = 15$  mm are within regular ranges. Five damage levels were simulated, where the horizontal crack width and vertical crack depth were quantified with respect to  $b$  and  $h$ , respectively (Figure 7.6). The label  $0.25b-0.33h$  indicates that the horizontal cracks accounted for 25% of the steel spacing, and the vertical cracks accounted for 33% of the concrete cover thickness. Damage was considered to occur simultaneously at the two rebars. The horizontal cracks initiated from the two rebars and propagated horizontally to each other, eventually becoming one delaminated layer. Meanwhile, the vertical cracks were assumed to occur and propagate on three sides simultaneously. The simulated damage development was consistent with the cracking process shown in Figure 7.3 and that reported by Zhang and Su [2021]. The sensor was installed on a fixed checkpoint (i.e.,  $x = -3b/8$  and  $y = 0$ ) on the bottom surface of the left delaminated area.

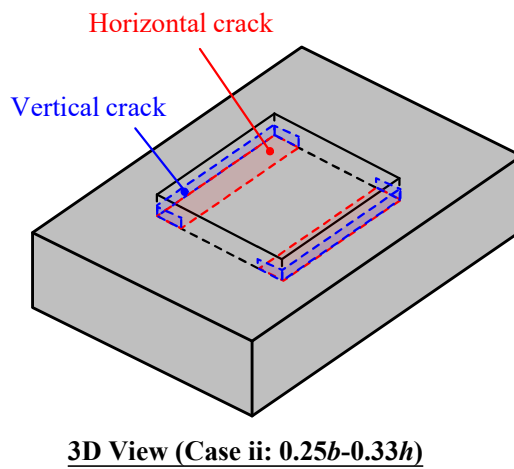
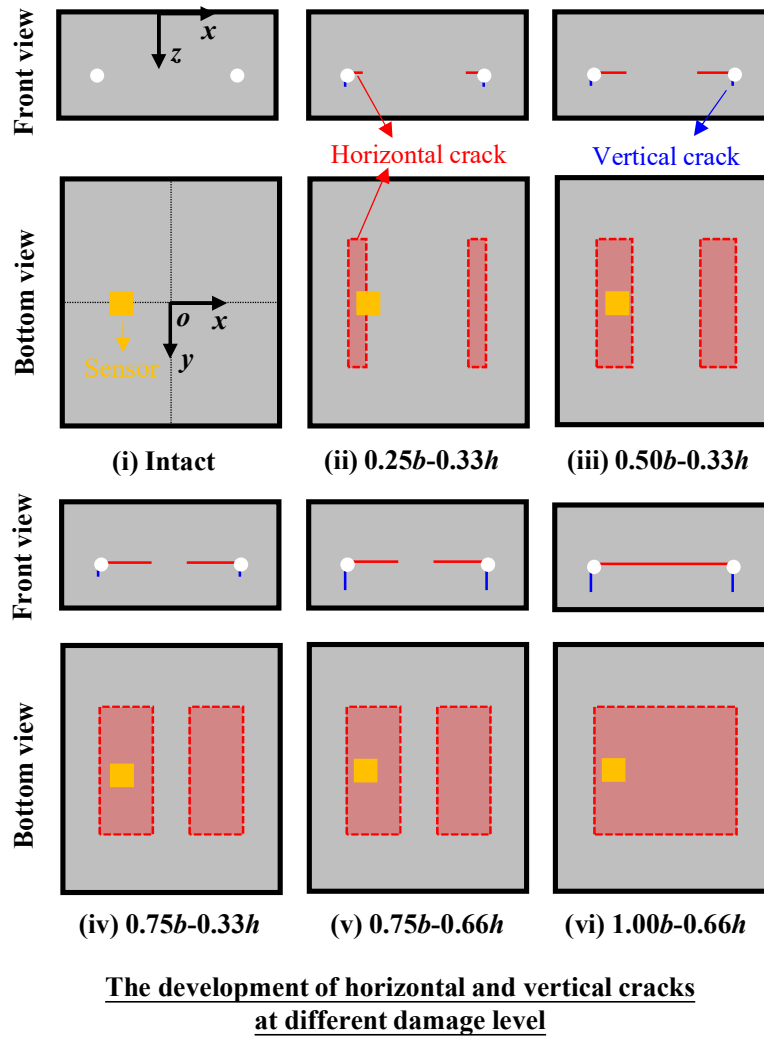


Figure 7.6 Different damage levels for simulating the spalling process

Figure 7.7 presents the signal spectra at different damage levels. The dimensionless

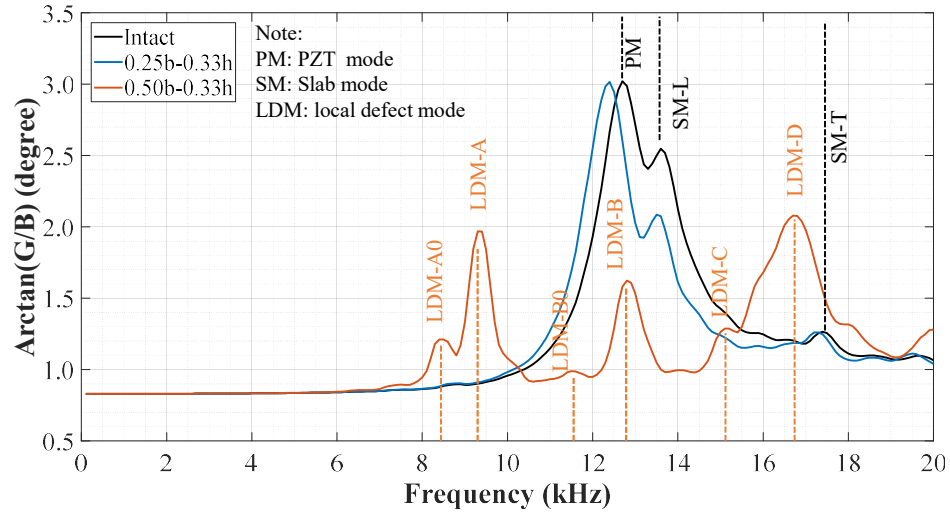
physical quantity  $\arctan(G/B)$  stands for the complementary angle of the phase and has been proven effective in capturing resonance peaks in the EMI spectra, see Chapter 3. The obtained frequency spectra were smoothed via a moving average operation with a 500-Hz span, which removed minor peaks that were caused by measurement noise and did not correspond to resonance peaks. Figure 7.8 shows the vibration mode shapes corresponding to several important peaks.

Figure 7.7(a) shows the signal spectra at the early stage of the spalling process. In Cases (i)-(iii), the sensor was located above the intact area, the boundary of the intact and delaminated areas, and the delaminated area, respectively. In the intact case (Case i), three peaks in the spectrum were labeled as PM ( $f_{PZT} = 12.7$  kHz), SM-L (13.6 kHz), and SM-T (17.4 kHz), whose corresponding mode shapes are shown in Figure 7.8(a). Peak PM corresponded to the attached PZT sensor mode, whose displacements were concentrated on the sensor and bonding layer. Consequently, the peak PM was highly dependent on the properties of the sensor and the adhesive layer. The peak SM-L (where L indicates that the sensor is on the left side) corresponded to a high-order concrete slab mode excited by the PZT sensor. Its vibration displacements mainly occurred on the sensor and at the edge of the slab. Peak SM-T corresponded to the thickness stretch mode of the concrete slab, which was governed by the thickness and properties of the concrete slab. In the intact case, no peaks were found in the low-frequency ranges (i.e.,  $< f_{PZT}$ ).

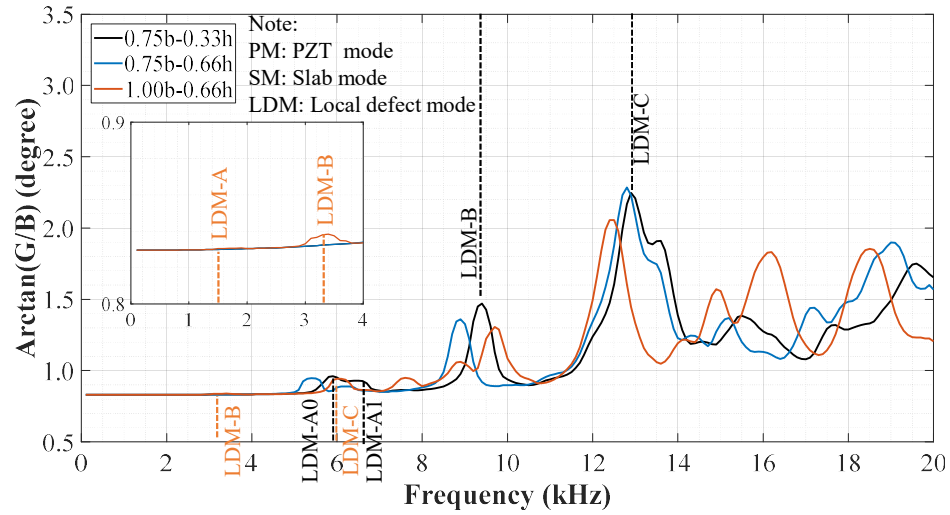
In Case ii (i.e.,  $0.25b$ - $0.33h$ ), the signal spectrum retained a similar pattern within the intact case. Peak PM moved leftward, and peak SM-L retained nearly the same frequency. Peak SM-T showed a slight change due to the changes in the local boundary conditions. In the third case (i.e.,  $0.50b$ - $0.33h$ ), the pattern of the signal spectrum changed considerably compared with those in the previous two cases. The sensor modes (PM) and two identified slab modes (SM-L and SM-T) were no longer captured. A series of peaks highly related to the local defect appeared in the signal spectrum. Six easily-observed peaks are labeled as the local defect mode in Figure 7.7(a), and their

mode shapes are shown in Figure 7.8(b). The first two peaks (LDM-A0 and LDM-A) corresponded to the first-order local defect mode, in which the major deformation was along the length of the delaminated layer. The first-order mode was split into two because of the simultaneous delamination appearance on the left and right sides. Peak LDM-A0 (8.5 kHz) showed the deformation of two delaminated areas on the left and right sides, while peak LDM-A (9.4 kHz) showed the mode only related to the left delaminated area. Similar phenomena were observed for peaks LDM-B0 (11.6 kHz) and LDM-B (12.8 kHz), both of which corresponded to the third-order mode along the length of the delaminated layer. The second-order mode was missing because the PZT sensor was installed on the symmetric plane. Peaks LDM-C (15.1 kHz) corresponded to the first-order mode along the width of the delaminated layer, and LDM-D (16.9 kHz) corresponded to the fifth-order modes along the length of the delaminated layer.

Figure 7.7(b) plots the signal spectra at the further development stage of the spalling process. The horizontal and vertical cracks continued to propagate in the three cases. By comparing Case iv ( $0.75b-0.33h$ ) with Case iii ( $0.50b-0.33h$ ) and Case v ( $0.75b-0.66h$ ), the effects of the horizontal and vertical cracks could be observed, respectively. In Case iv ( $0.75b-0.33h$ ), the local defect modes moved leftward compared with those in Case iii ( $0.50b-0.33h$ ), but the signal spectrum had the same pattern. Peaks LDM-A0 and LDM-A moved from 8.5 and 9.4 kHz to 5.9 and 6.6 kHz, respectively. Peak LDM-B0 became too weak to capture. Peaks LDM-C and LDM-D moved from 15.1 and 16.9 kHz to 9.4 and 12.9 kHz, respectively. The signal spectrum in Case v ( $0.75b-0.66h$ ) also had the same pattern as that in Case iv ( $0.75b-0.33h$ ). However, the leftward movement of the local defect modes induced by the vertical crack development was much smaller than that caused by the horizontal cracks. For example, Peaks LDM-A0 and LDM-A moved to 5.5 and 6.3 kHz, respectively, with only 0.4 and 0.3 kHz differences, respectively. Aside from the frequency movement, the magnitudes of the peaks also decreased as the horizontal and vertical cracks propagated.



(a) Minor delamination: Cases i to iii

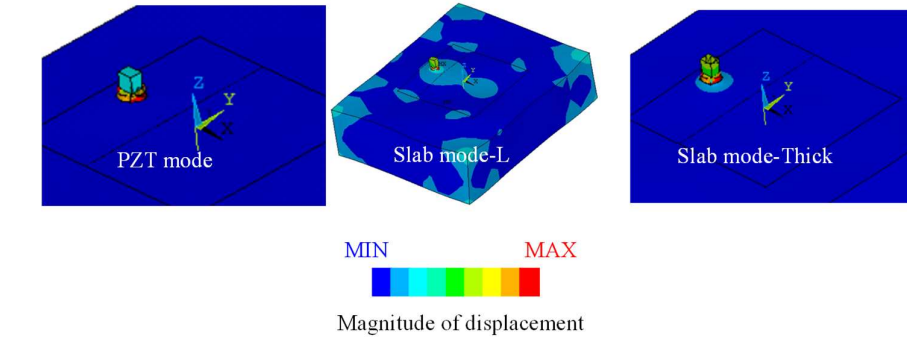


(b) Severe delamination: Cases iv to vi

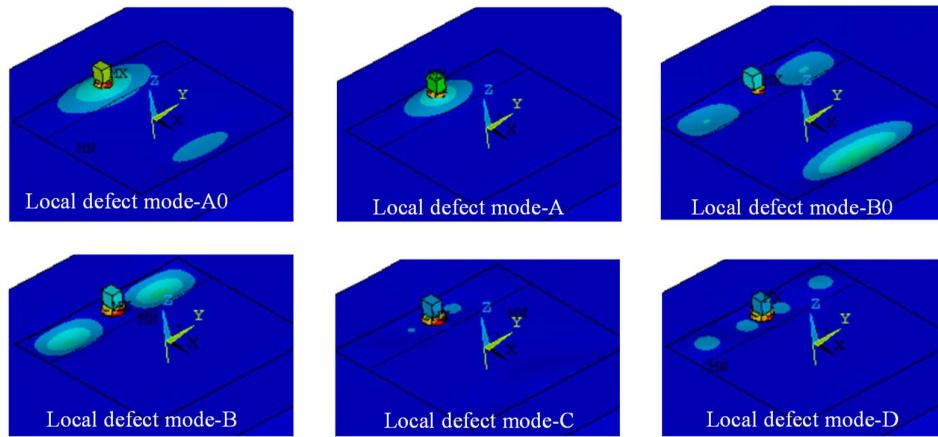
Figure 7.7 Signal spectra at different damage levels

In Case vi ( $1.00b-0.66h$ ), the two horizontal cracks merged, leading to a dramatic change in the detected region compared with the two other cases. The first several local defect modes moved leftward substantially. However, peak LDM-A was too weak to be captured. The PZT sensors typically have low sensitivity in the low-frequency range because of the high impedance of the capacitance-type sensor in this range, which prevents the generated charge from being retained and results in underestimated structure responses [Jenq and Chang, 1995]. For the adopted PZT sensor in this chapter,

a frequency range smaller than 2 kHz is not recommended when using the EMI technique in practice. Although the first-order local defect mode was missed, high-order local defect modes can still be captured in the signal spectrum.



(a) Mode shapes of the PZT sensor and slab (Case i: intact)



(b) First four captured local defect modes (Case iii:  $0.50b-0.33h$ )

Figure 7.8 Classic vibration mode shapes corresponding to the characteristic peaks in the spectra

### 7.3.3 Effect of Bonding Layer

Chapter 3 numerically and experimentally showed that the resonant frequencies of concrete cubes captured by the EMI technique do not vary with the properties of the rigid adhesive layer (e.g., epoxy). However, the detachable sensors used double-sided tape as the bonding material, which was considerably different from the traditional rigid bonding layers. Considering its weak bonding along the tangential direction of the contact surface, the effect of the flexible bonding layer is examined to show the

generalizability of the proposed method.

Large bonding thicknesses and high surface unevenness may affect through-transmission characteristics and reduce sensor sensitivity [ASTM E650/E650M, 2017; Ono, 2017]. In particular, using tape bonding can hardly ensure a perfect contact surface in practical measurement. Such undesirable weak bonding was simulated by reducing the modulus of elasticity of the bonding layer.

Figure 7.9 shows the effect of the modulus of elasticity ( $E_e$ ) of the bonding layer on the signals in the intact and damaged cases (i.e., Case i and Case iv:  $0.75b-0.33h$ ). The peak PM (corresponding to the PZT sensor mode) in the intact case was substantially affected by three  $E_e$  values (namely, 0.50, 0.85, and 1.20 GPa) in the signal spectrum (Figure 7.9(a)). As  $E_e$  increased, the PZT peaks moved rightward (from 10.6 kHz to 14.6 kHz) and upward (from 1.5 degrees to 3.8 degrees), indicating the higher transmission ability of the bonding layer. As the transmission ability increased, the resonance peaks of the slab (i.e., SM-L and SM-T) were strengthened and could easily be identified, but the frequencies of the two slab modes varied slightly.

In the damaged case (Case iv:  $0.75b-0.33h$ ) shown in Figure 7.9(b), as  $E_e$  increased, the frequencies of the first two local defect modes remained the same, while their magnitude showed a slight variation. But the frequencies of the high-order local defect modes slightly increased with increments in  $E_e$ . For example, the frequencies of LDM-B and LDM-C increased from 9.1 kHz to 9.5 kHz and from 11.8 kHz to 13.8 kHz, respectively. The likely reasons for the frequency increments of the local defect modes were: (1) the sizes of the PZT sensor and bonding layer were not ignorable compared with the delaminated area. (2) the resonant frequency of the PZT sensor shown in Figure 7.9(a) also fell in this frequency range and produced the disturbance to the local defect modes. Although decreasing the size of the PZT sensor could reduce the frequency shifting of the local defect modes, it may not be an ideal solution considering associated weak signal amplitudes [Liang et al., 1994]. Given that the goal of this chapter is to detect near-surface delamination in concrete structures, an approximate evaluation can

be accepted.

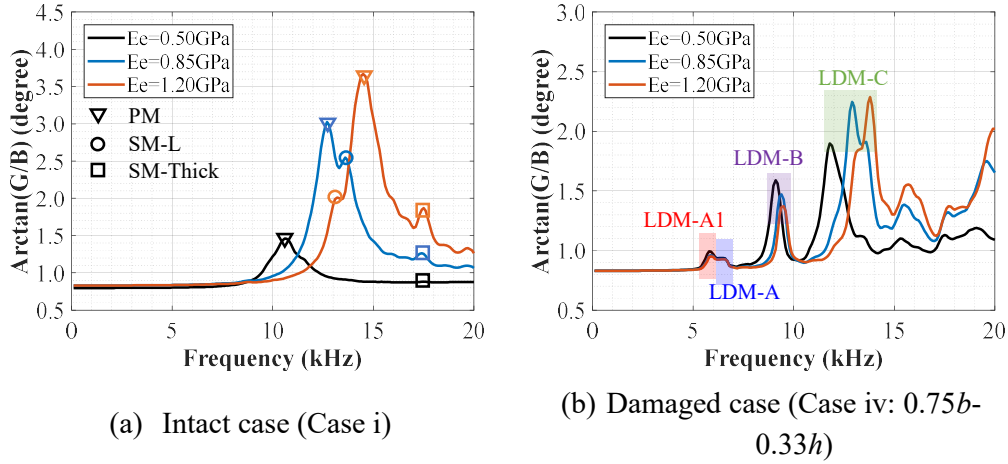


Figure 7.9 Effect of the modulus of elasticity of the bonding layer

To sum up, the bonding layer considerably affected the sensor peak and slightly influenced the structural peaks and the fundamental local resonant peak. It is worth noting that the modulus of elasticity of the concrete also affected the frequencies and responses of the sensor peaks, but the effect was not as remarkable as that of the bonding layer.

### 7.3.4 Effects of Slab Size and Boundary Conditions

Figure 7.10 shows the effects of varying the area and boundary condition of the slab on the intact and damaged cases. In the intact case (i.e., Case i), the signal spectrum became increasingly smooth as the slab area increased (Figure 7.10(a)). Meanwhile, mode SM-L disappeared whereas SM-T could still be captured, because the former and latter were sensitive to the slab area and thickness, respectively. When the boundary conditions changed from free to fixed, frequencies of peak SM-T still varied slightly. Similarly, the frequency of the PZT peak (i.e., PM) varies slightly with different areas and boundary conditions, as the sensor area was considerably smaller than the slab area. In the damaged case (i.e., Case iv:  $0.75b-0.33h$ ), the three labeled peaks exhibited smaller variations as the slab area and boundary conditions changed compared with those changes in Section 7.3.3 (Figure 7.10(b)). In general, the slab sizes and boundary conditions exerted limited effects on the signal spectra, implying the obtained findings



could be directly extended to slabs of larger sizes.

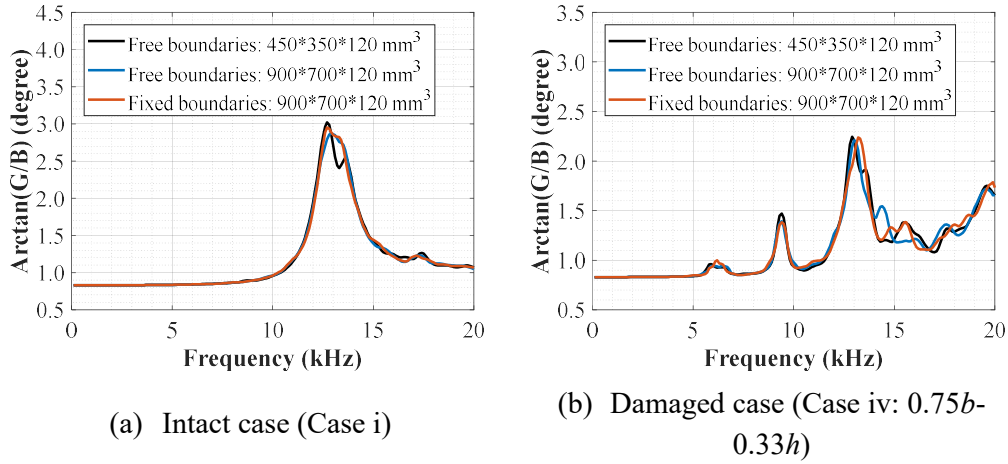


Figure 7.10 Effect of slab size and boundary conditions

### 7.3.5 Quantitative Analyses of the First Local Resonant Frequency

Although the first-order local defect mode is insensitive to the bonding layers, the slab size, and the slab boundary condition, it is still affected by multiple properties of the near-surface defect, such as delamination size (i.e., length of the horizontal and vertical cracks), shape, and boundary conditions. Therefore, the evaluation of defect size based on the local defect resonant frequency is still challenging. Flat-bottomed delamination with no vertical cracks was often simulated in composite structures [Solodov et al., 2013; De Angelis et al., 2012]. Solodov et al [2019] presented an equation to calculate the first-order resonant frequency of a rectangular defect with a flat bottom in a composite structure, in which the boundary conditions were simply assumed to be fixed (i.e., no rotation). The equation cannot be directly applied to near-surface concrete defects with complicated boundary conditions.

Kee and Gucunski [2016] categorized the boundary conditions of flat-bottomed square delaminated plates with width  $a$  and thickness  $h$  (without vertical cracks) into three types: (a) fully clamped boundary conditions are suitable for very shallow delamination ( $a/h > 20$ ); (b) for delamination with  $5 < a/h \leq 20$ , the boundary conditions are in between simply supported and fully clamped conditions; and (c) the boundary conditions are weaker than simply supported conditions for  $a/h \leq 5$ . The differences

arise from varying edge constraining effects. The analytical expression for the first-order resonant frequency of the flat-bottomed square defects, regressed from numerical simulation data by [Kee and Gucunski \[2016\]](#), is

$$f_1 = \varepsilon \frac{1}{h} \left( \frac{h}{a} \right)^2 \cdot \beta_1 C_p \quad (7.1)$$

where  $h$  and  $a$  are the thickness and fictitious width of the delaminated part, respectively;  $\varepsilon$  stands for the correction factor for the edge effects, as shown in Equation (7.2);  $\beta_1$  is the correction factor for Poisson's ratio ( $\mu_c$ ), as shown in Equation (7.3);  $C_p$  denotes the compressive wave velocity, as shown in Equation (7.4).

$$\varepsilon = 1.64e^{0.0014(a/h)} - 1.812e^{-0.22(a/h)} \quad (7.2)$$

$$\beta_1 = \frac{\pi\sqrt{(1-2\mu_c)}}{\sqrt{12(1-\mu_c)^2}} \quad (7.3)$$

$$C_p = \sqrt{\frac{E_c(1-\mu_c)}{\rho_c(1+\mu_c)(1-2\mu_c)}} \quad (7.4)$$

By removing the effect of material properties, the normalized first-order resonant frequency  $f_{1\text{-norm}}$  is obtained for generalization as follows:

$$f_{1\text{-norm}} = \frac{f_1}{\beta_1 C_p} = \varepsilon \frac{1}{h} \left( \frac{h}{a} \right)^2 \quad (7.5)$$

If the defect is a rectangle, the rectangular shape can be converted to a square shape with an equivalent edge dimension [\[Kee and Gucunski, 2016\]](#), as shown in Equation (7.6).

$$a = \frac{\sqrt{2}a_w a_l}{\sqrt{a_w^2 + a_l^2}} \quad (7.6)$$

where  $a_w$  and  $a_l$  stand for the width and length ( $a_l > a_w$ ) of rectangular delamination, respectively. For a long rectangle ( $a_l/a_w > 3$ ),  $a$  converges to  $\sqrt{2}a_w$ , indicating that the smaller width dominates the first-order defect resonant frequency. Considering that actual delaminated shapes may be unknown,  $a/\sqrt{2}$  can be approximately considered the lower bound of the delamination dimension, and  $a^2$  can be considered the lower bound of the delamination area.

The concrete material properties in Equation (7.4) may not be available in practice. Then, the compressive wave velocity  $C_p$  can be estimated from

$$f_{\text{thickness}} = \frac{\beta_2}{2T} C_p, \quad (7.7)$$

where  $T$  is the slab thickness, and  $\beta_2$  is the correction shape factor that depends on  $\mu_c$ . The values of 0.96 and 0.2 are recommended for  $\beta_2$  and  $\mu_c$ , respectively [Sansalone and Streett, 1997].

Table 7.2 compares the normalized first-order local resonant frequencies of a square defect obtained from the modal analyses of finite element models with the analytical expressions proposed by Kee and Gucunski [2016]. The delaminated layer thickness ( $h$ ) was from 10 mm to 30 mm, covering the common range of concrete covers. The defect width ( $a$ ) was from 100 mm to 200 mm, covering the normal steel rebar spacing in concrete structures. The simulated slab had a size of  $1000 \times 1000 \times 120 \text{ mm}^3$  with the boundaries clamped to represent a general situation. Notably, the correction factor in Equation (7.2) does not consider vertical cracks, corresponding to the damage case  $1.00a-0.00h$  defined in this chapter. But in the finite element models, two damage cases, namely,  $1.00a-0.00h$  and  $1.00a-0.75h$ , were simulated.

In the damage case  $1.00a-0.00h$ , the mean and maximum errors between the simulation and the prediction of Equation (7.5) were  $-6.4\%$  and  $-15.6\%$ , respectively, indicating a fair accuracy of Equation (7.5). Meanwhile, Equation (7.5) could not accurately predict the damage case  $1.00a-0.75h$  because the existence of the vertical cracks reduced resonant frequencies apparently.

Therefore, Equations (7.8–7.9) are regressed from the simulation results in Table 7.2 to estimate the fictitious width of the delamination part in a square shape, in which the units of defect size and frequency are meter and hertz, respectively. Considering vertical cracks with  $1.00h$  lead to the falling of spalled concrete, the cases with  $0.00h$  and  $0.75h$  are considered as the bounds of the vertical crack depths in practice. The estimated width ( $a$ ) corresponding to  $0.00h$  and  $0.75h$  are considered the upper and lower bounds of such width, respectively. If the delaminated area is a long rectangular

shape,  $a_w$  can be estimated by  $a/\sqrt{2}$ , as suggested by Equation (7.6).

$$a = 0.1892 - 0.1298f_{1-\text{norm}} + 5.873h + 0.03583f_{1-\text{norm}}^2 - 2.123f_{1-\text{norm}}h; \text{ for the upper bound; } R^2 = 0.98 \quad (7.8)$$

$$a = 0.1902 - 0.1515f_{1-\text{norm}} + 4.892h + 0.04918f_{1-\text{norm}}^2 - 2.054f_{1-\text{norm}}h; \text{ for the lower bound; } R^2 = 0.98 \quad (7.9)$$

To sum up, the proposed delamination detection method could be implemented as follows:

- (a) The PZT sensor was attached to a checkpoint on the target surface by using double-sided tape.
- (b) The EMI signal spectrum was recorded from 1 kHz to 20 kHz, and a moving average operation with a 500-Hz span might be applied if necessary.
- (c) The signal spectral pattern was assessed to determine whether delamination existed or not. If only a distinct peak was found in the frequency range of 10–15 kHz, the checkpoint was considered healthy. If multiple peaks were found in the 1–15 kHz range and the first peak appeared below 10 kHz, the checkpoint was considered delaminated.
- (d) The delaminated area was estimated by substituting the first resonant frequency into Equations (7.6), (7.8), and (7.9), if delamination was detected.
- (e) The sensor was subsequently detached, and detection was repeated at a new checkpoint by using the same sensor.

Table 7.2 The normalized first local defect resonance of a square defect

Defect size		$f_{1\text{-norm}}$ simulation		$f_{1\text{-norm}}$ by Eq. (7.5)	
$a$ (m)	$h$ (m)	$1.00a-0.00h$	$1.00a-0.75h$	$1.00a-0.00h$	Error (%)
0.100	0.010	1.436	1.188	1.462	1.9
0.125	0.010	1.011	0.790	0.994	-1.7
0.150	0.010	0.719	0.569	0.715	-0.5
0.175	0.010	0.536	0.416	0.536	0.0
0.200	0.010	0.421	0.303	0.416	-1.2
0.100	0.015	2.054	1.602	1.856	-9.6
0.125	0.015	1.376	1.084	1.315	-4.5
0.150	0.015	1.010	0.768	0.975	-3.5
0.175	0.015	0.755	0.556	0.748	-0.9
0.200	0.015	0.585	0.442	0.590	1.0
0.100	0.020	2.486	1.910	2.097	-15.6
0.125	0.020	1.682	1.354	1.531	-9.0
0.150	0.020	1.201	0.992	1.164	-3.1
0.175	0.020	0.973	0.721	0.912	-6.4
0.200	0.020	0.748	0.535	0.731	-2.3
0.100	0.025	2.604	1.978	2.244	-13.8
0.125	0.025	1.917	1.566	1.677	-12.5
0.150	0.025	1.397	1.106	1.300	-7.0
0.175	0.025	1.113	0.780	1.035	-7.0
0.200	0.025	0.930	0.695	0.842	-9.5
0.100	0.030	2.710	2.009	2.332	-13.9
0.125	0.030	1.998	1.639	1.776	-11.1
0.150	0.030	1.616	1.175	1.398	-13.5
0.175	0.030	1.207	0.995	1.128	-6.6
0.200	0.030	1.028	0.739	0.928	-9.7
Mean value					-6.4
Standard deviation					5.3

## 7.4 Laboratory Experimental Validations

Artificial delamination (i.e., flat delamination cracks parallel to the surface) was introduced in most previous detection studies. Although this introduction facilitated the comparison with the analytical and numerical results, it hindered the understanding of the development process of delamination; additionally, many cracks in concrete slabs are wavy with variable depths [Kee and Gucunski, 2016]. Therefore, the experimental validations in this section simulated a real spalling process induced by steel rebar

corrosion. The proposed method in [Section 7.3](#) was used to detect the delamination, and the evaluation results were verified by cutting the tested concrete slab.

#### 7.4.1 Experimental Setup and Procedure

[Figure 7.11](#) presents the geometry of the specimen and the details of the steel rebars. The cast concrete slab had a size of  $450 \times 350 \times 120 \text{ mm}^3$ , which was identical to those in the numerical model. The rectangular concrete slab was reinforced by two steel rebars (HRB 400), which had a diameter of 10 mm and a center-to-center spacing of 100 mm. The length of each steel rebars was 550 mm to allow for an electrical connection. The actual corroded length was only 300 mm. The ends of the steel rebars in the slab were coated with epoxy to prevent corrosion and avoid spalling in large areas, which was not the focus of this chapter. Given the limitation in installation precision, the concrete cover thickness was set to 15 and 20 mm, respectively, for the left (labeled as L) and right (labeled as R) steel rebars.

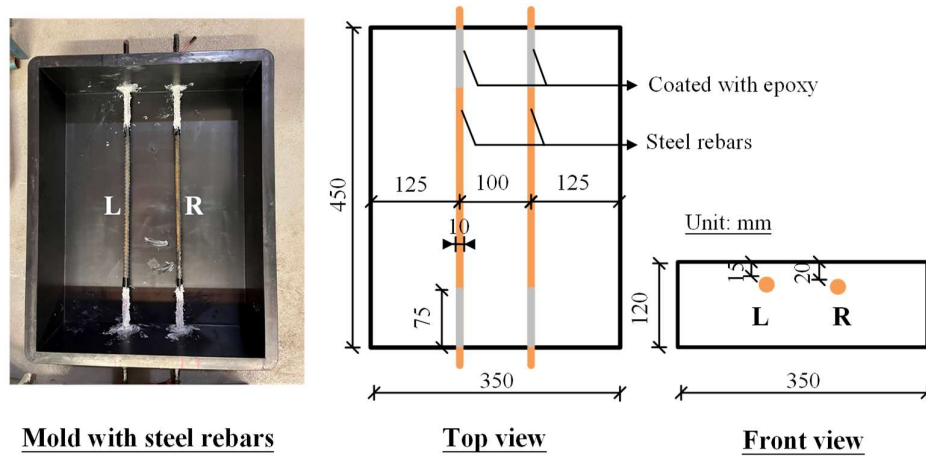


Figure 7.11 Geometry of the specimen and details of the steel rebars

A batch of concrete specimens was cast for measurement, including four 150-mm cubes and one slab. The cubes were used to measure the modulus of elasticity and compressive strength, where the former was measured by the EMI technique (as presented in [Chapter 4](#)), and the latter was obtained through uniaxial compressive testing. The mix proportions and measured material properties of concrete are summarized in [Table 7.3](#). To facilitate corrosion, 4% NaCl by weight of cement was

added to the concrete mix. The specimen was demolded after 24 hours and was cured in an air-dry condition for 28 days before the corrosion tests.

Table 7.3 Material proportions of the adopted concrete materials

Type	Mix proportion, by weight	Density (kg/m <sup>3</sup> )	$E_c$ (MPa)	$\mu_c$	$f_{cu}$ (MPa)
Normal Concrete	C: W: S: CA: FA: SP <sup>a</sup> =1:0.375:1.659:1.561:0.780: 0.006	2368	37100	0.20	47.1

<sup>a</sup>C = cement; W = water; S = sand; CA = 20 mm aggregate; FA = 10 mm aggregate; SP = superplastic

Accelerated corrosion techniques were employed to considerably reduce the duration of the corrosion period. Figure 7.12 presents the experimental setup for the accelerated corrosion tests and damage detection using the EMI technique. The wetting-drying cycle process was used. Figure 7.12(a) shows the wetting stage, in which a wet sponge containing a 5% NaCl solution (serving as the electrolyte) covered the top slab surface with a stainless-steel mesh. (serving as the cathode). Each steel rebar was connected to one DC power source and applied with constant current. Table 7.4 presents the corrosion procedure and the duration of each step, where corrosion duration refers to the duration of the electric current being applied. In the first 60-hour corrosion time, the current intensity was 500  $\mu\text{A}/\text{cm}^2$ . Then, the current density was increased to 750  $\mu\text{A}/\text{cm}^2$  in the rest of the corrosion procedure. Large damage might be produced because of the absence of a dissipation period for the radial pressure exerted at the steel/concrete interface [Mangat and Elgarf, 1999; Maaddawy and Soudki, 2003]. Considering that the goal of this experiment was to validate the effectiveness of the proposed delamination detection instead of predicting the corrosion procedure, high current densities are regarded as acceptable

Figure 7.12(b) shows the damage detection conducted during the dry stage with no current being applied, wherein only one sensor was attached to multiple checkpoints on the concrete slab for measurement. The sensor type and bonding tape were similar to those in Figure 7.2. When one measurement was finished, the sensor was detached

from the old checkpoint and attached to a new checkpoint using double-sided tape. The sensor was not permanently attached to the concrete slab and thus did not suffer corrosion or durability issues. The PZT sensor was excited with an AC voltage of 1 V, and the EMI spectra were measured by the LCR device (Keysight E4980AL) connected to a laptop. The frequency ranges and intervals were from 2–20 kHz and 25 Hz, respectively. The room temperature and humidity during measurement were around 20 °C and R.H. 60%, respectively.

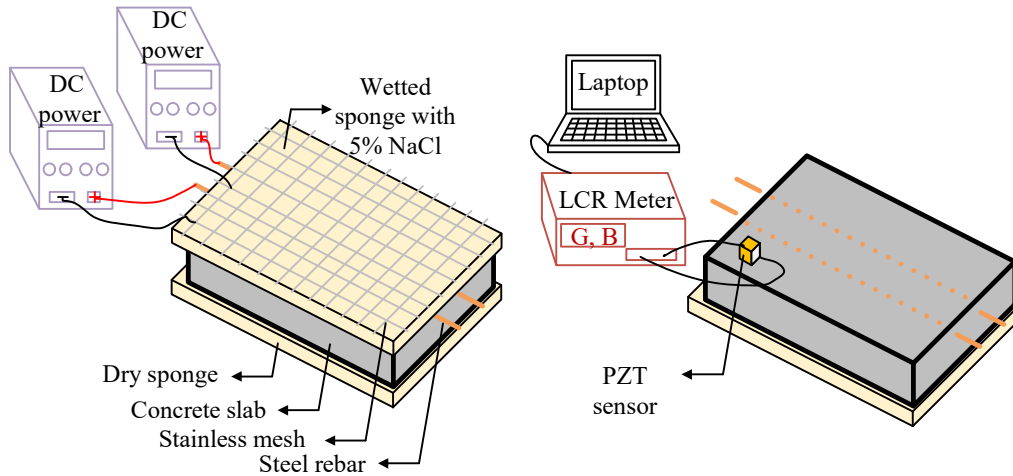
Figure 7.12(c) shows the experimental photo and the layout of checkpoints. The checkpoints were categorized into three groups according to their locations relative to the steel rebars, namely, between the steel rebars (i.e., Axis C), on the steel rebars (i.e., Axes L and R), and outside the steel rebars (i.e., Axes LO and RO). The center-to-center distance between the checkpoints was 50 mm, which made the checkpoints dense enough to examine the slab carefully. Checkpoint L75 refers to a point located on Axis L and 75 mm away from the bottom side of the slab.

Table 7.4 mentions the status “before cutting”, which happened about six months after Step 4. Considering that the six-month period and multiple times of transportation might have caused new damage, the delamination detection was conducted again as Step 5, aiming to correlate the final detection results to the cutting results of the slab.

Table 7.4 Corrosion time procedure at the wetting stage

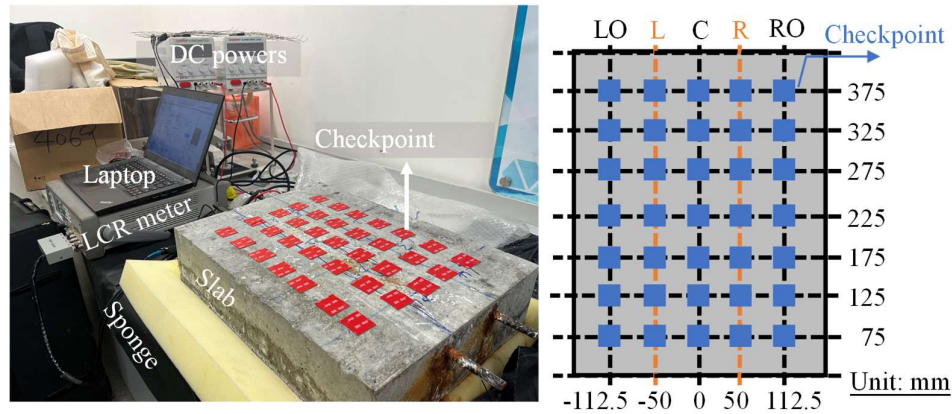
Step	Duration of each step for induced corrosion (hours)	Current density ( $\mu\text{A}/\text{cm}^2$ )	Accumulated corrosion time (hours)
1	0	0	0
2	60	500	60
3	48	750	108
4	72	750	180
5	Before cutting: the tested slab was placed in a dry condition in the laboratory for six months		





(a) Wetting: accelerated corrosion tests

(b) Drying: Damage detection



(c) Experimental photo and checkpoints

Figure 7.12 Experimental setup for the accelerated corrosion tests and delamination detection using the EMI technique

## 7.4.2 Damage Detection

Figure 7.13 presents the typical signal spectra recorded after 0 and 60 hours of corrosion. At this stage, no damage was visible on the concrete surface. The signal patterns at different checkpoints were similar, but the distinct peaks varied from 11.0 kHz to 13.2 kHz because of different surface unevenness at these points. The peaks of the PZT sensor modes were within the frequency range mentioned in Section 7.3.3, indicating the rationality of the modulus of elasticity of the double-sided tape assumed in Section 7.3.3. Meanwhile, modes SM-L and SM-T could be captured. Slight variations in the frequencies of modes SM-L and SM-T are likely caused by the

nonhomogeneous and nonuniform thickness of the concrete slab.

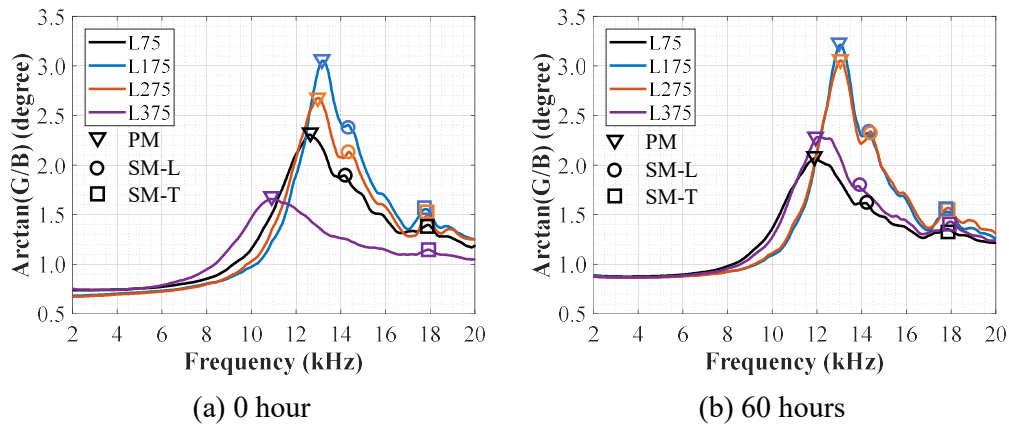
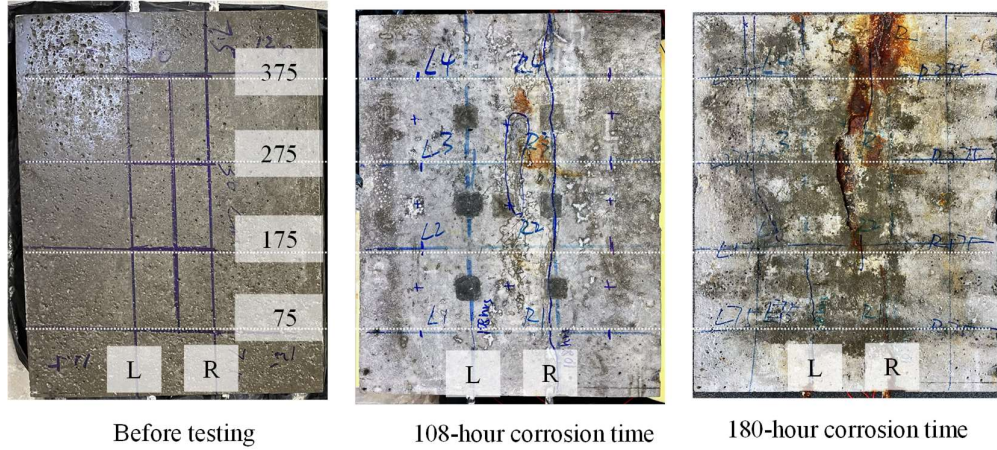
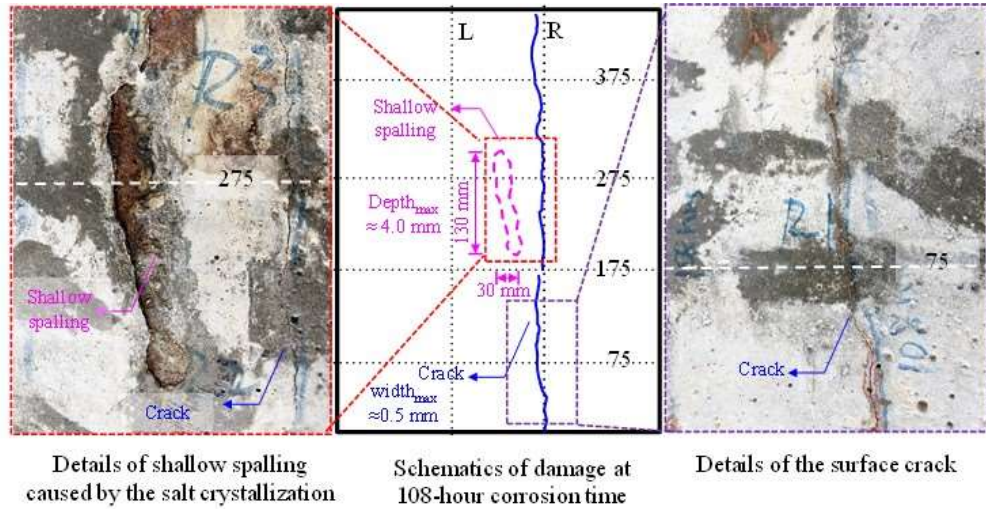


Figure 7.13 Signals comparison after 0 and 60 corrosion hours measured at different locations

Figure 7.14 presents the visual inspection of the concrete slab over time. No visible cracks were observed in the first two steps. After a 108-hour corrosion process (i.e., Step 3), two different damage types were observed on the slab surface (Figure 7.14(a)). The surface damage did not expand after the 180-hour corrosion time (i.e., Step 4). Figure 7.14(b) presents the details of the damage that occurred after 108-hour corrosion time. An extended surface crack appeared above the rebar on the right side. In addition, a 130-mm-long and 30-mm-wide approximately elliptical spalling area occurred at a shallow depth (around 4 mm) between Axes L and R and between Axes 225 and 375. The spalling of the superficial damage was caused by salt crystallization, a type of physical damage that occurs frequently during the wetting-drying cycle [Ting et al., 2021]. The damage is caused by internal stress arising from the formation of salt crystals in concrete when the pore solution becomes supersaturated. Given the skin effect of concrete, the maximum chloride concentration occurs in a shallow depth (i.e., ~3 mm) during the wetting-drying cycle [Cai et al., 2020]. In this chapter, a continuous surface crack with a width of ~0.05 mm was observed at the location of the R-rebar. The following discussions employed the checkpoints on Axes 175 and 275 for comparison.



(a) Visual inspection of the slab at different corrosion time



(b) Details of shallow spalling and cracks at 108-hour corrosion time

Figure 7.14 Visual inspection of the concrete slab over time

Figures 7.15–7.18 present the signal spectra of different checkpoints at different corrosion statuses. The checkpoints are discussed in the sequence from two sides to the center area of the slab. Figure 7.15 shows the signal spectra of the checkpoints on Axes LO and RO. At Location LO175, no LDM peaks were observed in the signal spectra except for the reduction in the magnitude of the distinct peak (i.e., labeled by the lower triangle symbol) (Figure 7.15(a)). Peaks SM-LO referred to a slab mode excited on Axes LO and RO, slightly different from mode SM-L because the global slab vibration modes were more or less related to the location of the PZT sensor on the concrete slab [Zhou et al., 1995]. At Location LO275, multiple peaks appeared at the 108-hour

corrosion time, and the first resonance peak was 8.4 kHz (Figure 7.15(b)). The diamond markers in the figure denote the first three easily identified peaks as references. The signal pattern at 180 hours was similar to that at 108 hours, but the peaks moved leftward. For example, the first resonance peak moved leftward to 7.0 kHz. The pattern of the signal spectrum changed at the status “before cutting” (i.e., Step 5), compared with those at the 108-hour and 180-hour corrosion time. The signal spectrum weakened considerably, indicating that new damage might have occurred because of slow corrosion in the six-month placement and the transportation of the slab, as mentioned in Table 7.4. The first resonance peak moved to 5.4 kHz, and the two other peaks were captured at around 8.0 kHz and 10.0 kHz. At Locations RO175 and RO275, as shown in Figures 7.15(c) and 7.15(d), respectively, the signal patterns remained unchanged, even with the reduced magnitude and slight changes in the sensor and slab mode.

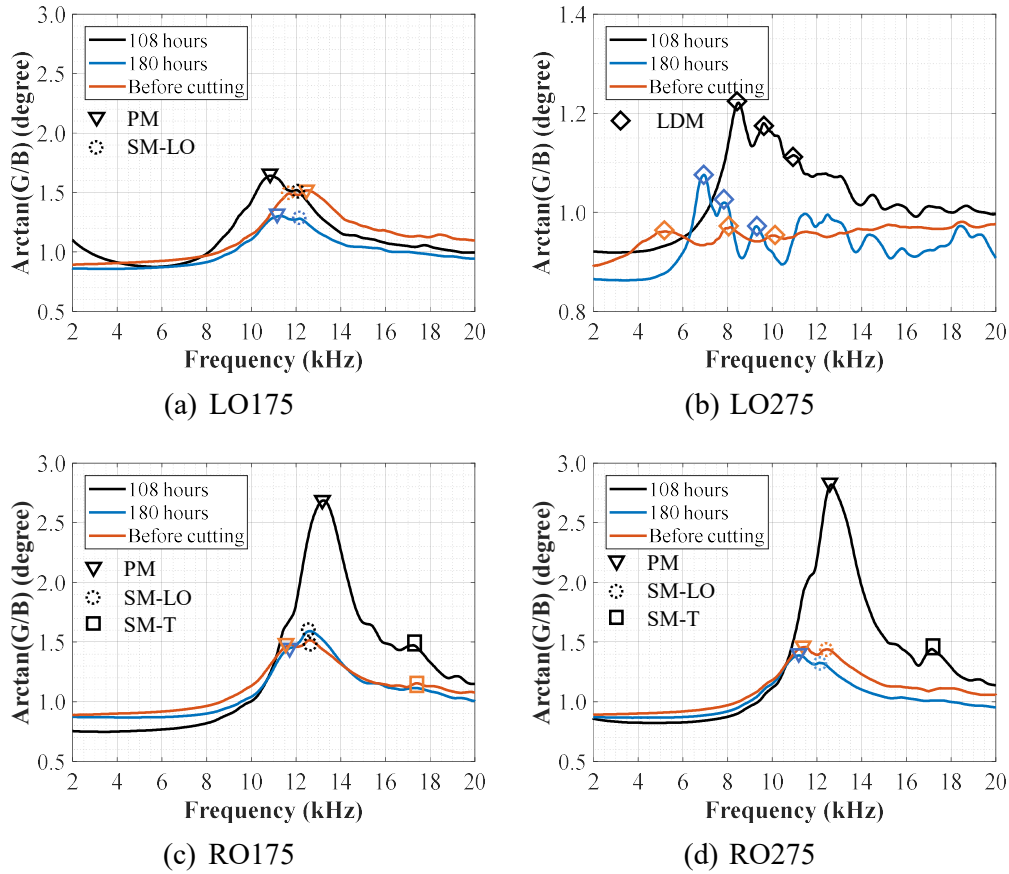


Figure 7.15 Signal spectra of the checkpoints on Axes LO and RO at different statuses

Figure 7.16 presents the signal spectra of the checkpoints above the rebars (on Axes L and R) at different corrosion statuses. At Location L175, the signal patterns at 108- and 180-hour corrosion time were consistent with those under the undamaged status (Figure 7.16(a)). The peak of the PZT sensor was larger than 11.0 kHz. At the status “before cutting”, dual peaks were observed below 10 kHz. The frequency of the first peak was 9.1 kHz, implying that local damage was detected. At Location L275, multiple peaks labeled as diamond markers were found at 108 hours (Figure 7.16(b)). The first peak appeared at 9.3 kHz and moved to 7.3 and 6.9 kHz at two other statuses. Although a continuous surface crack was observed above the right rebar (Figure 7.14(b)), it is interesting to observe that the pattern of the signal spectra in Figures 7.16(c) and 7.16(d) did not change considerably. Only at the “before cutting” status, the first dominant peak was moved to 9.6 kHz at Location L325.



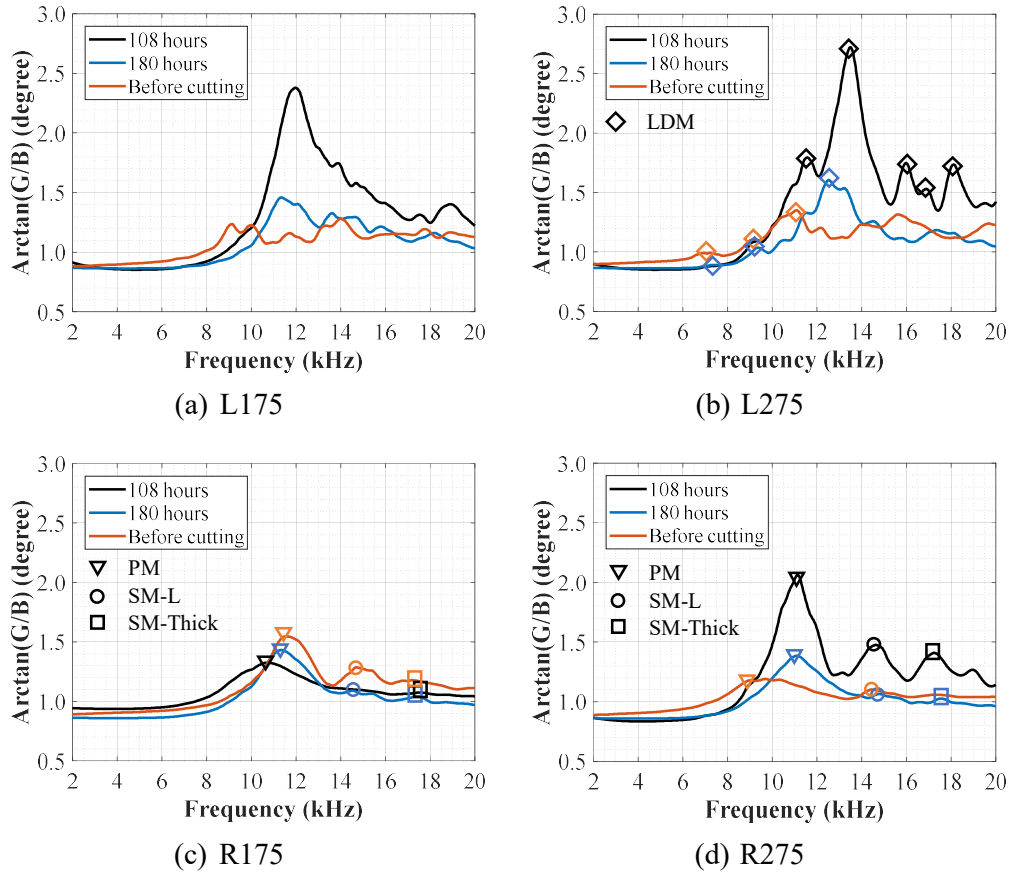


Figure 7.16 Signal spectra of the checkpoints above the rebars at different statuses

Figure 7.17 presents the signal spectra close to Axis C. The sensor was installed 25 mm to the left of the original Axis C to avoid the uneven surface induced by shallow spalling. The signal spectra substantially changed at these two checkpoints, and multiple peaks starting from 3.5 kHz were observed. At Location C175, as shown in Figure 7.17(a), the first resonance peak moved rightward from 4.3 kHz to 4.7 kHz as the corrosion time increased, which might be caused by the complicated changes in the boundaries. However, the first resonance peaks moved leftward to 4.2 kHz at the “before cutting” status. At Location C275, the signal spectra also presented multiple peaks moving leftward with the increasing corrosion time (Figure 7.17(b)). The first resonance peak moved leftward from 4.0 kHz to 3.5 kHz.

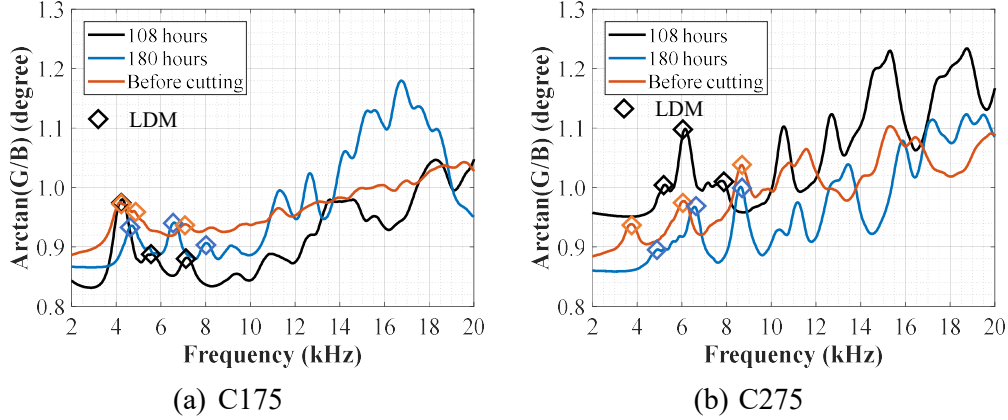


Figure 7.17 Signal spectra of the checkpoints on Axis C at different statuses

Figure 7.18 presents the maps showing the first resonant frequency in the selected frequency range, where four different colors are used to represent different frequency ranges and may correspond to different damage statuses. Red refers to the severe damage status, and blue refers to the healthy status. Yellow and orange denote intermediate statuses. The criterion behind this classification was as follows: (1) In a healthy status, variations in the bonding layers changed the sensor mode peak, but the distinct peak was always larger than 10 kHz, as shown in Figure 7.13; and (2) for the damaged status, Equation (7.5) calculates the first-order defect frequency with defect sizes  $100 \times 100 \times 15 \text{ mm}^3$  and  $125 \times 125 \times 10 \text{ mm}^3$  as around 6.8 and 4.8 kHz, respectively, for the given material properties. Therefore, 4.9, 6.9, and 10 kHz were set as the thresholds for classification, which was rather subjective and needs to be refined in the future. Although the surface crack was observed above the right-side steel rebar, the predicted delamination mainly appeared around the steel rebar on the left. As the corrosion time increased, more resonance peaks lower than the threshold were observed on the Axes LO and L, implying that the delamination may have occurred without visible surface phenomena. Based on the lowest frequency (i.e., 3.4 kHz) of the slab, the delamination area can be estimated using Equations (7.6), (7.8), and (7.9). The calculated lower and upper bounds of  $a$  were equal to 137 and 158 mm for square delamination with a 15-mm depth, respectively. For rectangular delamination, the estimated lower and upper bounds of  $a_w$  (short side) were 97 and 112 mm, respectively.

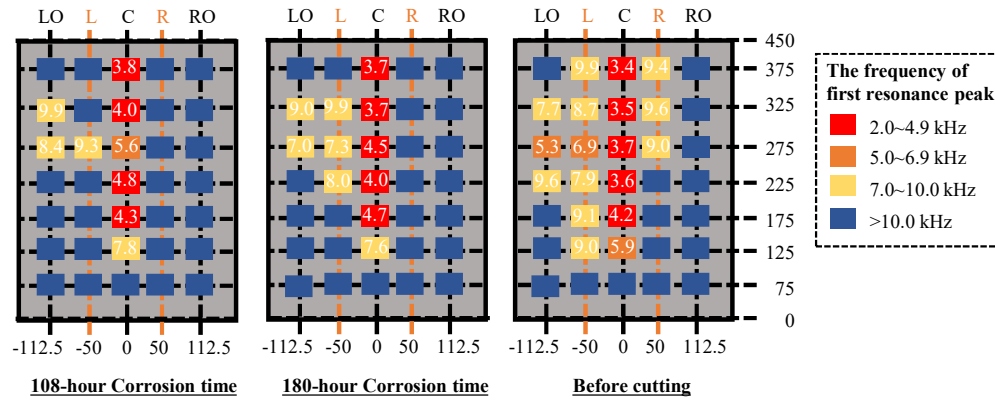


Figure 7.18 Maps of the first resonant frequencies

### 7.4.3 Cutting Results for Verification

The concrete slab was cut to verify the evaluation results for the delamination. Figure 7.19 shows the concrete cutting equipment. The slab was fixed to avoid unwanted movement. The blade of the cutting machine had a 0.5 m diameter. The cutting machine moved along a sliding track during its operation. The cutting sections of the slab were along Axes 75, 175, 275, and 375.

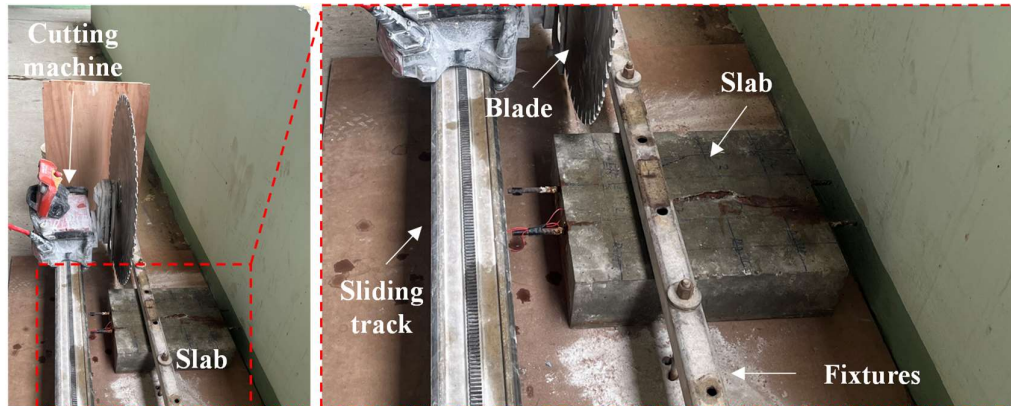


Figure 7.19 Setup for slab cutting

Figure 7.20 shows the pictures of the cutting sections and the corresponding drawings of the crack distributions. As indicated in Figure 7.20(a), the damage level on the left rebar was much more severe than on the right, which may be attributed to the thinner concrete cover. This observation was consistent with the prediction shown in Figure 7.18 but very different from surface visual inspection, indicating surface visual inspection could be unreliable. Regarding the comparison among different sections,



Section 75 was healthy and had only two small cracks around the right rebar, indicating the effectiveness of the protection coating of the steel rebar in this section. By contrast, the protection at Section 375 failed, but the damage was successfully detected. Except for Section 75, the three other sections had two major inclined cracks on the left bar, which were relatively wide. These two cracks developed through mortar and did not pass through aggregates. The inclined cracks between the Axes LO and L had different depths at the end. The depths in Sections 375, 275, and 175 were 15, 3, and 2 mm, respectively. Meanwhile, the inclined cracks between Axes L and C propagated to the near-surface spalling. The observed damage levels of the four sections in [Figure 7.20](#) agreed well with the predicted results of the proposed method in [Figure 7.18](#).

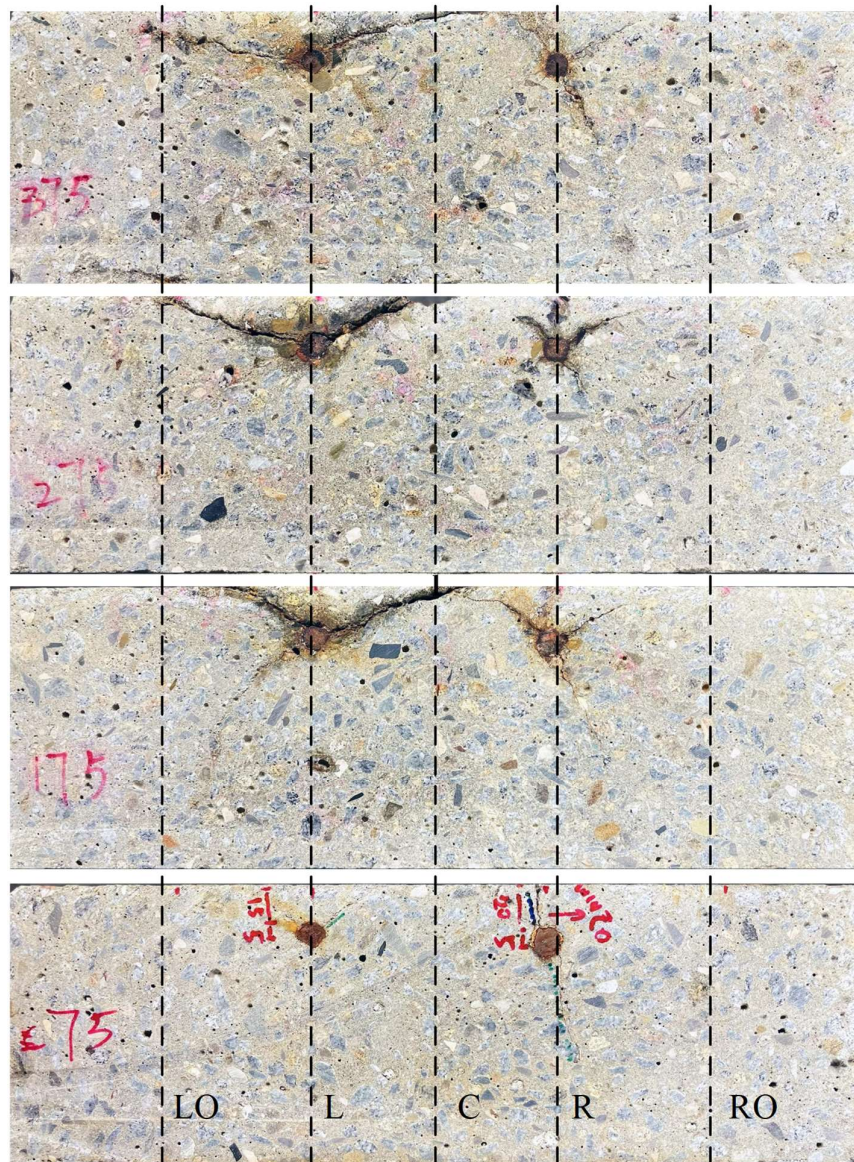
[Figure 7.20\(b\)](#) draws the crack distributions to thoroughly understand the corrosion-induced damage. The value besides the crack in the same color is the maximum width of the crack measured by the feeler gauge. The cracks were divided into four categories, namely, delamination cracks in the cover (red), inclined cracks in the cover (blue), internal cracks (green), and surface cracks (purple). Notably, both the delamination and inclined cracks were essentially inclined cracks. They are divided by considering their maximum width and length. The maximum widths of the delamination cracks were at least 0.40 mm, and the lengths of the delamination cracks were around 100 mm. So, the delamination cracks could be considered nearly horizontal, causing a delamination layer with a separation plane roughly parallel to the surface. Whereas the maximum widths of the inclined cracks were no more than 0.2 mm, and their lengths were smaller than 70 mm. Among the four sections, only Section 275 had the delamination layer between the Axes LO and L, which is in good agreement with the detection results in [Figure 7.18](#). The delamination cracks between Axes L and C propagated to the center axis in Sections 175, 275, and 375, which were well detected in [Figure 7.18](#). The internal cracks in [Figure 7.20\(b\)](#) had relatively small widths and were not the focus of this chapter. Although the surface cracks could be observed visually, they did not initiate from the steel rebars, or in other words, they did not

penetrate through the entire cover. The surface cracks perpendicular to the cover were caused by the expansion pressure from non-uniform rust, which induced tensile stress concentration on the point above the rebar [Su and Zhang, 2019]. Aside from the cracks, different debonding gap (in pink) statuses at the interfaces between the concrete and rebars were shown at Locations L175, L275, and L275. The underlined numbers in Figure 7.20(b) presented the angle extent relative to the center of the rebar. The longest and largest gap occurred at Location L275, with a  $130^\circ$  relative angle and 0.45 mm width. The damage was also successfully detected using the proposed method.

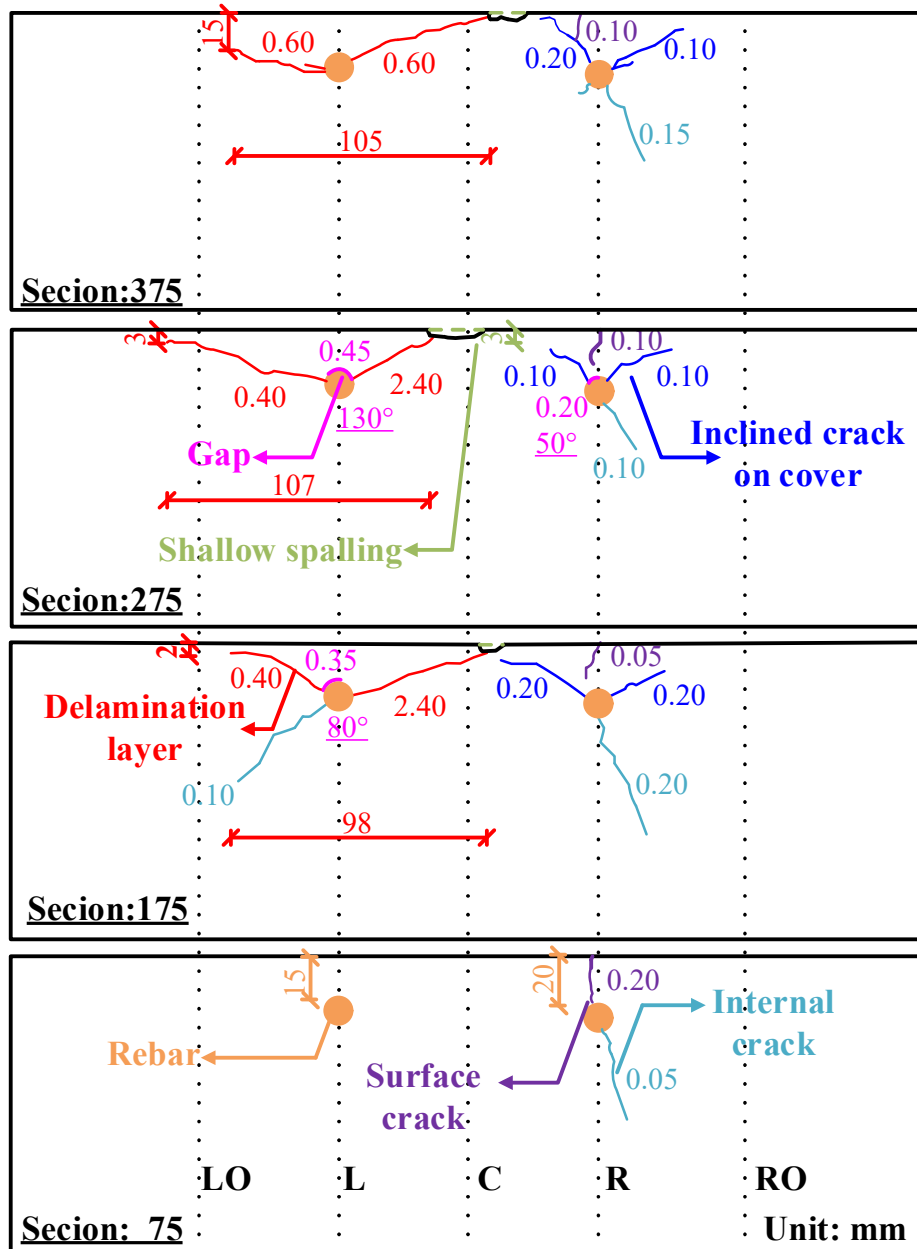
The cutting results also provided geometric information on the delamination, allowing a quantitative comparison between the experimental results and the prediction results. The average width of the delamination layer,  $a_w$ , was equal to 103 mm, close to the estimated results (i.e., from 97 mm to 112 mm). Given that only four sections were cut,  $a_l$  could not be accurately measured.

To sum up, although the actual corrosion-induced delamination was more complicated than the simulated conditions, it was successfully detected, localized, and quantified by the proposed method in the presented laboratory experiments. Even invisible damage on the left side of the concrete slab was successfully detected, showing the effectiveness of the proposed detection method.

It should be mentioned that the slab was also scanned using the GRP technology that was briefly introduced in Section 2.2.3. The air-coupled GRP antenna was a RoadScan horn antenna (2 GHz) from GSSI. However, no delamination could be detected, which may be attributed to the width of the delamination being much smaller than the detectable range of the technique.



(a) Pictures of the four cutting sections



(b) Schematics of the crack distributions (the value beside the crack in the same color is the maximum width, and the degree shown in pink refers to the angle extent relative to the center of the rebar)

Figure 7.20 Pictures of the cutting sections and schematics of the crack distributions

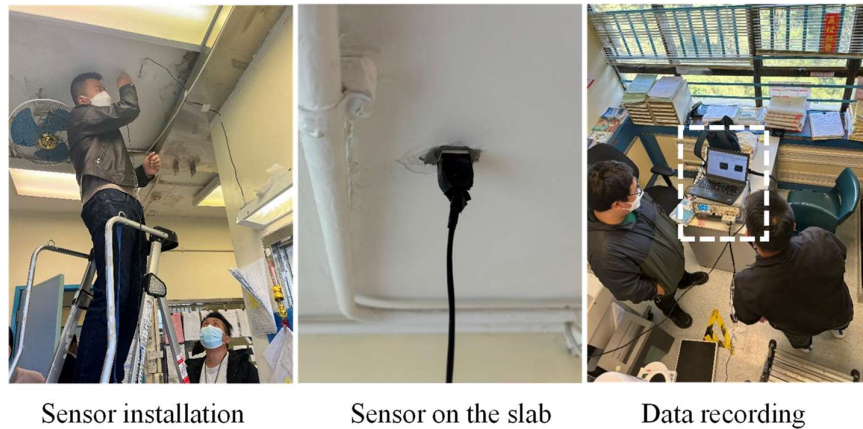
## 7.5 On-site Testing Validations

Given the successful numerical and experimental validations of the proposed method, on-site testing was conducted to further examine its applicability outside the laboratory environments and validate its real-world effectiveness.

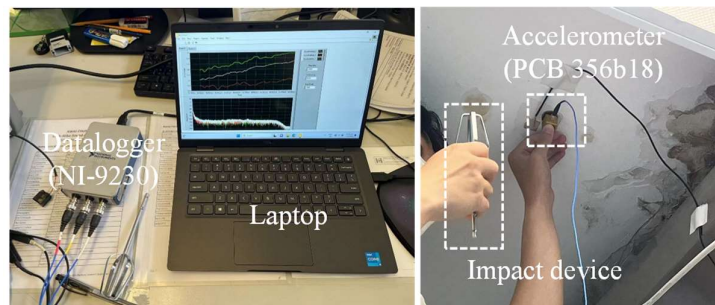


### 7.5.1 Site and Testing Information

On-site testing using the detachable PZT sensor and the EMI technique was conducted in an old building in Hong Kong, whose structural details are unavailable. In addition to the proposed method, the traditional impact-echo method was also applied for comparison. Two tests were conducted during a half year. Figure 7.21 presents the measured areas and details of the testing techniques. The same sensor, bonding tape, device, and data acquisition system as those in the laboratory experiments in Section 7.4 were used for the EMI technique (Figure 7.21(a)). Figure 7.21(b) illustrates the equipment employed for the impact-echo method, presented in Section 2.2.3, including a compact data acquisition system (NI-9230) with a maximum sampling rate of 12.8 kS/s, a high-fidelity triaxial accelerometer (PCB 356b18), and a stainless-steel bar.



(a) EMI technique



(b) Impact-echo method

Figure 7.21 On-site testing procedures and details of the testing techniques

### 7.5.2 Suspected Delamination Area and Corresponding Signals

After careful examination of two rooms, a suspected delaminated area was confirmed. Figure 7.22(a) illustrates the suspected delaminated area and the arrangement of the checkpoints. After the first test, a fixed PZT patch with a size of  $20 \times 20 \times 1.0 \text{ mm}^3$  was also employed for comparison. The PZT patch was bonded to Point B by using quick-hardening epoxy (Devcon 14270). The surface of the concrete slab had a 3-mm thick plaster layer. No visible cracks were found on the surface. Figure 7.22(b) shows the EMI spectra recorded at these points, in which the signal spectra range from 2 kHz to 20 kHz, considering the low sensitivity of the PZT sensor below 2 kHz, as discussed in Section 7.3.2. The delamination could be easily identified in the tested area, except for Point D, from the spectral pattern. Compared with Point D, the magnitude of peaks in other points was relatively lower. Meanwhile, multiple peaks were captured below 10 kHz, especially at Point C. The frequencies of the first resonance peaks for Points A, B, C, D, and E are 4.9, 8.5, 3.6, 10.4, and 7.4 kHz, respectively. Under the assumption that the modulus of elasticity of concrete was equal to 30 GPa, the density and Poisson's ratio of concrete equaled  $2368 \text{ kg/m}^3$  and 0.2, respectively. The concrete cover was assumed to be 20 mm. The upper bound of  $a$  for Points A, B, C, and E were 130, 101, 161, and 101 mm, respectively. By assuming a square delaminated area, the average dimension  $a$  for the four points was 123 mm, with a standard deviation of 29 mm. When the lowest frequency at Point C (i.e., 3.6 kHz) was used, the lower and upper bounds of delaminated dimension  $a$  were 136 and 161 mm, respectively.

Figure 7.23 plots the signal from the impact-echo methods at Points A and C. Given the maximum sampling rate of 12.8 kS/s, the maximum frequency reached 6.4 kHz after applying the frequency response function. However, the resonance peaks were difficult to identify even in the log-scale plot. The peaks at 5.2 and 3.6 kHz were captured by the impact-echo method at Points A and C, respectively, which were consistent with those captured by the EMI technique. This consistency confirms the

effectiveness of the proposed method. Meanwhile, the resonance peaks in the signal spectrum of the EMI technique were much easier to identify, indicating high signal-to-noise ratio and application advantages of the technique.

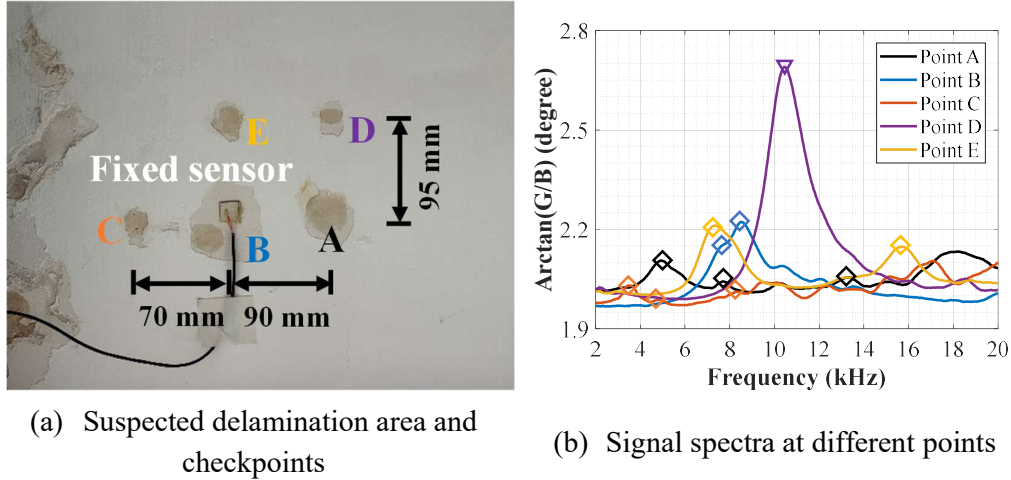


Figure 7.22 Suspected delamination area, checkpoints, and the corresponding EMI signals

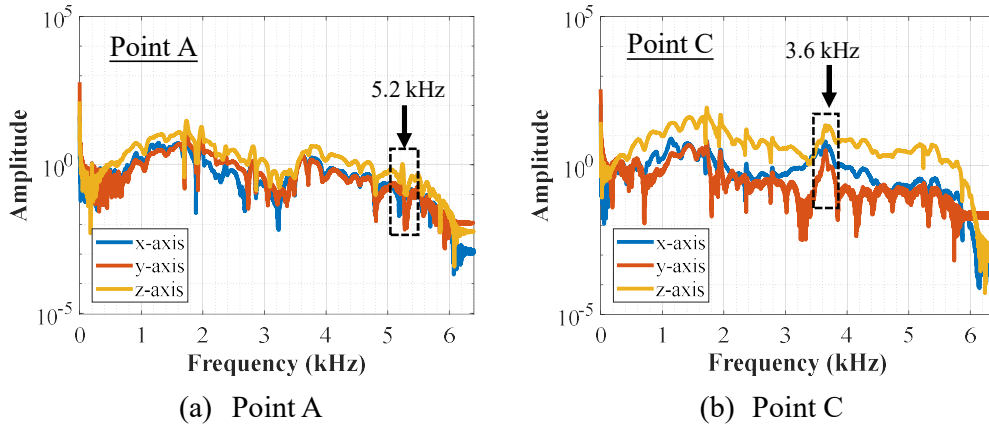


Figure 7.23 Signal spectra from the impact-echo method

Figure 7.24 presents the recorded signal spectra at Point B from two types of PZT sensors in two different tests. The signal spectra obtained at two different dates were generally consistent. Meanwhile, the first local defect resonance peak was moved slightly (Figure 7.24(a)). In general, the detachable sensor could produce stable and consistent results, as indicated in Figure 7.24(b). According to the results, detachable PZT sensors can be a convenient alternative to traditional fixed PZT sensors, particularly for short-term inspection of suspected areas.

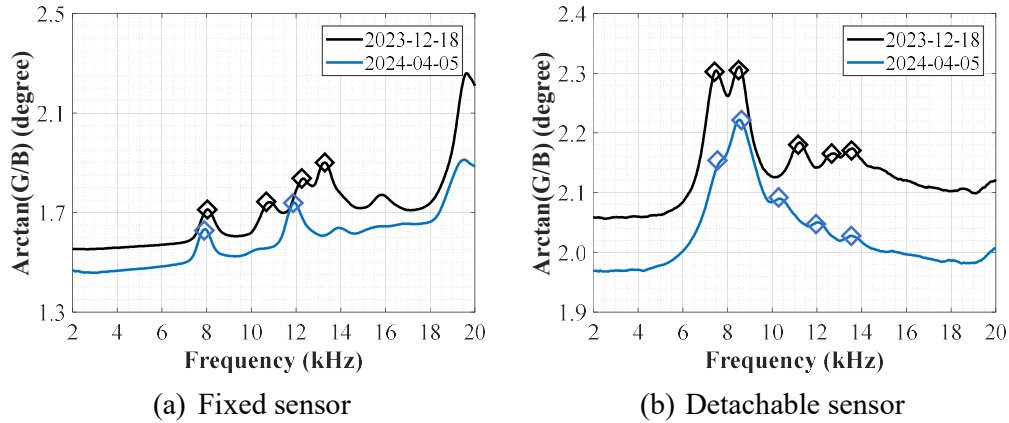


Figure 7.24 Signal spectra recorded at Point B at different times and with different sensors

### 7.5.3 Cover Opening for Verification

After the assessment in [Section 7.5.2](#), the tested area was opened by using a driller. The driller easily removed a layer with around 10 mm thickness. The opened area had about 250 mm length and 230 mm width, containing apparent flat interface caused by delamination, as shown in [Figure 7.25\(a\)](#). If the actual delamination depth (i.e., 10 mm) was substituted into Equations (7.6) and (7.8), the upper bound of  $a$  for the checkpoints A, B, C, and E were 103, 97, 126, and 90 mm, respectively. The average value of  $a$  on the basis of the four checkpoints was 104 mm. The predicted  $a$  value was within the opening area, indicating fair consistency. An 80-mm long and 70-mm wide brown area was found on this flat surface. After removing the concrete in the brown area, a corroded rebar with a 7-mm diameter was found ([Figure 7.25\(b\)](#)). Delamination evidence was also found at the boundary of the opening area, as shown in [Figure 7.25\(c\)](#). [Figure 7.25\(d\)](#) presents the collected fragments after the opening. The thickness of the concrete fragments was around 7 mm by deducting the thickness of plaster. The abovementioned information indicates that the expansion of the steel rebar caused delamination along a weak interface in the tested area. In summary, the on-site testing results validate the effectiveness of detecting the delamination of concrete cover using the proposed EMI technique.



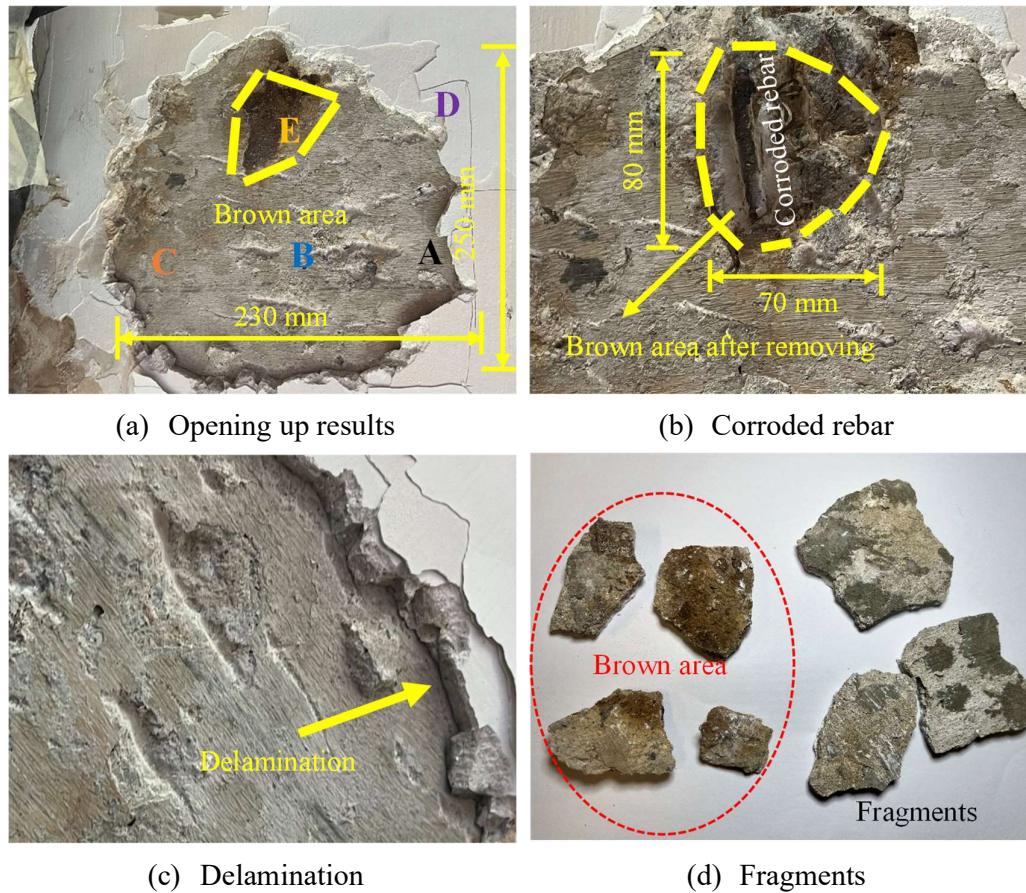


Figure 7.25 Opening results for verification

## 7.6 Summary

An improved EMI technique using a detachable sensor for detecting the delamination of the concrete cover was proposed, validated numerically and experimentally, and applied on-site. The following major conclusions were obtained:

1. The spectral patterns and characteristics could be used to quickly determine the delamination of concrete cover, confirming the effectiveness in detecting and localizing delamination damage using the proposed technique. In a healthy condition, only a distinct resonance peak above 10 kHz (corresponding to the sensor mode) could be observed; when the tested area was delaminated, multiple peaks below 10 kHz (corresponding to local defect resonances) could be captured.
2. The local defect resonances of the delaminated area were highly related to the defect size and material properties. The correlations between the first-order

frequency of the local defect resonance and defect size were established numerically for a quick approximate assessment.

3. The local defect resonance peaks were insensitive to the bonding materials and the boundary conditions of the slab.
4. The proposed method presented the signal spectra with a high signal-to-noise ratio. Hence, it can be directly implemented for on-site testing.

While the primary focus of this chapter is on detecting the delamination of the concrete cover in RC slabs, the proposed NDT method can be easily extended to long-term monitoring at crucial locations and to detection of the delamination of other materials and structures, paving a promising avenue for future research and application. The improvement of this chapter lies in choosing a more appropriate sensor and bonding materials to ensure the use of higher frequency signals to detect smaller and deep delamination.

## CHAPTER 8 CONCLUSIONS AND FUTURE WORK

### 8.1 Summary

As a local vibration-based model-free NDT method, the EMI techniques using PZT sensors have shown great promise in aerospace, mechanical, and civil engineering. Although traditional baseline-based EMI techniques can be directly implemented in the concrete field to detect damage, monitor hydrations, and predict strength, the accuracy of their results is heavily affected by ambient temperature, piezoelectric sensors, and bonding layers, among other influencing factors, which limit accurate quantitative assessment in the concrete field. Recently, baseline-free EMI techniques using SBP have been established for small metal beams and thin metal plates in aerospace and mechanical engineering. However, in the concrete field, host structures usually differ significantly in geometries and sizes. Consequently, the existing baseline-free methods cannot be directly extended to the concrete field, which motivates the development of specialized baseline-free EMI techniques for concrete. The potential applications of EMI techniques to concrete were explored in this thesis, focusing on the improvements in sensor installation strategies, signature modes identifications, and the corresponding assessment methods for different goals. This objective was achieved by conducting the following major tasks:

- (1) Based on the identification of the signal characteristics having high repeatability and being physically interpretable, a baseline-free EMI technique using SBP was proposed, for the first time, to measure the modulus of elasticity of 100-mm standard concrete cubes. A series of numerical and experimental investigations were conducted to show the insensitivity of the proposed technique to the variations in sensor geometries, bonding layers, and ambient temperature. The assessment method was derived through numerical analyses and then validated through experiments on two types of concrete. The experimental results confirmed the effectiveness and accuracy of the proposed technique in measuring the modulus of elasticity of concrete.

- (2) In consideration of the convenient installation of SBP, an improved baseline-free EMI technique with a novel sensor installation strategy was proposed for the first time, which realized the simultaneous measurement of the elastic constants (e.g., modulus of elasticity and Poisson's ratio) of standard concrete cubes. The accuracy of the proposed method after considering the material anisotropy and inhomogeneity of concrete cubes was examined numerically first. Experimental validations on two types of standard concrete cubes were conducted to show the stability and accuracy of the proposed method in comparison with the traditional resonance method recommended by ASTM C215.
- (3) A novel baseline-free EMI technique that can measure the elastic constants (e.g. shear modulus and Poisson's ratio) of concrete cubes at very early ages by using EBP installed inside the mold before casting was proposed. Unique vibration modes that can be identified at high damping and are highly related to shear modulus were selected for assessment. Experimental validations on the measurement of concrete properties within 48 hours were conducted to present the advantage and accuracy of the proposed method in comparison with the traditional resonance method.
- (4) Deliberately utilizing high-symmetry installations of PZT sensors can reduce the number of identified modes (i.e., the density of modes) and enable the use of the modes in a wide frequency range in the EMI technique. The optimal installations of PZT sensors in large-size concrete prisms were explored to develop a baseline-free EMI technique using special vibration modes insensitive to prism length. Six installation strategies corresponding to different numbers of symmetric axes were studied, involving both SBP and EBP. Experimental validations on five prisms were conducted to show the effectiveness and accuracy of the proposed method.
- (5) A baseline-free EMI technique utilizing a novel detachable PZT sensor was proposed for the first time to achieve convenient routine detection of delamination of concrete covers in indoor RC structures. Numerical analyses were conducted to

illustrate the feasibility of the technique. Experimental validations on a concrete slab subjected to corrosion-induced damage were performed in the laboratory to show the effectiveness of the proposed method. Then, on-site tests in an existing building in Hong Kong were conducted to show the applicability of the proposed method.

In the abovementioned tasks, Task 1 (presented in [Chapter 3](#)) aims to propose a baseline-free EMI technique that can stably measure the modulus of elasticity of concrete concerning different sensory systems and temperature variations. Tasks 2 and 3 (presented in [Chapters 4](#) and [5](#), respectively) concentrate on using EMI techniques and concrete cubes to measure the elastic constants (including Poisson's ratio) of concrete that traditional methods can hardly work on. Task 4 (presented in [Chapter 6](#)) focuses on extending the applicability of the baseline-free EMI technique to larger specimens using specially selected resonant modes in the middle-frequency range. Task 5 (presented in [Chapter 7](#)) seeks to improve the flexibility of the EMI technique by using detachable sensors to achieve quick and convenient detection for a wide area with concrete cover delamination.

## 8.2 Conclusions

A series of baseline-free EMI techniques are proposed and investigated progressively, with the major conclusions summarized as follows:

- (1) The proposed dimensionless signal index,  $\arctan(G/B)$ , can consider more information from the recorded signals. The EMI technique using this index can easily show a series of resonance modes of the coupled system. The resonant frequencies of concrete cubes in the low-frequency range (i.e.,  $< 70$  kHz) are highly related to the concrete properties but insensitive to the size of PZT patches and the properties of the adhesive layer. Among various tested PZT patches of different widths and thicknesses, the wider and thinner PZT patch ( $20 \times 20 \times 1.0$  mm<sup>3</sup>) showed the highest sensitivity. Concerning the bonding layer, a thickness of no more than 0.5 mm was recommended to obtain strong signal responses. The

good repeatability of the resonant frequencies at varying ambient temperatures (i.e., from 5 °C to 45 °C) was validated numerically and experimentally.  $E_{cd}$  could be accurately measured using the resonant frequencies and the predetermined correlations by assuming a fixed Poisson's ratio  $\mu_c$ . The proposed EMI technique for measuring  $E_{cd}$  was successfully validated using two types of concrete (i.e., SSC and HSC).

- (2) The EMI technique was further improved to accurately measure elastic constants of concrete, including modulus of elasticity and Poisson's ratio. The improved EMI technique selects special vibration modes after considering their symmetric types. A novel sensor installation method using two PZT patches can actuate and extract target vibration modes. The evaluation results, especially for Poisson's ratio, were insensitive to the material anisotropy and wall effect of the concrete cubes. Experimental validations showed that the proposed method could accurately and stably measure the elastic constants and outperformed the traditional resonance method recommended by ASTM C215.
- (3) The EMI technique was further developed to measure the elastic constants (i.e., shear modulus and Poisson's ratio) of very-early-age concrete cubes using EBP. Vibration modes highly dependent on shear modulus can be selected and utilized for assessment using the proposed sensor installation strategies (i.e., EBP-0° and EBP-45°). Both installation strategies can accurately measure the shear modulus, but only Strategy EBP-0° was recommended for measuring Poisson's ratio. Concerning the sensitivity of the size of the specimen, specimens in small sizes (i.e., 100 mm cubes) presented higher responses to the signals, benefiting the early monitoring, but certain modification is required. Strategy EBP-0° could measure the shear modulus and Poisson's ratio of concrete as early as 3 hours after casting.
- (4) The EMI technique was further developed to measure the material properties using length-insensitive modes of a concrete prism to extend its applicability to larger specimens. The symmetric concept can be effectively utilized in sensor

installations to reduce the identified number of modes. Sensor installation strategies with more symmetric planes were preferred. Strategies EBP-E-// and EBP-C-// were optimal for ease of mode identification, accessibility, and evaluation accuracy. The evaluation from high-symmetry length-insensitive modes in the middle-frequency range presented good consistency with those from the global resonant modes, showing promise to overcome the limitation of working frequency of PZT sensors.

- (5) An EMI technique using detachable piezoelectric sensors was successfully developed to detect the delamination of concrete cover quickly and conveniently. A PZT cuboid and double-sided tape could achieve the goal. The signal pattern obtained could qualitatively determine the delamination of the tested point. When the checkpoint was healthy, only a peak of the sensor above 10 kHz could be observed. When the checkpoint was delaminated, multiple peaks (i.e., local defect resonance) below 10 kHz were captured. The first-order local defect resonant frequency was effective for an approximate assessment of the size of the delamination area. Moreover, the proposed method presented signal spectra with a high signal-to-noise ratio, making it suitable for direct on-site inspection.

In conclusion, this thesis developed a series of high-performance baseline-free EMI techniques for material characterization and delamination detection by selecting special vibration modes, designing corresponding sensor installation strategies, and establishing quantitative assessment methods. Through the EMI technique, (a) the elastic constants (including modulus of elasticity and Poisson's ratio) of concrete cubes can be accurately measured, outperforming the traditional NDT methods; (b) the elastic constants (including shear modulus and Poisson's ratio) of very-early-age concrete cubes can be measured, which can hardly be covered by other traditional NDT methods. (c) the local material properties of concrete prisms can be directly measured, providing a new way to assess concrete structures; and (d) the delamination of concrete covers of indoor structures can be detected, localized, and approximated assessed.

### 8.3 Future Work

Despite the progress and applications achieved successfully in this thesis, which will benefit the laboratory and on-site work to some extent, numerous research issues and limitations remain to be addressed in future work. In this thesis, all the analyses and assessments were conducted on the basis of the assumption that concrete materials are elastic, isotropic, and homogenous. Meanwhile, only plain concrete material was investigated and characterized; while internal reinforcing bars (i.e., longitudinal and transverse reinforcements) were not considered in the material characterization part, limiting the direct implementation in reinforced concrete structures. Therefore, to understand concrete materials further and facilitate practical industrial applications, future work may start by removing these basic assumptions and considering other practical scenarios. A series of future works in material characterization are planned at specimens and structural levels.

#### **Material characterization at the specimen level**

- (1) In this thesis, concrete was regarded as an isotropic material, and its elastic constants could be accurately measured by the improved EMI technique presented in [Chapter 4](#). However, real-world concrete still presents weak anisotropy, which cannot be ignored in some scenarios (such as low-strength concrete and 3D printing concrete). The casting (printing) direction and shape of the structural members result in a noticeable level of anisotropy. Even in conventional cast concrete, the compressive strength presents approximately 10% anisotropy along different directions of beams, columns, slabs, and walls. Therefore, an anisotropy matrix containing nine independent parameters is highly important for thoroughly understanding such differences in cast-in-place concrete. An EMI technique for measuring the anisotropy matrix remains lacking. Future research may start with carefully selecting the vibration modes of standard concrete cubes that are sensitive to certain anisotropic elastic constants, and then design proper sensor installation strategies for extracting the target vibration modes and identifying the anisotropy



matrix. Detachable sensors are preferred from the perspective of economy and convenience.

- (2) This thesis has presented a series of methods for characterizing material properties in intact status. However, in-service concrete usually works with different damage introduced by thermal and loading actions. Different damage types may have diverse effects on concrete material properties. For example, temperature may introduce isotropic damage to concrete, while uniaxial loading may lead to anisotropic damage. Future research needs to establish correlations between the deterioration of elastic constants and microdamage in concrete specimens. In particular, Poisson's ratio, which was accurately measured in [Chapter 4](#), promises to become a new damage index for quantifying microdamage. Given the assessment of Poisson's ratio, the modulus of elasticity may be modified on the basis of the laboratory testing results of standard concrete cubes. The microdamage (e.g., cracks and voids) can be quantified by employing CT scanning techniques. Once the gap between the micro-damage and elastic constants is bridged, the baseline-free EMI technique may become a powerful NDT tool for quickly and directly assessing the in-situ concrete properties of in-service structures.
- (3) Mesoscale analyses are becoming a popular tool for removing the homogenous assumption of concrete materials. However, most are still limited to numerical analyses and present only qualitative discussions. No effective tool is available for conducting experimental investigations. As discussed in [Chapter 2](#), EMI techniques can measure specimens from 10 mm to 1000 mm, allowing the measurement of coarse aggregate (typically at least 10 mm in diameter). Mortar specimens, typically cubes with a dimension of over 20 mm, can be easily measured using the EMI technique. After the properties of aggregates and mortar are determined, a mesoscale model can be quantitatively built to study the effects of various components, such as the volumetric ratio and material properties of the aggregate, and the interface between the aggregate and mortar at different curing ages and

statuses (e.g., temperature and humidity).

- (4) Although most existing studies considered concrete an elastic material, some research showed that concrete should be treated as a viscoelastic material. The creep of concrete makes the measured elastic properties highly related to the strain rates of the testing method. In static destructive tests, the measured modulus of elasticity is lower than the actual value; by contrast, the measured modulus of elasticity in dynamic testing will be higher. This feature makes the correlations between the static and dynamic modulus of the elasticity difficult to determine at early ages when the creep effect is significant. Therefore, future research on baseline-free EMI techniques may need to consider the viscoelastic properties of concrete materials. Then, the correlations between the static and dynamic modulus of elasticity should be established by considering the parameters describing creep. Once this objective is achieved for standard specimens, EMI technique-based tests and evaluations can completely replace those traditional destructive tests. Moreover, the compressive strength of concrete can be easily predicted at any age using established empirical relationships between elastic constants and compressive strength in standards and codes.

#### **Material characterization at the structural level**

- (5) At the structural level, future works may start by extending the existing baseline-free EMI technique in [Chapter 6](#) to RC members (e.g., columns and beams). Suitable vibration modes can be found by considering the effects of different boundary conditions. For example, length-insensitive modes, which are affected by the boundaries at the ends, may be directly used for columns; meanwhile, special modes may be selected for beams, especially for beams with a large height-to-width ratio. Moreover, the impact of the reinforcing materials may be considered for a highly realistic assessment.
- (6) Based on the works in [Chapters 6](#) and [7](#), vibration modes highly related to thickness can be utilized to measure the in-place modulus of elasticity of concrete directly for

wall and slab structures. A detachable sensor is preferred to achieve this objective. Future research may start to design a proper detachable sensor that can offer strong sensitivity and high mobility during the testing to facilitate the implementation. Then, the assessment method is supposed to consider the effects of reinforcing materials and surface coating materials of structures.

- (7) The abovementioned methods are built on specific structural vibration modes, such as section and thickness-related modes. However, a challenge will arise when the applied EMI technique cannot excite structural modes, such as when sensors are installed on a semi-infinite space surface. This challenge may be overcome by examining the shift of  $f_{PZT}$  as the index. The semi-infinite space can be considered an elastic constraint to PZT sensors. The stiffness provided by the host structure can be obtained by considering the interactions among sensors, bonding layers, and host structures. As a result, the modulus of elasticity in a local area can be obtained. One issue with this method is that the detectable range would be confined to a small area. If the detachable range is extremely small, the wall effect and aggregate distribution may lead to unavoidable disturbances in the evaluation results.

### **Debonding detection in composite structures**

In addition to material characterization, future opportunities remain for debonding detection in composite structures using the proposed method.

- (8) Because of the shrinkage of concrete, debonding between strengthening layers and concrete materials occurs. Based on [Chapter 7](#), debonding detection may be achieved using the proposed EMI technique and the detachable sensor. Through adjusting the signal processing method, the proposed method in [Chapter 7](#) is a promising alternative for detecting such damage in actual practice. Future research may explore the detection of debonding in confined concrete.

## REFERENCES

- ACI (American Concrete Institute). (2008). "Building code requirements for structural concrete and commentary." ACI 318-08, Farmington Hills, MI.
- ACI (American Concrete Institute). (2003). "In-place methods to estimate concrete strength." ACI 228.1R-03, Farmington Hills, MI.
- ACI (American Concrete Institute). (2004). "Nondestructive test method for evaluation of concrete structures." ACI 228.2R-98, Farmington Hills, MI.
- Ahmed, L. (2018). "Dynamic measurements for determining Poisson's ratio of young concrete." *Nordic concrete research*, 58(1): 95-106.
- Ai, D., Li, H. and Zhu, H. (2023). "Flexure-critical stress and damage identification in RC beam structure using embedded piezoelectric transducers: 2D modelling and experimental investigations." *Construction and Building Materials*, 409: 134017.
- Ai, D., Lin, C., Luo, H. and Zhu, H. (2020). "Temperature effect on electromechanical admittance-based concrete structural health monitoring." *Structural Health Monitoring*, 19(3): 661-692.
- Ai, D., Lin, C. and Zhu, H. (2021). "Embedded piezoelectric transducers based early-age hydration monitoring of cement concrete added with accelerator/retarder admixtures." *Journal of Intelligent Material Systems and Structures*, 32(8): 847-866.
- Ai, D., Luo, H., Wang, C. and Zhu, H. (2018). "Monitoring of the load-induced RC beam structural tension/compression stress and damage using piezoelectric transducers." *Engineering Structures*, 154: 38-51.
- Ai, D., Luo, H. and Zhu, H. (2017). "Diagnosis and validation of damaged piezoelectric sensor in electromechanical impedance technique." *Journal of Intelligent Materials Systems and Structures*, 28(7): 837-850.
- Ai, D., Luo, H. and Zhu, H. (2019). "Numerical and experimental investigation of flexural performance on pre-stressed concrete structures using electromechanical admittance." *Mechanical Systems and Signal Processing*, 128: 244-265.

- Ai, D., Zhang, D. and Zhu, H. (2024). "Damage localization on reinforced concrete slab structure using electromechanical impedance technique and probability-weighted imaging algorithm." *Construction and Building Materials*, 424: 135824.
- Ai, D., Zhu, H., Luo, H. (2016). "Sensitivity of embedded active PZT sensor for concrete structural impact damage detection." *Construction and Building Materials*, 111: 348-357.
- Ai, D., Zhu, H., Luo, H. and Wang, C. (2018). "Mechanical impedance based embedded piezoelectric transducer for reinforced concrete structural impact damage detection: A comparative study." *Construction and Building Materials*, 165: 472-483.
- Aili, A., Vandamme, M., Torrenti, J., Masson, B. and Sanahuja, J. (2016). "Time evolutions of non-ageing viscoelastic Poisson's ratio of concrete and implications for creep of C-S-H." *Cement and Concrete Research*, 90: 144-161.
- Annamdas, V.G.M. and Soh, C.K. (2007). "Three-dimensional electromechanical impedance model. I: formulation of directional sum impedance." *Journal of Aerospace Engineering*, 20(1): 53-62.
- Annamdas, V.G.M. and Soh, C.K. (2008). "Three-dimensional electromechanical impedance model for multiple piezoceramic transducers-structure interaction." *Journal of Aerospace Engineering*, 21(1): 35-44.
- Annamdas, V.G.M. and Soh, C.K. (2010). "Application of electromechanical impedance technique for engineering structures: review and future issues." *Journal of Intelligent Materials Systems and Structures*, 21(1): 41-59.
- Annamada, V.G.M. and Yang, Y. (2012). "Practical implementation of piezo-impedance sensors in monitoring of excavation support structures." *Structural Control and Health Monitoring*, 19: 231-245.
- Annamdas, V.G.M., Yang, Y. and Soh, C.K. (2010). "Impedance based concrete monitoring using embedded sensors." *International Journal of Civil and Structural Engineering*, 1: 414.

- Anson, M. and Newman, K. (1966). "The effect of mix proportions and method of testing on Poisson's ratio for mortars and concretes." *Magazine of Concrete Research*, 18(56): 115-130.
- ASTM C1074 (2019). "Standard test method for estimating concrete strength by the maturity method." American Society for Testing and Materials, West Conshohocken PA.
- ASTM C1198. (2020) "Standard test method for dynamic Young's modulus, shear modulus, and Poisson's ratio for advanced ceramics by sonic resonance." American Society for Testing and Materials, West Conshohocken PA.
- ASTM C1259. (2021) "Standard test method for dynamic Young's modulus, shear modulus, and Poisson's ratio for advanced ceramics by impulse excitation of vibration." American Society for Testing and Materials, West Conshohocken PA.
- ASTM C1548. (2002). "Standard test method for dynamic Young's modulus, shear modulus, and Poisson's ratio of refractory materials by impulse excitation of vibration." American Society for Testing and Materials, West Conshohocken PA.
- ASTM C1740. (2016). "Standard test method for evaluating the condition of concrete plates using the impulse-response method." American Society for Testing and Materials, West Conshohocken PA.
- ASTM C215. (2019). "Standard test method for fundamental transverse, longitudinal, and torsional resonant frequencies of concrete specimens." American Society for Testing and Materials, West Conshohocken PA.
- ASTM C39/C39M. (2020). "Standard test method for compressive strength of cylindrical concrete specimens." American Society for Testing and Materials, West Conshohocken PA.
- ASTM C469/C469M. (2022). "Standard test method for static modulus of elasticity and Poisson's ratio of concrete in compression." American Society for Testing and Materials, West Conshohocken PA.
- ASTM C597. (2022). "Standard test method for ultrasonic pulse velocity through

- concrete.” American Society for Testing and Materials, West Conshohocken PA.
- ASTM C747. (2023). “Standard test method for moduli of elasticity and fundamental frequencies of carbon and graphite materials by sonic resonance.” American Society for Testing and Materials, West Conshohocken PA.
- ASTM C805/C805M (2018). “Standard test method for rebound number of hardened concrete.” American Society for Testing and Materials, West Conshohocken PA.
- ASTM C848. (2020). “Standard test method for Young’s modulus, shear modulus, and Poisson’s ratio for ceramic whitewares by resonance.” American Society for Testing and Materials, West Conshohocken PA.
- ASTM D3497. (2003) “Standard test method for dynamic modulus of asphalt mixtures.” American Society for Testing and Materials, West Conshohocken PA.
- ASTM E1876, Standard test method for dynamic Young’s modulus, shear modulus, and Poisson’s ratio by impulse excitation of vibration, American Society for Testing and Materials, West Conshohocken PA, 2022.
- ASTM E650/E650M. (23017). “Standard guide for mounting piezoelectric acoustic emission sensors.” American Society for Testing and Materials, West Conshohocken PA.
- Ayorinde, E.O. and Yu, L. (1999). “On the use of diagonal modes in the elastic identification of thin plates.” *Journal of Vibration and Acoustic*, 21: 33-40.
- Ayorinde, E.O. and Yu, L. (2005). “On the elastic characterization of composite plates with vibration data.” *Journal of Sound and Vibration*, 283: 243-262.
- Ayres, J.W., Lalande, F., Chaudhry, Z. and Rogers, C.A. (1998). “Qualitative impedance-based health monitoring of civil infrastructures.” *Smart Materials and Structures*, 7: 599-605.
- Bahr, O., Schaumann, P., Bollen, B. and Bracke, J. (2013). “Young’s modulus and Poisson's ratio of concrete at high temperatures: Experimental investigations,” *Material & Design*, 45: 421-429.
- Balamonica, K., Jothi Saravanan, T., Bharathi Priya, C. and Gopalakrishnan, N. (2020).

- “Piezoelectric sensor-based damage progression in concrete through serial/parallel multi-sensing technique.” *Structural Health Monitoring*, 19(2): 339-356.
- Bažant, Z.P. (1983). “Comments on orthotropic models for concrete and geomaterials.” *Journal of Engineering Mechanics*, 109(3): 849-865.
- Bassim, R. and Issa, M. (2020). “Dynamic- and static-elastic moduli and strength properties of early-age Portland cement concrete pavement mixture.” *Journal of Materials in Civil Engineering*, 32(5): 04020066.
- Baptista, F.G. and Filho, J.V. (2009). “A new impedance measurement system for PZT-based structural health monitoring.” *IEEE Transactions on Instrumentation and Measurement*, 58(10): 3602-3608.
- Baptista, F.G. and Filho, J.V. (2010). “Optimal frequency range selection for PZT transducers in impedance-based SHM systems.” *IEEE Sensors Journal*, 10(8): 1297-1303.
- Baral, S., Adhikari, S., Negi, P. and Bhalla, S. (2022). “Development and evaluation of reusable piezo sensors for health monitoring of thin-walled steel structures.” *Journal of Civil Structural Health Monitoring*, 12: 647-657.
- Bertoldo, C., Gorski, R.K.S. and Gonçalves, R. (2020). “Evaluation of elastic anisotropy of concrete using ultrasound wave propagation.” *Journal of Materials in Civil Engineering*, 32(4): 04020056.
- Bezerra, A.K.L., Melo, A.R.S., Freitas, I.L.B., Babadopulos, L.F.A.L., Carret, J. and Soares, J.B. (2023). “Determination of modulus of elasticity and Poisson’s ratio of cementitious materials using S-wave measurements to get consistent results between static, ultrasonic and resonant testing.” *Construction and Building Materials*, 398: 132456.
- Bhalla, S. and Soh, C.K. (2003). “Structural impedance based damage diagnosis by piezo-transducers.” *Earthquake Engineering and Structural Dynamics*, 32: 1879-1916.
- Bhalla, S. and Soh, C.K. (2004a). “Electromechanical impedance modeling for



- adhesively bonded piezo-transducers.” *Journal of Intelligent Materials Systems and Structures*, 15: 955-972.
- Bhalla, S. and Soh, C.K. (2004b). “Structural health monitoring by piezo-impedance transducers. I: modeling.” *Journal of Aerospace Engineering*, 17(4): 154-165.
- Bharathi Priya, C., Jothi, Saravanan, T., Balamonic, K., Gopalakrishnan, N. and Rama Mohan Rao, A. (2018). “EMI based monitoring of early-age characteristics of concrete and comparison of serial/parallel multi-sensing technique.” *Construction and Building Materials*, 191: 1268-1284.
- Bois, C. and Hochard, C. (2004). “Monitoring of laminated composites delamination based on electro-mechanical impedance measurement.” *Journal of Intelligent Material Systems and Structures*, 15(1): 59-67.
- BS 1881 (1986). British standard testing concrete for recommendations for measurement of velocity of ultrasonic pulses in concrete.
- Cai, R., Hu, Y., Yu, M., Liao, W., Yang, L., Kumar, A. and Ma, H. (2020). “Skin effect of chloride ingress in marine concrete: A review on the convection zone.” *Construction and Building Materials*, 262: 120566.
- Cai, X., Peralta, L., Gouttenoire, P., Olivier, C., Peyrin, F., Langier, P. and Grimal, Q. (2017). “Quantification of stiffness measurement errors in resonant ultrasound spectroscopy of human cortical bone.” *The Journal of the Acoustical Society of America*, 142(5): 2755-2765.
- Can, O., Kabir, M. and Ozevin, D. (2018). “Periodic assembly of steel truss systems for efficient analyses and early detection of localized damage using impulse response method.” *Journal of Structural Engineering*, 144(5): 04018032.
- Capozzoli, L. and Rizzo, E. (2017). “Combined NDT techniques in civil engineering applications: laboratory and real test.” *Construction and Building Materials*, 154: 1139-1150.
- Carino, N.J. (2001). “The impact-echo method: an overview.” *Structures 2001: A Structural Engineering Odyssey*, 1-18.

- Carrazedo, R., Haach, V.G., Monfrinato, E.F., Perissin, D.A.M. and Chaim, J.P. (2018). "Mechanical characterization of concrete by impact acoustics tests." *Journal of Materials in Civil Engineering*, 30(4): 05018001.
- Carrillo, J., Rzmirez, J. and Lizarazo-Marriage, J. (2019). "Modulus of elasticity and Poisson's ratio fiber-reinforced concrete in Colombia from ultrasonic pulse velocities." *Journal of Building Engineering*, 23: 18-26.
- Cawley, P. (1984). "The impedance method of non-destructive inspection." *NDT International*, 17(2): 59-65.
- Cawley, P. (1985). "The operation of NDT instruments based on the impedance method." *Composite Structures*, 3: 215-228.
- Cawley, P. and Nguyen, D. (1988). "The use of the impedance method of non-destructive testing on honeycomb structures." *Mechanical Systems and Signal Processing*, 2(4): 309-325.
- Chen, H. and Leon, G. (2019). "Direct determination of dynamic elastic modulus and Poisson's ratio of rectangular Timoshenko prisms." *Journal of Engineering Mechanics*, 145(9), 04019071.
- Chen, A., Pan, Z. and Ma, R. (2016). "Mesoscopic simulation of steel rebar corrosion process in concrete and its damage to concrete cover." *Structure and Infrastructure Engineering*, 13(4): 478-493.
- Choi, H., Shams, S. and Azari, H. (2018). "Frequency wave number-domain analysis of air-coupled impact-echo tests in concrete slab." *Journal of Infrastructure Systems*, 24(3): 04018015.
- Clem, D.J., Popovics, J.S., Schumacher, T., Oh, T., Ham, S. and Wu, D. (2013). "Understanding the impulse response method applied to concrete bridge decks." *The 39<sup>th</sup> Annual Review of Progress in Quantitative Nondestructive Evaluation*, 1511: 1333-1340.
- Constantinides, G., Ulm, F.J. and Van Vliet, K. (2003). "On the use of nanoindentation for cementitious materials." *Material and Structures*, 36: 191-196.

- Czarnecki, S. and Sadowski, L. (2022). "Morphological properties of the cement skin: Understanding the effect of contact with formwork." *Case Studies in Construction Materials*, 16: e01007.
- Czekanski, A. and Zozulya, V.V. (2020). "Dynamics of vibrating beams using first-order theory based on Legendre polynomial expansion." *Archive of Applied Mechanics*, 90: 789-814.
- Davis, A.G. (2003). "The nondestructive impulse response test in North America: 1985-2001." *NDT&E International*, 36: 185-193.
- Dawood, E.T. and Ramli, M. (2011). "High strength characteristics of cement mortar reinforced with hybrid fibres." *Construction and Building Materials*, 25(5): 2240-2247.
- De Angelis, G., Meo, M., Almond, D.P., Pickering, C.G. and Angioni, S.L. (2012). "A new technique to detect defect size and depth in composite structures using digital shearography and unconstrained optimization." *NDT&E International*, 45: 91-96.
- Demarest, H.H. 1971. "Cube-resonance method to determine the elastic constants of the solids." *The Journal of the Acoustical Society of America*, 49, 768.
- Diamanti, N. and Redman, D. (2012). "Field observations and numerical models of GRP response from vertical pavement cracks." *Journal of Applied Geophysics*, 81: 106-116.
- Dinh, K. and Gucunski, N. (2021). "Factors affecting the detectability of concrete delamination in GRP images." *Construction and Building Materials*, 274: 121837.
- Ekstein, H. and Schiffman, T. 1956. "Free vibration of isotropic cubes and nearly cubic parallelepipeds." *Journal of Applied Physics*, 27(4): 405-412.
- El Maaddawy T.A. and Soudki, K.A. (2003). "Effectiveness of impressed current technique to simulate corrosion of steel reinforcement in concrete." *Journal of Materials in Civil Engineering*, 15(1): 41-47.
- Evensen, D.A. (1976). "Vibration analysis of multi-symmetric structures." *AIAA Journal*, 14(4): 446-453.

- Ezvan, O. Zeng, X., Ghanem, R. and Gencturk, B. (2018). “Dominant vibration modes for broadband frequency analysis of multiscale structures with numerous local vibration modes.” *International Journal for Numerical Methods in Engineering*, 117(6): 644-692.
- Fan, S., Zhao, S., Kong, Q. and Song, G. (2021). “An embeddable spherical smart aggregate for monitoring concrete hydration in very early age based on electromechanical impedance method.” *Journal of Intelligent Material Systems and Structures*, 32(5): 537-548.
- Fan, W. and Qiao, P. (2011). “Vibration-based damage identification methods: a review and comparative study.” *Structural Health Monitoring*, 10(1): 83-111.
- Fine, M.E. (1952). “Dynamic methods for determining the elastic constants and their temperature variation in metals.” Symposium on Determination of Elastic Constants, 43–70.
- Fu, J., Tan, C. and Li, F. (2015). “Quantitative electromechanical impedance method for nondestructive testing based on a piezoelectric bimorph cantilever.” *Smart Material and Structures*, 24: 065038.
- Gassman, S.L. and Zein, A.S. (2008). “Change in impact-echo response during fatigue loading of concrete bridge T-girder.” *ACI Materials Journal*, 105(4): 395-403.
- Gazis, D.C. (1959). “Three-dimensional investigation of the propagation of waves in hollow circular cylinders. I. analytical foundation.” *Journal of the Acoustical Society of America*, 31: 568-573.
- GB/T 50081 (2019). Standard for test methods of concrete physical and mechanical properties, National Standard of the People’s Republic of China.
- Ghafari, E., Yuan, Y., Wu, C., Nantung, T. and Lu, N. (2018). “Evaluation the compressive strength of the cement paste blended with supplementary cementitious materials using a piezoelectric-based sensor.” *Construction and Building Materials*, 171: 504-510.

- Gianesini, B., Cortez, N.E., Antunes, R.A. and Filho, J.V. (2020). "Method for removing temperature effect in impedance-based structural health monitoring systems using polynomial regression." *Structural Health Monitoring*, 20(1): 202-218.
- Giurgiutiu, V. (2014). *Structural health monitoring with piezoelectric wafer active sensors*. 2<sup>nd</sup> ed.; Elsevier Academic Press: Amsterdam, The Netherlands.
- Giurgiutiu, V. and Rogers, C.A. (1998). "Recent advancements in the electro-mechanical (E/M) impedance method for structural health monitoring and NDE." In: *Proceedings of SPIE*, San Diego, California, USA, Vol. 3329: 536-574.
- Giurgiutiu, V. and Zagrai, A.N. (2002). "Embedded self-sensing piezoelectric active sensors for on-line structural identification." *Journal of Vibration and Acoustics*, 124(1): 116-125.
- Gresil, M., Yu, L., Giurgiutiu, V. and Sutton, M. (2012). "Predictive modeling of electromechanical impedance spectroscopy for composite materials." *Structural Health Monitoring*, 11(6): 671-683.
- Gu, H., Song, G., Dhonde, H., Mo, Y.L. and Yan, S. (2006). "Concrete early-age strength monitoring using embedded piezoelectric transducers." *Smart Materials and Structures*, 15:1837-1845.
- Gucunski, N. (2013). *Nondestructive testing to identify concrete bridge deck deterioration*, Transportation Research Board, National Research Council.
- Haach, V.G., Carrazedo, R., Ribeiro, P.O., Ferreira, L.P.A. and Abe, I. P. (2020). "Evaluation of elastic anisotropic relations for plain concrete using ultrasound and impact acoustic tests." *Journal of Materials in Civil Engineering*, 33(2), 04020448.
- Han, S. and Kim, J. (2004). "Effect of temperature and age on the relationship between dynamic and static elastic modulus of concrete." *Cement and Concrete Research*, 34: 1219-1227.

- Han, S.G., Lauridsen, J.T. and Hoang, L.G. (2018). "Experimental and statistical investigation of the compressive strength anisotropy in structural concrete." *Cement and Concrete Research*, 107: 304-316.
- Hill, M., McHugh, J. and Turner, J.D. (2000). "Cross-sectional modes in impact-echo testing of concrete structures." *Journal of Structural Engineering*, 126(2): 228-234.
- Hu, G., Yang, Y., Mohanty, L., Chae, S., Ishizeki, K. and Tang, L. (2024). "An electromechanical impedance measurement-based solution for monitoring fresh concrete maturity." *Journal of Intelligent Material Systems and Structures*, 35(10): 907-919.
- Hu, X., Zhu, H. and Wang, D. (2014). "A study of concrete slab damage detection based on the electromechanical impedance method." *Sensor*, 14: 19897-19909.
- Hu, Y., Li, W., Zhang, C., Lan, Z. and Deng, M. (2024). "Quantitative assessment of delamination in composites using multiple local-defect-resonance modes." *Journal of Sound and Vibration*, 589: 118499.
- Huang, Q. Li, C. and Song, X. (2022). "Spatial distribution characteristics of ellipsoidal coarse aggregates in concrete considering wall effect." *Construction and Building Materials*, 327: 126922.
- Hughes, B.P. and Ash, J.E. (1970). "Anisotropy and failure criteria for concrete." *Matériaux et Construction*, 3: 371-374.
- Huh, J., Tran, Q.H., Lee, J., Han, D., Ahn, J. and Yim, S. (2016). "Experimental study on detection of deterioration in concrete using infrared thermography technique." *Advances in Materials Science and Engineering*, 1053856: 12 pages.
- Huynh, T.C. and Kim, J.T. (2018). "RBFN-based temperature compensation method for impedance monitoring in prestressed tendon anchorage." *Structural Control and Health Monitoring*, 25: e2173.
- Jana, D. (2007). "Delamination-a state-of-the art review." *Proceedings of the Twenty-Ninth Conference on Cement Microscopy*, Quebec City, PQ, Canada.

- Jenq, S.T. and Chang, C.K. (1995). "Characterization of piezo-film sensors for direct vibration and impact measurements." *Experimental Mechanics*, 35: 224-232.
- Ji, Y., Chen, A., Chen, Y., Han, X., Li, B., Gao, Y. Liu, C. and Xie, J. (2023). "A state-of-the-art review of concrete strength detection/monitoring methods: with special emphasis on PZT transducers." *Construction and Building Materials*, 362: 129742.
- Jin, X. and Li, Z. (2001). "Dynamic property determination for early-age concrete." *ACI Materials Journal*, 98(5): 365-370.
- Jordan, R.W. (1980). "The effect of stress, frequency, curing, mix and age upon the damping of concrete." *Magazine of Concrete Research*, 32(113): 195-205.
- Jothi Saravanan, T., Balamonica, K., Bharathi Priya, C., Gopalakrishnan, N. and Murthy, S.G.N. (2017). "Piezoelectric EMI-based monitoring of early strength gain in concrete and damage detection in structural components." *Journal of Infrastructure Systems*, 23(4): 04017029.
- Jothi Saravanan, T., Balamonica, K., Bharathi Priya, C., Likhith Reddy, A. and Gopalakrishnan, N. (2015). "Comparative performance of various smart aggregates during strength gain and damage states of concrete." *Smart Materials and Structures*, 24: 085016.
- Kang, S., Wu, Y.C., David, D.S. and Ham, S. (2022). "Rapid damage assessment of concrete bridge deck leveraging an automated double-sided bounce system." *Automation in Construction*, 138: 104244.
- Kaur, N., Li, L., Bhalla, S. and Xia, Y. (2016). "A low-cost version of electro-mechanical impedance technique for damage detection in reinforced concrete structures using multiple piezo configurations." *Advances in Structural Engineering*, 20(8): 1247-1254.
- Kee, S and Gucunski, N. (2016). "Interpretation of flexural vibration modes from impact-echo testing." *Journal of Infrastructure Systems*, 22(3): 04016009.
- Kee S., Oh, T. Popovics, J.S., Arndt, R.W. and Zhu, J. (2012). "Nondestructive bridge deck testing with air-coupled impact-echo and infrared thermography." *Journal of*

- Bridge Engineering*, 17(6): 928-939.
- Khan, M.S. (2003). "Detecting corrosion-induced delaminations." *Concrete International*, 25(7): 73-78.
- Kheder, G.F. (1999). "A two stage procedure for assessment of in situ concrete strength using combined non-destructive testing." *Material and Structures*, 32: 410-417.
- Kim, H., Liu, X., Ahn, E., Shin, M., Shin, S.W. and Sim, S. (2019). "Performance assessment method for crack repair in concrete using PZT-based electromechanical impedance technique." *NDT and E International*, 104: 90-97.
- Kim, J., Lee, C., Park, S. and Koh, K. (2013). "Real-time strength development monitoring for concrete structures using wired and wireless electro-mechanical impedance techniques." *KSCE Journal of Civil Engineering*, 17(6): 1432-1436.
- Kim, M.K., Kim, E.J., Park, H.W. and Sohn, H. (2011). "Reference-free impedance-based crack detection in plates." *Journal of Sound and Vibration*, 330: 5949-5962.
- Kocherla, A. and Subramaniam, K.V.L. (2020). "Embedded electrical impedance-based PZT sensor for monitoring hydrating concrete: development and evaluation." *Smart Materials and Structures*, 29: 055038.
- Kolluru, S.V., Popovics, J.S. and Shah, S.P. (2000). "Determining elastic properties of concrete using vibrational resonance frequencies of standard test cylinders." *Cement, Concrete, and Aggregates*, CCAGDP, 22(2): 81-89.
- Komlos, K., Popovics, S., Nurnbergerova, T., Babal, B. and Popovics, J.S. (1996). "Comparison of five standards on ultrasonic pulse velocity testing of concrete." *Cement, Concrete, and Aggregates*, CCAGDP, 18(1): 42-48.
- Kong, Q., Fan, S., Bai, X., Mo, Y. and Song, G. (2017). "A novel embeddable spherical smart aggregate for structural health monitoring: part I. fabrication and electric characterization." *Smart Materials and Structures*, 26: 095050.
- Kong, Z. and Lu, N. (2020). "Improved method to determine Young's modulus for concrete cylinder using electromechanical spectrum: principle and validation." *Journal of Aerospace Engineering*, 33(6): 04020079.



- Krauß, M. and Hariri, K. (2006). "Determination of initial degree of hydration for improvement of early-age properties of concrete using ultrasonic wave propagation." *Cement and Concrete Composites*, 28: 299-306.
- Krejiger, P.C. (1984). "The skin of concrete composition and properties." *Matériaux et Construction*, 17: 275-283.
- Kuang, Y., Li, G. and Chen, C. (2006). "An admittance function of active piezoelectric elements bonded on a cracked beam." *Journal of Sound and Vibration*, 298: 393-403.
- Lan, C., Liu, H., Zhuang, S., Wang, J., Li, W. and Lin, G. (2024). "Monitoring of crack repair in concrete using spherical smart aggregates based on electromechanical impedance (EMI) technique." *Smart Materials and Structures*, 33: 025031.
- Lange, Y.V. (1994). "The mechanical impedance analysis method of nondestructive testing (a review)." *Nondestructive Testing and Evaluation*, 11(4): 177-193.
- Lee, B.J., Kee, S., Oh, T. and Kim Y. (2017). "Evaluating the dynamic elastic modulus of concrete using shear-wave velocity measurements." *Advances in Materials Science and Engineering*, Article ID 1651753.
- Lee, C.J., Lee, J.C., Shin, S.W. and Kim, W.J. (2012). "Investigation of setting process of cementitious materials using electromechanical impedance of embedded piezoelectric patch." *Journal of the Korea Institute of Building Construction*, 12(6): 607-614.
- Lee, K., Kim, D. and Kim, J. (1997). "Determination of dynamic Young's modulus of concrete at early ages by impact resonance test." *KSCE Journal of Civil Engineering*, 1(1): 11-18.
- Lee, T., Lakes, R.S. and Lai, A. (2000). "Resonant ultrasound spectroscopy for measurement of mechanical damping: comparison with broadband viscoelastic spectroscopy." *Review of Scientific Instruments*, 71(7), 2855.
- Leshchinsky, A.M. (1990). "Anisotropy of concrete strength." *Cement, Concrete, and Aggregate*, 12(2), 117-119.

- Li, C.Q., Zheng, J.J., Lawanwisut, W. and Melchers, R.E. (2007). "Concrete delamination caused by steel reinforcement corrosion." *Journal of Materials in Civil Engineering*, 19(7): 591-600.
- Li, D., Dong, L. and Laes, R.S. (2012). "Resonant ultrasound spectroscopy of cubes over the full range of Poisson's ratio." *Review of Scientific Instruments*, 83, 113902.
- Li, G. and Gladden, J.R. (2010). "High temperature resonant ultrasound spectroscopy: a review." *International Journal of Spectroscopy*, Article ID:206362, 1-13.
- Li, G., Luo, M., Huang, J. and Li, W. (2023). "Early-age concrete strength monitoring using smart aggregate based on electromechanical impedance and machine learning." *Mechanical Systems and Signal Processing*, 186: 109865.
- Li, H., Li, D. and Song, G. (2004). "Recent applications of fiber optical sensors to health monitoring in civil engineering." *Engineering Structures*, 26(11): 1647-1657.
- Li, P., Xu, S., Xu, D. and Xu, C. (2024). "Structural health monitoring of an aircraft wing using a portable wireless electromechanical impedance analyzer." *IEEE Sensors Journal*, 24(14): 22855.
- Li, T. and Xiao, J. (2021). "The damping property of damaged recycled aggregate concrete after loading." *Journal of Building Engineering*, 35: 102906.
- Li, W., Kong, Q., Ho, S.C.M., Lim, I. Mo, Y.L. and Song, G. (2016). "Feasibility study of using smart aggregates as embedded acoustic emission sensors for health monitoring of concrete structures." *Smart Materials and Structures*, 25: 115031.
- Li, W., Wang, J., Liu, T. and Luo, M. (2020). "Electromechanical impedance instrumented circular piezoelectric-metal transducer for corrosion monitoring: modeling and validation," *Smart Materials and Structures*, 29: 035008.
- Li, Y., Ma, Y. and Hu, X. (2021). "Early-age strength monitoring of the recycled aggregate concrete using the EMI method." *Smart Materials and Structures*, 30: 055017.
- Liang, C., Sun F.P. and Rogers, C.A. (1994). "Coupled electro-mechanical analysis of adaptive materials systems-determination of the actuator power consumption and

- system energy transfer.” *Journal of Intelligent Material Systems and Structures*, 5(1): 12-20.
- Lim, Y.Y., Simith, S.T., Padilla, R.V. and Soh, C.K. (2021). “Monitoring of concrete curing using the electromechanical impedance technique: review and path forward.” *Structural Health Monitoring*, 20(2): 604-636.
- Lin, Y. and Sansalone, M. (1992). “Detecting flaws in concrete beams and columns using the impact-echo method.” *ACI Materials Journal*, 89(4): 394-405.
- Liu, B., Tang, J., Xie, M. and Li, F. (2023). “Monitoring of curing process of concrete based on modulus and internal friction measurement using a quantitative electromechanical impedance method.” *Acta Mechanical Sinica*, 39: 423025.
- Liu, Q., Dai, G., Wang, C., Wu, X. and Ren, X. (2023). “Interfacial effect on quantitative concrete stress monitoring via embedded PZT sensors based on EMI technique.” *Buildings*, 13(2): 560.
- Lu, X., Lim, Y.Y. and Soh, C.K. (2018a). “A novel electromechanical impedance-based model for strength development monitoring of cementitious materials.” *Structural Health Monitoring*, 17(4): 902-918.
- Lu, X., Lim, Y.Y. and Soh, C.K. (2018b). “Investigation the performance of “smart probe” based indirect EMI technique for strength development monitoring of cementitious materials-modelling and parametric study.” *Construction and Building Material*, 172: 134-152.
- Lu, X., Lim, Y.Y., Izadgoshasb, I. and Soh, C.K. (2020). “Strength development monitoring and dynamic modulus assessment of cementitious materials using EMI-Miniature Prism based technique.” *Structural Health Monitoring*, 19(2): 373-389.
- Lu, X., Sun, Q., Feng, W. and Tian, J. (2013). “Evaluation of dynamic modulus of elasticity using impact-echo method.” *Construction and Building Materials*, 47: 231-239.
- Lydon, F.D. and Balendran, R.V. (1986). “Some observations on elastic properties of

- plain concrete.” *Cement and Concrete Research*, 16(3): 314-325.
- Ma, Z., Zhu, F. and Ba, G. (2019). “Effects of freeze-thaw damage on the bond behavior of concrete and enhancing measures.” *Construction and Building Materials*, 196: 375-385.
- Malone, C., Sun, H. and Zhu, J. (2023). “Nonlinear impact-echo test for quantitative evaluation of ASR damage in concrete.” *Journal of Nondestructive Evaluation*, 42: 93.
- Mangat, P. and Elgarf, M. (1999). “Flexure strength of concrete beams with corroding reinforcement.” *ACI Structural Journal*, 96(1): 149-158.
- Maruo, I.I.C., Giachero, G.F., Júnior, V.S. and Neto, R.M.F. (2015). “Electromechanical impedance-based structural health monitoring instrumentation system applied to aircraft structures and employing a multiplexed sensor array.” *Journal of Aerospace Technology and Management*, 7(3): 294-306.
- McCann, D.M. and Forde, M.C. (2001). “Review of NDT methods in the assessment of concrete and masonry structures.” 34: 71-84.
- McNiven, H.D. (1961). “Extensional waves in a semi-infinite elastic rod.” *The Journal of the Acoustic Society of America*, 33(1): 23-27.
- McNiven, H.D. and Shah, A.H. (1967). “The influence of the end mode on the resonant frequencies of finite, hollow, elastic rods.” *Journal of Sound and Vibration*, 6(1): 8-19.
- Measurement Specialties. (1999). Piezo film sensors: technical manual. (Norristown, PA: Measurement Specialties Inc.)
- Mehta, P.K. and Monteiro, P.J.M. (1993). Concrete-microstructure, properties, and materials, McGraw-Hill, 3<sup>rd</sup> edition.
- Meola, C. and Carlomagno, G.M. (2004). “Recent advances in the use of infrared thermography.” *Measurement Science and Technology*, 15: R27-R58.
- Mesbah, H.A., Lachemi, M. and Aïtcin, P. (2002). “Determination of elastic properties of high-performance concrete at early ages.” *ACI Materials Journal*, 99(1): 37-41.

- Migot, A. and Giurgiutiu, V. (2023). "Numerical and experimental investigation of delamination severity estimation using local vibration techniques." *Journal of Intelligent Materials Systems and Structures*, 34(9): 1057-1072.
- Mindlin, R.D. (1956). "Simple modes of vibration of crystals." *Journal of Applied Physics*, 27(12): 1462-1466.
- Mindlin, R.D. and Fox, E.A. (1960). "Vibrations and waves in elastic bars of rectangular cross section." *Journal of Applied Physics*, 27(1):152-158.
- Moharana, S. and Bhalla, S. (2019). "Development and evaluation of an external reusable piezo-based concrete hydration-monitoring sensor." *Journal of Intelligent Material Systems and Structures*, 30(18-19): 2770-2788.
- Na, S., Tawie, R. and Lee, H. (2012). "Electromechanical impedance method of fiber-reinforced plastic adhesive joints in corrosive environment using a reuseable piezoelectric device." *Journal of Intelligent Material Systems and Structures*, 23(7): 737-747.
- Nagy, A. (1997). "Determination of  $E$ -modulus of young concrete with nondestructive method." *Journal of Materials in Civil Engineering*, 9(1): 15-20.
- Narayanan, A., Kocherla, A. and Subramaniam, K.V.L. (2017). "Embedded PZT sensor for monitoring mechanical impedance of hydrating cementitious materials." *Journal of Nondestructive Evaluation*, 36: 64.
- Narayanan, A. and Subramaniam, K.V.L. (2016). "Sensing of damage and substrate stress in concrete using electro-mechanical impedance measurements of bonded PZT patches." *Smart Materials and Structures*, 25: 095011.
- Narayanan, A., Kocherla, A. and Subramaniam, K.V.L. (2018). "Understanding the coupled electromechanical response of a PZT patch attached to concrete: influence of substrate size." *Measurement*, 124: 505-514.
- Narayanan, S. (2024). "Effect of size and shapes of test specimen on compressive strength of concrete." *Concrete International*, 46(1): 45-51.
- Nazarian, S. and Reddy, S. (1996). "Study of parameters affecting impulse response

- method.” *Journal of Transportation Engineering*, 122(4): 308-315.
- Nehdi, M. and Soliman, A.M. (2009). “Early-age properties of concrete: overview of fundamental concepts and state-of-the art research.” *Construction Materials*, 164(2): 57-77.
- Neville, A.M. and Brooks, J.J. (2010). *Concrete technology*, 2<sup>nd</sup> ed. SA: Pearson Education.
- Oh, T., Popovics, J.S. and Sim, S. (2013). “Analysis of vibration for regions above rectangular delamination defects in solids.” *Journal of Sound and Vibration*, 332: 1766-1776.
- Ohtsu, M. and Alver, N. (2009). “Development of non-contact SIBIE procedure for identifying ungrouted tendon duct.” *NDT&E International*, 42: 120-127.
- Oliver, J. (1957). “Elastic wave dispersion in a cylindrical rod by a wide-band short duration pulse technique.” *Journal of the Acoustical Society of America*, 29: 189-194.
- Oluokun, F.A., Burdette, E.G. and Deatherage, J.H. (1990). “Early-age concrete: strength prediction by maturity-another look.” *ACI Materials Journal*, 87(6): 565-572.
- Omar, T. and Nehdi, M.L. (2017). “Remote sensing of concrete bridge decks using unmanned aerial vehicle infrared thermography.” *Automation in Construction*, 83: 360-371.
- Omar, T., Nehdi, M.L. and Zayed, T. (2018). “Infrared thermography model for automated detection of delamination in RC bridge decks.” *Construction and Building Materials*, 168: 313-327.
- Ono, K. (2017). “Through-transmission characteristics of AE sensor couplants.” *Journal of Acoustic Emission*, 34: 1-11.
- Ozman, G.C., Safaei, M., Lan, L. and Inan, O.T. (2021). “A novel accelerometer mounting method for sensing performance improvement in acoustic measurements from the knee.” *Journal of Vibration and Acoustics*, 143(3): 031006.

- Pan, H.H. and Huang, M. (2020). "Piezoelectric cement sensor-based electromechanical impedance technique for the strength monitoring of cement mortar." *Construction and Building Materials*, 254: 119307.
- Papageorgiou, A.V. and Gantes, C.J. (2010). "Equivalent modal damping ratios for concrete/steel mixed structures." *Computers and Structures*, 88: 1124-1136.
- Park, G., Cudney, H.H. and Inman, D.J. (2000). "Impedance-based health monitoring of civil structural components." *Journal of Infrastructure Systems*, 6(4): 153-160.
- Park, G., Kabeya, K., Cudney, H.H. and Inman, D.J. (1999). "Impedance-based structural health monitoring for temperature varying applications." *JSME International Journal Series A Solid Mechanics and Material Engineering*, 42(2): 249-258.
- Park, G., Sohn, H., Farrar, C.R. and Inman, D.J. (2003). "Overview of piezoelectric impedance-based health monitoring and path forward." *The Shock and Vibration Digest*, 35(6): 451-463.
- Park, S. and Park, S. (2010). "Quantitative corrosion monitoring using wireless electromechanical impedance measurements." *Research in Nondestructive Evaluation*, 21: 184-192.
- Park, S., Shin, H. and Yun, C. (2009). "Wireless impedance sensor nodes for functions of structural damage identification and sensor self-diagnosis." *Smart Materials and Structures*, 18: 055001.
- Park, S., Yun, C., Roh, Y. and Lee, J. (2006). "PZT-based active damage detection techniques for steel bridge components." *Smart Materials and Structures*, 15: 957-966.
- Pauw, A. (1960). "Static modulus of elasticity of concrete as affected by density," *ACI Journal Proceedings*, 57(12): 679-688.
- Peairs, D.M., Park, G. and Inman, D.J. (2004). "Improving accessibility of the impedance-based structural health monitoring method." *Journal of Intelligent Material Systems and Structures*, 15(2): 129-139.

- Persson, B. (1999). "Poisson's ratio of high-performance concrete." *Cement and Concrete Research*, 29: 1647-1653.
- Piezo system, "Technique specifications of support documents (America: wildwood Avenue)," 2024, <https://support.piezo.com/article/62-material-properties>.
- Popovics, S. (1975). "Verification of relationships between mechanical properties of concrete-like materials." *Matériaux et Constructions*, 8(3): 183-191.
- Popovics, S. (1998). "Strength and related properties of concrete: a quantitative approach." John Wiley & Sons, New York.
- Popovics, J.S. (2008). "A study of static and dynamic modulus of elasticity of concrete." ACI-CRC Final Report.
- Press Releases, The Government of the Hong Kong Special Administrative Region. <https://www.info.gov.hk/gia/general/200101/17/0117185.htm>
- Qing, X.P., Chan, H., Beard, S.J., Ooi, T.K. and Marotta, S.A. (2006). "Effect of adhesive on the performance of piezoelectric elements used to monitor structural health." *International Journal of Adhesion and Adhesives*, 26(8): 622-628.
- Raja, B.N.K., Miramini, S., Duffield, C., Sofi, M. and Zhang, L. (2021). "Infrared thermography detection of delamination in bottom of concrete bridge decks." *Structural Control and Health Monitoring*, 29: e2886.
- Rao, S.S. (2007). *Vibration of continuous system*. 1<sup>st</sup> edition. John Wiley & Sons.
- Rehman, S.K.U., Ibrahim, Z., Memon, S.A. and Jameel, M. (2016). "Nondestructive test methods for concrete bridges: a review." *Construction and Building Materials*, 107: 58-86.
- Roth, W. and Giurgiutiu, V. (2017). "Structural health monitoring of an adhesive disbond through electromechanical impedance spectroscopy." *International Journal of Adhesion and Adhesives*, 73: 109-117.
- Sabat, R.G., Mukherjee, B.K., Ren, W. and Yang, G. (2007). "Temperature dependence of the complete material coefficients matrix of soft and hard doped piezoelectric lead zirconate titanate ceramics," *Journal of Applied Physics*, 101(6): 064111.



- Sajid, S. Chouinard, L. and Taras, A. (2021). "Developing a new understanding of the impulse response test for defect detection in concrete plates." *Journal of Engineering Mechanics*, 148(1): 04021125.
- Sansalone, M. (1997). "Impact-echo: the complete story." *ACI Structural Journal*, 94(6): 777-785.
- Sansalone, M. and Streett, W.B. (1997). *Impact-echo: nondestructive testing of concrete and masonry*, Bullbrier Press, Jersey Shore, PA.
- Sant, G., Dehadrai, M., Bentz, D., Lura, P., Ferraris, C.F., Bullard, J.W. and Weiss, J. (2009). "Detecting the fluid-to-solid transition in cement pasts." *Concrete International*, 31(6): 53-58.
- Shin, S.W., Qureshi, A.R., Lee, J. and Yun, C.B. (2008). "Piezoelectric sensor based nondestructive active monitoring of strength gain in concrete." *Smart Materials and Structures*, 17: 055002.
- Shin, S.W. and Oh, T.K. (2009). "Application of electro-mechanical impedance sensing technique for online monitoring of strength development in concrete using smart patches." *Construction and Building Materials*, 23(2): 1185-1188.
- Shokouhi, P., Wöstmann, J., Schneider, G., Milmann, B., Taffe, A., and Wiggerhauser, H. (2011). "Nondestructive Detection of Delamination in Concrete Slabs: Multiple-Method Investigation." *Transportation Research Record*, 2251(1): 103-113.
- Shoukry, S.N., William, G.W., Downie, B. and Riad, M.Y. (2011). "Effect of moisture and temperature on the mechanical properties of concrete," *Construction and Building Materials*, 25(2): 688-696.
- Simmons, J.C. (1955). "Poisson's ratio of concrete: a comparison of dynamic and static measurements." *Magazine of Concrete Research*, 7(20): 61-68.
- Smith, I.M. and Kidger D.J. (1991). "Properties of the 20-node brick." *International Journal for Numerical and Analytical Methods in Geomechanics*, 15: 871-891.
- Smith, J., Wyrick, M. and Poole, J. (1990). "An evaluation of three techniques for

- determining the Young's modulus of mechanically alloyed materials." *Dynamic Elastic Modulus Measurements in Materials*, ed. A. Wolfenden (West Conshohocken, PA: ASTM International, 1990): 195–207.
- Smith, P.A. and Wood, J.R. (1990). "Poisson's ratio as a damage parameter in the static tensile loading of simple crossply laminates." *Composites Science and Technology*, 38: 85-93.
- Singh, S.K., Shanker, R. and Ranjan, A. (2024). "Health monitoring of steel structures using surface mountable and detachable PZT sensor." *Journal of Intelligent Material Systems and Structures*, 35(4): 380-392.
- Soh, C.K. and Bhalla, S. (2005). "Calibration of piezo-impedance transducers for strength prediction and damage assessment of concrete." *Smart Materials and Structures*, 14: 671-684.
- Soh, C.K., Tseng, K.K, Bhalla, S. and Gupta, A. (2000). "Performance of smart piezoceramic patches in health monitoring of a RC bridge." *Smart Materials and Structures*, 9: 533-542.
- Solodov, I., Bai, J. and Busse, G. (2013). "Resonant ultrasound spectroscopy of defects: Case study of flat-bottomed holes." *Journal of Applied Physics*, 113: 223512.
- Solodov, I. Rahammer, M. and Kreutzbruck, M. (2019). "Analytical evaluation of resonance frequencies for planar defects: effect of a defect shape." *NDT and E International*, 102: 274-280.
- Song, G., Gu, H. and Mo, Y. (2008). "Smart aggregate: multifunctional sensors for concrete structures- a tutorial and a review." *Smart Materials and Structures*, 17: 003001.
- Song, G., Gu, H., Mo, Y.L., Hsu, T.T.C. and Dhong, H. (2007). "Concrete structural health monitoring using embedded piezoceramic transducers." *Smart Materials and Structures*, 16: 959-968.
- Song, H., Lim, H.J. and Sohn, H. (2013). "Electromechanical impedance measurement from large structures using a dual piezoelectric transducer." *Journal of Sound and*

*Vibration*, 332: 6580-6595.

- Soutsos, M.N., Bungey, J.H., Long, A.E. and Henderson, G.D. (2000). "In-situ strength assessment of concrete- the European concrete frame building project." *Proceedings of the 5<sup>th</sup> International Conference on NDT in Civil Engineering*, T. Uomoto, ed., Apr. Elsevier Science, Tokyo: 583-592.
- Su, R. K. L. and Zhang, Y. (2019). "A novel elastic-body-rotation model for concrete cover spalling caused by non-uniform corrosion of reinforcement." *Construction and Building Materials*, 213: 549-560.
- Su, Y.F, Han, G., Amran, A., Nantung, T. and Lu, N. (2019). "Instantaneous monitoring the early age properties of cementitious materials using PZT-based electromechanical impedance (EMI) technique." *Construction and Building Materials*, 225: 340-347.
- Su, Y.F, Han, G., Nantung, T. and Lu, N. (2020). "Novel methodology on direct extraction of the strength information from cementitious materials using piezo-sensor based electromechanical impedance (EMI) method." *Construction and Building Materials*, 259: 119848.
- Sun, F.P., Chaudhry, Z., Liang, C. and Rogers, C.A. (1995). "Truss structure integrity identification using PZT sensor-actuator." *Journal of Intelligent Materials Systems and Structures*, 6(1): 134-139.
- Sun, F.P., Liang, C. and Rogers, C.A. (1994). "Structural modal analysis using collocated piezoelectric actuator/sensors—an electromechanical approach." *Proceedings of the SPIE*, 2190: 238-249.
- Sun, H., Zhu, J. and Ham, S. (2018). "Automated acoustic scanning system for the delamination detection in concrete bridge decks." *Journal of Bridge Engineering*, 23(6): 04018027.
- Swamy, N. and Rigby, G. (1971). "Dynamic properties of hardened paste, mortar and concrete." *Matériaux et Constructions*, 4(19): 13-40.
- Swamy, R. N. (1971). "Dynamic Poisson's ratio of Portland cement past, mortar and

- concrete.” *Cement and Concrete Research*, 1(5), 559-583.
- Tamhance, D., Thalapil, J., Banerjee, S. and Tallur, S. (2021). “Smart cathodic protection system for real-time quantitative assessment of corrosion of sacrificial anode based on electro-mechanical impedance (EMI).” *IEEE Access*, 9: 12230-12240.
- Tamrakar, P., Nazarian, S. Garibay, J.L. and Azari, H. (2018). “Feasibility of impulse response test for characterizing railway ballasts.” *Journal of Materials in Civil Engineering*, 30(2): 04017287.
- Tang, Z.S., Lim, Y.Y., Smith, S.T. and Padilla, R.V. (2020). “Modelling of the electromechanical impedance technique for prediction of elastic modulus of structural adhesives.” *Structural Health Monitoring*, 20(5): 2245-2260.
- Tawie, R. and Lee, H.K. (2010). “Monitoring the strength development in concrete by EMI sensing technique.” *Construction and Building Materials*, 24: 1746-1753.
- Tenek, L.H., Henneke, E.G. and Gunzburger, M.D. (1993). “Vibration of delaminated composite plate and some application to non-destructive testing.” *Composite Structures*, 23: 253-262.
- Tennakoon, S. (2016). “Temperature and pressure effects on elastic properties of relaxor ferroelectrics and thermoelectric: a resonant ultrasound spectroscopy study.” Ph.D. thesis, University of Mississippi, Mississippi, American.
- Tenreiro, A.F.G., Lopes, A.M. and da Silva, L.FM. (2022). “A review of structural health monitoring of bonded structures using electromechanical impedance spectroscopy.” *Structural Health Monitoring*, 21(2): 228-249.
- Theobald, P., Zeqiri, Bajram., and Avison, J. (2008). “Couplants and their influence on AE sensor sensitivity.” 28<sup>th</sup> European Conference on Acoustic Emission Testing, Krakow, Poland, 17-19 September.
- Thomaz, W.A., Miyaji, D.Y. and Possan, E. (2021). “Comparative study of dynamic and static Young’s modulus of concrete containing basaltic aggregates.” *Case Studies in Construction Materials*, 15: e00645.

- Ting, M.Z.Y., Wong, K.S., Rahman, M.E. and Meheron, S.J. (2021). "Deterioration of marine concrete exposed to wetting-drying action." *Journal of Cleaner Production*, 278: 123383.
- Trainer, M. (2003). "Kelvin and piezoelectricity." *European Journal of Physics*, 24: 535-542.
- Tseng, K.K. and Wang, L. (2004). "Smart piezoelectric transducers for in situ health monitoring of concrete." *Smart Materials and Structures*, 13: 1017-1024.
- Tzou, K.I., Wickert, J.A. and Akay, A. (1998). "In-plane vibration modes of arbitrarily thick disks." *Journal of Vibration and Acoustics*, 120(2): 384-391.
- Vakhshouri, B. (2018). "Modulus of elasticity of concrete in design codes and empirical models: analytical study." *Practical Periodical on Structural Design and Construction*, 23(4): 04018022.
- Van Paepegem, W., De Baere, I., Lamkanfi, E. and Degrieck, J. (2010). "Monitoring quasi-static and cyclic fatigue damage in fibre-reinforced plastic by Poisson's ratio evolution." *International Journal of Fatigue*, 32(1): 184-196.
- Venkiteela, G., Sun, Z. and Najm, H. (2013). "Prediction of early age normal concrete compressive strength based on dynamic shear modulus measurements." *Journal of Materials in Civil Engineering*, 25(1): 30-38.
- Wang, D., Li, Z. and Zhu, H. (2016). "A new three-dimensional electromechanical impedance model for an embedded dual-PZT transducer." *Smart Material and Structures*, 25: 075002.
- Wang, D., Song, H. and Zhu, H. (2013). "Numerical and experimental studies on damage detection of a concrete beam based on PZT admittances and correlation coefficient." *Construction and Building Materials*, 49: 564-574.
- Wang, D., Song, H. and Zhu, H. (2014). "Embedded 3D electromechanical impedance model for strength monitoring of concrete using a PZT transducer." *Smart Materials and Structures*, 23: 115019.
- Wang, S., Leng, Z. and Sui, X. (2023). "Detectability of concealed cracks in the asphalt

- pavement layer using air-coupled ground-penetrating radar.” *Measurement*, 208: 112427.
- Wang, Z., Chen, D., Zheng, L., Huo, L. and Song, G. (2018). “Influence of axial load on electromechanical impedance of embedded piezoceramic transducers in steel fiber concrete.” *Sensors*, 18: 1782.
- Wang, Z., Gao, Z., Wang, Y., Cao, Y., Wang, G., Liu, B. and Wang, Z. (2015). “A new dynamic testing method for elastic, shear modulus and Poisson’s ratio of concrete.” *Construction and Building Materials*, 100: 129-135.
- Wetzel, A., Glotzbach, C., Maryamh, K. and Middendorf, B. (2015). “Microstructural investigation on the skinning of ultra-high performance concrete.” *Cement and Concrete Composites*, 57: 27-33.
- Xi, Y., Zhang, W., Pi, Y., Zou W. and Yang, F. (2021). “Comparative study on damping test methods of concrete materials.” *Construction and Building Materials*, 300: 124367.
- Xie, M. and Li, F. (2020). “A modified piezoelectric ultrasonic composite oscillator technique for simultaneous measurement of elastic moduli and internal frictions at varied temperature.” *Review of Scientific Instruments*, 91: 015110.
- Xu, B. and Giurgiutiu, V. (2005). “A low-cost and field portable electromechanical (E/M) impedance analyzer for active structural health monitoring.” 5<sup>th</sup> *International Workshop on Structural Health Monitoring*, Stanford University, Standford, CA.
- Yang, M. and Qiao, P. (2005). “Modelling and experimental detection of damage in various materials using the pulse-echo method and piezoelectric sensors/actuators.” *Smart Materials and Structures*, 14(6): 1083.
- Yan, W., Chen, W.Q., Cai, J.B. and Lim, C.W. (2007a). “Quantitative structural damage detection using high-frequency piezoelectric signatures via the reverberation matrix method.” *International Journal for Numerical Methods in Engineering*, 71: 505-528.

- Yan, W., Lim, C.W., Cai, J.B. and Lim, C.W. (2007b). "An electromechanical impedance approach for quantitative damage detection in Timoshenko beams with piezoelectric patches." *Smart Materials and Structures*, 16: 1390.
- Yan, W., Lim, C.W., Chen, W.Q. and Cai, J.B. (2007c). "Modeling of EMI response of damaged Mindlin-Herrmann rod." *International Journal of Mechanical Sciences*, 49: 1355-1365.
- Yang, Y., Divsholi, B.S. and Soh, C.K. (2010). "A Reusable PZT transducer for monitoring initial hydration and structural health of concrete." *Sensors*, 10: 5193-5208.
- Yang, Y., Hu, Y. and Lu, Y. (2008). "Sensitivity of PZT impedance sensors for damage detection of concrete structures." *Sensors*, 8: 327-346.
- Yang, Y., Lim, Y.Y. and Soh, C.K. (2008a). "Practical issues related to the application of the electromechanical impedance technique in the structural health monitoring of civil structures: I. experiment." *Smart Materials and Structures*, 17(3): 035008.
- Yang, Y., Lim, Y.Y. and Soh, C.K. (2008b). "Practical issues related to the application of the electromechanical impedance technique in the structural health monitoring of civil structures: II. numerical verification." *Smart Materials and Structures*, 17(3): 035009.
- Yilmaz, C., Akalin, C., Kocaman, E.S., Suleman, A. and Yildiz, M. (2016). "Monitoring Poisson's ratio of glass fiber reinforced composites as damage index using biaxial fiber Bragg Grating sensors." *Polymer Testing*, 53: 98-107.
- Yu, H., Lu, L. and Qiao, P. (2020). "Assessment of wave modulus of elasticity of concrete with surface bonded piezoelectric transducers." *Construction and Building Materials*, 242: 118033.
- Yoon, Y.G., Choi, H. and Oh, T.K. (2020). "Study on prediction and application of initial chord elastic modulus with resonance frequency test of ASTM C215." *Applied Sciences*, 10: 5464.
- Zagrai, A. and Giurgiutiu, V. (2002). "Electro-mechanical impedance method for crack

- detection in thin plates.” *Journal of Intelligent Materials Systems and Structures*, 12(10): 709-718.
- Zahedi, F. and Huang, H. (2017). “Time-frequency analysis of electromechanical impedance (EMI) signature for physics-based damage detection using piezoelectric wafer active sensor (PWAS).” *Smart Material and Structures*, 26: 055010.
- Zein, A.S. and Gassman, S.L. (2010). “Frequency spectrum analysis of impact-echo waveforms for T-beams.” *Journal of Bridge Engineering*, 15(6): 705-714.
- Zhang, C., Wang, X., Yan, Q., Vipulanandan, C. and Song, G. (2020). “A novel method to monitor soft soil strength development in artificial ground freezing projects based on electromechanical impedance technique: theoretical modeling and experimental validation.” *Journal of Intelligent Material Systems and Structures*, 31(2): 1477-1494.
- Zhang, J., Ling, X. and Guan, Z. (2017). “Finite element modeling of concrete cover crack propagation due to non-uniform corrosion of reinforcement.” *Construction and Building Materials*, 132: 487-499.
- Zhang, X., Zhang, Y., Liu, B., Liu, B. Wu, W. and Yang, C. (2021). “Corrosion-induced spalling of concrete cover and its effect on shear strength of RC beams.” *Engineering Failure Analysis*, 127: 105538.
- Zhang, X., Zhou, W. and Li, H. (2019). “Electromechanical impedance-based ice detection of stay cables with temperature compensation,” *Structural Control and Health Monitoring*, 26: e2384.
- Zhang, Y. and Su, R.K.L. (2021). “Experimental investigation of process of corrosion-induced cover delamination using digital image correlation.” *Construction and Building Materials*, 312: 125287.
- Zhao, S., Fan, S., Yang, J. and Kitipornchai, S. (2020a). “Numerical and experimental investigation of electro-mechanical impedance based concrete quantitative damage assessment.” *Smart Material and Structures*, 29: 055025.



- Zhao, S., Fan, S., Yang, J. and Kitipornchai, S. (2020b). "A spherical smart aggregate sensor based electro-mechanical impedance method for quantitative damage evaluation of concrete." *Structural Health Monitoring*, 19(5): 1560-1576.
- Zheng J.J., Li, C.Q. and Jones, M.R. (2003). "Aggregate distribution in concrete with wall effect." *Magazine of Concrete Research*, 55(3): 257-265.
- Zheng, X., Wang, Y., Zhang, S., Xu, F., Zhu, X., Jiang, X., Zhou, L., Shen, Y., Chen., Q., Yan, Z., Zhao, W., Zhu, H. and Zhang. Y. (2022). "Research progress of the thermophysical and mechanical properties of concrete subjected to free-thaw cycles." *Construction and Building Materials*, 330:127254.
- Zhou, S.W., Liang, C. and Rogers, C.A. (1994). "A dynamic model of piezoelectric actuator-driven thin plates." *SPIE Proceedings*, 550-562.
- Zhou, S., Liang, C. and Rogers, C.A. (1995). "Integration and design of piezoelectric patch actuators." *Journal of Intelligent Materials Systems and Structures*, 6(1): 125-133.
- Zhou, Y., Gao, J., Sun, Z. and Qu, W. (2015). "A fundamental study on compressive strength, static and dynamic elastic moduli of young concrete." *Construction and Building Materials*, 98: 137-145.
- Zhu, J. and Popovics, J.S. (2007). "Imaging concrete structures using air-coupled impact-echo." *Journal of Engineering Mechanics*, 133(6): 628-640.
- Zhu, J., Wang, Y. and Qing, X. (2019). "A novel electromechanical impedance model for surface-bonded circular piezoelectric transducer." *Smart Materials and Structures*, 28: 105052.
- Zuo, C., Feng, X. and Zhou, J. (2013). "A three-dimensional model of the effective electromechanical impedance for an embedded PZT transducer." *Mathematical problems in Engineering*, Article ID: 218026: 10 pages.